Gas thickness and the radial spin current

What the observations resolve in NGC 2403

Between **10.93 and 16.89 kpc**, thirteen rotation measurements overlap both the H I column map and a published radial thickness profile. If neutral hydrogen supplies the entropy density in the original ESFD galaxy equation, the weighted radial spin current must increase **3.96-fold** between those endpoints. Thickness gives the reconstruction a physical depth. Polarimetry leaves the microscopic direction undetermined.

Measurement	Result	What enters the calculation
Disk orientation	Inclination 63°, receding axis at position angle 124°	Constrains the orientation of bulk rotation. A ring's angular-momentum normal has zero radial projection within its local plane.
Radio polarization	28 ± 5 mJy integrated, 30–50 μJy per beam typical after smoothing	Constrains the sky projection of the ordered magnetic field. The disk signal is faint.
Neutral disk thickness	Published Gaussian scale height 0.08 to 0.68 kpc at 0.64 to 17.61 kpc	The authors infer the heights from H I kinematics and vertical hydrostatic balance in a fitted potential.
Extraplanar hydrogen	Flux-weighted exponential scale height 0.93 kpc	Li et al. model a distinct fountain component out to 12.5 kpc. The main-disk calculation uses the disk heights above.

Heald et al. report **21 ± 4°** for the optical spiral pitch. Their polarization data leave the radial sign of the microscopic spin expectation open. Linear polarization has a 180° ambiguity. Faraday rotation measures a line-of-sight field weighted by free electrons. Neither supplies the directed spin density in $J = \varepsilon S u/2$ without an independently calibrated material response. A spin temperature constrains level populations, and opposite magnetic-sublevel imbalances can have the same temperature and entropy.

Heald et al., Table 1 and NGC 2403 notes · Mancera Piña et al., disk dynamics · Authors' radial tables · Li et al., extraplanar H I.

Converting the measured column into volume entropy

In the original stationary spherical weak-gravity reduction, $Q = \beta_s s J_r/c^2 = (v^2 - v_b^2)/(4\pi G r)$. The galaxy residual determines Q. To obtain s, identify it with the midplane neutral-hydrogen hyperfine entropy. Write $L = \sqrt{(2\pi)}h$ for a Gaussian of standard deviation h, $N = \Sigma_{HI}/m_H$ and $s = N k_B H/L$, where H is dimensionless entropy per atom. This uses a disk midplane tracer for the radial field in a spherical effective calculation.

Braun's 53 ± 15 K sightline at 2.620 kpc fixes the entropy scale under equal occupation of the triplet magnetic sublevels. Here h = 0.1424 kpc, L = 0.3570 kpc, and the inferred midplane entropy is $\mathbf{1.486 \times 10^{-17}\ J\ K^{-1}\ m^{-3}}$. The rotation inversion then gives $\mathbf{\beta_s J_r/c^2 = 4.044 \times 10^{15}\ kg\ K\ m/J}$. An independent oriented spin density would separate β_s from J_r. The anchor uses a pencil-beam temperature, an annular H I column and an interpolated rotation residual at the same radius.

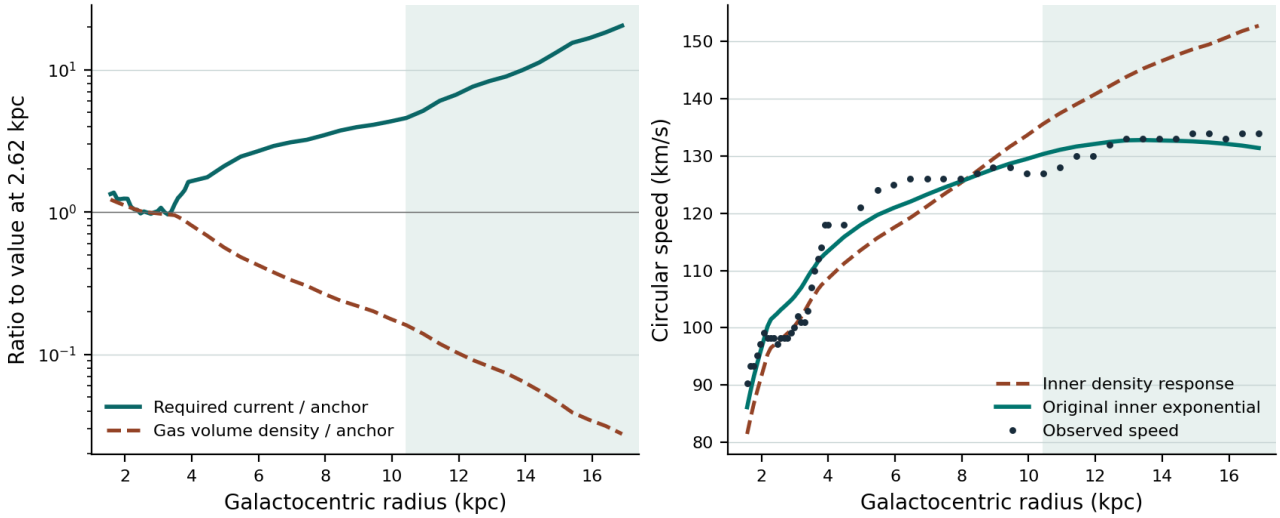

The shaded region starts beyond the last training radius. The left panel reconstructs the source from the measured speed. On the right, both model curves use the inner data alone. All calculations retain the archived baryonic mass contributions. The thickness tables use a distance of 3.2 Mpc for NGC 2403. Their radii and heights have been scaled together to the project distance of 3.16 Mpc.

Braun, 21-cm absorption, Table 3 · HALOGAS map release · SPARC rotation curves · Thickness supplement.

What drives the rise inside the SFD equation?

Across the same thirteen outer rings the fitted log slopes are −0.599 for Q, −2.941 for the H I column, and +0.798 for the scale height. At constant per-atom entropy this gives a volume-density slope of −3.739 and a required current slope of **+3.140**. The alternative halo-concentration prior gives +3.121. Drawing the reported speed errors independently yields +2.97 to +3.30 for the primary fit, conditional on the baryonic model, geometry and H I profile. The former +3.470 result applied to the current per depth over a longer interval reaching 20.87 kpc.

> $J_r/J_{r,0} = (Q/Q_0)\,(\Sigma_0/\Sigma)\,(h/h_0)\,(H_0/H)$.

Keeping the current constant would require h to fall with slope −2.34, whereas the measured gas model flares. If the same atoms also supply the spin tensor, J_r scales with number density times signed radial spin fraction P. The corresponding P rises with slope +6.88. The largest $|P/P_0|$ is 738 in the measured donor profile. The bound $|P| \le 1$ implies $|P_0| \le 0.00136$ under this common-carrier and near-maximal-entropy approximation. Significant sublevel polarization would require recomputing H.

A source constraint in the original theory

The stationary SFD equation reads $\beta_s \operatorname{div} J = 2\gamma_s \Delta s - U'(s)$. The measured endpoint ratio of $r^2\beta_s J_r$ is **9.47**. Its nominal value increases across all twelve adjacent shells. The shell mean of $(2\gamma_s \Delta s - U')/c^2$ ranges from 3.11×10^{-4} to 8.61×10^{-4} kg K/J under the adopted entropy normalization. These are finite differences of the flux, with shared rings and correlated systematics. They supply a target for the material dynamics.

With a regular center, the enclosed mean is $\langle U' \rangle = 6\gamma_s s'/r - 3c^2 Q/(rs)$. The fitted entropy decreases across every outer interval while Q is positive. Positive stiffness therefore requires a negative enclosed mean potential derivative wherever s' is negative. Many potentials and material spin states satisfy this condition. The sign and shell strengths narrow the original equations without identifying a unique microscopic source.

Original ESFD direct action and SFD entropy variation, as reproduced in the preceding studies · Disk thickness model and its halo priors. Numerical checks and shell-by-shell results accompany the paper.

Transferring the same weights to other galaxies

Every target uses the NGC 2403 normalization at 2.62 kpc. Let $x = (\Sigma/h)/(\Sigma_0/h_0)$. Constant current predicts $Q/Q_0 = x$, and constant spin fraction in the same gas predicts x^2. A third test allows $J/J_0 = x^p$, with $p = \mathbf{-0.9258}$ fitted solely to 38 NGC 2403 measurements at 1.57–10.43 kpc. It predicts $Q/Q_0 = x^{0.0742}$. This exponent summarizes the donor data. The original equations supply the force and circular speed. The comparison imposes no outer speed or asymptotic slope.

Prescription	NGC 2403 outer, 13 rings	Two other spirals, 39 rings	Ten dwarfs, 307 rings
Baryons alone	71.27	40.29	20.34
Original inner exponential	1.62	10.89	28.81
Fixed H I column weight	38.36	18.52	10.19
Fixed volume current	61.13	33.20	13.28
Fixed spin fraction	70.40	38.91	18.58
Inner density response	13.80	12.36	18.88

Entries give mean per-galaxy speed RMSE in km/s. The density response improves on baryons in both comparison spirals and six dwarfs. The simpler column weight improves nine dwarfs. On the 137 outer dwarf rings the density response gives 21.34 km/s, the column weight 7.86, and baryons 24.24. Only one outer comparison-spiral ring has all three inputs, so their column reports the full joint radial coverage.

NGC 2403's outer speed slope is +0.090. The fitted density response predicts +0.242 and the original exponential +0.004 on the held rings. The exponential reproduces this finite near-plateau while ultimately decaying, and transfers poorly to these dwarfs. The density response supplies a partial explanation for the inferred rise in the donor, but does not establish a common spin law or flat speeds at arbitrarily large radius.

SPARC · Oh et al., resolved mass models · Hunter et al., dwarf H I distributions · Mancera Piña et al..

What hydrogen spin measures in NGC 2403

One spin-temperature detection and four radial limits

At a disk radius of **2.62 kpc**, Braun measured an effective 21-cm spin temperature of **53 ± 15 K** in NGC 2403. This measures the relative occupations of the atomic hydrogen singlet and triplet. It supplies an observational constraint independent of fitting the galaxy's rotation curve. The continuum source is an H II region inside the galaxy. Uncertain foreground depth and beam filling affect the measurement.

Disk radius, kpc	Spin temperature	H I column, solar masses/pc²	Required Q / H I mass column
2.62	53 ± 15 K	6.85	4.20
8.49	>62 K	4.32	5.94
11.32	>63 K	2.85	7.23
13.94	>45 K	1.76	10.47
17.56	>63 K	0.73	22.18

These are all the sightlines with a spin detection or limit inside the archived rotation curve. A fifth limit, >9 K at 32.03 kpc, lies beyond it. Three additional sightlines have no spin constraint. Radii use Braun's disk-plane angles and the project distance of 3.16 Mpc. The table pairs a pencil-beam temperature with the azimuthally averaged hydrogen column and the rotation-inferred source at that radius.

How much entropy does the line measure?

Write $T_{hf} = h\nu/k_B = 0.068169$ K and $p_1/p_0 = 3\exp(-T_{hf}/T_s)$. For equal occupation of the three triplet sublevels, the entropy per atom in units of k_B is $h_{hf} = -p_0 \ln p_0 - p_1 \ln(p_1/3)$. At the detection, $p_1 = 0.749759$ and $h_{hf} = 1.38629421$. The maximum is $\ln 4 = 1.38629436$. At each of the three outer limits the fractional deficit from that maximum is below $\mathbf{1.56 \times 10^{-7}}$ in this effective-temperature calculation.

Braun's independent spectral-shape analysis gives kinetic temperatures of 87, 90, 94, 94 and 108 K in five radial zones centered between 1.76 and 15.55 kpc. These fits characterize the bright H I filament network. Identifying its kinetic and spin temperatures would give the same near-saturation. Unresolved mixtures and polarized sublevels can carry different entropy at the same reported effective temperature.

Braun, absorption measurements, Table 3 · Braun, emission-line fits, Table 3 · HALOGAS intensity maps · Laboratory measurement of the hydrogen hyperfine splitting.

Where the slower falloff enters the rotation curve

The original stationary spherical ESFD source obeys $Q_r = \beta_s s J_r/c^2 = (v^2 - v_b^2)/(4\pi G r)$. The baryonic force retains the project's disk geometry. On the 21 outer measurements, between 10.93 and 20.87 kpc, the inferred Q_r has a logarithmic slope of **−0.651**. The original inner exponential gives **−0.922** on those same radii. Across the span of the three outer absorption sightlines, that slope difference corresponds to a **12.6%** relative change. The measured level-population entropy per atom has too little temperature dependence to account for it.

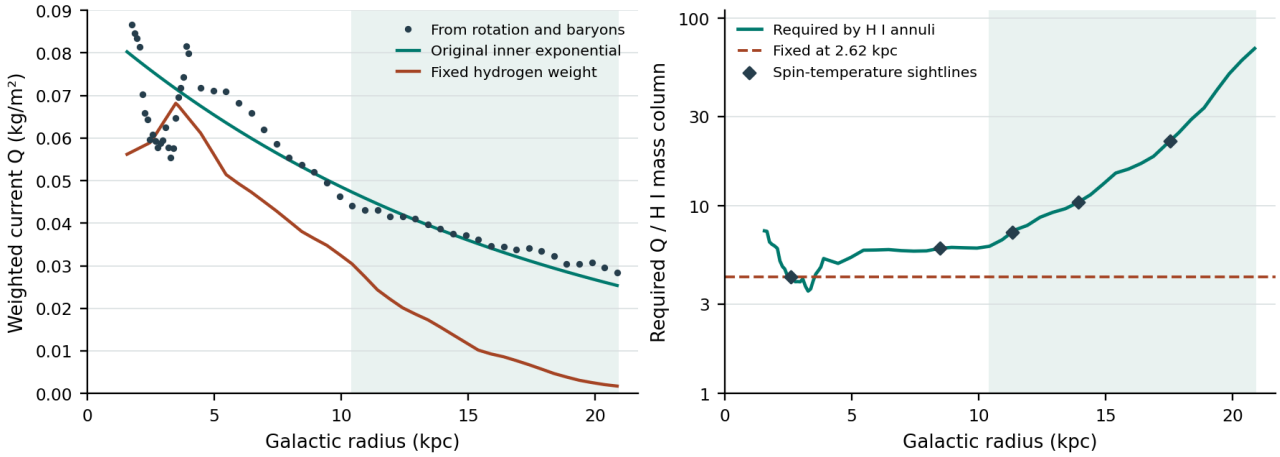

The shaded region is the outer half of the measured radius. Dots on the left are inferred from speeds and the baryonic model. Diamonds on the right mark radii with independent spin-temperature information. The gas-column prediction uses the single 2.62 kpc calibration. The near equality of the triplet/singlet entropy across these temperatures makes the ratio on the right effectively independent of its tiny temperature correction.

Speed, baryons and the explicit radial factor

The measured Q slope splits as **−1 + 0.162 + 0.187**. The −1 comes from the explicit 1/r. The other terms come from the variation of the observed squared speed and the decline in the modeled baryonic squared speed, respectively. The split uses exact adjacent differences in $\ln(v^2 - v_b^2)$, with the same log-radius fit for every term. It explains the observed kinematics conditional on the mass model.

Drawing independent speeds from their quoted uncertainties gives a conditional 95% slope range of −0.819 to −0.497. Varying the stellar disk mass-to-light ratio from 0.4 to 0.6 shifts the nominal slope from −0.682 to −0.618. These checks hold distance and inclination fixed. The reconstruction is a finite-disk measurement and leaves the behavior beyond 20.87 kpc open.

Original ESFD/SEFD equation guide §§8–10 · SPARC rotation and baryonic mass models · The numerical decomposition, noise draws and map-coverage checks are in the research files.

What the original entropy equation adds

The radio measure supplies an entropy **per area** if the neutral-hydrogen hyperfine states represent the SFD carrier. Let N be the face-on H I number column, $L = N/n$ its effective depth, and $S_A = N k_B h_{hf}$. Then $s = S_A/L$ and

$$Q_r/S_A = \beta_s J_r/(c^2 L).$$

At 2.62 kpc the annular column gives $S_A = \mathbf{163.7\ J\ K^{-1}\ m^{-2}}$ and $Q_r = \mathbf{0.06010\ kg\ m^{-2}}$. Their ratio is $\mathbf{3.67 \times 10^{-4}\ kg\ K/J}$. A single Gaussian with 1 kpc full width at half maximum would give a midplane s of 4.98×10^{-18} J K^{-1} m^{-3}. At 3 kpc width it would be 1.66×10^{-18}. Line-profile observations admit a thin disk plus a more slowly rotating thick component. Those illustrative single-layer conversions require a choice of which material carries the field.

A sign test inside SFD

For a regular center, the original stationary equation $\beta_s \nabla\cdot J = 2\gamma_s \nabla^2 s - U'(s)$ integrates to

$$c^2 Q_r = \gamma_s (s^2)' - (s/r^2) \int_0^r t^2\, U'(s(t))\, dt.$$

If the entropy potential is constant throughout the enclosed region, positive stiffness γ_s requires Q_r and $(s^2)'$ to have the same sign. For neutral hyperfine entropy in a layer of fixed or increasing effective depth, the outer gas profile makes $(s^2)'$ negative. **All 21 NGC 2403 outer points require positive Q_r.** All 99 covered outer rows in the ten primary dwarfs also require a positive source under the archive's fiducial baryonic disks, while their published smooth H I profiles decline. The best nonnegative constant-potential gradient coefficient fitted to NGC 2403's 38 inner gas-matched rows is zero.

For a general potential the same equation gives the volume average $\langle U' \rangle_{<r} = 6\gamma_s s'/r - 3c^2 Q_r/(rs)$. Positive Q_r, positive s and a negative s' require a **negative enclosed mean potential derivative** for positive stiffness. This condition can discriminate among proposed entropy potentials without choosing one from the rotation data.

The H I column itself has slope −4.121 across the 21 radii. The required $\beta_s J_r/L$ must therefore have slope +3.470 under this carrier assumption. Requiring 90% H I detection within each annulus shortens the span to 17.39 kpc and gives +2.429. Both estimates require the remaining factor to grow outward.

With a measured volume entropy profile and a specified U', the original equation would give $\gamma_s = [c^2 \nabla\cdot(Q_r \hat{r}/s) + U'(s)]/(2\nabla^2 s)$ wherever $\nabla^2 s$ is nonzero. Thus a measured thickness and independently constrained potential would make a radial consistency test for one constant γ_s possible. A calibrated J_r would then give β_s directly from the gravity equation.

Original stationary SFD entropy equation under the project's metric convention · Schaap, Sancisi & Swaters on NGC 2403's vertical gas structure · The sign test includes signed baryonic residuals in the archival sample.

Cancelling the unknown potential at equal entropy

NGC 2403's H I column rises from 6.38 to 7.79 solar masses/pc^2 between 1.5 and 3.5 kpc and declines on the far side of that peak. The same column therefore occurs at two different radii. If the layer has constant effective depth and saturated hyperfine entropy per atom, these two radii have the same volume entropy. They must have the same $U'(s)$ for any single-valued potential. Subtracting the original SFD equations at the two radii cancels U' exactly.

Let $x = r/(1\ \text{kpc})$, let f be the numerical H I mass column in solar masses/pc^2 and write $s = s_0 f$. Define $A = f'' + 2f'/x$ and $B = (Q/f)' + 2(Q/f)/x$, with primes here taken with respect to x. The original equations then give

$$K_\gamma \Delta A = \Delta B, \text{ with } K_\gamma = 2\gamma_s s_0^2/[c^2\ (1\ \text{kpc})].$$

The difference is between two radii with the same f. This constrains an entropy-stiffness combination independently of β_s and the shape of U. Its sign equals the sign of γ_s. Its magnitude still contains the volume-entropy normalization, hence the unknown layer depth.

What the measured inner peak gives

Five common columns span 6.8–7.6 solar masses/pc^2. Shape-preserving interpolation pairs radii of 2.60–3.21 kpc with 3.88–4.64 kpc. Rotation-inferred Q is averaged in the same 1 kpc rings. All five pairs share those measurements.

Interpolation of both profiles	Signed K_γ, kg/m^2	95% range from speed errors alone
Shape-preserving cubic	−0.000171	−0.000596 to +0.000240
Natural cubic	−0.000872	−0.002185 to +0.000405
Akima	−0.000199	−0.000658 to +0.000167

All nine combinations of gas and current interpolants prefer a negative signed coefficient. With $\gamma_s \geq 0$, every nominal fit lands at zero. Every conditional interval also includes positive values. The 1 kpc spacing limits the second radial derivative, and uncertainty in the volume entropy adds to the quoted intervals. A positive stiffness remains unresolved.

The same subtraction can be made *between* dwarfs at equal column if both share the same effective depth and potential. Thirty-nine of 45 pairs among the ten dwarfs have enough common coverage, giving 195 correlated comparisons. The nonnegative NGC fit predicts zero divergence difference. The unconstrained signed NGC value changes the mean pair discrepancy from 0.04864 to 0.04709 kg/m^2 and improves 24 of 39 pairs. This small change concerns the differentiated field equation. The next pages test the directly calibrated hydrogen weight against velocities.

Original SFD stationary equation §8 and gravity equation §9 · HALOGAS · LITTLE THINGS H I fits · The released code also recovers the known stiffness in a smooth example with a nonconstant potential.

One hydrogen weight carried to other galaxies

Define the dimensionless weight w by $Q_{trial} = w \Sigma_{HI} h_{hf}/\ln 4$, with the mass column in kg/m^2. The NGC 2403 sightline and rotation source at 2.62 kpc give **w = 4.19845**. Holding w fixed tests constant $\beta_s J_r/L$ across the disk and between galaxies. For disks with no measured spin temperature we use the saturated value ln 4. No target rotation speed enters this calibration.

Common coverage	Baryons alone, km/s	Original inner exponential, km/s	Fixed hydrogen weight, km/s
NGC 2403 outer, 21 rows	75.46	3.73	51.30
NGC 3198, 25 rows	50.44	5.74	13.98
NGC 5055, 14 rows	30.15	16.05	23.07
Ten dwarfs, 221 covered rows	17.05	22.71	12.70
Same dwarfs, 99 outer rows	21.38	26.05	11.70

Values are mean per-galaxy speed RMSE. The dwarf rows use the archive's fiducial baryonic disks and Hunter et al.'s H I fits inside the observed 90%-mass radius. Seven of ten dwarfs improve relative to baryons over the covered curves and eight improve over their covered outer halves. The paired outer improvement is 9.68 km/s, with a 95% galaxy-bootstrap range of 4.26–15.25 km/s. Across all covered radii the corresponding interval includes zero. Fitting w on all 38 gas-matched inner NGC 2403 rows gives 5.26245 and an outer dwarf error of 11.63 km/s. On NGC 2403 itself that alternative still gives 46.96 km/s.

Two additional sightlines measure atomic spin

Applying the same aperture convention to the 21-cm emission at each absorption position gives an independent check on the use of annular columns. The NGC 2403 calibration becomes w = 3.62 using the local, optically thin face-on column. At NGC 247's background absorption sightline (63 ± 15 K), it predicts 90.1 km/s against an interpolated 80.3. At dwarf NGC 2366's internal H II sightline (145 ± 60 K), it predicts 56.9 against 30.3 km/s. The latter is a weak, statistically integrated absorption detection. On this aperture convention the inferred local weights are 2.69 and 0.66 respectively. Optical depth, the fraction of emitting gas in front of a continuum source and spatial averaging limit this comparison.

Hunter et al., observed H I distributions and Table 2 · Oh et al., LITTLE THINGS rotation curves · Braun, individual H I sightlines.

Dwarf results with the observers' baryonic models

Oh et al. published the total and baryon-subtracted curves with separate radius and velocity normalizations. Undoing each normalization and matching actual radii recovers the authors' baryonic term $b = v_{total}^2 - v_{subtracted}^2$. On the 90 covered outer rows with a real baryon-only circular speed, **$w = 4.19845$ lowers mean error from 18.40 to 11.62 km/s**. It improves seven of ten dwarfs. The paired 95% interval for the mean reduction is 0.23–13.64 km/s, conditional on these ten galaxies.

Galaxy	Covered rows	Baryons alone, km/s	Fixed hydrogen weight, km/s
CVnIdwA	6	4.87	20.37
DDO 52	16	32.15	8.34
DDO 70	15	13.80	3.41
DDO 101	6	46.98	33.39
DDO 133	16	22.05	7.52
DDO 210	7	4.43	3.19
DDO 216	12	7.12	2.37
IC 1613	55	4.15	12.64
NGC 1569	24	3.85	21.86
UGC 8508	17	16.55	11.21

The table includes both inner and outer covered rows. The mean changes from 15.60 to 12.43 km/s over these 174 rows. CVnIdwA, IC 1613 and NGC 1569 worsen. The individual results show why a smaller average cannot establish a universal weight. Using the project's three gas-disk scale choices on identical rows gives outer hydrogen-model errors of 11.93, 12.05 and 12.21 km/s.

The published decomposition encodes the authors' modeled mass subtraction and shares rotation data with the total curve. Some residual velocities were unreported. Restoring six outer rows with a negative reconstructed baryonic force gives 96 rows for a squared-speed check. Mean RMSE falls from 1,095 to 826 $(km/s)^2$. Seven dwarfs already matched to the wider SPARC catalog and five additional Oh galaxies have separate scores. Among the five additional systems, two of five improve on covered curves and all four with outer coverage improve in ordinary speed.

Oh et al., published Data series in Figures 2–4, panels A and C · Hunter et al., Tables 1 and 2 · The archive includes the source tables, radius matches, signed force results and every galaxy's scores.

Does the slower exponential transfer without gas data?

The project also has **385 other galaxies** with rotation curves. On this larger set the original exponential $Q_r = C \exp(-r/r_s)$ can be tested using the known baryonic curve alone. Starting with $C = 0.08817$ kg/m^2, $r_s = 16.75$ kpc, keep the original Q at the 10.435 kpc calibration boundary. Matching NGC 2403's measured outer log slope sets **$C = 0.07342$ kg/m^2 and $r_s = 23.72$ kpc**. These two effective profile parameters are frozen for every target. NGC 2403's outer speeds helped choose this slope, so its own change from 3.73 to 3.16 km/s is a retrospective fit.

Transfer sample	Original → slower, whole curves	Original → slower, outer halves	Outer curves improved
130 other SPARC	31.38 → 28.23	37.06 → 32.35	104 of 130
245 PROBES	37.26 → 37.47	36.39 → 35.53	161 of 245
10 LITTLE THINGS dwarfs	23.67 → 20.81	26.74 → 23.38	9 of 10
255 external galaxies	36.73 → 36.82	36.01 → 35.05	170 of 255

All entries are mean per-galaxy RMSE in km/s. Every curve contributes on its own outer half, including short curves. The 255 external galaxies comprise PROBES plus the ten project dwarfs. The paired external outer reduction is 0.96 km/s, with a 95% interval of 0.70–1.23. On whole external curves the change is +0.09 km/s, with interval −0.10 to +0.28. On whole dwarf curves, baryons alone give 18.77 km/s. Changing the exponential length improves the original dwarf prediction while the hydrogen measurements supply more information where available. A finite exponential still declines faster than the 1/r current needed for a flat excess speed at arbitrarily large radius.

Which weight still needs an observation?

With equal triplet sublevels the mean projected spin is zero. If that isotropic gas alone supplies the spin tensor in the project's single-fluid axial current, it gives $J_r = 0$. The hydrogen-weight test uses the gas as a tracer of scalar entropy and asks how much directional current is still required. At fixed singlet/triplet ratio, exchanging the m = +1 and −1 populations of an oriented sample preserves its entropy and reverses its spin. Even for known s, the original equations allow $\beta_s \to a\beta_s$ and $J_r \to J_r/a$. Faraday rotation supplies a magnetic-field integral weighted by free-electron density. A calibrated measurement of the radial spin tensor in the source material and its effective depth would allow β_s to be inferred. The volume entropy profile and the response of its potential would independently test γ_s.

SPARC · PROBES public release · LITTLE THINGS · Heald et al., polarized radio and Faraday measurements.

Do the same spin–entropy weights fit other galaxies?

The original current predicts part of the speed excess

Christopher Grenke's original spherical galaxy equation uses the weighted radial spin current $Q_r = \beta_s s J_r / c^2$. Its exponential trial profile, $Q_r = C \exp(-r/r_s)$, has two measurable curve parameters. The 52 inner measurements of NGC 2403 give $\mathbf{C = 0.08817\ kg/m^2}$ and $\mathbf{r_s = 16.75\ kpc}$. The remaining 21 measurements give a speed error of 3.73 km/s. The following test carries those same two values into other galaxies. Each contributes its own baryonic speed curve.

Whole measured curves	Baryons alone, km/s	With original current, km/s	Galaxies improved
Other SPARC	48.33	31.38	104 of 130
PROBES	68.79	37.26	237 of 245
LITTLE THINGS dwarfs	18.77	23.67	4 of 10
External surveys combined	66.82	36.73	241 of 255

Errors are means of individual galaxy root-mean-square errors (RMSE). The 255 external galaxies supply 16,381 speed measurements. The paired mean reduction is 30.10 km/s, with a conditional 95% galaxy-bootstrap interval of 28.34 to 31.79 km/s. The smaller dwarf sample goes in the opposite direction. Keeping only the outer halves of eligible external curves gives 73.14 km/s for baryons and 36.51 km/s for the same fixed original current. It improves 236 of 243 outer curves with zero target-speed fitting.

Does another calibration of C close the gap?

With r_s fixed, 130 other SPARC galaxies select 0.8291 times the NGC 2403 amplitude. This lowers the mean error within held SPARC folds, yet raises the external error from 36.73 to **39.21 km/s**. Allowing both original parameters to move gives C = 0.05420 kg/m² and r_s = 110.55 kpc. Its external error is **36.90 km/s**. The paired change of +0.17 km/s has a 95% interval from −0.35 to +0.69.

The archive also scales amplitude by baryonic mass and disk area, and length by disk size. Refitting that prescription changes its external error from 44.68 to 41.75 km/s. The archived population slower-rise benchmark gives 32.76 km/s on these curves. These comparisons establish predictive value for the original radial current and identify how much error persists under different existing prescriptions.

Project equation guide §9 · November 22 galaxy_transfer.py · SPARC mass models · PROBES release · LITTLE THINGS rotation curves. Every paired score and both fitted weights are in the research files.

What the original field equations let gravity measure

With a stationary, spherical extra field and a regular integration constant, the archive gives $v^2 - v_b^2 = 4\pi G r Q_r$. Baryons retain their adopted disk model. The spin–entropy equation in the same convention is $\beta_s \nabla \cdot J = 2\gamma_s \nabla^2 s - U'(s)$. Integration to r gives

$$c^2 Q_r = \gamma_s (s^2)' - sI(r)/r^2, \text{ where } I(r) = \int_0^r t^2 U'(s(t))\, dt.$$

This determines a combination of the entropy gradient and restoring potential. The signed reconstruction covers 19,413 speed rows in 386 galaxies. Across 19,269 distinct radii, 574 give $Q_r \le 0$ under the adopted baryonic models. Those radii remain in the results. For NGC 2403, Q_r at 20.87 kpc is 0.02835 kg/m^2. Integrating Q_r from 0.16 to 20.87 kpc gives 3.351×10^{19} kg/m. Mass, inclination and distance uncertainties propagate into this inversion.

Why two separate microscopic numbers do not emerge

Suppose U' vanishes on the field range. This is an allowed example of the unspecified potential. For a given measured Q and fixed $\gamma_s > 0$, the radial equations then admit

$$s^2(r) = s^2(r_0) + (c^2/\gamma_s)\int_{r0}^r Q_r(t)\, dt, \text{ and } J_r(r) = c^2 Q_r(r)/(\beta_s s(r)).$$

Different central entropies and nonzero values of β_s give the same Q and the same speeds wherever the chosen s^2 is positive. Both radial equations hold for every pair. An independent matter equation with measured inputs could select one pair. The normalized entropy variable $\sigma = \sqrt{(2\gamma_s)}s$ identifies $\beta_s/\sqrt{(2\gamma_s)}$ as the coupling independent of entropy units. The speed derivatives for multiplying s or J_r by a constant are identical. The resulting two-column matrix has rank one across all 16,381 external measurements.

Can an amplitude produce a flat exterior?

Flat excess speed requires $Q_r \propto 1/r$. In the constant-potential example, s^2 must grow as ln r over that interval. The field equations admit such a profile with suitable current and boundary conditions. The original exponential gives $d \ln v_x / d \ln r = (1 - r/r_s)/2$ for the excess speed v_x. Its slope vanishes at r_s and becomes negative beyond it, whatever C is. Changing the weight alone cannot extend that flat point into an asymptotically flat curve. The original action leaves the material current and the entropy potential to be specified.

Across NGC 2403's 21 outer radii, a log–log fit to the inferred Q gives a slope of −0.651. The frozen exponential gives −0.922 on exactly those radii. Multiplying C can shift the whole curve up or down, but the predicted radial falloff stays too steep for this mass model.

Original equations §§6, 8–10 · direct_source.csv contains signed measurements summarized per galaxy · field_checks.json verifies the entropy equation and its integral on three different entropy/current solutions.

Two combinations of spin and entropy in a regular core

Write a smooth spherical scalar as $s = s_0 + s_2 r^2 + s_4 r^4 + \dots$ and a smooth radial current as $J_r = j_1 r + j_3 r^3 + \dots$. Substituting into the original stationary entropy equation fixes two relations between the coefficients. U'_0 and U''_0 denote derivatives of the entropy potential at s_0.

$$3\beta_s j_1 = 12\gamma_s s_2 - U'_0. \quad 5\beta_s j_3 = 40\gamma_s s_4 - U''_0 s_2.$$

For $Q_r = q_1 r + q_3 r^3 + \dots$, the gravitational source measures $c^2 q_1 = \beta_s s_0 j_1$ and $c^2 q_3 = \beta_s (s_0 j_3 + s_2 j_1)$. Thus $q_3/q_1 = j_3/j_1 + s_2/s_0$ whenever $s_0 j_1$ is nonzero. It is possible to recover the sum of the relative spin and entropy curvatures. Assigning either part separately requires an independent radial measurement.

Apply the result to the archive's slower-rise profile

The later profile specifies $v_x^2 = V^2[1 - \arctan(x)/x]$, with $x = r/r_c$, $V^2 = \sqrt{(GM_b a_*)}$ and $r_c = \eta R_d$. Its series determines $q_1 = V^2/(12\pi G r_c^2)$ and $q_3 = -V^2/(20\pi G r_c^4)$. The earlier exponential has a nonzero radial magnitude at the center and a central density cusp. This smooth-core expansion applies to the later branch.

NGC 2403, using its inner 52 points	Combination inferred from the fit
Core radius and force normalization	$r_c = 1.6555$ kpc and $a_* = 2.0019 \times 10^{-10}$ m/s^2
Central weighted-source coefficients	$q_1 = 2.391 \times 10^{-21}$ kg/m^3 and $q_3 = -5.497 \times 10^{-61}$ kg/m^5
Relative spin and entropy curvature	$j_3/j_1 + s_2/s_0 = -3/(5r_c^2) = -0.2189$ kpc^{-2}

These values extrapolate a fitted profile to the center. The first NGC 2403 measurement lies at 0.097 core radii. In 172 of the 242 eligible PROBES galaxies even the first radius lies beyond the fitted core radius, so their separate core parameters can be weakly constrained.

Dropping one occupied inner kiloparsec at a time shifts the NGC curvature sum from −0.326 to −0.159 kpc^{-2}. Dropping the 2–3 kpc bin raises the original exponential's outer error from 3.73 to 8.10 km/s. These are eleven sensitivity tests using the same outer measurements.

Multiplying the source by 1.0887 increases q_1 and q_3 by the same fraction. It preserves q_3/q_1 and the core radius. At fixed mass it raises a_* by 18.53% and the limiting speed by 4.34%. The flat outer speed already appears in the chosen slower-rise profile. Its gravitational curve is identical to a pseudo-isothermal halo with matching amplitude and core radius.

Equation guide §§6, 8–10 · archived NGC2403_field_study/analysis/kinematics.py · source_combinations.csv includes the model-inferred central coefficients, fitted boundaries and radial coverage of every eligible galaxy.

The 8.87% change in other resolved galaxies

The archived NGC 2403 slower-rise fit gives an outer RMSE of 4.8967 km/s. It underpredicts 20 of 21 outer speeds. Optimizing the source multiplier on those 21 points gives 1.088725. The chat's rounded 1.0887 reproduces **1.9851 km/s** and changes the final prediction from 128.40 to 133.10 km/s against 134.00 observed. Inner error rises from 6.31 to 7.21 km/s. The original chat used these outer points to find the adjustment.

Application of the same 1.0887 multiplier	Before, km/s	After, km/s	Galaxies improved
Other SPARC, own inner fit → outer radii	13.78	16.26	26 of 94
External, own inner fit → outer radii	25.81	27.16	92 of 243
External, frozen NGC parameters → whole curve	36.66	35.53	197 of 255

In the first two rows, a galaxy's inner half fixes its amplitude and core size before the multiplier is applied to its outer half. In the last row, NGC 2403 supplies the fitted acceleration and size ratio, the target supplies mass and disk size, and all target speeds are held out. The improvement reverses sign between these two questions. Only one external LITTLE THINGS dwarf meets the inner-fit sampling rule.

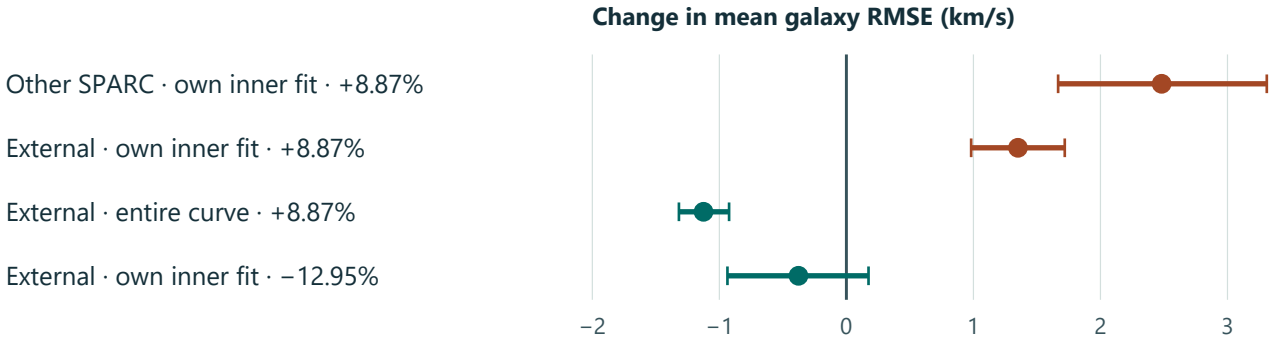

Whiskers show conditional 95% intervals from paired galaxy resampling. A positive difference means larger error. For the external outer halves, the 8.87% increase costs **1.35 km/s [0.98, 1.72]** on average. A single multiplier learned instead from 94 other SPARC outer curves is **0.8705**. It gives 25.43 km/s externally, a change of −0.38 km/s [−0.94, +0.17], and improves 113 of 243 galaxies. Applied to NGC 2403, that same independent correction raises the outer error to 11.48 km/s.

NGC2403_replay.csv · calibrations.csv · summary.csv · archive_checks.csv. The archive's 712 matched rotation scores reproduced within 0.00050 km/s. These tests reuse previously explored surveys and condition on their baryonic models.

An independent speed proxy and the missing measurement

The archive contains 11,758 additional galaxies with integrated 21 cm hydrogen line widths. Its selection excludes matches to the resolved samples. The inclination- and redshift-corrected half-width gives one speed proxy per galaxy. The slower-rise model predicts an asymptotic speed $(GM_b a_*)^{1/4}$. The line width samples the emitting disk over a finite range of radii and can differ from this limit. The original exponential decays at infinity. A finite-radius width prediction for that profile would require the distribution of emitting gas and its velocity profile.

Stellar-mass estimate and sample	Galaxies	Speed-proxy RMS before → after, km/s	Improved
Taylor, all eligible	11,758	39.89 → 40.97	4,317
Taylor, higher-quality subset	4,372	39.87 → 41.33	1,556
McGaugh, all eligible	11,647	43.11 → 45.76	2,832

The same 8.87% source increase raises the aggregate width error under both archived stellar-mass estimates. The higher-quality subset requires inclination 45–75 degrees and signal-to-noise at least ten. Widths and resolved rotation residuals have different observational meanings and are reported separately.

What else in ESFD could determine the weights?

Existing branch or data	Independent information needed for the coupling
Direct ESFD spin tensor and polarization	The original J_s is the axial projection of the antisymmetric spin tensor. A calibrated signed radial spin density in the relevant material would supply J_r. H I maps and flows measure gas column and motion. Radio intensities and polarization constrain magnetic fields or photons.
Entropy dynamics and stellar thresholds	A measured entropy mode with known normalization could constrain $U''/(2\gamma_s)$. A confirmed stellar crossing with independently known B, Ω and Λ_{tim} would fix $\kappa_s s = \Lambda_{tim}/\Omega - B$ in that object. The archived timing supplies no such matched crossing.
Rotation and lensing	Speeds measure a gravitational potential. Lensing constrains a combination of metric potentials. Another gravity measurement alone leaves the split between spin and entropy ambiguous.

At the same radius in a galaxy, an independently normalized s(r) and signed $J_r(r)$ would give $\beta_s = c^2 Q_r/[s(r)J_r(r)]$. With U' fixed and $\nabla^2 s$ nonzero, γ_s would then follow from $[\beta_s \nabla\cdot J + U'(s)]/(2\nabla^2 s)$. These are tests in the original variables. The archived neutron polarization and mixed-mode grids are model calculations. They supply no coincident radial measurement of these fields.

ALFALFA source tables · Durbala et al., ALFALFA–SDSS catalog · original equation guide §§2, 6, 8 and 12 · width_checks.csv independently replays the archived width controls before applying the NGC 2403 weight.

Which weights do the ESFD equations determine?

Three corrections inside the original theory

The starting point is Christopher Grenke's June ESFD action and its SEFD spin–entropy extension. This revision follows the symbols through the original equations before introducing an observational model. It finds a tensor convention that can switch off two interactions, eliminates one explicit weight in the spherical entropy equation, and corrects the time reference used in the archived merger test.

Original issue	Resolution
The same spin tensor is called symmetric and antisymmetric.	Only its antisymmetric part couples to Maxwell's field or enters the defined spin current. The explicit Dirac tensor in the later direct manuscript supplies that part.
The entropy field and three weights have no fixed numerical normalization.	A change of entropy units changes all three weights together. The combinations below can be analyzed before assigning any microscopic numbers.
The GW170817 photon window was centered on the Earth-based time reference.	Moving it to Fermi's location changes the count from five to six. The expected background is about eight. This observation supplies no measured precursor time to fit.

Which spin reaches the force and clock equations?

The draft 21.docx calls S symmetric in its introductory postulate and again in its action discussion. In its clock section it calls the contraction one between antisymmetric tensors. Let $S = S_{sym} + S_{anti}$. Interchanging the two dummy indices proves $S_{sym}\cdot F = 0$, since F changes sign and S_{sym} retains its sign. Contracting S with the antisymmetric volume tensor in $J^{\mu}{}_{s} = \varepsilon^{\mu\nu\rho\sigma}S_{\nu\rho}u_{\sigma}/2$ makes the same projection.

The explicit spinor definition in 4.1.docx resolves which field to use in these operators. If a symmetric alignment tensor is retained elsewhere, it needs its own symbol and observable. Under identical normalizations the direct and consolidated spin–field coefficients obey $\alpha_C = -2\alpha_J$. Using the same numerical coefficient in both drafts would change the sign and magnitude of the interaction.

The direct saturation energy $\lambda_S(X-\Phi_0{}^2)^2/4$ fixes a preferred X for positive λ_S. Its minimum sets no time by itself. The susceptibility, inertia and damping of the material determine how it approaches that state. The earlier interface and gas-current studies in the master describe explicitly conditional extensions.

Original record · 21.docx, paragraphs 67, 182 and 267 · 4.1.docx, paragraph 78 · 6-3-spin ESFD current, paragraph 81 · ESFD and SEFD from first principles, §§3, 6 and 8. Full parameter register and source locations accompany this paper.

Remove one unknown before fitting a galaxy

Use the archive's sign convention $\Box s = \partial^2_t s - \nabla^2 s$. At fixed current its original entropy equation is $2\gamma_s \Box s + U'(s) = -\beta_s \nabla \cdot J_s$. In the stationary, regular, spherically symmetric branch, integrate over a sphere of radius r. The center has no point source and no singular gradient. With $I(r) = \int_0^r x^2 U'(s(x))\,dx$, this gives

> $\beta_s J_r = 2\gamma_s s' - I(r)/r^2$. Substituting into $Q_r = \beta_s s J_r / c^2$ gives $c^2 Q_r = \gamma_s (s^2)' - sI(r)/r^2$.

This eliminates the explicit β_s from the combined radial equation. The solution for s can still depend on the spin dynamics, boundary conditions and β_s. The source potential U and the physical entropy profile remain inside the result. Stationarity and spherical symmetry apply to this reduction. The adopted baryonic mass model retains its disk geometry.

For NGC 2403 the original weak-gravity relation gives $Q_r = (v^2 - v_b^2)/(4\pi G r)$. At 10.43 kpc the inferred value is 0.04413 ± 0.00117 kg/m². At 20.87 kpc it is 0.02835 ± 0.00155 kg/m². These uncertainties propagate the speed error alone. Integrating the measured profile between those radii gives **1.166×10^{19} kg/m** for the combined gradient and potential terms divided by c^2. Assigning that number entirely to $\gamma_s \Delta(s^2)/c^2$ would additionally require the integrated potential contribution to vanish. This calculation uses 73 measured radii and the original mass model.

Which weights can be separated?

Change the entropy unit by a factor a. The original entropy action and stellar index retain their predictions under $s \to as$, $\beta_s \to \beta_s/a$, $\gamma_s \to \gamma_s/a^2$, $\kappa_s \to \kappa_s/a$ and $U_{new}(y) = U(y/a)$. The entropy-only threshold likewise requires $\Lambda_s \to a\Lambda_s$. For positive γ_s, defining $\sigma = \sqrt{(2\gamma_s)}\, s$ identifies $\beta_s/\sqrt{(2\gamma_s)}$ and $\kappa_s/\sqrt{(2\gamma_s)}$ as independent of the choice of units.

A measurement of the material's entropy or spin polarization in fixed units would break this ambiguity. A measured small-oscillation gap constrains $U''/(2\gamma_s)$ in a stable background. The present rotation data constrain the weighted current. Fitting new values to each microscopic coefficient independently would count the same information more than once.

ESFD and SEFD from first principles, §§6, 8–10 and 12 · SPARC mass models. The algebra, independent differentiation check and reconstruction at all 3,032 SPARC radii are supplied in research/original_weights/.

Fit the original galaxy weights and predict the exterior

The project's original radial trial is $Q_r = C \exp(-r/r_s)$. It gives $v^2 = v_b^2 + 4\pi G C r \exp(-r/r_s)$. Both C and r_s are present in the equation guide. At fixed r_s the squared-speed equation is linear in C. Solving its weighted least-squares amplitude exactly leaves a one-dimensional search for r_s.

For NGC 2403, fit only the 52 measurements inside half the maximum radius, then predict the remaining 21. Equal weights on the inner squared-speed measurements give $C = 0.08817$ kg/m^2 and $r_s = 16.75$ kpc. The held outer RMSE is **3.73 km/s**. The predicted final speed is 127.84 km/s against 134.0 ± 3.12 km/s observed. This is an extrapolation from the interior of the same galaxy. It supplies no independent measurement of entropy or intrinsic spin.

Original exponential current	Fitted r_s, kpc	Held outer RMSE, km/s
Equal weight per inner velocity row in squared speed	16.75	3.73
Weights from the reported velocity errors	13.55	8.18
Equal total weight per occupied inner kpc bin	13.66	9.01

These fits use the same original equation and the same radii. The differences are real consequences of how discrepant inner measurements are weighted. The measurements alone do not establish which error model best captures distance, gas geometry and stellar mass uncertainties. Selecting the weighting after seeing the outer errors would overstate the prediction.

Using identical equal-row training, the archived revised core gives 6.93 km/s and the later slower-rise profile gives 3.61 km/s for NGC 2403. Across 99 eligible SPARC curves and 1,025 held outer measurements, the original exponential law gives a mean galaxy error of 19.40 km/s, and the revised core gives 14.14 km/s. The original exponential reaches the allowed scale boundary in 43 galaxies, which limits its interpretation as a measured physical scale. All individual parameters, limits and held scores are provided.

The separate eight-galaxy experiment in the following supplement gave a much larger residual when it set the spin-current carrier proportional to radial hydrogen flow. That assumption belongs to the experiment. The 3.73 km/s result above comes directly from the project's archived equation with its own two fitted weights.

ESFD and SEFD from first principles, §§9–11 · SPARC. Numerical records · native_fit_scores.csv, native_fit_summary.csv, ngc2403_native_predictions.csv and inferred_weighted_current.csv.

Resolve the timing reference and the torque units

The June direct manuscript defines an observing window from 5.0 to 0.5 ms before coalescence. Its width is 4.5 ms. The companion 21.docx gives a broader proposed lead of 1–10 ms and a second possible trigger based on a torque rate. These are predictions and search definitions. The archive contains no detected precursor assigned an observed-minus-predicted time of four milliseconds.

The archived GW170817 test counted spacecraft photons relative to the rounded geocentric GW epoch, GPS 1187008882.43. For the optical source direction, the joint paper measured a light-travel correction of −3.176 ms from Earth's center to Fermi. Projecting Fermi's archived orbital position onto the source direction independently gives −3.179 ms at the adopted epoch. Applying the published correction places the original search window at −8.176 to −3.676 ms relative to the Earth-based timestamp.

Fixed window	Photons in NaI 1 / 2 / 5	Total and expected background
Archived geocentric placement	2 / 1 / 2	5 observed, 8.00 expected
Corrected spacecraft placement	1 / 1 / 4	6 observed, 8.00 expected

The corrected count shows no excess. This is a physical timing correction of the requested order of magnitude. Identifying it with a particular recalled residual would require that residual's original event and reference time.

A separate problem within the proposed trigger

Section 2.2 of 21.docx correctly sets $[d\tau/dt] = N\cdot m/s = W$ for mechanical torque τ. Sections 9 and 11 use J/s^2 for the threshold. These dimensions differ by one inverse second. The suggested scaling $(c^3/\mu_0)\rho_{charge}L^3/B$ has SI dimensions $A^4\ m^2\ s^2/kg^2$. An additional factor with units $kg^3/(A^4\ s^5)$ would be needed to make this a torque rate. The original draft flags a dimensional mismatch. It also treats mechanical power $\tau\cdot\Omega$ as interchangeable with $d\tau/dt$. A constant torque at finite angular speed distinguishes the two observables.

The same example takes $c^3/\mu_0 \approx 10^{36}$. Its SI numerical value is 2.14×10^{31}. Correcting that arithmetic still leaves the dimensional factor to determine. In the alternative original index $\chi_{tot} = \Omega(B+\kappa_s s)/\Lambda_{tim}$, a confirmed crossing would fix $\kappa_s s = \Lambda_{tim}/\Omega - B$ if Ω and B were independently known. Six background-compatible photons cannot fix that weight or an emission delay. The register traces these dependencies through clocks, material response, stars, galaxies and cosmology.

21.docx §§2.2–2.3, 9.1 and 11.1 · 4.1.docx, precursor search · GW epoch · Joint LIGO–Fermi timing, §2.2 · Optical position.

Testing the spin-current source of gravity

Can a measured current predict a galaxy's speed?

The question raised in the latest ESFD discussions is whether a spin field can predict both the location and the strength of extra gravity before a galaxy's rotation curve is known. Christopher Grenke's proposed source is the divergence of an entropy-weighted spin current. This study tests whether neutral hydrogen transports the relevant spin and entropy in fixed proportion to its mass. That assumption makes the current measurable up to one shared coefficient.

> For NGC 2403 the gas-current model predicts 57.3 km/s at 16.89 kpc. The measured speed is 134.0 km/s. Its predicted excess gravity peaks toward the inner edge of the tested region, while the required excess in squared speed peaks at the outer edge.

Question	Result
Does measured radial gas flow supply the missing gravity?	Across eight galaxies and 115 outer speed measurements, the mean per-galaxy error is 78.6 km/s. Ordinary matter alone gives 80.3 km/s.
Does the empirical mass-based equation still transfer?	Across 255 external galaxies, the frozen slower-rise model gives 32.76 km/s against 66.82 km/s for ordinary matter. A pseudo-isothermal halo with the same mass scaling gives identical predictions.
Can lensing distinguish model branches?	Fitting a constant response to light on other mass bins leaves far-field errors of 78.3 and 28.1 km/s for the two previously calibrated branches.
Which earlier calculation can be completed?	The causal-diamond boundary is now solved through face overlap and complete spatial coverage. Its integrated area recovers the exact volume of the quotient space.

The accompanying register revisits each of the 75 earlier branches and adds the completed geometry calculation. It records which equations, calibrations or observations would discriminate the remaining claims. The source of gravity and the mechanism that would hold a real galaxy at critical spin response remain open.

Observational basis · Radial H I flow measurements · SPARC · Weak lensing. Equations and interpretation · ESFD source manuscripts and preceding studies in this master.

What the source equation actually fixes

Write $\rho_x = \nabla\cdot Q$ and $\nabla^2\Psi_x = 4\pi G\rho_x$, with the phenomenological normalization absorbed into Q. Its units are mass per area. Around a finite isolated source, collisionless tracers respond to the gravitational potential Ψ. For an axisymmetric current with only an azimuthal component the divergence vanishes, even if the azimuthal flow is large. Ordered rotation alone therefore supplies no source in this equation.

A closure that can be tested without using the target speeds

Let $Q_R = \tau\rho_{HI}u_R$, with a signed conversion time τ and radial gas speed u_R positive outward. Assume axial symmetry, a regular center and vanishing flux through the upper and lower disk faces. Define $F(R) = 2\pi R\int\rho_{HI}u_R\,dz$. Vertical integration of the divergence and then integration over the disk give two exact identities for this closure.

> $\Sigma_x(R) = \tau\,F'(R)/(2\pi R)$ and $M_x^{cyl}(<R) = \tau\,F(R)$.

A radially constant flow contributes no local source within that annulus. Where the flow returns to zero, the cumulative excess mass also returns to zero. A compensated disk can still exert a force inside it. The calculation integrates the force of signed annuli, including matter outside the test radius. Treating this disk as a sphere would change the prediction.

The ideal, infinitely extended Mestel disk has $\Sigma = V^2/(2\pi GR)$ and constant circular speed V. For this particular disk the required flow gradient is $F' = V^2/(G\tau)$. This is a diagnostic for a constant excess speed. The forward test on the next page uses the measured F(R) point by point. Its input contains no flat-speed condition.

What remains invisible to rotation

Adding the curl of any regular vector potential to Q leaves ρ_x unchanged. Compact support preserves the boundary flux as well. If Q is the product of specific spin entropy and a spin current, multiplying one factor by an arbitrary positive function and dividing the other by it also preserves Q. Separate transport or spin measurements are necessary to recover the factors. Circular speeds constrain still less, because they sample one derivative of a potential on the disk.

ESFD · current-divergence branch and November source reconciliation. Thin-disk comparison · Mestel, On the Galactic Law of Rotation. Gas flow convention · Schmidt et al..

NGC 2403 gives a test of location and strength

Schmidt and colleagues published 54 radial H I mass-flow measurements for NGC 2403. Reading the centers and uncertainty bars of their vector plot recovers an outer mean of −1.196 M/yr, agreeing with their tabulated −1.20 M/yr. Of those 54 rings, 33 lie outside the optical radius. At the SPARC distance of 3.16 Mpc the common outer interval contains 20 circular-speed observations from 7.45 to 16.89 kpc.

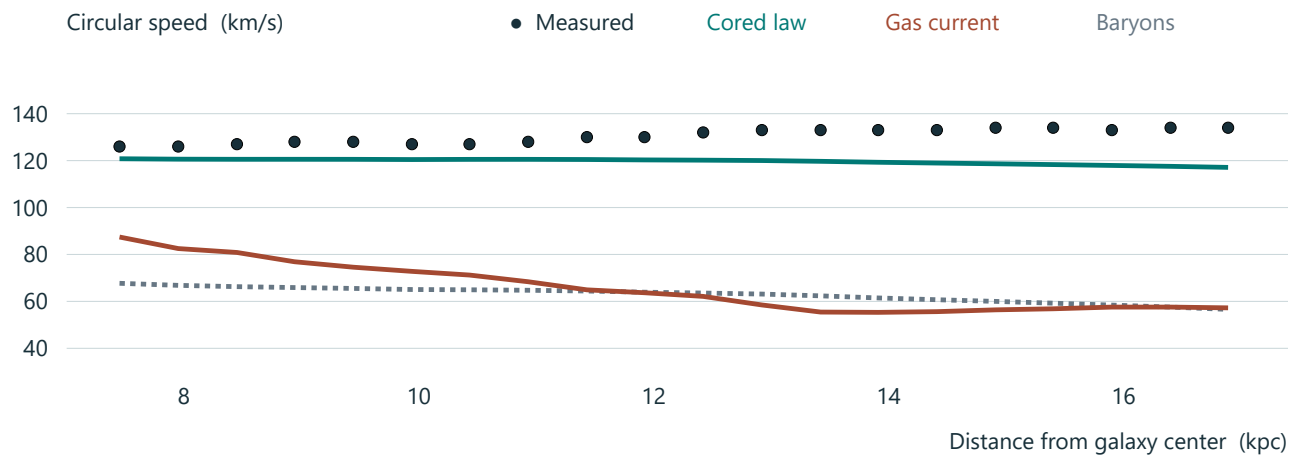

The signed conversion fitted on the other seven galaxies is $\tau = -0.709$ Gyr. Its sign describes how the proposed gravitational charge would follow an inflow. It does not measure a gas travel time. The predicted excess in squared speed reaches its maximum at 7.45 kpc. The required excess reaches its maximum at 16.89 kpc. Their Pearson correlation across these 20 radii is −0.84. Neighboring radii share errors, so this is descriptive.

The median required excess is 13,099 $(\mathrm{km/s})^2$. The median predicted excess is 33 $(\mathrm{km/s})^2$. As a scale check, the ideal flat-disk gradient from the preceding page is −4.29 M/yr/kpc, while the measured gradient across the 31 flux rings between the first and last speed measurements is +0.31 M/yr/kpc. The disk integral in the figure uses the full measured profile and its outer continuation.

The gas-current speed RMSE is 65.98 km/s. Baryons give 67.84 km/s and the archived, separately calibrated cored curve gives 11.55 km/s on these same radii. Replacing every observed NGC 2403 speed with zero leaves its forward current prediction exactly unchanged. The two surveys can share gas geometry and line-of-sight systematics.

Measurements · Schmidt et al., figure 8 and table 1 · SPARC mass models and rotation curves. Reproduction · forward_current/results/held_predictions.csv and force_locations.csv.

Eight galaxies test whether the calibration transfers

The ten published flow profiles contain 304 rings. Their reconstructed optical-exterior means agree with all ten tabulated rates to within 0.006 M/yr. Eight galaxies enter the archived SPARC selection. NGC 925 and NGC 3621 have measured flows and lack a curve in this 131-galaxy cut. Every included galaxy has at least two outer speed points inside its mapped flow extent. Six of the eight have mean inflow, and two have mean outflow. All eight have a positive median spherical-equivalent excess mass. Its sign alone cannot determine the disk force.

Eight held galaxies	Mean speed RMSE (km/s)	Mean squared-speed RMSE ((km/s)^2)
Baryons	80.34	25,897
Signed measured flow plus baryons	78.63	25,427
Constant excess in squared speed, trained on other galaxies	30.34	12,215
Archived cored model, calibrated on other SPARC folds	20.20	8,750

Each speed score is an average of eight galaxy-level errors. Each current coefficient is fitted on the other galaxies using squared speeds and equal galaxy weight. The finite disk model has a 0.5 kpc gravitational softening length and returns the measured flux to zero over 5 kpc beyond the last ring. Changing the softening to 0.25 or 1 kpc gives 79.10 or 77.24 km/s. Changing the taper to 2 or 10 kpc gives 77.98 or 79.43 km/s.

NGC 6946 has a nearly face-on geometry and a particularly uncertain flow. Excluding it from training and testing reverses the small advantage over baryons on squared speeds and produces one negative predicted speed square. Taking absolute flow also gives one such point. Shifting all rings coherently by their reported errors yields two or eighteen invalid speeds. These are stress tests. The paper's quoted outer uncertainty is an average ring uncertainty, and published ring covariances are unavailable.

Three galaxies also have H I intensity maps and total-disk radio field estimates. On their 28 common outer speeds, the measured-flow model gives 65.92 km/s, radio weighting gives 66.23, and a constant-drift model using the gas density map gives 55.71. A fitted constant offset gives 11.08. A mean equipartition field supplies no radial measurement of the ordered spin current.

THINGS gas flows · HALOGAS maps · Radio field estimates. Numerical tables include scores, sensitivity variants, disk assumptions and sign conventions.

What survives the larger galaxy comparison

The archive contains 3,032 SPARC rows in 131 galaxies, 16,120 PROBES rows in 245 and 706 LITTLE THINGS rows in 17. That is 19,858 velocity rows across 393 catalog entries. Seven dwarfs coincide on the sky with entries in the wider SPARC catalog. Removing them leaves 386 curves and 19,413 rows. The earlier count of 19,008 designates distinct galaxy–radius pairs in SPARC plus PROBES. Some two-sided measurements share a radius.

> $v^2 = v_b^2 + \sqrt{(GM_b a_*)}\,[1 - \arctan(x)/x]$, $x = R/(0.679624\,R_d)$, $a_* = 1.163796 \times 10^{-10}$ m/s².

Model	Frozen parameters, 255 external galaxies	Matched refit, 386 galaxies
Ordinary matter	66.82	60.55
Slower-rise empirical law	32.76	27.95
Revised cored law	33.73	28.11
Radial acceleration relation	33.60	28.40
Shared NFW / Burkert profiles	See matched refit	28.15 / 28.94

Values are mean per-galaxy RMSE in km/s. The frozen column uses the latest slower-rise coefficients and the older archived core and radial-acceleration calibrations. Including all 17 dwarfs gives 32.17 km/s for the frozen slower-rise law, consistent to 0.01 with the chat's 32.16. Its 27.38 km/s combined score and 32.9 km/s core score use a different calibration. The full benchmark file linked in that chat was unavailable. The matched refit here minimizes mean galaxy RMSE on the same SPARC training partitions for each profile. The paired slower-rise advantage over RAR is 0.45 km/s, with a conditional galaxy-bootstrap interval of 0.12–0.76 km/s.

For a spherical pseudo-isothermal halo, $\rho = \rho_0/(1+x^2)$ gives $M(<R) = 4\pi\rho_0 r_c^2[R - r_c \arctan(x)]$. Set $4\pi G\rho_0 r_c^2 = \sqrt{(GM_b a_*)}$ and use the same r_c. The two curves then agree at every radius. Computing both expressions separately across all 19,858 rows gives a maximum difference below 10^{-12} km/s. The scaling transfers. Deciding which physics sets that scaling requires an independent observable.

SPARC · PROBES · LITTLE THINGS · Empirical radial acceleration relation. Shared halo fits here use the declared baryonic mass and scale prescription.

What light and cosmic expansion add

Massive bodies in the weak field constrain the time potential Ψ. Lensing responds to the sum of Ψ and the spatial potential Φ. For this test only, let the extra components obey $\Phi_x = \eta_x \Psi_x$ with η_x constant. Keep the baryons at their usual response. The lensing-equivalent speed then satisfies $v_L^2 = v_b^2 + (1+\eta_x)v_x^2/2$. This effective relation assumes the same projected profiles and constant slip over the tested band.

For each excluded baryonic-mass bin, fit one coefficient on the 18 cells at 50–300 kpc in the other three bins. Predict the four cells at 300–1,000 kpc in the excluded bin. All 16 outer predictions use the rotation-calibrated carrier models from the preceding edition. This is a retrospective cross-bin check on published late-type galaxy stacks.

Carrier model	Unit response, outer RMSE	Fitted response, outer RMSE
Fixed microscopic stiffness	88.62 km/s	78.28 km/s
Critical stiffness retuned with carrier filling	28.61 km/s	28.09 km/s

The four fitted η_x values span 1.41–1.73 for fixed stiffness and 0.97–1.07 for retuned stiffness. A constant lensing rescaling does little to change the gap. The stacks share calibration uncertainties. The ranges across fits are descriptive. Deriving η_x requires field equations for both potentials.

Can the galaxy equation also drive cosmic acceleration?

A homogeneous, isotropic universe admits no preferred spatial current in its rest frame. More generally the integral of a regular spatial divergence over a closed spatial slice vanishes. The galaxy source by itself therefore supplies no homogeneous density through that term. A covariant four-divergence could include a time derivative. It requires an evolution law and a stress-energy tensor.

The acceleration equation involves $\rho + 3p/c^2$. An additive constant in a candidate generally covariant matter action shifts vacuum energy and pressure without fixing the galaxy current law. An equation of state, conservation law, background solution and perturbation behavior are necessary to compare this theory with expansion and structure measurements. The geometry on the next page can be calculated without choosing these quantities.

Mistele et al., lensing data and assumptions · Zhang et al., testing the metric potentials · Riess et al., supernova expansion measurements.

The causal diamond through complete coverage

Keep the archived static round metric with curvature radius R on the Poincaré dodecahedral space. Two events occur at the same spatial point separated by 2T. At the symmetry time the waist is the boundary of the geodesic ball reached by first arrival. Write $\chi = cT/R$ and $f = \pi/10$. Past the first face, each of the twelve face normals removes a cap from the sphere of directions with limiting cosine $u = \tan(f)/\tan(\chi)$. Adjacent normals have dot product $d = 1/\sqrt{5}$.

Between the face and first edge the surviving solid angle is $\Omega = 4\pi - 24\pi(1-u)$. The edge occurs at $\chi = 0.364864$. Beyond it, add the overlap of each of 30 adjacent cap pairs. Before full coverage there is no triple overlap with positive area. With $\theta = \arccos u$ and $\delta = \arccos d$, a single spherical lens has solid angle $L = 2\pi - 2\gamma - 4u\alpha$, where $\cos\alpha = \cot\theta \tan(\delta/2)$ and $\cos\gamma = (d-u^2)/(1-u^2)$. These angles follow from the spherical triangle between the two cap centers and one intersection point.

> Beyond the first edge, $A/R^2 = \sin^2\chi\,[4\pi - 24\pi(1-u) + 30L]$. At $\chi = \arctan[\tan(f)/\sqrt{((1+2d)/3)}] = 0.388140$ the slice is fully covered and its first-arrival boundary area is zero.

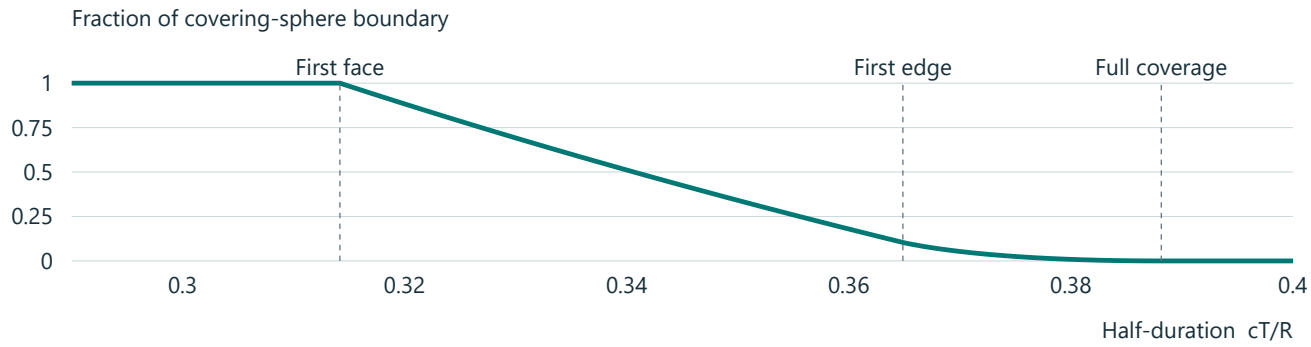

At $\chi = 0.348$ the original figure's surviving fraction is 0.374073. Integrating the new area through complete coverage gives $V/R^3 = 0.16449340668474$, agreeing with $2\pi^2/120$ to 9×10^{-14} in absolute units. A second calculation traces 150,000 directions and agrees within 0.00031 in surviving fraction. This completes the static geometric baseline. Establishing cosmic topology or spin dynamics requires observational predictions beyond that construction.

Geometry · Luminet et al., Poincaré dodecahedral space. Original marked figure · archived Pattern Nexus dodecahedron package. Independent implementations and checks · spin_entropy/diamond.py and diamond_checks.json.

What the complete project review resolves

The register preserves every earlier branch and its source, including proposed experiments with no calibrated signal. Its November 29 columns state the present result or the specific missing observable. The new geometry entry makes 76 entries. The separate equations for an empirical galaxy curve, an interface-mediated force and a current transported by gas have different physical inputs and different experimental tests.

Area	Result and remaining measurement
Critical spin response	The effective stiffness is $a_R - 4\pi G\lambda^2$ in the reciprocal coupling model. At zero stiffness a quartic spin energy gives $v \propto R^{1/6}$. A cubic energy from neutral two-dimensional interface modes can give $v_\infty{}^4 = GMa_D$. A galactic carrier census, gap or independently measured susceptibility would set the scale and test whether criticality persists.
Stars and pulsar timing	The original BΩ threshold using timing-inferred B ranks inverse characteristic age. Five of 22 eligible confirmed magnetars pass. For one star the earlier study also inferred a field from spectroscopy, subject to line identification and redshift. Independent fields and event exposure are required for a population test.
Material spin and laboratory tests	In the specified quartic reversible model the coefficients obey $c_1c_5 = 3c_3{}^2$. A four-state reversal removes additive offsets. Independent magnetometry, same-material sweeps and a phase-sensitive readout would distinguish joint-parity backgrounds and test the prediction.
Particles, compact objects and clocks	The Pauli operator and repaired clock diagnostic are specified. A clock Hamiltonian, collider interference coefficients and a conserved material or stellar stress tensor remain separate quantitative requirements.
Expansion and global spacetime	The spatial-divergence average vanishes on a closed slice. The static topology calculation is complete. A time-dependent source, pressure and exterior matching would be needed to predict accelerated expansion or a global bounce.

The 255-galaxy population result is the clearest transferable prediction in this revision. The resolved gas experiment now supplies a quantitative constraint on one proposed carrier of that gravity. A measurement of ordered spin polarization and its transport independent of the circular speeds could distinguish a different carrier from the halo-equivalent mass law.

McGill Magnetar Catalog · Independent stellar spectroscopy. Project references · branch_register.csv, spin_response/, stars/, critical_response/ and the preceding studies in this master.

Critical spin response and outer galaxy speeds

Can ESFD produce flat rotation curves?

There is a conditional route. Christopher Grenke's saturation energy supplies a spin stiffness that a universal gravitational coupling can reduce. Its vanishing defines a calculable phase boundary. If neutral, effectively zero-temperature Dirac modes also live on spin-domain interfaces, their energy produces the force exponent needed for flat outer speeds. No rotation speed, halo density profile or Tully–Fisher relation enters that derivation.

> At the phase boundary, the predicted low-acceleration force is $g - g_b \approx \sqrt{(a_D g_b)}$. Outside a finite isolated mass M this gives $v_\infty^4 = GMa_D$.

Here g_b is the inward acceleration from the ordinary stars and gas. The spin–gravity coupling, the existence of two-dimensional modes and the mechanism that keeps the stiffness at its critical value remain open. The original three-dimensional quartic spin energy alone gives a different exponent.

Test	Result
131 SPARC rotation curves	Letting the stiffness and interface strength vary selected a positive residual stiffness and zero interface term. Fixing the system at criticality changed held-out speed error only from 21.54 to 21.66 km/s.
245 external PROBES curves	Frozen predictions gave 39.19 km/s for the free fit and 39.43 km/s for the critical interface fit. Disk velocities alone gave little leverage to distinguish these limits.
Weak lensing at 300–1,000 kpc	The same two calibrations gave 106.6 and 28.6 km/s RMS error. The free disk fit declined too rapidly. Simple MOND gave 24.6 km/s on the same 16 cells.

With the reference stellar masses, two models that differ by a quarter of a km/s in external disk error differ by almost 78 km/s on the distant stacks. A 20% upward shift in the SPARC stellar masses reverses their lensing ranking. The interface hypothesis was developed after examining the quartic and spin-wave results on this previously studied archive. Its subsequent fits excluded the scored galaxies. This is a retrospective comparison.

ESFD · 4.1.docx §§3.1–3.3 and 11.2, 21.docx §3.2, November master §9 and the preceding spin-gravity study. Data · SPARC, PROBES and Mistele et al. weak lensing.

Where the critical response comes from

In 4.1.docx the saturation energy is $\lambda_s(X-\Phi_0^2)^2/4$ with $X = S_{\mu\nu}S^{\mu\nu}$. Project a rest-frame spatial spin tensor onto a dimensionless vector p, so $X = 2S_*^2|p|^2$. The quadratic coefficient becomes $a = a_{mat}-2\lambda_s S_*^2\Phi_0^2$. The saturation term contributes $4\lambda_s S_*^4$ to the quartic coefficient b_4. The clock proposal motivates a weak gravitational potential Ψ under the additional universal-lapse assumption of the preceding study.

Write $g = \nabla\Psi$ as an outward potential gradient. Matter accelerates along $-g$. A static reciprocal energy density for spin and gravity is

$$\rho_b\Psi + |g|^2/(8\pi G) - \lambda\, p\cdot g + a|p|^2/2 + b_4|p|^4/4 + D|\nabla p|^2/2.$$

Varying Ψ gives $\nabla\cdot(g-\kappa p) = 4\pi G\rho_b$, with $\kappa = 4\pi G\lambda$. The same λ drives p when the energy is varied with respect to spin. In a uniform longitudinal response or a spherical radial field, write $y = \kappa p$ and $g = g_b + y$ in signed radial components. Substitution into the spin equation gives $h_b = (a-a_c)p + b_4p^3$, where $h_b = \lambda g_b$. Consequently

$$a_c = 4\pi G\lambda^2,\ \delta = (a-a_c)/a_c,\ \chi_{long}(k) = 1/(a-a_c+Dk^2).$$

The $k = 0$ longitudinal susceptibility diverges at $a = a_c$. The transverse susceptibility of the disordered state is $1/(a+Dk^2)$. Thus gravity's feedback supplies the shift in stiffness and determines the threshold once λ is known. No evolution equation in these manuscripts selects $a = a_c$ for every galaxy.

An explicit microscopic control parameter

As a model of the manuscript's spin entropy, take n classical orientable moments per volume. Their one-site partition function is proportional to $\sinh z/z$. Its mean polarization is $\coth z - 1/z$, hence $z = 3p + 9p^3/5 + \ldots$. Entropic stiffness then contributes $a_{mat} = 3nk_BT$ and b_4 gains $9nk_BT/5$. With no other quadratic term, $T_c = [2\lambda_s S_*^2\Phi_0^2 + 4\pi G\lambda^2]/(3nk_B)$. It is a model transition temperature. The data contain no measurement of this spin temperature, density or coupling.

Saturation potential and proposed spin entropy · 4.1.docx §§3.2 and 11.2. The reciprocal energy, susceptibility and orientable-moment matching are developed here. Mean-field comparison · Arrott (1957).

Can the quartic energy alone make a plateau?

On its stable disordered branch, $g_b = \delta y + y^3/a_q^2$ with $a_q^2 = \lambda\kappa^3/b_4$. The coefficient δ measures the distance above the critical stiffness. At $\delta = 0$ the excess force is proportional to $g_b^{1/3}$ and the speed around an isolated mass eventually rises as $R^{1/6}$. For positive δ the linear term takes over in the weakest fields. At large R, g tends to $(1+1/\delta)GM/R^2$ and the speed declines as $R^{-1/2}$.

Between these limits the equations can produce a shallow stretch without imposing a flat velocity. For a compact point mass, define $t = (y/a_q)^2$. Differentiating the **total** circular speed, including baryons, gives

$$\beta = d \ln v / d \ln R = -\tfrac{1}{2} + 2t / [(\delta+3t)(1+\delta+t)].$$

Its maximum occurs at $t = \sqrt{[\delta(1+\delta)/3]}$ and equals $-\tfrac{1}{2} + 2/[3+4\delta+2\sqrt{(3\delta(1+\delta))}]$. A locally horizontal tangent is possible for positive $\delta \le 5/2-\sqrt{6} \approx 0.05051$. This condition was derived from the force law. It was never imposed on the calibration.

What the galaxies selected

Fitting all SPARC curves gave $\delta = 0.11696$ and $a_q = 5.84 \times 10^{-11}$ m/s². The five training-fold estimates of δ spanned 0.1042–0.1483. With the all-SPARC fit the shallowest possible isolated point-mass slope is −0.0763. For 10^{11} solar masses this occurs near 40.1 kpc at 209 km/s. Any complete radial doubling around that compact mass loses at least 5.15% in speed. A disk with continuing enclosed baryons can have a shallower slope or a rising curve over the same radii.

Permitting this residual stiffness reduced external rotation error from 40.64 to 39.19 km/s against the exactly critical quartic. It improved the individual error in 187 of 245 galaxies. Whole-galaxy resampling gave a conditional 95% interval of −1.64 to −1.25 km/s for the change in cohort RMS. Setting δ to zero also eliminates the eventual Keplerian decline, but the resulting unbounded slow rise misses the much larger lensing radii in the opposite direction.

Sensitivity to the assumed stellar masses

We also changed the SPARC stellar contribution by ±20% at fixed gas, recalibrated on SPARC, and left the external inputs fixed. With 20% lighter stars the free three-term model on page 4 retained a nonzero interface term and selected $\delta = 0.0850$. The critical and free models gave 24.7 and 97.0 km/s in the far lensing stacks. With 20% heavier stars both fits dropped the interface term. The free fit selected $\delta = 0.00474$ and gave 46.8 km/s versus 81.9 km/s for the critical quartic limit. The reference-mass preference is sensitive to the baryonic decomposition.

Force derivatives and fit · calibrations.csv, detuning_profile.csv, point_mass_plateaus.csv and external_paired.csv. The temperature and microscopic stiffness cannot be recovered individually from these rotation fits.

A flat-speed exponent from a Dirac spectrum

The recovered action contains a three-dimensional Dirac matter field and a Pauli spin–field term. Consider an added microscopic condition. A sign-changing gapped bulk could support an effectively two-dimensional, neutral Dirac mode on an interface. Assume its energy near neutrality is $E_{\pm}(k) = \pm\sqrt{[(\hbar v_D k)^2+\Delta^2]}$, with $\Delta = J\,p\cdot n$ for surface normal n. Such a mass response has a concrete condensed-matter realization. The archived ESFD action specifies neither these interfaces nor this coupling in galaxies. Qi, Hughes & Zhang (2008)

At zero temperature, fill the negative-energy branch of N cones. With an energy cutoff Λ, its change in energy per area is

$$-N\,[(\Lambda^2+\Delta^2)^{3/2} - \Lambda^3 - |\Delta|^3] \,/\, [6\pi(\hbar v_D)^2].$$

Expansion at small gap shifts the quadratic stiffness and leaves $\mathbf{+N|\Delta|^3/[6\pi(v_D)^2]}$. The power comes from the two-dimensional momentum measure k dk and linear dispersion. It was not set by a galaxy slope. For isotropic interface normals, the mean of $|\cos\theta|^3$ is ¼. With area per unit volume Σ, the bulk energy therefore gains $c_3|p|^3/3$ with $c_3 = \Sigma N|J|^3/[8\pi(\hbar v_D)^2]$. Use a_R for the quadratic stiffness after its cutoff-dependent shift, and retain a positive renormalized b_4.

In this cutoff model $a_R = a_{bare} - \Sigma N\Lambda J^2/[6\pi(\hbar v_D)^2]$, using $\langle\cos^2\theta\rangle = ⅓$. If a_{bare} exceeds a_c, increasing the interface area can itself drive the response through criticality. The required area density is $\Sigma_c = 6\pi(\hbar v_D)^2(a_{bare}-a_c)/(N\Lambda J^2)$. This threshold depends on short-distance matching. The model gives no mechanism that stabilizes the area at Σ_c.

$$g_b = \delta y + y^2/a_D + y^3/a_q{}^2,\ \delta = (a_R-a_c)/a_c,\ a_D = \lambda\kappa^2/c_3\ (y \ge 0).$$

At criticality the quadratic force term dominates at small y. For $g_b = GM/R^2$ it gives $y \approx \sqrt{(a_D GM)}/R$ and $v_\infty{}^4 = GMa_D$. A positive residual δ eventually restores a Keplerian decline. A proportionality scale was fitted, while the exponent and its sign followed from the state counting.

Range of the argument. Temperature, nonzero chemical potential or finite interface size rounds the cusp below its energy scale. A strict infinite-radius limit requires cold, gapless interfaces and critical tuning. A finite-T transition can give a finite scaling interval. Interacting fluctuations could change this free-fermion, mean-field result. The archived three-dimensional bulk spectrum alone supplies no two-dimensional density of states.

Original matter and saturation terms · 4.1.docx §3.2. The interface ensemble, its area density, gap matching and baryonic coupling are additional hypotheses. The release verifies the sign and coefficient by independent momentum quadrature.

A check using ordinary spin waves

There is a second mechanism that appears to give the same exponent. In a three-dimensional continuously ordered spin medium, a weak aligned source stiffens two orientational modes. Subtracting the zero-field fluctuation integral gives $\int[1/k^2-1/(k^2+m^2)]d^3k/(2\pi)^3 = m/(4\pi)$. Since m^2 is proportional to the source, the polarization change is proportional to its square root. This ordered-phase effect is well established in short-range spin models. Campostrini et al. · Engels & Mendes

Gravity changes this calculation. Only the longitudinal Fourier component of p can be followed by $g = \nabla\Psi$. Eliminating g leaves a positive penalty $a_c|P_T p|^2/2$ for nonzero wavevectors, where P_T projects perpendicular to the wavevector. In a single ordered patch take $p_0^2 = (a_c-a)/b_4$ and spin stiffness $\rho_s = Dp_0^2$. In the limit of a stiff amplitude, the two tangent modes acquire squared gaps proportional to 1 and $\cos^2\theta$, with θ the angle between order and wavevector.

Define $d = \kappa p_0$, $m_d^2 = a_c p_0^2/\rho_s$, $\varepsilon = k_B T m_d/(8\pi\rho_s)$ and $x = g_b/d$. The driven change about the ordered reference gives

$$y = \varepsilon d\, H(x),\quad H(x) = 3[\sqrt{(1+x)}-1]/2 + (x/2)\,\mathrm{asinh}(1/\sqrt{x}).$$

The angular integral uses $\sqrt{(1+x)}-1$ for one mode and averages $\sqrt{(\cos^2\theta+x)}-|\cos\theta|$ for the other. For $x \ll 1$, $H(x) = x[¾ + (\ln 2)/2 - (\ln x)/4] + O(x^2)$. Thus the weak-field correction grows relative to baryons only logarithmically. $H \approx 2\sqrt{x}$ at large x, but a dominant extra force then requires $\Delta p/p_0 = y/d > g_b/d \geq 1$. That violates the small-fluctuation expansion which produced this result.

The unrestricted SPARC fit reached exactly the square-root boundary with singular fluctuation amplitude. Restricting ε and $\Delta p/p_0$ to at most 0.1 on training radii gave 46.35 km/s external error, versus 38.07 km/s for the formal square-root shape. No scored radius combined a dominant extra force, the high-x regime and a controlled perturbation. This calculation also assumes any ordered background has been subtracted in a local frame. An isotropic galactic arrangement with a canceled background requires its own model.

Ordered-phase fluctuation integral and ESFD gravity projector · derivation here. The numerical check verifies the angular integral independently. Result tables · wave_validity.csv and cohort_scores.csv.

What the rotation curves can distinguish

All fits used actual measured galaxy speeds and the archived baryonic curves. We trained on four whole-galaxy SPARC folds and scored the fifth, then fitted on all SPARC galaxies and froze each model for PROBES. We minimized squared differences between predicted and measured speeds, weighting galaxies equally. Every model used the same observations. No outer slope or lensing point entered the fit.

Gravity law	SPARC · 131 galaxies	PROBES · 245 galaxies
Baryons alone	55.30	74.08
Exact critical quartic	21.76	40.64
Free stiffness, quartic	21.54	39.19
Critical interfaces + quartic	21.66	39.43
Free stiffness, interfaces + quartic	21.54	39.19
Pure square-root excess	22.63	38.07
Simple MOND	21.30	39.31
Previous ESFD cored law	21.52	39.56

Entries are the square root of the mean of per-galaxy mean squared speed errors, in km/s. The free combined fit set the coefficient of y^2 to zero on all five training folds and in the full SPARC fit. When δ was fixed to zero, the full sample instead gave $a_D = 1.52 \times 10^{-10}$ and $a_q = 6.69 \times 10^{-11}$ m/s^2. The slope-generating coefficient is identifiable conditional on criticality. The disk fits supply no independent evidence for surface fermions.

Outer slopes and NGC 2403

We measured d ln v/d ln R over the outer radial half in 122 SPARC and 232 PROBES galaxies with adequate sampling. For critical interfaces the median absolute slope error was 0.097 and 0.157, versus 0.133 and 0.179 for a constant-speed prediction. On the 44 SPARC curves with near-Keplerian baryonic profiles, the median observed slope was −0.061, versus −0.075 for critical interfaces and −0.088 for free stiffness. Only eight external galaxies qualified for this compact-baryon comparison.

For NGC 2403 the critical interface model predicted 124.0 km/s at 20.87 kpc, compared with 134.0 ± 3.1 km/s observed. Its full-curve error was 7.68 km/s and its outer slope was +0.035, versus +0.070 observed. The freely fitted quartic gave 7.57 km/s and +0.010. These disk calculations use the spherical algebraic force with the measured radial baryonic field. Three-dimensional disk solutions could change the numbers.

SPARC inputs · PROBES I. Results · galaxy_scores.csv, NGC2403_curve.csv and cohort_scores.csv. The earlier cubic-energy fit is the pure square-root control here.

The larger radii separate the predictions

The late-type lensing stacks extend well past the measured disks. We froze every acceleration scale at its full-SPARC value, used the tabulated mass for each bin, and compared predicted speeds with the published shear-inferred speeds. This requires equal spatial and temporal metric potentials and an approximately isolated, compact baryonic source. Neither condition follows from the spin clock by itself.

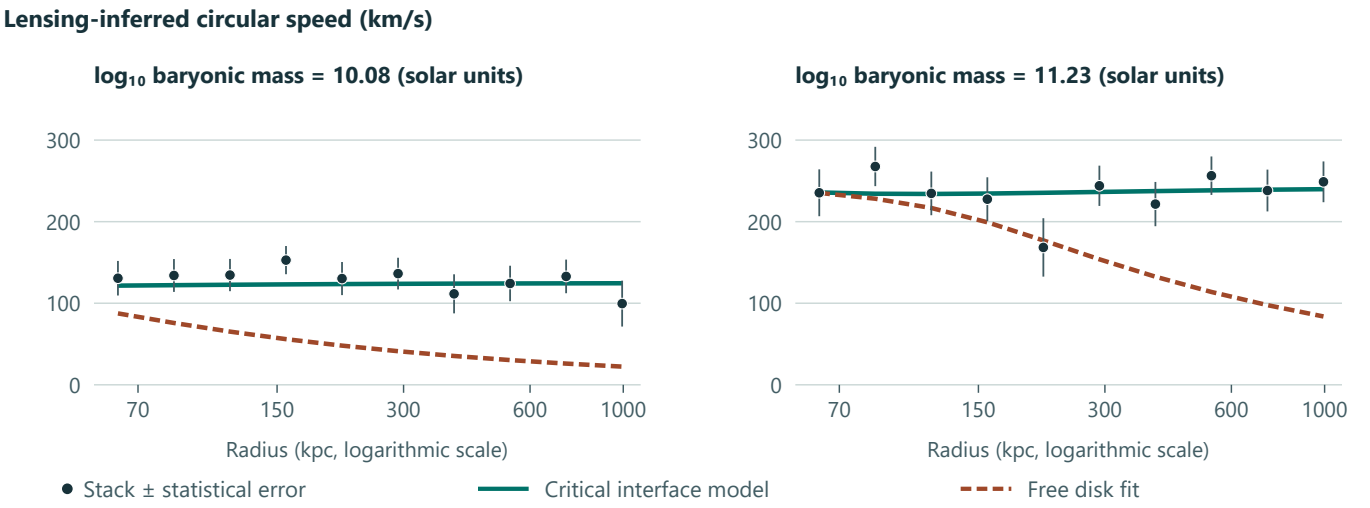

Frozen model	50–300 kpc · 24 cells	300–1,000 kpc · 16 cells
Free stiffness, quartic	63.1 km/s	106.6 km/s
Exact critical quartic	37.8 km/s	102.4 km/s
Critical interfaces + quartic	22.3 km/s	28.6 km/s
Pure square-root excess	33.8 km/s	31.4 km/s
Simple MOND	24.1 km/s	24.6 km/s

The plotted points use the publication's statistical speed errors. Additional systematic errors are retained in the accompanying table. At 300–1,000 kpc the free quartic predictions averaged 102.9 km/s below the measurements, and the exact critical quartic averaged 96.6 km/s above them. The critical interface model averaged 14.9 km/s high. For the highest mass bin at 993.86 kpc it gave 239.8 km/s, versus 248.8 ± 25.0 statistical ± 29.7 systematic km/s.

Individual outer stacks have considerable scatter. Their four measured log slopes span −0.519 to +0.090, while the critical interface slopes span +0.004 to +0.011. The table reports unweighted RMS discrepancies in amplitude. Bin mass spread, isolation, extended gas and correlated shear errors preclude a joint significance claim from these cells.

Mistele et al. (2024), weak lensing of isolated galaxies. Archived late-type table 1 and companion masses. Derived files · lensing.csv, lensing_slopes.csv and lensing_scores.csv.

How close to criticality would a galaxy have to be?

The critical-interface fit predicts flat limiting speeds of 125, 174, 206 and 242 km/s for the four published lensing masses. A small positive δ eventually stops that scaling. At a fixed measured radius we can ask how large δ could be before the linear term becomes as large as the y^2 term. This is a requirement of the fitted model, rather than a confidence interval inferred from shear.

Baryonic mass, solar units	δ for linear = quadratic at 993.86 kpc	δ for linear = 10% of quadratic
1.20×10^{10}	0.00235	0.000316
4.57×10^{10}	0.00458	0.000612
8.91×10^{10}	0.00638	0.000850
1.70×10^{11}	0.00878	0.00117

For the lowest-mass bin the renormalized quadratic stiffness must lie within about **0.24% above its critical value** for the interface term to exceed the residual linear term there, with a_D and a_q held at their critical-fit values. A ten-to-one dominance needs about 0.032%. The calculation retains the quartic correction. The free disk fit's δ ≈ 0.117 is much larger and has a different nonlinear coefficient.

Which assumptions still need physics

The coupling $-\lambda p \cdot \nabla \Psi$ used in the reciprocal energy presumes a **polar current**. Intrinsic spin in a rest frame is an axial vector. Identifying the two directly in a parity-even isotropic medium would forbid the coupling. A parity-odd background or a derived polar spin-transport current could supply the required matching. The master's entropy-weighted current is a candidate for the latter. A universal value of λ for neutral matter remains to be shown.

The observed curves fix combinations of constants, including $\lambda\kappa^2/c_3$. They do not separately fix the interface area density, Dirac velocity, spin gap J, or the independent spin susceptibility. Locating a gap proportional to spin, measuring the low-energy density of states, and measuring the current response to a separate drive would test the proposed carrier. The resolved radio measurements in the previous study constrain ordinary magnetic-field gradients. They do not measure these interface quantities.

A flat-speed law continued indefinitely gives a logarithmically growing potential. A global model with a finite lapse therefore needs an outer boundary or different physics beyond the measured range. Maintaining the requisite stiffness throughout the observed galaxies and their surroundings remains the central unresolved step for ESFD.

Calculation · criticality_scales.csv. Reproduction · research/critical_response/README.md, analyze.py and checks.py. The research bundle includes the source manuscripts, frozen galaxy inputs, numerical outputs and editable study.

Can the interface population keep itself critical?

A sign change of a bulk Dirac mass gives a concrete construction for the surface spectrum used on page 4. Let $M(z)$ have opposite signs on the two sides of an interface, with the positive side at $z > 0$. At zero in-plane momentum the Dirac equation is $[-i\hbar v_D \alpha_z \partial_z + \beta M(z)]\psi = 0$. In the $+1$ eigenspace of $i\alpha_z\beta$ its solution is proportional to $\exp[-\int_0^z M(s)ds/(\hbar v_D)]$. It decays on both sides. A mass kink $M_0 \tanh(z/L)$ gives the normalizable profile $\cosh(z/L)^{-M_0 L/(\hbar v_D)}$. The in-plane Dirac matrices preserve this subspace and yield the linear two-dimensional dispersion.

The original manuscript uses a bulk mass m. Its isotropic vector saturation energy has a connected sphere of ordered directions. A connected set of directions does not require a wall between two discrete signs. A discrete mass-generating order, anisotropy or another independent reason for mass inversion is needed. The ordinary geometric thinness of a luminous galaxy disk does not produce the required quantum spectrum.

Testing whether the threshold is selected

Write the zero-drive free energy as the sum of an interface population energy $f_{wall}(\Sigma)$ and the spin free energy. At the onset $p \to 0$ the Σ-dependent terms multiplying p^2 and $|p|^3$ vanish. Stationarity in Σ then requires $f'_{wall}(\Sigma) = 0$. Criticality separately requires $a_R(\Sigma) = 4\pi G\lambda^2$. Neither variation makes the two conditions identical. For example, positive wall tension with $f_{wall} = \sigma\Sigma + u\Sigma^2/2$, $\sigma,u > 0$, gives $\Sigma = 0$ in the disordered equilibrium. A feedback or conservation law fixing a nonzero critical area remains to be supplied.

The same example gives a way to distinguish the mechanism experimentally. Changing the interface area at fixed Dirac velocity, gap coupling J and cutoff Λ simultaneously lowers the quadratic stiffness and increases the cubic energy. In the ideal cutoff model their slopes must satisfy

$$dc_3/d(a_{bare} - a_R) = 3|J|/(4\Lambda).$$

A measurement of the gap coupling, the band scale and the two changes in the equation of state could check this relation independently of rotation curves. The cutoff-dependent ratio is specific to the specified microscopic model. The $|\Delta|^3$ exponent is the more general spectral prediction.

ESFD bulk Dirac and saturation terms · 4.1.docx §§3.1–3.3. Example of interface mass inversion and a surface Dirac mass · Qi, Hughes & Zhang. The population-energy check and linked stiffness prediction are derived here.

Can particles hold the interfaces open?

Positive surface tension shrinks an empty interface. Suppose a conserved number density n of mobile Dirac quasiparticles occupies its upper band. Spreading the particles over more area lowers their kinetic energy. Let Σ be the area per unit volume, σ the positive net tension at zero filling, N the number of cones, and $w = \hbar v_D$. The zero-temperature, zero-polarization number and energy per area are $Nk_F^2/(4\pi)$ and $Nwk_F^3/(6\pi)$. Counting the states gives the following energy per volume.

$$F(\Sigma) = \sigma\Sigma + 4\sqrt{\pi}\, w\, |n|^{3/2} / [3\sqrt{(N\Sigma)}].$$

At fixed $n \neq 0$ the minimum has $E_F = wk_F = (12\pi\sigma w^2/N)^{1/3}$ and $\Sigma = 4\pi|n|w^2/(NE_F^2)$. This yields a finite, stable area and a specific filling energy. Changing n changes the area. The minimum meets the gravitational critical-stiffness condition only for a further relation among density, tension and the microscopic couplings. The manuscripts provide no such relation.

The price of filling the surface band

Let $\Delta = Jp\cdot\hat{n}$ be the spin-dependent gap and Λ the ungapped band cutoff. For fixed number per area, upper- and lower-band energies cancel for momenta below k_F. With $H(E) = (E^2+\Delta^2)^{3/2} - E^3$, the energy change per area is $N[H(E_F) - H(\Lambda)]/(6\pi w^2)$. At zero filling $H(0) = |\Delta|^3$. For any $E_F > 0$ both terms are analytic in Δ^2 near zero. This removes the cubic energy responsible for the strictly flat limit. A nearly flat interval can survive where the spin-induced gap is large compared with the filling energy.

Write $t = \kappa E_F/|J|$ as an acceleration, $y = \kappa|p|$, and $u = |\cos\theta|$. At fixed background area and fixed filling on each patch, the neutral coefficient y^2/a_D in the force acquires the following orientation average.

$$I(y,t) = 4\int_0^1 u^2\sqrt{(t^2+y^2u^2)}\, du,\ g_b = y\, I(y,t)/a_D + y^3/a_q^2.$$

Keeping the neutral microscopic stiffness fixed gives $I = 4t/3 + 2y^2/(5t) + \ldots$ at small y. The residual linear stiffness becomes $4t/(3a_D)$, so isolated speeds ultimately decline as $R^{-1/2}$. Compensating this stiffness by hand replaces I by $I - 4t/3$. The surviving cubic force then gives $v \propto R^{1/6}$. Both cases recover $I = y$ as $t \to 0$ at fixed y.

A smooth adjustment of area cannot restore the missing cusp. Here the area stiffness is $K = 3\sigma/(2\Sigma_0)$ at equilibrium. If the quadratic spin stiffness is $r(\Sigma)$, relaxation moves the area by $-r'(\Sigma_0)p^2/(2K)$ and shifts the quartic coefficient by $-r'(\Sigma_0)^2/(2K)$. The zero-field stiffness $r(\Sigma_0)$ survives. The compensated limit assumes a positive effective quartic. The data test holds the area and particle number per patch fixed as spin responds. The tension and the rate of particle exchange between patches remain unmeasured.

The wall tension, conserved filling and spin-dependent surface gap are added hypotheses. State counting and the force are derived here. For the underlying surface spectrum see Qi, Hughes & Zhang. Numerical integration independently checks the occupied-band cancellation and angular average.

How much filling do the galaxies allow?

We kept the neutral model's two nonlinear coefficients fixed at their existing SPARC training estimates and varied only $t = \kappa E_F/|J|$. Each SPARC prediction uses a fit that excluded the whole galaxy. All 245 PROBES curves and both lensing bands use the all-SPARC calibration. Disks receive equal weight per galaxy and lensing receives equal weight per populated mass–radius cell. The earlier results on these samples were known when the new mechanism was proposed.

Model or fixed filling	SPARC · 131 disks	PROBES · 245 disks	Lensing · 16 far cells
Neutral critical interface	21.66	39.43	28.61
Filled, t fitted on SPARC	21.65	39.51	88.62
Filled, $t = 10^{-12}$ m/s²	21.66	39.43	22.86
Compensated, same t	21.68	39.36	48.79

Entries are RMS speed errors in km/s. The far lensing band spans 300–1,000 kpc. Keeping the microscopic stiffness fixed gave $t = 7.96 \times 10^{-12}$ m/s² on all SPARC. The five training-fold estimates ranged from 6.30 to 9.33 × 10^{-12} m/s². This changes the held-out disk error by only 0.009 km/s, but raises the far lensing error by 60.0 km/s. The compensated variant selected zero filling on every training fold.

At the smaller, fixed value 10^{-12} m/s² the distant discrepancy decreased. That value was one of seven points on a sensitivity grid. The lensing cells share uncertainties. Their RMS differences give no statistical detection of finite filling. Lowering the assumed stellar masses in SPARC by 20% gave far errors of 24.66 km/s for neutral interfaces and 88.05 km/s for disk-fitted filling at fixed stiffness. Raising the stellar masses by 20% set the interface weight to zero in the neutral calibration, leaving its filling unmeasurable.

Where an observation is most sensitive

For the lowest mass stack at 993.86 kpc, the neutral model gives 124.48 km/s. A 5% drop at fixed microscopic stiffness occurs at $t = 2.40 \times 10^{-13}$ m/s². When stiffness is compensated, a 5% rise occurs at 8.57×10^{-14} m/s². The observed value is 99.54 ± 28.14 statistical ± 13.54 systematic km/s. The 5% criterion describes sensitivity of the model prediction. The observation does not measure t to that precision.

For NGC 2403 at 20.87 kpc the disk-calibrated filled model predicts 122.24 km/s, compared with 123.98 for the neutral interface and 134.0 ± 3.1 observed. The local gap scale J, velocity v_D, area density and coupling κ remain unmeasured. Determining whether conserved carriers can support ESFD interfaces in a galaxy requires an independent estimate of their filling and tension.

The mass calibration and lensing assumptions follow pages 6–8. SPARC · PROBES · Lensing. Reproduce all seven supplemental tables with research/critical_response/carrier_filling.py --check.

From spin fields to galaxy gravity

A force law from the ESFD equations

Christopher Grenke's clock law couples elapsed time to the local spin–field contraction. His spin–entropy equation assigns gravitational mass density to the divergence of a collective current. Taken together, they allow two different questions to be tested. Can the measured magnetic field supply the missing radial force? Can a collective spin response produce the force even where a local magnetic field has little radial gradient?

The collective calculation gives a specific prediction. If the reversible quartic spin coordinate carries the current, responds to the gravitational potential gradient, and has the critical susceptibility derived on page 3, the spherical acceleration is

$$g = g_b + (a_q^2\, g_b)^{1/3}.$$

Here g_b is the Newtonian acceleration of the observed baryons and a_q is one common acceleration scale. Far outside an isolated finite mass, this model predicts a 12% increase in speed each time the radius doubles. That exponent follows from the quartic energy. The identification of a spin current and the value of its susceptibility are physical assumptions.

Test	Result
Five independent radio profiles	The direct magnetic prediction raised the held-out equivalent-speed error from 48.6 to 56.5 km/s relative to baryons alone. One galaxy required the opposite sign.
376 archived rotation curves	The collective quartic law reduced the galaxy-weighted speed error from 55.3 to 21.8 km/s in SPARC and from 74.1 to 40.6 km/s in external PROBES. Other gravity laws gave comparable errors.
NGC 2403	With the entire galaxy held out of calibration, the quartic law reached 7.24 km/s RMS error across 73 measured radii. It predicted 128.4 km/s at the last point, where the measured speed was 134.0 km/s.

The data favor a collective acceleration tied to the baryonic distribution over an extra force proportional to the gradient of the measured field squared in these tests. They leave open whether the collective response is carried by spin. That identification requires physics beyond rotation-curve fitting.

ESFD manuscripts · 21.docx §3.2, 4.1.docx §§11.2–11.3, November master §9, and the 27 November spin-response revision. Galaxy inputs · SPARC, PROBES and LOFAR.

How a spin-dependent clock could produce attraction

The clock branch in 21.docx gives $\Phi_{EM} = \kappa_{EM} S_{\mu\nu} F^{\mu\nu}$ and $d\tau = \exp(-\xi\Phi_{EM})\, dt$. The earlier 4.1.docx also gives an exponential clock law and motivates gravity through $F = T\nabla S$. Use the dimensionless quantity $u = -\ln(d\tau/dt)$ for a clock at rest. Treating that rate as the lapse N of a stationary metric common to all matter, and assuming geodesic free fall, gives the weak, slow-motion limit

$$\Psi = c^2 \ln N = -c^2 u,\ a = -\nabla\Psi = c^2\nabla u,\ v_c^{\,2} = -c^2\, du/d\ln R.$$

A larger u near the center therefore gives an inward acceleration. A shift confined to one clock transition would require different physics. Universality is essential. The printed coefficients in the draft's clock example do not supply a measured universal coupling.

An explicit inverse-square solution

Promote u to an independent collective amplitude. Let u_B denote its preferred local spin–magnetic part. Give gradients of $u-u_B$ a stiffness K and couple rest mass density ρ_b to the same lapse. One trial static energy is

$$E = \int [\ \tfrac{1}{2}K\,|\nabla(u-u_B)|^2 + \rho_b c^2\,(e^{-u}-1)\ ]\, d^3x.$$

With fixed u_B and fields vanishing at infinity, stationarity gives $\nabla^2(u-u_B) = -(\rho_b c^2/K)e^{-u}$. At first order, a point mass M gives $u-u_B = G_{eff}M/(c^2 r)$, where $G_{eff} = c^4/(4\pi K)$. The gradient yields the ordinary inward force per unit mass, $G_{eff}M/r^2$. Matching measured G requires $K = 9.63 \times 10^{42}$ N. This calibrates a stiffness. Its microscopic value and the universal coupling to neutral mass remain to be derived.

The same equation supplies the ordinary baryonic potential used in the radio test. Its extra effective density is $\rho_x = -(K/c^2)\nabla^2 u_B = \nabla\cdot Q$ with $Q = -(K/c^2)\nabla u_B$, in kg/m². A strictly local identity $u = \xi\kappa_{EM} S\cdot F$ leaves no independent mode to vary. Introducing the collective degree of freedom adds that missing assumption. A finite correlation length λ, modeled by $K(u-u_B)^2/(2\lambda^2)$, would cut off the point-source field as $\exp(-r/\lambda)/r$.

Author's clock and entropy proposals · 21.docx §§3.2–3.3 and 4.1.docx §§11.2–11.3. The energy, stiffness matching and weak-field derivation on this page are proposed here.

The quartic spin response fixes an outer slope

Start independently from the November master's $\rho_x = \nabla\cdot Q$, with Q proportional to its entropy-weighted spatial current sJ_s. Its weak-field Poisson equation is $\nabla\cdot(\nabla\Psi - 4\pi G Q) = 4\pi G\rho_b$. In a regular spherical configuration define the positive outward gradient $g = \partial\Psi/\partial r$ and $y = 4\pi G Q_r$. Integration on a sphere gives $g - y = GM_b(<r)/r^2 = g_b$. Test bodies accelerate inward. Both g and y have acceleration units.

The previous revision's reversible spin coordinate obeys $ap + bp^3 = h$, with $a,b > 0$ and measured drives in principle from field or rotation. Try a gravitational matching $h = \lambda g$ and $y = \kappa p$ with positive alignment. Eliminating p gives $g = A\,y + y^3/a_q^{\,2}$, with $A = a/(\lambda\kappa)$ and $a_q^{\,2} = \lambda\kappa^3/b$. This new drive and current identification require a microscopic justification.

> $g_b = (A-1)y + y^3/a_q^{\,2}$. At $A = 1$, $g = g_b + (a_q^{\,2} g_b)^{1/3}$.

Both static equations follow by varying one energy. Write y as a vector parallel to the equilibrium spin current. At A = 1 the energy density is $\rho_b\Psi + [\tfrac{1}{2}|\nabla\Psi - y|^2 + |y|^4/(4a_q^{\,2})]/(4\pi G)$. Varying Ψ gives the weighted-current Poisson equation. Varying y gives $\nabla\Psi = y + |y|^2 y/a_q^{\,2}$. Its two field-energy terms are nonnegative. Replacing the quartic term with $|y|^3/(3a_c)$ gives the cubic-energy alternative below.

For $A > 1$ the weak-source response is asymptotically proportional to g_b. $A = 1$ cancels the linear term and exposes the nonlinear spin response. This is a tuned critical susceptibility. For an isolated finite mass in the regime $y \gg g_b$, the extra circular speed obeys $v_x^{\,6} = GMa_q^{\,2}r$ and the total speed approaches the same $r^{1/6}$ scaling. An indefinitely flat rotation curve would contradict this asymptote in that regime.

Two flat-speed comparisons

Changing the leading nonlinear spin energy to $|p|^3$ gives a signed $p|p|$ term in the response. With the same critical matching, $g - y = y^2/a_c$ for $y \geq 0$. Thus $g = g_b + \sqrt{(a_c g_b)}$, giving $v_x^{\,4} = GMa_c$ outside the mass. This change to the spin energy is a candidate modification. The analytic p^4 term alone gives the other exponent.

A separate control takes $4\pi GQ = [1 - \mu(g/a_s)]\nabla\Psi$, with $\mu(x) = x/(1+x)$. The divergence equation becomes the AQUAL modified Poisson equation. In spherical symmetry $g = [g_b + \sqrt{(g_b^{\,2} + 4a_s g_b)}]/2$. Its flat limit gives $v^4 \to GMa_s$. This is the established simple MOND interpolation. Its success cannot distinguish an ESFD current from an equivalent force law.

Extended indefinitely, the quartic excess potential grows as $r^{1/3}$ and the flat-speed potentials as $\ln r$. A global solution with finite lapse needs an environmental boundary or a further change in the response. The data below probe finite radii.

ESFD · November master §9 and research/spin_response. Nonlinear potential theory and the simple interpolation · Bekenstein & Milgrom (1984) and Famaey & Binney (2005).

A direct test with measured magnetic fields

In a magnetic rest frame with negligible electric terms, choose the spin convention S:F = 2 s·B. For weak, aligned spin response at fixed susceptibility and negligible rotation drive, $p \propto B$, so $u_B = qB^2$. Define $C = c^2q$. The local excess in squared circular speed is $-C\, dB^2/d \ln R$. A uniform magnetic field supplies zero extra radial force. A constant extra speed over a radial interval requires B^2 to fall linearly with $\ln R$ there.

$$\int (v_{obs}^2 - v_b^2)\, d \ln R = C\,[B^2(\text{inner}) - B^2(\text{outer})].$$

This integral uses the potential difference directly and avoids differentiating a noisy digitized field profile. The right side comes from radio observations. The left side comes from the rotation curve and its baryonic decomposition. Annular equipartition strengths approximate the spin-weighted field. In particular, squaring an annular mean and averaging the true local B^2 are different operations.

We rescaled radio radii to each SPARC distance. Of 201 archived radio rings, 183 lie within the native rotation curves. At each radius we integrated a piecewise-linear interpolant of squared speed in $\ln R$. We averaged the integral and B^2 over the first and last quarters of retained rings, then divided the contrast by the separation of their mean log radii. The square root of the resulting mean v^2 is the interval-equivalent speed. Each row below is one galaxy.

Galaxy	Inner → outer field, μG	Observed speed, km/s	Magnetic + baryons, km/s
NGC 2841	8.42 → 7.58	315.4	217.6
NGC 2976	9.58 → 10.39	44.0	18.8
NGC 3198	10.71 → 8.61	94.2	80.0
NGC 5033	15.28 → 8.51	220.1	199.1
NGC 5055	17.53 → 8.27	195.1	266.7

Each prediction used a single nonnegative C fitted on the other four galaxies. Each field value shown is the root mean square of the published annular estimates in its endpoint group. Folds used unweighted squared-speed loss across galaxies. Correlated rings share photometry, geometry and interpolation. They do not provide 183 independent tests.

Radio field estimates · Heesen et al. (2023), Appendix D. Kinematics and mass models · Lelli, McGaugh & Schombert (2016). Matched inputs and digitized rings are in the release.

Where the magnetic prediction fails

The sign mismatch occurs in NGC 2976. The equivalent baryonic speed is 33.7 km/s and the measured value is 44.0 km/s, requiring extra inward acceleration on average. The rise in field strength gives an outward contribution. In NGC 5055 the field falls steeply and predicts too much acceleration. In NGC 2841 the field falls too little for the large required excess.

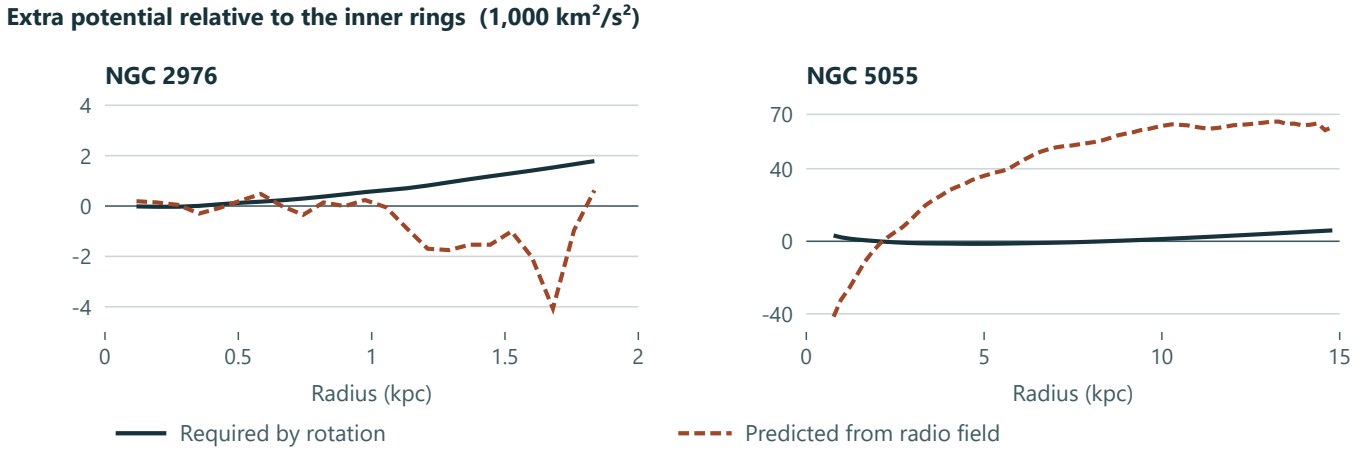

The solid curve is the integrated excess potential from rotation. The dashed curve uses the field and the coefficient fitted on the four other galaxies. Each is referred to its own inner-group mean. The panels have different vertical scales. Zero extra field-induced potential at all radii would track NGC 5055 more closely than the held-out prediction.

Prediction	RMSE of equivalent v^2, km²/s²	RMSE of equivalent speed, km/s
Baryons alone	24,590	48.6
Baryons + magnetic term	27,912	56.5
Baryons + constant excess v^2	24,562	65.3
Previously calibrated cored law	15,688	29.9
Local spin term alone	51,275	138.0 over 4 valid speeds

The local-only law gives negative v^2 for NGC 2976. The other rows have five valid speeds. Changing the magnetic response from B^2 to the full quartic crossover at 10 μG or to $B^{4/3}$ gives 58.1 and 58.6 km/s. Unrestricted signs leave the primary fit unchanged. Fractional-error refitting gives 49.5 versus 48.6 km/s for baryons. Tightening the allowable native radial gap to 1.5 kpc leaves four galaxies and raises magnetic error to 182.5 km/s. The small sample is sensitive to radial coverage and weighting.

On exactly these five intervals, the collective quartic, cubic and simple MOND predictions give 31.0, 29.4 and 31.2 km/s, respectively. Each used 105 other SPARC galaxies for training. The magnetic fits had four other galaxies with independent field profiles.

Tables · magnetic_scores.csv, magnetic_folds.csv, magnetic_profiles.csv and magnetic_profile_errors.csv. The radio error bars in the source describe annular scatter. No significance level is assigned to these five-galaxy contrasts.

Rotation-curve tests across 376 galaxies

Each collective model used one acceleration scale. For SPARC, that scale was fitted on four archived galaxy folds and predictions were scored on the fifth. For the external test, each scale was calibrated once on all 131 SPARC galaxies and frozen on 245 PROBES galaxies. No observed velocity from a scored galaxy entered its collective force prediction. The analysis used 3,032 distinct galaxy–radius pairs from SPARC and 15,976 from PROBES. Repeated radii were combined in squared speed.

Force law	SPARC · 131 galaxies	PROBES · 245 galaxies
Baryons alone	55.30 / 44.73	74.08 / 64.82
Critical quartic spin energy	21.76 / 14.20	40.64 / 30.93
Critical cubic spin energy	22.63 / 12.78	38.07 / 28.96
Simple MOND interpolation	21.30 / 13.04	39.31 / 29.80
Archived cored law	21.52 / 12.45	39.56 / 29.92

All figures are km/s. The first number is the square root of the equally weighted mean of the galaxies' mean squared velocity errors. The second is the median per-galaxy RMS error. Both use each galaxy's full sampled curve. The earlier inner-anchored outer-disk experiment asked a different question and used different errors.

The full-SPARC acceleration scales were 4.83×10^{-11} m/s² for the quartic law, 6.40×10^{-11} m/s² for the cubic law and 1.10×10^{-10} m/s² for simple MOND. Quartic spin improved on baryons in 123 of 131 SPARC and 239 of 245 PROBES cases. It beat the archived cored law in 58 and 85, respectively. The cubic-energy modification beat quartic in 174 external galaxies and had the lowest external average error here. In SPARC its average error was the largest of the three collective laws.

Scope of the disk calculation

The radial formula is exact in spherical symmetry. For disks we substituted $g_b = v_b^2/R$ using the archived disk baryon model. A full nonlinear field solution requires the three-dimensional mass and boundary conditions. PROBES uses approximate exponential stellar and gas disks and redshift-based distances. Gas distribution, inclination and stellar mass uncertainties affect the absolute errors. These common inputs let the data distinguish some response laws without identifying their microscopic source.

SPARC mass models · PROBES I data · Archived external sample selection, folds and baryon models. Reproducible outputs · collective_galaxies.csv and collective_scores.csv.

NGC 2403 gives a concrete field target

The quartic law fitted without NGC 2403 gives $a_q = 4.92 \times 10^{-11}$ m/s² and an RMS error of 7.24 km/s over its 73 radii. Simple MOND gives 7.46, the cubic modification 10.63, the archived cored law 11.08 and baryons alone 50.70 km/s. The quartic prediction at 20.87 kpc is 128.44 km/s, compared with 134.0 ± 3.12 km/s observed. This local agreement coexists with weaker quartic performance across the external sample.

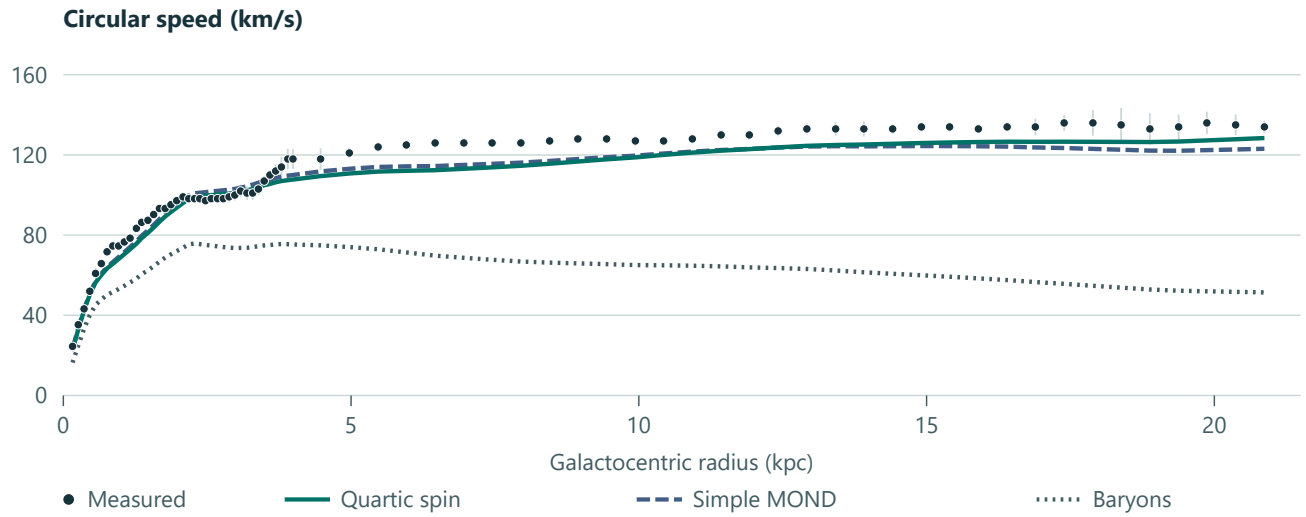

An independent way to check the magnetic explanation

From 10.435 to 20.87 kpc the measured curve requires an extra potential rise I = 9,770.6 km²/s² beyond baryons. The implied inner-minus-outer spin lapse is $I/c^2 = 1.087 \times 10^{-7}$. As a clock signal that would correspond to 32.6 m/s in equivalent redshift after separating baryonic, kinematic and other contributions. This is an inferred target from rotation.

The five-galaxy retrospective fit gives C = 91.54 (km/s)²/μG². At that value the weak magnetic law requires $B^2(10.435\ \text{kpc}) - B^2(20.87\ \text{kpc}) = 106.7\ \mu\text{G}^2$. Even zero outer field requires an inner field of at least 10.33 μG. The four-galaxy values of C range from 61.64 to 268.77, so this target depends strongly on calibration. The archive's 5.7 μG value is a disk mean. Sparse line-of-sight Faraday data do not establish either annulus's total field. A radially resolved measurement across both annuli would test the stated requirement.

SPARC kinematics and Chyży et al. (2017), disk field. Curve and integral · NGC2403_curve.csv and outer_lapse_targets.csv. Error bars in the chart are the archived SPARC speed errors.

Does the same field bend light?

A clock gives the temporal potential Ψ. Weak lensing also depends on the spatial potential Φ, through $(\Psi+\Phi)/2$ in the convention with spatial metric $(1-2\Phi/c^2)\delta_{ij}$. A purely conformal metric $e^{-2u}\eta_{\mu\nu}$ gives $\Phi = -\Psi$ and zero light deflection in this isolated weak-field construction. The archived late-type galaxy stacks have nonzero shear, with inferred circular speeds of 130.2–267.7 km/s across the 24 cells used here. Pure conformal rescaling on flat spacetime fails as the sole origin of that lensing.

A second trial completion sets $\Phi = \Psi$. Then the shear-inferred circular acceleration is the one predicted by the radial force law under spherical isolation. For each of four published baryonic mass bins, we treated its tabulated mass as compact at 50–300 kpc, used the SPARC-calibrated acceleration scales, and made predictions at all six available radii. This adds a metric assumption while introducing no fitted lensing parameter.

Model for nonzero lensing	RMS against 24 tabulated speeds
Compact Newtonian baryons	139.3 km/s
Quartic spin, equal potentials	37.8 km/s
Cubic spin, equal potentials	33.8 km/s
Simple MOND, equal potentials	24.1 km/s

A direct look at radial shape

Between inner and outer pairs of lensing radii, the observed logarithmic speed slopes are +0.006, +0.182, +0.074 and −0.174 in order of increasing bin mass. Quartic spin predicts +0.155, +0.140, +0.126 and +0.106. It requires a rise in all four bins over this range. The observed slopes vary in sign. Projection, bin mass distributions, possible extended gas, environment and inter-bin covariance limit the comparison. These unweighted errors and slopes are descriptive.

The data require a source of light deflection. The spin-dependent clock supplies no equation for Φ. Equal potentials work appreciably better than the purely conformal choice in this test, but a causal relativistic spin theory still has to derive the spatial response.

Mistele et al. (2024), isolated-galaxy lensing. Source table 1, LTG mass bins, 62.71–291.07 kpc within the chosen 50–300 kpc window. Results · lensing.csv and lensing_slopes.csv.

What the measurements now demand of ESFD

A collective carrier. Ordinary attraction follows conditionally from a long-range spin mode with positive stiffness and a rest-mass coupling. The microscopic theory would have to derive the coupling for neutral, unpolarized matter, identify the current Q and determine whether its linear susceptibility reaches the critical value. A fit to rotation fixes one scale in each model. It does not measure any of these three ingredients.

A decision about the outer force. Quartic spin gives a rising outer speed around an isolated finite mass. A leading $|p|^3$ energy gives a flat outer speed and performed better on the external rotation curves. The two predictions can be separated with independently measured baryon mass profiles and extended dynamical or lensing radii. The near-flat limit of the cubic law also has a characteristic high-acceleration transition different from simple MOND. A physical spin sector must explain the form of its energy and its range of validity.

A measured field gradient. The five galaxy-specific values of C required by the radio test are +3,761, −95, +254, +170 and +18 $(km/s)^2/\mu G^2$ in the order on page 4. A single common coefficient misses both the sign and the range of amplitudes. Density-dependent susceptibility, differences between ordered and turbulent fields, or a rotation-driven response remain possible. Each would require an independently constrained spin model or observable. Fitting a separate C to each galaxy would remove the prediction being tested.

A target for additional galaxies. We integrated the outer radial half wherever at least three distinct measured radii cover that part of a curve. All 129 eligible SPARC galaxies and 243 of 245 eligible PROBES galaxies require a positive extra potential difference. The median required inner-minus-outer u is 7.18×10^{-8} and 1.38×10^{-7}, respectively. Two short SPARC outer curves miss the sampling rule. These values specify the sign and amplitude that future independent spin measurements must reproduce.

Reproducing the study

The research bundle contains the seven input tables, the method specification, the analysis and checks, all thirteen derived result files, and this manuscript and its rendering source. Run **python research/spin_gravity/checks.py** from its extracted root. The checks regenerate the numerical results, verify radial integration and force identities, recover known synthetic scales, and check that a held-out galaxy's velocities cannot set its magnetic prediction.

Project provenance · recovered 21.docx and 4.1.docx, November master §9, and Pattern Nexus ESFD research archive. Numerical provenance and the timing of exploratory choices · research/spin_gravity/README.md.

Electromagnetic Spin–Field Dynamics

A material response model and new astrophysical tests

Research revision · 27 November 2026

Christopher Grenke's ESFD program began with a spinning top. As the top gained or lost stability, did its rotation change the alignment of its microscopic spins in a way a magnetic measurement could detect? This revision brings that question down to two independently varied quantities, an applied magnetic field and an angular speed. It then tests what two astronomical branches actually predict from the available observations.

The new material prediction

If a specimen's magnetic moment and spin angular momentum follow one equilibrated degree of freedom, a small change in rotation is equivalent to a signed shift in applied magnetic field. One measurement fixes the conversion between the two. It must then predict the shift at a second field and rotation rate. The simplest quartic version also fixes a fifth-order coefficient from two lower-order measurements. Both predictions can fail.

What the data changed

Question	Result in this revision
Does the ESFD curve predict outer speeds?	Across 21 held-out NGC 2403 radii, a flat extrapolation had a 6.64 km/s error and the anchored cored law had a 9.80 km/s error. The latter had a modest median advantage in two larger samples.
Does a magnetar stay on one side of the boundary?	One recovered spin-down range for 1E 1048.1−5937 spans index values of 0.345 to 1.260. A separate star supplies a test using an X-ray spectral feature.
Must an outward-moving model star return?	The archived logarithmic force confines every finite-energy orbit. An explicit outer flux that compensates at large radius permits escape for some of the same launch states.

The calculation uses the 123-page master, the posted Pattern Nexus edition, archived study inputs, the ESFD chats and 33 additional Word sources identified by file hash. New work and its assumptions appear on the following pages. The full master edition includes the earlier paper after this revision.

Pattern Nexus research edition · Published research tools

The recovered drafts define different fields

The 59-page June 3 manuscript and the 22-page *Proof* were already in the supplied packet. A separate ZIP and five adjacent Word files supply 34 distinct Word files in total. One is byte-identical to the June 3 manuscript. The other 33 are additional file versions. All 17 drafts named in the June consolidation can now be traced to files. Three other recalled inputs remain unnamed.

Source	Field definition or role in that source
4.1, §§3.1–3.3 · June 3, §3.3	Both use $X = S_{\mu\nu}S^{\mu\nu}$ and $V = \lambda(X - \Phi_0^2)^2/4$. Draft 4.1 prints $\Phi = \lambda^{-1/2}\sqrt{X}$. June 3 prints $\Phi = \sqrt{X}$. Their printed amplitude scales differ.
21, §§3.2–3.3	The clock proposal uses a contraction of spin with the electromagnetic field, $\Phi = \kappa\, S_{\mu\nu}F^{\mu\nu}$. A later expression introduces a charge normalization. At fixed spin this contraction reverses when the field reverses.
41, first synthesis §§1.3, 3.2–3.3 · 4.5, §3.2	The composite choice $\Phi = \kappa^2 X$ weights the Maxwell term by $\exp(-\xi\Phi)$. X is even under reversal of spin and independent of F at fixed spin. The first synthesis treats the scalar kinetic term as optional.
Spin-Entropy Field Dynamics · November master, §9	The recovered manifesto sets out the physical motivation. The quantitative current and effective-density equations used here are traced to the consolidation record and the November reconstruction.

A correction to the clock example

Draft 21 §3.2.1 inserts charge density, radius, angular speed and field into $\Pi = \rho_q R^2 \Omega B$. Its laboratory factors, multiplied by the stated 10^{-36}, give 2.09×10^{-31}. Its neutron-star powers give 10^{-9}, or 6.28×10^{-9} with the stated angular rate. The printed values are 10^{-9} for the laboratory and approximately one for the star. The original clock-rate estimates cannot be inferred from those substitutions.

In SI, Π has units of pressure. Multiplication by the draft's area-valued κ gives a force. One possible repair is $\Phi = \Pi/P_*$, with a pressure scale P_* calibrated independently. A clock test would constrain ξ/P_* and must identify which charge co-rotates. The arithmetic above supplies no measured clock offset.

Primary evidence in the companion archive · recovered-sources/source-manifest.csv and research-history.md. The 96-page Word metadata for 41 identifies a saved consolidation conversation. Its identity as the recalled standalone long master remains open.

From intrinsic spin to a rotating specimen

Start with the June 3 action, with direct interaction $\alpha S_{\mu\nu} F^{\mu\nu}$ and saturation energy $\lambda(X - \Phi_0^2)^2/4$. Bulk angular speed does not specify the spin tensor. To close that gap for a single material, consider a uniform specimen at fixed temperature with a reversible axial spin polarization p. Choose a rest frame and aligned axes. Take $S_{0i} = 0$ and $S_{ij} = S_* \varepsilon_{ij3} p$, so that $X = 2S_*^2 p^2$ in this coherent approximation. Spin fluctuations beyond this mean-field projection require extra material parameters.

Energy at prescribed field and rotation

$$f(p) = a\,p^2/2 + b\,p^4/4 - g\,p\,B - \ell\,p\,\Omega$$

Here B is the calibrated axial field drive conjugate to magnetization, in tesla, with a consistent internal-field or demagnetization correction. Ω is the signed angular speed in rad/s. The dimensionless p carries magnetization $M = gp$ and spin angular-momentum density $j = \ell p$. Thus a and b have units J/m^3, g has units A/m, and ℓ has units $J\,s/m^3$. The two drive terms are energy densities. The spin part of the rotational work is $-\Omega j$. These are effective material coefficients.

Expanding the source potential with this projection gives $b = 4\lambda S_*^4$ and $a = a_{mat} - 2\lambda S_*^2 \Phi_0^2$ in a common unit convention. The additional material stiffness a_{mat} is an assumption. The direct spin–field term sets a contribution to g after field normalization and coarse graining. Neither g nor ℓ is determined by measuring the rigid-body angular speed alone.

What follows for the positive-stiffness branch

$$h = gB + \ell\Omega,\quad a\,p + b\,p^3 = h,\quad K = a + 3b\,p^2$$

For $a > 0$ and $b > 0$, K is positive and the stationary point is unique. At small drive $f_{min} = -h^2/(2a) + b\,h^4/(4a^4) + \ldots$. Its mixed energy term is $-(g\ell/a)B\Omega$. This supplies one material interpretation of a signed $B\Omega$ product. The curvature stays positive as the product changes. A universal collapse threshold needs additional physics. The model applies locally in the reversible range before higher powers, domains or hysteresis become important.

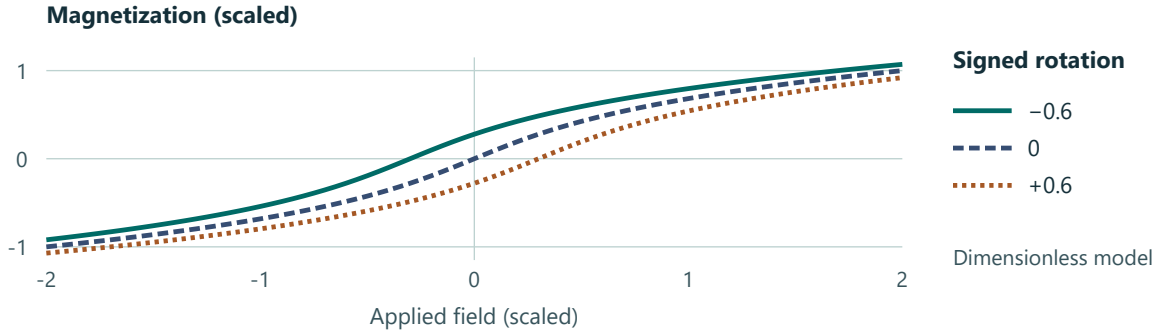

June 3, §§3.2–3.4 · recovered 4.1, §3 · November master, §§3–4. Background on magnetization by rotation and the magnetic equation of state.

Two ways to test the material model

Field and rotation must give the same shift

> $M(B, \Omega) = M(B + \ell\Omega/g, 0)$ for $g \neq 0$

At a given operating point, the derivatives of (M, j) with respect to (B, Ω) are $K_{BB} = g^2/K$, $K_{B\Omega} = K_{\Omega B} = g\ell/K$ and $K_{\Omega\Omega} = \ell^2/K$. Consequently $K_{BB}K_{\Omega\Omega} - K_{B\Omega}{}^2 = 0$. The determinant tests whether one coordinate supplies both responses after background subtraction. Reciprocity alone gives equality of the cross derivatives. Two responsive coordinates with different magnetic-to-angular ratios give a positive determinant when both stiffnesses are positive.

Determine ℓ/g on one slow field sweep with signed rotation. Use it to predict an independently repeated field sweep at a second Ω. A field-dependent shift, outside calibrated uncertainty, rejects the one-coordinate model with constant couplings. A full determinant test also needs independent angular-momentum readout and subtraction of rigid-body inertia. Measure field gradients, apparatus torque and ordinary magnetomechanical effects on separate controls. Ordinary magnetization can satisfy this null too.

A fifth-order prediction from two fitted coefficients

> $M(B, 0) = c_1B + c_3B^3 + c_5B^5 + \dots$, $c_1c_5 - 3c_3{}^2 = 0$

Series inversion gives $c_1 = g^2/a$, $c_3 = -bg^4/a^4$ and $c_5 = 3b^2g^6/a^7$. These are Taylor coefficients, with the factorials absorbed. A sixth-order term in the energy changes c_5. An independent two-state spin response proportional to $\tanh(B/B_0)$ gives $c_1c_5/c_3{}^2 = 1.2$. The quartic branch gives 3. Fit the first and third coefficients on a reversible calibration range, freeze the fifth-order prediction and test it against independent symmetric-field sweeps. Report coefficient covariance and field-window sensitivity. Use the undivided residual when c_3 is near zero.

The companion code checks the derivatives by finite differences across four states, the Taylor relation by exact rational arithmetic, and the determinant on a two-mode control. Its 243 sweep rows are model outputs. With a free-electron gyromagnetic magnitude only as a scale reference, 1 Hz of mechanical rotation corresponds to 35.68 pT. A specimen requires its own signed coefficient.

Derivation in this revision · research/spin_response/response.py and response_checks.json. Free-electron scale from NIST CODATA.

The far field of the direct coupling

The *Proof* proposes that spin–field energy generates an effective gravitational metric. Its displayed interaction permits a narrower calculation immediately. Hold the background geometry flat, use ordinary Maxwell propagation outside a compact source, take the spin tensor as a stationary localized source, and consider a neutral probe. This fixes the spatial decay of the direct electromagnetic channel.

$$H^{\mu\nu} = F^{\mu\nu}/\mu_0 - \kappa S^{\mu\nu},\ j_{\mathrm{pol}}{}^{\nu} = \kappa\, \partial_{\mu} S^{\mu\nu}$$

The effective polarization current is conserved by antisymmetry. Its net electric charge is proportional to the surface integral of S^{i0} at infinity. That integral vanishes for localized spin. For a purely spatial, stationary spin distribution the leading nonzero external magnetic field can be a dipole. Its axial amplitude scales as r^{-3}.

Probe response at large r	Energy scaling	Force scaling
Permanent aligned moment in a dipole field	$-\mu B \propto r^{-3}$	Magnitude $\propto r^{-4}$, with orientation dependence
Linear induced moment with fixed polarizability	$-\alpha_m B^2/2 \propto r^{-6}$	Magnitude $\propto r^{-7}$, with material dependence
Universal Newtonian monopole target	$-GMm/r$	Magnitude GMm/r^2

A vanishing dipole gives still faster falloff for these channels. This restricts the proposal that the direct local coupling alone supplies ordinary gravity from an isolated neutral rotating body. Extended currents, a separate propagating field or a metric response change the assumptions and need their own source law. The June action's Einstein–Hilbert term already transmits a long-range gravitational response to total stress with an input G.

What a gravity completion must calculate

A separate gravity branch must specify which field carries the monopole, why its source follows total mass-energy, and how neutral probes of different materials respond. Galaxy kinematics constrain the slow-matter potential Ψ. Lensing constrains the combination $\Psi + \Phi$ of metric potentials. A single fitted acceleration profile cannot determine both. The compensated example on the next page supplies a source diagnostic while leaving the metric matching open.

Proof of the Electromagnetic Spin–Field Dynamics Theory, pp. 1–4 · June 3, §3.2 · November master, §§4 and 9. The falloff follows by differentiating the two probe energies above.

Will a displaced star return?

The saved simulator export has 271 radii. At 20.6 kpc its ESFD circular speed is 143.323 km/s. The export was in baryons-only mode, where the circular speed is 67.975 km/s. Its separate ESFD column reproduces the published force law. Preserving the orbital velocity while switching to baryons alone can release a star because the local baryonic escape speed is only 98.066 km/s.

Write $r_c = 4.179$ kpc and $V^4 = GM_b a_*$ for the archived synthetic disk. Its additional inward acceleration is $g_0 = V^2 r/(r^2 + r_c^2)$. Its logarithmic potential grows without bound. In the spin–entropy branch the effective density is a spatial divergence, $\rho_x = \nabla \cdot Q$, with the phenomenological normalization absorbed in Q. A local Euclidean spherical example that compensates at infinity is

$$g_t(r) = g_0(r)\, R_t^2/(r^2 + R_t^2),\ Q_r = g_t/(4\pi G),\ M_x(<r) = r^2 g_t/G.$$

For a regular center the extra enclosed mass tends to zero at both ends. Its derivative changes sign. The negative outer contribution is an effective density correction. Choosing a reach R_t is an assumption. The closed-space integral constraint alone fixes no transition radius.

For $a = r_c^2$ and $b = R_t^2$, the potential with zero at infinity is $\Phi_t = V^2 b \ln[(r^2 + a)/(r^2 + b)]/[2(b - a)]$ for $b \neq a$. At 40 kpc reach the effective density crosses zero at 40.84 kpc. This radius identifies where outer matter-tracer or lensing observations could start to distinguish the source shapes, once their coupling to light is specified.

Stationary potential	Escape speed at launch	Outer turn after +12 km/s	Outer turn after +180 km/s
Baryons only	98.1 km/s	Escapes	Escapes
Reach 40 kpc	187.4 km/s	27.3 kpc	Escapes
Reach 80 kpc	234.8 km/s	22.8 kpc	258.0 kpc
Reach 160 kpc	277.9 km/s	22.1 kpc	91.8 kpc
Original logarithm	Unbounded	21.9 kpc	80.3 kpc

Every row starts at 20.6 kpc with tangential speed 143.323 km/s and the indicated outward speed. The 12 km/s value matches one simulator nudge. The 180 km/s value illustrates reach sensitivity. The turning radii solve the energy equation with angular momentum fixed in each potential. Large excursions extrapolate beyond the exported disk. A past screenshot alone cannot recover a particular trajectory.

Archive · Research/3D_Galaxy/physics.py and model.js. Supplied simulator export and numerical checks · research/spin_entropy/.

How much of the causal diamond is geometry?

The stored three-panel figure marks $\chi = cT/R = 0.348$, with endpoints separated by 2T. Its comparison is between the round 3-sphere and its Poincaré dodecahedral quotient at the same curvature radius R. The figure supplied the coordinate. The following area is calculated directly from the face geometry.

The centered spherical cell has twelve nearest faces at angular distance $f = \pi/10$. On a geodesic sphere of radius $R\chi$, each face excludes the directions in a cap whose limiting direction cosine is $u = \tan(f)/\tan(\chi)$. Up to the first edge at $\chi \approx 0.364864$ the caps are disjoint. Each covers a fraction $(1 - u)/2$ of the angular sphere. Thus, in the interval $f < \chi < \chi_{edge}$,

$$A_{quotient}/A_{sphere} = 1 - 6(1 - u),\ A_{sphere}/R^2 = 4\pi \sin^2\chi.$$

At 0.348 the two areas divided by R^2 are 0.546665 and 1.461388. The quotient area is **62.593% smaller**. Testing 60,000 nearly uniform directions independently gives a surviving fraction of 0.373767 versus the analytic 0.374073. This reproduces the earlier chat's rounded 62.6% with the spin current set to zero. It is a geometric baseline for the model.

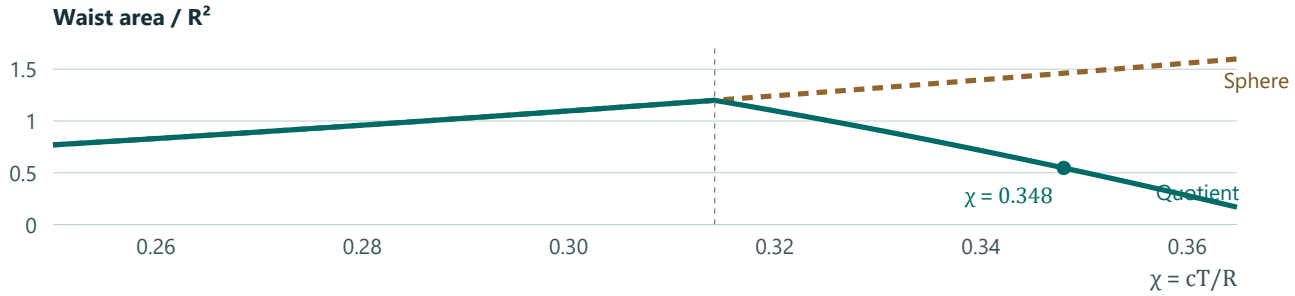

A wave observable with a separate source test

On this static quotient the first two nonconstant scalar harmonics have k = 12 and 20. Write $\omega_k^2 = \omega_0^2 + c_s^2 k(k+2)/R^2$ for the linear entropy mode. The shortest light loop takes $\tau = \pi R/(5c)$. Consequently

$$\tau \sqrt{(\omega_{20}^2 - \omega_{12}^2)} = (\pi/5)\sqrt{272} \cdot (c_s/c) = 10.3625 \cdot (c_s/c).$$

The curvature radius and the common frequency offset cancel. In the archived linearized field equation the imposed drive is proportional to $-\beta_s \nabla_\mu J_s^\mu$. Reversing a prescribed current reverses the driven perturbation at identical initial conditions after subtracting the undriven solution. Its sign tests a source coupling. The separate identity $\int \nabla_i (s J_s^i)\, dV = 0$ holds on a closed spatial slice. It constrains total effective density. Neither result establishes the topology of our universe.

Original Poincaré-space model · Scalar modes, Table 1 · Injectivity radius · Published figure discussion.

NGC 2403 and the shape of the outer curve

The SPARC table gives 134.00 ± 3.12 km/s at 20.87 kpc. Reserve all 21 radii beyond 10.435 kpc. The last three distinct inner radii have speeds of 128, 127 and 127 km/s. Anchor each model to their median before extrapolating its shape. This gives a flat extrapolation and two shaped predictions with the same information about inner speed.

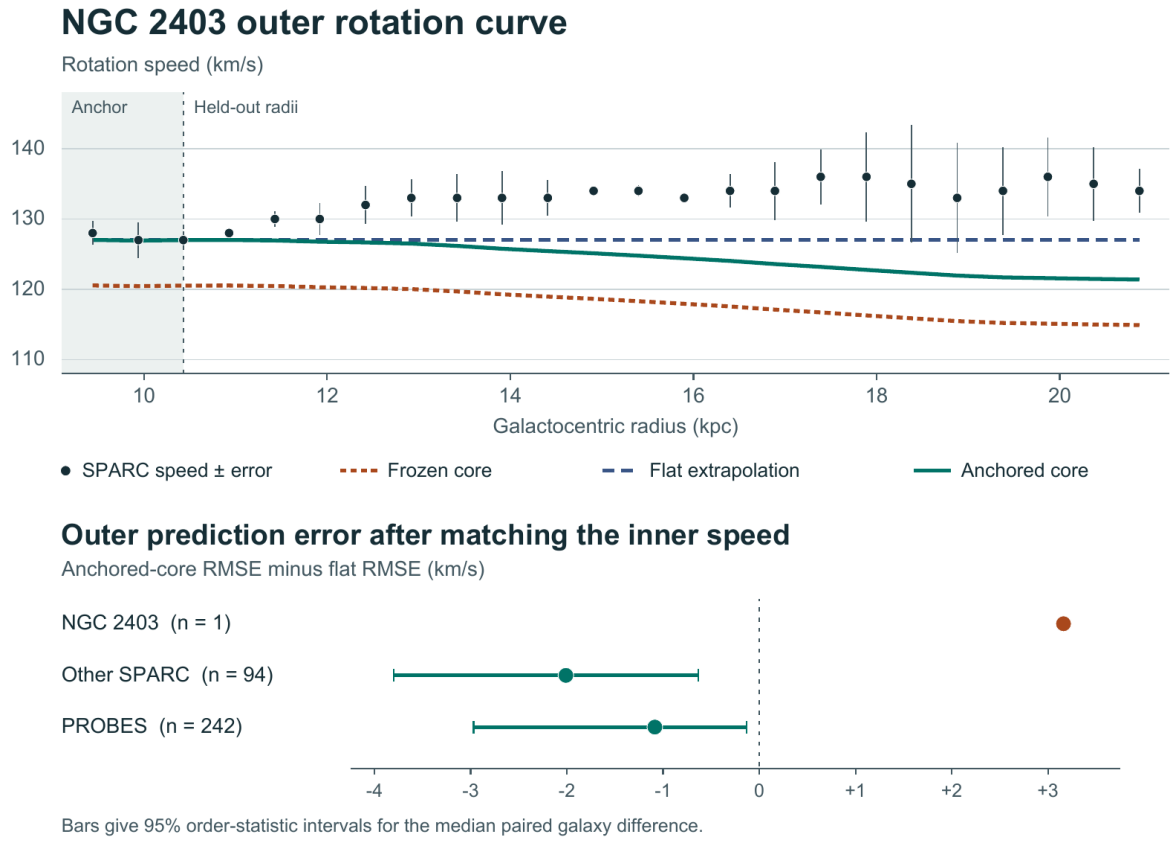

The archived frozen core has an outer root-mean-square error of 15.98 km/s. Anchoring lowers it to 9.80 km/s. The anchored baryonic shape gives 14.65 km/s and the flat extrapolation gives 6.64 km/s. A separate two-parameter slow-approach model fitted to the inner data in the prior master reaches 4.90 km/s. The figure shows the published speed errors. The held-out scores are unweighted and the comparison is retrospective.

Across other eligible galaxies, the anchored core beats flat in 58/94 SPARC and 139/242 PROBES cases. The median paired differences in km/s are −2.01 [−3.80, −0.64] and −1.09 [−2.97, −0.13]. The 95% order-statistic intervals treat galaxies as independent within each selected sample. Shared survey systematics remain. The predictor uses baryonic inputs and an empirical acceleration. Independent field measurements would be needed to attribute a shape advantage to electromagnetic dynamics.

SPARC measurements · PROBES data, Stone et al. · read research/galaxy/README.md for eligibility, matched baselines and per-galaxy scores.

A magnetar can cross the timing boundary

The June manuscript uses $\chi = B\Omega/\Lambda$ with $\Lambda = 6.28 \times 10^{14}$ G rad/s. With an equatorial timing estimate $B = 3.2 \times 10^{19}\sqrt{(P\dot{P})}$ G and $\Omega = 2\pi/P$, its meaning is fixed algebraically.

> $\chi = \sqrt{(\tau_*/\tau_c)}$, $\tau_c = P/(2\dot{P})$, $\tau_* = 1{,}624.076$ years.

The catalog ratio ranks sources in exactly the same order as inverse characteristic age. Among 2,898 positive ATNF timing pairs, five of 22 anomalous X-ray pulsar tagged sources and four of 2,876 others pass $\chi \geq 1$. The ranking probability (AUC) is 0.936686 using either χ or inverse characteristic age. These are catalog classifications. Characteristic age is a timing proxy.

Using the separate McGill primary selection, five of 22 uncensored confirmed magnetars pass. Two more confirmed sources have upper limits already below one. The source lists six spin-down ranges beyond the alternate point estimates in the archived atlas. Their endpoints summarize changes over observing intervals. Each uses the primary period because that alternate row omits a period.

Star	Timing reference in the McGill table	Recalculated χ range
1E 1048.1–5937	gk04 · then dkg09	0.345–1.260 · then 0.445–0.891
1E 1547.0–5408	crj+08	1.078–1.250
PSR J1622–4950	lbb+12	0.471–0.678
SGR 1806–20	wkf+07	1.971–3.319
XTE J1810–197	ccr+07	0.282–0.439

One star, two different classifications

For 1E 1048.1–5937 the primary χ is 0.598. The broader published range in $\dot{P}$ spans 7.5×10^{-12} to 1.0×10^{-10} s/s. At the listed period this crosses one. The source associates no timestamp with these two extrema. A time series, contemporaneous activity records and monitored exposure would be needed to test whether crossings precede events.

McGill Magnetar Catalog · Original torque monitoring · ATNF catalog. See research/stars/ for every recovered range.

Testing the threshold with an independent field estimate

An X-ray line provides information beyond the period derivative. A quiescent XMM-Newton observation of 1E 2259+586 on 29 July 2014 measured a period of 6.979164(1) s. Pizzocaro and colleagues fitted a broad absorption feature in that same observation. The result below asks what the ESFD threshold would imply if the feature is a proton cyclotron fundamental.

> $B_{line}/(10^{14}\ G) = E_{line}(1 + z)/(0.63\ keV)$, $B_{\chi=1} = \Lambda P/(2\pi)$.

At the assumed redshift z = 0.25, the period sets $B_{\chi=1} = 6.976 \times 10^{14}$ G. A proton fundamental at that field would be observed at **3.516 keV**. The observed feature was fitted at much lower energy in both detector analyses.

Same observation	Fitted centroid	Conditional ESFD index
EPIC-pn	0.68 ± 0.07 keV	0.193 ± 0.020
EPIC-MOS	0.87 ± 0.02 keV	0.247 ± 0.006

The errors propagate the published centroid and period uncertainties at fixed redshift. The instrument-dependent difference illustrates a larger interpretive uncertainty. Line identity, continuum choice, redshift and the relation between local and large-scale field affect the result. Both estimates describe one target at one epoch.

A prospective event comparison

Specify the physical field in the index before scoring. Define the flare-energy threshold, monitoring window and treatment of non-detections before inspecting events. Estimate fields using pre-event observations independent of $\dot{P}$ and retain instrument and epoch information. Compare held-out stars with a timing-age model using the same exposure. A calibrated excess in the high-index group would support that field-specific prediction. A null limits its event-rate contrast at the sensitivity achieved. This test needs observing data beyond the recovered snapshot.

Pizzocaro et al., §§3–5 and Table 2 · XMM observation 0744800101 · research/stars/results.json contains the two instrument estimates and assumptions.

What remains open across the program

The final archived master register contains 75 branches. The companion research package preserves every original register row and adds revision entries to 13. The other rows retain the evidence assigned to them in that master. The requirements below identify measurements or calculations that could change the interpretation of particular branches.

Branch	What would move it forward
Rotation, material response and superconductors	Measure the signed M(B, Ω) shift on one calibrated specimen. Record temperature, magnetic history and the blank apparatus response. Use frozen coefficients for held-out sweeps. The existing ring, disk, phase and downward-probe runs are simulations. A force on a separate probe needs an independent acceleration channel.
Gravity, inertia and galaxy fields	Supply a conserved stress or a matter metric, its normalization and couplings to neutral matter and light. Freeze the outer radial law and independently measure ordered field, gas density and their gradients where an outer speed prediction is tested. An inverse field profile calculated from those speeds reuses the target.
Compact objects, bursts and collapse	Use independent field measurements and event exposure. A collapse calculation needs an equation of state, stable and unstable solutions, and an identifiable signal. Timing thresholds alone cannot give a black-hole boundary.
Quantum coherence, collider and cosmology	Specify a detector observable and alternate-model prediction using common acceptance and uncertainties. The archived Bell, off-shell Higgs, lensing, cosmic topology and bounce discussions concern different underlying tests. A shared spin symbol does not fix their couplings.
Waves, solar activity and other tests	The standing-wave and material simulations establish behavior for specified sources. Time-domain solar or high-energy event tests need held-out epochs and exposure-aware null models. Raw files for some historical FDTD, GRMHD and rotor-clock claims remain unlocated.

The next measurement with the shortest path back to the original spinning-top question is a calibrated, reversible field-and-rotation response. It addresses the distinction between rigid-body motion and microscopic polarization before introducing a gravitational or astronomical coupling. For the galaxy branch, an independently measured field profile is the missing input with the most direct bearing on the proposed force.

Archived register · branch_register.csv in the prior November master package. This revision's full register and verification are in research/branch_register.csv and research/source_audit.json.

Sources and reproduction

Project record

The supplied 495,972,821-byte research ZIP has 638 members. All 637 catalogued files verified against their SHA-256 values. The catalog itself is the remaining member. The master PDF and NGC 2403 data ZIP match the retained Pattern Nexus upload byte-for-byte. The 3D galaxy page also carries the same numerical payload. The private recovery ledger records the accessible chat windows, original filenames and unresolved leads. File identity and page metadata alone do not authenticate scientific claims.

Run the calculations

Extract the companion research ZIP and run **python research/run_checks.py** with Python 3.9 or newer. The four research calculations use the Python standard library and read included inputs. The runner regenerates the numerical outputs in a temporary folder and compares them with the delivered tables. The individual methods and data names appear alongside each analysis. The optional source audit reads the original 496 MB ZIP to recheck the historical catalog and register.

Folder or file	What it contains
research/spin_response	Equilibrium response, exact expansion coefficients, reversal sweep, determinant tests and draft 21 arithmetic.
research/spin_entropy	The 271-row simulator export, compensated source profiles, orbital turning points, face-cap area calculation and mode spacing.
research/galaxy	Two frozen curve inputs, 19,152 radius rows across 376 galaxies, eligibility and paired prediction errors.
research/stars	Frozen timing inputs, row-level range audit, June example recalculations and the independent spectral comparison.
recovered-sources · research-history.md	Original recovered research files, hashes, chat and manuscript identification, and outstanding recovery leads.

Primary references for the relevant calculations accompany each chapter. The following releases identify the observing teams and the versions underlying the data selections. Historical expressions are attributed to their source drafts. The closure, compensated example and new comparisons are research extensions introduced here.

SPARC · PROBES · ATNF · McGill · XMM analysis · ESFD master and original tools.

Electromagnetic Spin–Field Dynamics

Unified framework and full research rerun

Christopher Grenke
Original research program

Rotational stability, spin and coherence, inertia and time, effective gravity, compact objects, and cosmic structure.
Equations and experimental tests of superconducting rotation, gravity, radio polarization, galaxy lensing, and neutron-star structure.

New observational tests begin on page 107
Galaxy rotation, magnetic measurements, magnetars and pulsed superconductors

Contents

1 The unified ESFD research program 3
2 Notation, versions and reference benchmarks 8
3 Spin from particles to rotating matter 10
4 Actions and field equations 13
5 A solved ESFD instability 17
6 Laboratory spin, phase, and inertia 21
7 Pulsars, magnetars, and flares 23
8 Neutron stars, mergers, and black holes 26
9 Gravity, geometry, and the spin–entropy proposal 28
10 Galaxies, the Great Attractor, and the dark sector 31
11 Spin–torsion collapse, white holes, and daughter universes 36
12 Quark and gluon spin, the Higgs field, and CERN 38
13 Exceptional symmetry and ultraviolet completion 40
14 Quantum coherence, collapse, and observers 41
15 Solar, geophysical, and vacuum extensions 42
16 Local spin-field response 45
17 Data-model expansions across scales 47
18 Limits on proposed macroscopic extensions 52
19 Maxwell, Tesla and the ESFD standing wave 55
20 Force balance, curvature, and the ESFD coupling 59
21 Dense spin, bounces, and a laboratory discriminator 63
22 Full rerun and extended results 65
23 Recomputed wave and gravity results 69
24 What the proposed field equations imply 71
25 Superconductors as the required experimental phase 75
26 Independent observations and a revised galaxy equation 80
27 Compact stars, quantum measurements and cosmic horizons 82
28 Numerical outcomes from this revision 84
29 Validation plan and decision criteria 89
30 Appendix A. Reconstruction ledger 93
31 Appendix B. Reproducible calculations and data dictionary 95
32 What would establish the unified claim? 97
33 Sources and references 100

1 The unified ESFD research program

Research question. Can the coupling of spin to electromagnetic fields organize a common description of rotational stability, the properties of matter, quantum coherence, inertia, time and gravity? Christopher Grenke began from an observation about spinning tops and whether adding energy changed the conditions for wobble and loss of stability. The project then extended the question from mechanical rotors to elementary spin, collective polarization, compact objects and the formation of large-scale structure. The original papers propose that spin and field response can change character at saturation. Later work treats the dynamics of fields, the formation of measurable particle states, and the emergence of spacetime as connected questions. A1 A4 A5 A6

There are two gravitational claims in the source history. The stronger claim in the Proof develops gravity and inertia as collective electromagnetic spin-field behavior. A related formulation explores the importance of electromagnetism in specific environments while retaining a gravitational action. In dilute ionized media, directed fields, radiation and currents can organize baryons. To explain the same gravitational effects for compact bodies, neutral collisionless matter and light, a model must turn that organization into an effective metric with quantitative predictions. A model of field-induced motion and an emergent geometry model can share microscopic variables while making different predictions for lensing, universality and wave propagation. A1 A4 A6

The archive attaches several mathematical meanings to *spin–field saturation*. A local Dirac bilinear can change polarization when matter aligns or its field back-reacts. An energy balance can bound a rapidly rotating, magnetized star. A threshold in a coupled field theory can correspond to a mode becoming unstable. Phase coherence can decay in an environment with fluctuating couplings. The unified claim becomes quantitative when these events are connected by equations whose coefficients and characteristic scales are determined independently. This edition computes those connections where a specified closure allows it and records which links still require constitutive or microscopic information.

The Maxwell section of this edition supplies an explicit link between wave overlap and the covariant gauge coupling. Counterpropagating waves change $F_{\mu\nu}F^{\mu\nu}$ with their relative polarization while keeping the mean energy fixed. If the composite spin amplitude is dynamical, that cross term can drive a narrow parametric band. Bulk motion needs a second link from the same coupling to the response of matter. Equations (35)–(44) derive the stress, the sign and size required for terrestrial force balance, a spin–torsion normalization, and the shared-mode link between a force range and resonance frequency. A10

1.1 Results that change the interpretation

The restored *Proof* proposes an inverse-distance interaction between neutral bodies. Its printed local spin tensor has no independent kinetic term. The simplest propagating quadratic completion can be diagonalized exactly, and the fluctuation force in an explicitly symmetric scalar example has a different radial power. A biased or collectively ordered material offers a separate route. Grenke's superconducting condition supplies a controllable phase switch. The niobium ring data measure a magnetic rotation response, while YBCO gravimetry directly limits a change in acceleration in the tested geometry. The new theory, material matching and comparison with both experiments are in Field proofs and Superconductors.

The most encouraging astronomical finding for the electromagnetic hypothesis is an incremental association between polarized radio emission and rotation in 26 galaxies after controls for size, star formation and total radio emission. A revised baryon-linked cored speed law improved substantially on the historical spin–entropy profile. Its whole-galaxy errors are competitive with the radial acceleration relation. Independent lensing favors the radial acceleration relation in the primary comparison, and the revised speed law still lacks a microscopic spin source. Joint mass–radius data for two neutron stars give a separate lead for a specified compact-star stress. The results and counterexamples are collected in Independent observational tests and Numerical outcomes.

1.2 The chain from fields to observables

Level	Variables in the available ESFD work	Observable and matching requirement
Particle and vacuum	Dirac or quark fields, the tensor bilinear $S_{\mu\nu}$, field strength $F_{\mu\nu}$, charge and magnetic moments	Match a Pauli or other gauge-invariant operator to magnetic moments and scattering. Intrinsic spin belongs to a representation of the rotation group. A macroscopic spin frequency is measured in angular units per time.
Material and plasma	Spin polarization and correlations, conductivity, vorticity, local electromagnetic invariants, entropy current	Specify the correlation function or susceptibility, particle species, temperature and density. Distinguish reversible spin precession, magnetization, transport, heating and dissipation.
Rotor, clock and quantum device	Bulk orientation, mechanical angular momentum, microscopic polarization, geometry and measurement basis	Predict a particular signed torque, damping rate, clock frequency residual, or coherence signal while controlling ordinary forces, field-induced clock responses and environmental noise.

Level	Variables in the available ESFD work	Observable and matching requirement
Pulsar, magnetar, merger and remnant	Rotation and spin-down, surface and internal fields, equation of state, magnetic geometry, pressure and angular momentum	Evaluate stability in an EOS and field configuration. Inference from timing is correlated with age and spin-down torque. Independent polarimetry, event rates and waveforms probe other combinations of quantities.
Galaxy and cluster	Plasma flow, magnetic fields, baryon distributions, spin or entropy correlations, effective stress	Derive a radial velocity or acceleration *and* the metric potentials relevant to lensing. Field energies, ordinary Lorentz forces and proposed collective gravitational effects have different radial dependencies and source budgets.
Cosmology and geometry	Curvature, torsion, collective stress, wave modes, shear, and the state of the vacuum	Specify the background equation of state, perturbations and symmetry or statistical isotropy. Translate the result to spectra, distances, lensing, or an explicitly defined remnant signature.

A microscopic polarization tensor supplies a local source only after averaging over the physical state. At long wavelengths the first moment $\langle S_{\mu\nu} \rangle$ describes mean order. A quadratic action depends also on the connected covariance in $\langle S_{\mu\nu} S^{\mu\nu} \rangle$. Rotational angular momentum includes the motion of matter. A theory that uses one measured spin frequency to predict both moments needs a transport and alignment law. That is the source of the scale-matching problem from a top to a magnetar or galaxy.

1.3 Which equation is being tested

Source	Defining element in the text	Physical difference
June 3 manuscript, §3	Einstein–Hilbert, Dirac and Maxwell terms, direct $\alpha S_{\mu\nu}F^{\mu\nu}$, and $V_{\text{sat}}(X)$ for $X = S_{\mu\nu}S^{\mu\nu}$	Direct polarization source in the Maxwell equation. A specified spinor variation yields a saturation term in its evolution.
Proof, p. 2 and §§2–3	Vacuum $-F^2/(4\mu_0)+(\kappa/2)S^{\mu\nu}F_{\mu\nu}-V(S)$ and proposals for effective gravity and inertia	The displayed vacuum action supplies a distinct normalization and a starting electromagnetic response. A separate microscopic or collective equation is needed for dynamical spin and emergent geometry.
Merged covariant excerpts	Curvature with a connection, $Z(\Phi_{\text{EM}})F^2$, and the spin-composite $\Phi_{\text{EM}} = \kappa_{\text{EM}}^2 X$ in one formulation	The response multiplies the photon kinetic term and depends on the spin variables. A quadratic local spin invariant has a vanishing first derivative at zero spin in a one-component reduction.
v150 excerpt	Tensor-bilinear squared multiplied by F^2	An interaction with two powers of F and two powers of the spin bilinear. The scale power and normalization require verification in the original canvas.
Spin–entropy consolidation	A spin-entropy current, a current-divergence term and a corresponding effective density proposal	A legitimate local divergence carries a boundary condition. Its volume integral is controlled by the surface flux.
Testing and Re-Evaluation papers	Energy-balance ratio in *Testing* and a schematic spin interaction coefficient in *Re-Evaluation*	The normalize-by-binding-energy variable and a coupling coefficient encode different experiments.
September 2026 CERN and observer material	Correlations of the joint decay state and field or observer response	An independent spin-density residual and a physical observer or field variable are required to take the interpretation to an experiment.

The June $B\Omega/\Lambda_{\text{tim}}$ criterion is a bulk diagnostic supplied alongside the local action. In the original

neutron-star example, its numerator treats a timing field and bulk angular frequency as proxies for the relevant spin-field state. Verify that substitution in the appropriate medium before using the same constant for a laboratory rotor, a galactic plasma or a black-hole horizon. The covariant record also uses other spin invariants. The June Word $\Phi_{\mathrm{EM}} = \sqrt{X}$ and the merged $\Phi_{\mathrm{EM}} = \kappa_{\mathrm{EM}}^2 X$ carry different dimensions before normalization. An independent scalar Φ adds a propagating degree of freedom. These choices lead to testably different photon and matter equations. A1 A2 A3 A4 A6 A9

1.4 Source recovery and standards of evidence

The recovered June 3 editable manuscript records 59 pages and 14,740 words in saved Word metadata. Three project PDFs provide the 22-page *Proof*, the 18-page *Re-Evaluation*, and the five-page *Testing*. The recovered archive contains the editable Proof and the related article and observer material. The later CERN text specifically identifies the June saturation and entanglement manuscript as one part of the larger program. Its original is preserved alongside the earlier source materials. A1 A4 A5 A8 A9

Historical lead	Evidence recovered
June consolidation of twenty documents	Seventeen names appear in the recovered conversation excerpts. The spin–entropy, *Electromagnetic Universe* and many numbered originals are still missing.
ESFD Master Paper v150, June 6, 2025	Canvas title, textdoc ID and excerpts of the tensor-squared action. The complete canvas and definitions are missing.
June 10 master on emergent mass, gravity and collapse	Living-document title and scope from the conversation. Exact revisions and supporting artifacts are missing.
August 2025 *Unified Analysis and Validation of Electromagnetic Spin–Field Dynamics*	An old report reference and an attachment identifier. The original long document remains inaccessible.
Roughly 90-page original recalled by the author	The file and its version remain unidentified.
Early GPT-3 and GPT-4 work cited by the author	The recovered files and records preserve some later versions. The earliest complete discussion and originating model provenance remain unavailable.

An equation proved within its mathematical assumptions, a benchmark regenerated from data, a hypothesis consistent with a published observation, and a research lead have different evidentiary force. The sections below document the actual base inputs, reduction, parameters and outcome for each calculation. Original rotor/clock, FDTD, GRMHD and some historical correlations are reported in the surviving manuscripts and conversation excerpts. The necessary run files for reproducing those claims have yet to be recovered. A2 A6

The reconstructed operator families and conservation equations are in Actions and field equations. The original saturation potential and composite response are in Local spin-field response. Catalog and observational checks appear in Full rerun and extended results. The wave calculation, gravity coupling and laboratory simulations are developed in Maxwell, Tesla and the ESFD standing wave, Force balance, curvature, and the ESFD coupling and Recomputed wave and gravity results. Cross-scale and tentative applications include Limits on proposed macroscopic extensions.

2 Notation, versions and reference benchmarks

Electromagnetic Spin–Field Dynamics (ESFD) began with Christopher Grenke's question about why rotating systems lose stability and whether the local electromagnetic environment and the spins of their constituents can supply a common mechanism. The most expansive versions move from intrinsic spin and phase coherence through mass, inertia, and curvature to compact stars, cosmic structure, and the observer. A narrower formulation retains Einstein dynamics and asks where a measurable spin-dependent electromagnetic term changes the behavior of matter. This paper develops both formulations to the level permitted by the recovered equations and evidence. It preserves the early conjectures, specifies where a conjecture becomes a mathematical model, and evaluates the predictions that can be computed. A1 A2 A3 A4 A5 A6

Abstract. We reconstruct the June spin-tensor action, a later covariant exponential electromagnetic coupling, and the spin–entropy extension. The archived symbol χ denotes several dimensionally and operationally different quantities. Variational reconstruction distinguishes composite Dirac polarization from an independent collective field and gives a dimensionally closed independent-scalar example. In a quadratic scalar background, dynamical electromagnetic perturbations give a long-wavelength transverse instability above a specified field, with its own angular and finite-size conditions. Direct integration agrees with the predicted growth. This threshold follows from the new benchmark assumptions and involves an independently measurable product of field-theory scales. Its relation to stellar rotation requires a material response model. Archived catalog and observational tests were rerun from hashed snapshots. The timing-based $B\Omega$ index is exactly a transform of characteristic age and its historical cutoff selects 5 of 22 eligible ATNF AXP-tagged objects and 5 of 22 confirmed McGill magnetars with uncensored positive timing. An added projection cannot increase the passes at fixed field. The archived galaxy profile fits some data, with weaker performance on withheld outer radii than the tested NFW and pseudo-isothermal controls. A new magnetic-energy estimate quantifies the field needed if Maxwell energy supplies the inferred missing acceleration. Further development treats spin and chirality, quark and nucleon matching, gravitation and lensing, compact-object collapse, curved-space propagation, the Higgs and E_8 proposals, black-to-white-hole cosmology, and quantum and observer extensions as explicit research questions. The combined record yields falsified historical rules, reproducible reference results, and new conditional predictions for defined actions.

Research materials. The companion reproducibility archive includes source papers, the previous catalog pipeline and its raw input snapshots, the new spin calculations and figures, the editable manuscript, the historical claim register, and a branch-by-branch evidence index. This revision draws on 19 recovered originals, two related Pattern Nexus articles in local project working material, and identifiable excerpts from 2025–2026 project conversations. The archive logs 40

historical recovery leads, including original runs and file versions still unavailable. The reported GPT model versions of the earliest work are the author's recollection. Available file metadata dates versions and does not establish their model generation history. A1 A6 A8

Result	Evidentiary meaning
$B_{\text{tim}}\Omega/\Lambda_{\text{tim}} = \sqrt{1624.08\,\text{yr}/\tau_c}$	Algebraic identity with the adopted pulsar timing convention. The joint field and rotation interpretation requires a field estimate independent of the torque.
$B_c = \sqrt{2e}\, f_\Phi m_0/\lvert\xi\rvert$	Onset in the infinite homogeneous quadratic independent-scalar model for transverse waves. Finite size, angle, and medium response change the domain.
$p = 1.55 \times 10^{-4}$ at 10^{15} G	Population imbalance for the ideal zero-temperature neutron gas at $0.16\,\text{fm}^{-3}$. It is an explicit scale comparison for a proposed spin-alignment mechanism.
Median required $B_{\text{rms}} = 5.93 \times 10^4\,\mu$G	Magnetic-energy mass proxy from one outer point per fitted SPARC galaxy. The estimate tests ordinary Maxwell energy in a spherical weak-field approximation.
$a/a_b = [1 + (t/t_b)^2]^{1/3}$	Exact flat homogeneous toy bounce with dust and a negative stiff spin correction. The interior of a rotating black hole is a separate boundary-value problem.

2.1 The chronology and the hypotheses

The recovered June 3, 2025 manuscript sets out the two-form $S_{\mu\nu}$, the $B\Omega$ threshold, a saturation potential, and lab, merger, and heavy-ion tests. The adjacent chat synthesis and the later field draft introduce the exponential gauge-kinetic function and an Einstein–Cartan connection. A June quantum rewrite emphasizes the dipole operator. The spin–entropy and Electromagnetic Universe drafts introduce extra sources, and the July E_8 synthesis suggests a high-energy embedding. The later proof and re-evaluation papers include strong-field QED, energy accounting, compactness and rotational limits, torsion, and inertia. The 2026 CERN rewrite moves toward an off-shell spin-density observable. The subsequent observer work argues for a deeper organization of spacetime and measurement. These are dated version records and conceptual continuities. Chronology alone supplies no prospective prediction score. A1 A2 A3 A4 A5 A6

Three propositions organize this edition. **Spin response in an electromagnetic environment** is an operator and constitutive problem that can be interrogated in laboratory systems and stars. **A dynamical threshold or crossover** requires explicit unstable modes, competing timescales, or an energy landscape. **Emergence of gravity, time, or geometry** requires a derivation of an effective metric, its dynamics, and universal coupling from specified degrees of freedom. The three propositions carry distinct empirical burdens. A standard spin response or an ordinary

electromagnetic instability establishes a baseline for testing the first two.

2.2 Conventions and the several quantities called chi

Use $c = \hbar = 1$ inside field-theory formulas, metric signature $(+ - - -)$, and Heaviside–Lorentz electromagnetic normalization $-\frac{1}{4}F^2$. Unit conversions and astronomical estimates state SI or Gaussian units explicitly. Write $M_{\mathrm{P}}^{-2} = 8\pi G$ for the reduced Planck scale. Let $F_{\mu\nu} = \partial_\mu A_\nu - \partial_\nu A_\mu$, $\tilde{F}^{\mu\nu} = \epsilon^{\mu\nu\rho\sigma}F_{\rho\sigma}/2$, $F^2 = 2(B^2 - E^2)$, and set the dual convention so $F\tilde{F} = -4\mathbf{E}\cdot\mathbf{B}$. The symbol Ω refers to a measured rotation rate or a vorticity specified by a model. For a timing period P, $\Omega = 2\pi/P$. One tesla equals 10^4 gauss. Threshold constants carry the units of their numerators.

Quantity	Definition and role
χ_{tim}	$B_{\mathrm{tim}}\Omega/\Lambda_{\mathrm{tim}}$, with $\Lambda_{\mathrm{tim}} = 6.28 \times 10^{14}$ G rad s^{-1}. Fixed June-draft astrophysical index.
χ_E	$(E_{\mathrm{rot}} + E_{\mathrm{mag}})/\lvert W\rvert$. Canonical energy comparison in *Testing*. Versions normalized by support energy use a different ratio.
b_e	B/B_Q, with $B_Q = m_e^2/e$ in natural units, 4.414×10^{13} G. Electron QED scale.
$\mathcal{C}$, a_*, χ_{eff}	$GM/(Rc^2)$, $cJ/(GM^2)$, and waveform mass-weighted aligned binary spins. Three relativistic quantities with different observables.
d_i or α	Low-energy species-dependent Pauli coefficient, mass dimension -1. The historical 10^{-3} label can parameterize a dimensionless moment convention after matching.
Φ, X	Dimensionless collective scalar and spin-bilinear invariant $X = S_{\mu\nu}S^{\mu\nu}$, with $[X] = 6$. A relation such as $\Phi = c_X X/M^6$ is an explicit model choice.
ξ, Λ_g	Slope of $Z(\Phi)$ and cosmological term in the historical gravitational action. They are independent of the timing normalization.

3 Spin from particles to rotating matter

3.1 Relativistic spin, polarization, and angular momentum

Wigner's massive one-particle spin label is specified by the Pauli–Lubanski vector $W^\mu = \frac{1}{2}\epsilon^{\mu\nu\rho\sigma}P_\nu J_{\rho\sigma}$ and $W^2 = -m^2 s(s+1)$ in these units. Quantum spin is a representation of rotations and Lorentz symmetry. A macroscopic rotor has angular momentum obtained from momentum density and any polarized constituent contribution. In flat space a decomposition reads

$$J^{ij} = \int d^3x\, [x^i T^{0j} - x^j T^{0i} + \mathcal{S}^{0ij}],$$

with a chosen stress and spin-current convention. Improvements of the stress tensor can move density between the orbital and spin pieces while preserving total charges under suitable boundary conditions. In a local rest frame a magnetic moment density can source a magnetization current, while bulk rotation can carry angular momentum in neutral, almost unpolarized matter. A galaxy's J, a Kerr remnant's a_*, a nucleon's spin, and a magnetar's polarized spin density accordingly require different measurement maps. R01 R04 R58

The recovered polarization tensor and the Dirac contribution to the spin current are related spinor constructions with different index structure:

$$S_{\mu\nu} = \tfrac{1}{2}\bar{\psi}\sigma_{\mu\nu}\psi, \qquad \sigma_{\mu\nu} = \tfrac{i}{2}[\gamma_\mu, \gamma_\nu], \qquad \mathcal{S}^{\lambda\mu\nu} = \tfrac{1}{4}\bar{\psi}\{\gamma^\lambda, \sigma^{\mu\nu}\}\psi.$$

The antisymmetrized Dirac spin current is dual to an axial current $J_5^\mu = \bar{\psi}\gamma^\mu\gamma^5\psi$ up to conventions. A torsion equation sourced by $\mathcal{S}^{\lambda\mu\nu}$ needs a tetrad and spin connection. A constitutive equation involving $S_{\mu\nu}$ instead models polarization or tensor order. With ε_S and $\mathbf{s}_S$ conventions analogous to the electric and magnetic parts of F, $X = 2(|\mathbf{s}_S|^2 - |\boldsymbol{\varepsilon}_S|^2)$. Thus $\sqrt{X}$ as printed in one manuscript requires a magnetic-type sector, $X \geq 0$, or a specified alternative norm. A potential minimized at $X = \Phi_0^2$ can model a preferred tensor invariant. Its minimum alone gives neither a hard upper bound on amplitudes nor a stable Hamiltonian for a general dynamical tensor. A1 R01

For a medium with four-velocity u^μ, define $B^\mu = \tilde{F}^{\mu\nu}u_\nu$, $E^\mu = F^{\mu\nu}u_\nu$, and the vorticity vector $\omega^\mu = \frac{1}{2}\epsilon^{\mu\nu\rho\sigma}u_\nu\nabla_\rho u_\sigma$. The positive field magnitude is $\sqrt{-B_\mu B^\mu}$. A covariant candidate for a rotation–field projection is $-B_\mu\omega^\mu$. In a rigid, slowly rotating local patch it reduces to $\mathbf{B}\cdot\boldsymbol{\Omega}$ when $\frac{1}{2}\nabla\times\mathbf{v} = \boldsymbol{\Omega}$. A spin dipole can also couple to B^μ in a medium at rest. A zero bulk vorticity therefore leaves spin magnetization possible. The action rather than the timing index determines vacuum decoupling.

3.2 Direction, chirality, and field helicity

Helicity is angular momentum projected on the direction of momentum. Chirality projects relativistic fields with $P_{L,R} = (1 \mp \gamma^5)/2$. For massless free fermions, particle helicity tracks chirality with the conventional particle/antiparticle assignments. A massive fermion can be observed from a frame where its momentum direction reverses. A reversal of rotor direction, a flip of a magnetic field, and a reversal of microscopic spin polarization implement different operations. $\mathbf{B}$ and $\boldsymbol{\Omega}$ are axial vectors, so $\mathbf{B}\cdot\boldsymbol{\Omega}$ is parity even and time-reversal even under simultaneous reversal. $\mathbf{E}\cdot\mathbf{B}$ is parity odd and time-reversal odd. Operators with $\tilde{F}$, pseudoscalars, and handed backgrounds can therefore be tested through parity-specific signatures rather than collected under a generic spin label. R03 R30

Magnetic helicity $K_B = \int_V \mathbf{A}\cdot\mathbf{B}\, d^3x$ quantifies field linkage for a closed boundary with $\mathbf{B}\cdot\hat{\mathbf{n}} = 0$. Its time evolution is $dK_B/dt = -2\int_V \mathbf{E}\cdot\mathbf{B}\, d^3x$ plus surface flux. Open solar and astrophysical volumes require relative helicity with an appropriate reference field. Fluid helicity $\int \mathbf{v}\cdot(\nabla\times\mathbf{v})\, dV$ is a different scalar under rotations and pseudoscalar under parity. Ideal MHD conserves magnetic topology under appropriate flux constraints, while reconnection and boundary flows can change connectivity. A rotating magnetosphere can possess structured helicity when the spatial average of the fermion tensor spin is small. Comparing a candidate ESFD onset with current-sheet formation and helicity injection isolates a physically distinct test.

A chiral magnetic current in a model with nonzero axial chemical potential has the response $\mathbf{j}_{\mathrm{CME}} = N_c \sum_f q_f^2 \mu_5 \mathbf{B}/(2\pi^2)$ in the standard homogeneous constitutive idealization. The finite lifetime of the collision field, charge conservation, axial relaxation, equilibrium boundary conditions, and hadronization are essential in applying it. The axial anomaly connects $F\tilde{F}$ and the gluonic topological density with the divergence of J_5^μ, alongside fermion masses. It gives a baseline mechanism for handed charge separation. It supplies neither a conversion of quark spin to an object's classical Ω nor a normalization for the historical universal cutoff. R17 R18 R30

3.3 From microscopic correlations to field order

Consider N independent spin-$\frac{1}{2}$ projections along one direction, $s_i = \pm 1$, with $\langle s_i \rangle = p$. Their mean-square average is

$$\left\langle \left(\frac{1}{N} \sum_i s_i \right)^2 \right\rangle = \frac{1}{N} + \left(1 - \frac{1}{N}\right) p^2.$$

For interacting spins the right hand side acquires $N^{-2} \sum_{i \neq j} \mathrm{Cov}(s_i, s_j)$. This is the microscopic place to put coherence or a polarization correlation length. A macroscopic mean is order Np. Zero mean can coexist with order-N total variance. Long-range order changes the scaling, and a fluid or galaxy model must specify whether its effective field sees a mean, a renormalized local composite, or a spatially integrated correlation. In particular $\langle S_{\mu\nu} S^{\mu\nu} \rangle$ and $\langle S_{\mu\nu} \rangle \langle S^{\mu\nu} \rangle$ are different expectation values. Their separation matters for both the proposed halo and the Einstein–Cartan fluid.

A useful control is a free spin doublet with magnetic energy $-\mu B s$, giving $p_{\mathrm{th}} = \tanh(\mu B / k_B T)$. Independent electrons at 4 T and 4 K yield $p_{\mathrm{th}} = 0.586$ in this simple limit. At 10 μG and 8000 K the same expression gives 8.40×10^{-14}. Conducting, ordered, and degenerate matter need an appropriate susceptibility. For cold free neutrons of total number density n, spin populations $n_\pm = n(1 \pm p)/2$ give nonrelativistic Fermi energies $E_{F,\pm} = E_F (1 \pm p)^{2/3}$ with $E_F = \hbar^2 (3\pi^2 n)^{2/3}/(2m_n)$. Equating chemical potentials including Zeeman energy yields

$$(1+p)^{2/3} - (1-p)^{2/3} = \frac{2|\mu_n| B}{E_F}, \qquad p \simeq \frac{3|\mu_n| B}{2E_F}.$$

At $n = 0.16\,\mathrm{fm}^{-3}$ the illustrative E_F is 58.45 MeV. The population imbalance is 1.55×10^{-4} at 10^{15} G and 0.0155 at 10^{17} G. The independent-spin thermal expression at 10^8 K yields 0.604 at the first field. The zero-temperature free model reaches full polarization around 7.69×10^{18} G. Near that scale magnetic stresses and interaction, composition, relativistic, and superconducting corrections require a realistic equation of state. For the same ideal gas $M = n|\mu_n|p$, and the SI weak-field differential susceptibility gives $\mu_0\, dM/dB = 3\mu_0 n \mu_n^2/(2E_F) \simeq 3.0 \times 10^{-3}$. This scale can anchor a weak-field closure before strong interactions and composition corrections. The calculation shows how a naive use of thermal alignment can inflate a candidate gravitational or electromagnetic source. It is a new controlled benchmark using physical constants and an assumed density.

3.4 Spin dynamics and electromagnetic dominance by regime

A minimal local closure in matter uses a magnetization response tensor $\delta M_i(\omega, \mathbf{k}) = \mathcal{X}_{ij}(\omega, \mathbf{k}) \delta B_j + \mathcal{Y}_{ij} \delta \omega_j$ with a stated equilibrium, constituent densities, and relaxation times. One rest-frame model

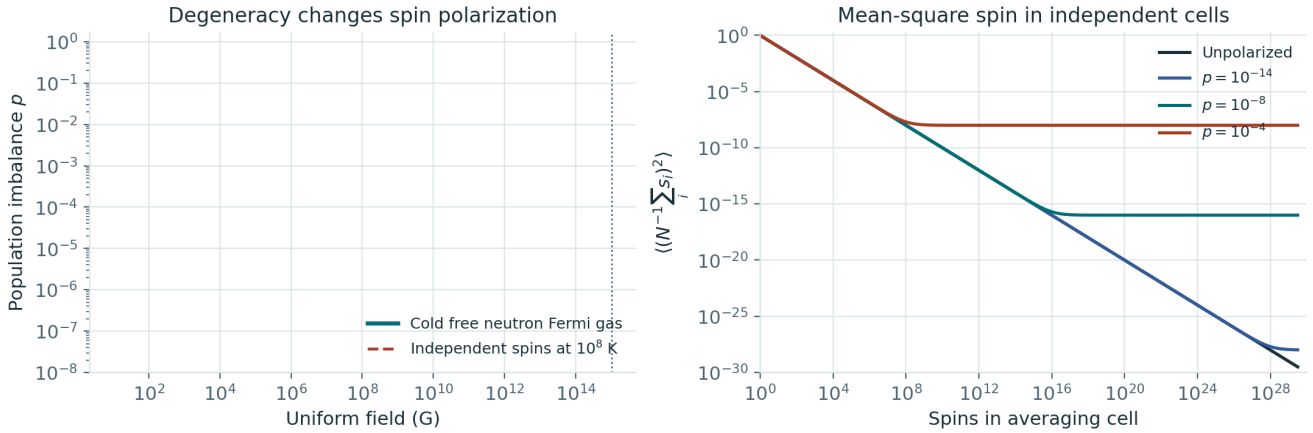

Figure 1. Spin polarization and coarse graining. Left, independent thermal neutron spins at an assumed temperature and a zero-temperature free gas at nuclear density. Right, the mean-square signed projection for independent spins at prescribed average polarization. Both are theoretical controls for the ESFD spin source.

adds $\dot{\mathbf{M}} = \gamma\,\mathbf{M} \times \mathbf{B} - (\mathbf{M} - \mathbf{M}_{\mathrm{eq}})/T_1$ for a single relaxation scale. Distinct longitudinal/transverse relaxation, spin transport, and backreaction enter realistic calculations. For a passive equilibrium the absorptive and dispersive parts of a causal susceptibility are related through Kramers–Kronig. An instability corresponds to a pole in the appropriate response or a negative second variation with dynamical constraints specified. Merely increasing a parameter that multiplies a current fails to define where a mode grows.

A separate comparison uses the magnetization parameter $\sigma_{\mathrm{MHD}} = B_{\mathrm{com}}^2/(\mu_0 w)$, where w is enthalpy density including rest energy, and the plasma beta $\beta_{\mathrm{pl}} = 2\mu_0 p_{\mathrm{gas}}/B_{\mathrm{com}}^2$. A tenuous magnetosphere may have $\sigma_{\mathrm{MHD}} \gg 1$ and be electromagnetically dominated in its plasma dynamics. An electrically neutral galaxy can have a dynamically important organized field in its gas, while total gravity determines stellar orbits and lensing. The two statements use different equations and energy inventories. A field that controls flows can be far too weak in mass-equivalent energy to account for measured gravitational potentials. Electromagnetic and gravitational forces between individual charged particles give a poor measure of collective charge neutrality, field stress, or universal coupling. R05 R08 R26

4 Actions and field equations

4.1 The June Dirac–Pauli version

With $\mathfrak{S}$ for the action and a historical cosmological constant label, the June manuscript gives

$$\mathfrak{S}_{6\text{–}3} = \int d^4x\sqrt{-g}[\frac{R-2\Lambda_{\mathrm{cc}}}{16\pi G} + \bar{\psi}(i\gamma^\mu D_\mu - m)\psi - \frac{1}{4}F_{\mu\nu}F^{\mu\nu} + \alpha S_{\mu\nu}F^{\mu\nu} - \frac{\lambda_S}{4}(X-\Phi_0^2)^2]. \tag{1}$$

Here $[A] = 1$, $[F] = 2$, $[\psi] = 3/2$, $[S] = 3$, $[\alpha] = -1$, $[\Phi_0] = 3$, and $[\lambda_S] = -8$ as mass dimensions. Expanding the potential gives a vacuum term, a dimension-six four-fermion interaction,

and a dimension-twelve eight-fermion interaction. The vacuum term is part of the vacuum-energy matching. A nonzero minimum at positive X could break Lorentz symmetry in a specified state. The potential sets the energetics of the invariant, and the constitutive map to a macroscopic $B\Omega$ must still be supplied. A1 A2

For the variation fix the current convention by $D_\mu = \nabla_\mu + iqA_\mu$, so minimal coupling contributes $-J^\mu A_\mu$ and $J^\mu = q\bar{\psi}\gamma^\mu\psi$. At fixed tetrad and spin connection, with the standard Hermitian Dirac kinetic term understood, variation gives

$$\begin{aligned} \nabla_\mu H^{\mu\nu} = J^\nu, \qquad H^{\mu\nu} = F^{\mu\nu} - 2\alpha S^{\mu\nu}, \\ 0 = \left[i\gamma^\mu D_\mu - m + \frac{\alpha}{2}\sigma_{\mu\nu}F^{\mu\nu} - \frac{\lambda_S}{2}(X - \Phi_0^2)S^{\mu\nu}\sigma_{\mu\nu} \right] \psi. \end{aligned} \tag{2}$$

The factors follow from $\delta_{\bar{\psi}} X = S^{\mu\nu}\delta\bar{\psi}\,\sigma_{\mu\nu}\psi$ and $\delta F_{\mu\nu} = 2\partial_{[\mu}\delta A_{\nu]}$. The Hermitian Dirac form also fixes how the connection and volume element vary in a torsion treatment. Gauge invariance gives $\partial_\nu(\sqrt{-g}J^\nu) = 0$ from the antisymmetric excitation, with $dF = 0$. In torsion spacetime use the exterior derivative for F, and express the Maxwell equation as a density divergence or as an exterior form. Using a torsionful covariant curl without torsion compensation changes the gauge transformation. Ordinary QED includes a spin magnetic moment even at zero bulk rotation. α represents an additional matched dipole in a physical application. R01 R02

The pure Pauli vertex has a transverse photon insertion, schematically $\delta\Gamma^\nu \propto \sigma^{\nu\mu}q_\mu$, with $q_\nu\delta\Gamma^\nu = 0$. A prescribed constant S makes the interaction linear in F a boundary term in free Maxwell variation. Changes in wave dispersion then require a dynamical spin response, nonuniform backgrounds, or other quadratic terms. A self-energy linear in a constant, antisymmetric $S^{\mu\nu}$ by itself supplies no consistent photon mass. Gauge-invariant media can have dispersive collective modes, and a longitudinal massive mode requires its own mechanism. The 10^{-9}–10^{-8} eV and 10–100 GeV scales associated in the June draft differ by about 10^{18}–10^{20} in energy, depending on endpoints. Photon splitting and pair creation require separate QED kinematics involving the background and polarization. A1 R06

4.2 The recovered covariant exponential action

The June 3 synthesis and later recaps use a different electromagnetic sector. With the connection written explicitly, the recovered form is

$$\begin{aligned} \mathfrak{S}_{\text{exp}} = \int d^4x\sqrt{-g}[\frac{R(\Gamma) - 2\Lambda_g}{16\pi G} - \frac{1}{4}e^{-\xi\Phi_{\text{EM}}}F_{\mu\nu}F^{\mu\nu} \\ + \frac{1}{2}\partial_\mu\Phi_{\text{EM}}\partial^\mu\Phi_{\text{EM}} - V(\Phi_{\text{EM}}) + \mathcal{L}_{\text{matter}}(\psi, D\psi; g, \Gamma)]. \end{aligned} \tag{3}$$

One historical potential uses a quadratic plus quartic, with positive quadratic curvature for a massive excitation. The historical discussion gives $\Phi_{\text{EM}} = \kappa_{\text{EM}}^2 X$ and also uses $\kappa_{\text{EM}} = 1/\Lambda_{\text{tim}}$ when normalizing $B\Omega$. In natural units $B\Omega$ and a Dirac bilinear each have dimension three. The numerical matching between the bulk product and the local operator needs material physics and a chosen conversion. A historical variant gives $\Phi_{\text{EM}} \propto S_{\mu\nu}F^{\mu\nu}$ instead. An exponent requires a dimensionless product. With $[\Phi] = 0$, $[\xi] = 0$ and a coefficient f_Φ^2 in front of the kinetic term supplies its required mass dimension. Three consistent implementations follow. They have different propagating variables and tests. A6

4.2.1 Independent dimensionless scalar

Take $Z = e^{-\xi\Phi} > 0$, $f_\Phi > 0$, and $\mathcal{L}_\Phi = f_\Phi^2(\partial\Phi)^2/2 - V(\Phi)$, with $[V] = 4$. In the minimally specified model,

$$\begin{aligned} \nabla_\mu(ZF^{\mu\nu}) &= J^\nu, \\ f_\Phi^2\Box\Phi + V'(\Phi) &= -\frac{1}{4}Z'(\Phi)F^2 = \frac{\xi}{4}ZF^2. \end{aligned} \tag{4}$$

A separately declared matter coupling $+\Phi c_X X/M^2$ adds $+c_X X/M^2$ on the right of the scalar equation. It also changes the matter equation. The spin source in this version is an extra operator. The archival variation simultaneously used a function of the spinor and a freely varied scalar. Equation (4) is the independent-field result with the matter dependence spelled out. A new spin closure must tie the local field to spin density or spin correlations to make the independent scalar specifically predictive of rotation.

4.2.2 Composite scalar built from spin

Set $\Phi = C(X) = c_X X/M^6$ before varying. Then $Z(C)$ multiplies the photon kinetic term. Its leading mixed operator is $+\xi c_X XF^2/(4M^6)$. If the composite kinetic term is retained it becomes $f_\Phi^2(\partial C)^2/2$, a derivative interaction of the spinor. Assuming no explicit F in C, the scalar-sector contribution to the Dirac variation is $\mathcal{E}_C\, C'(X)S^{\mu\nu}\sigma_{\mu\nu}\psi$, where

$$\mathcal{E}_C = -f_\Phi^2\Box C - V'(C) - \frac{1}{4}Z'(C)F^2. \tag{5}$$

$\mathcal{E}_C$ is a variation factor and becomes an independent field equation only in the independent branch. In the constrained formulation add $+\ell(\Phi - C)$, where ℓ is a multiplier of mass dimension four. The ℓ equation ensures $\Phi = C$, the Φ equation sets $\ell = -\mathcal{E}_C$, and the $\bar\psi$ equation then reproduces (5). Derivative composite interactions are used perturbatively within their cutoff unless a controlled extra-mode analysis is supplied.

If instead $C = c_{SF}S_{\mu\nu}F^{\mu\nu}/M^5$, C depends directly on F. With the derivative term included, the excitation is $H^{\mu\nu} = ZF^{\mu\nu} - 2\mathcal{E}_C\,\partial C/\partial F_{\mu\nu}$, up to any separate Pauli term. This expression uses the Euler derivative of the full scalar sector and integrates by parts before varying F. In the algebraic limit it includes the Z' and V' contributions to the excitation. Treating this model as a background scalar Maxwell dielectric would omit the implicit-field terms. Its higher variations and symmetries require a distinct audit. A6

4.2.3 Independent two-form and spin transport

A classical tensor can instead be given healthy auxiliary dynamics as a massive antisymmetric two-form $Q_{\mu\nu}$ of mass dimension one. A test completion on torsionless spacetime uses $K = dQ$ and

$$\begin{aligned} \mathcal{L}_Q &= \frac{1}{12}K_{\mu\nu\rho}K^{\mu\nu\rho} - \frac{m_Q^2}{4}Q_{\mu\nu}Q^{\mu\nu} + \frac{g_Q}{2}Q_{\mu\nu}F^{\mu\nu}, \\ \nabla_\rho K^{\rho\mu\nu} + m_Q^2 Q^{\mu\nu} &= g_Q F^{\mu\nu}. \end{aligned} \tag{6}$$

For $m_Q > 0$, the massive two-form has three spin-one degrees of freedom in four dimensions. The leading long-wavelength elimination gives $Q \simeq g_Q F/m_Q^2$ and $Z_{\text{eff}} = 1 - g_Q^2/m_Q^2$, which must be positive for a healthy photon kinetic term. For this quadratic model the shift $Q \mapsto Q - g_Q F/m_Q^2$ preserves K by $dF = 0$ and diagonalizes the action locally. An observable needs additional stated response terms, for example a $Q_{\mu\nu}S^{\mu\nu}$ coupling and matched boundary conditions. The unqualified $D^2S + \partial V/\partial S = \chi F$ in the E_8 working notes leaves open the kinetic sign, constraints, and relation to the fermion bilinear. Equation (6) illustrates a way to address these requirements. A6

4.3 Stress, curvature, and connection response

In the torsionless benchmark define $T_{\mu\nu} = 2\delta\mathfrak{S}_m/(\sqrt{-g}\delta g^{\mu\nu})$. Write $G_{00}^{\text{geom}} = 3H^2$ in flat FLRW. With the positive stress variation for signature $(+---)$, take $R_{\text{archive}} = -R_{\text{geom}}$ in the positive Einstein–Hilbert term of (1) and (3). The result is $G_{\mu\nu}^{\text{geom}} - \Lambda_g g_{\mu\nu} = 8\pi G\, T_{\mu\nu}$ in (3), and the corresponding equation with Λ_{cc} in (1). Equivalently absorb the cosmological term into a vacuum stress. For independent Φ the two stress contributions are

$$\begin{aligned} T_{\mu\nu}^F &= Z\left[-F_{\mu\alpha}F_{\nu}{}^{\alpha} + \frac{1}{4}g_{\mu\nu}F^2\right], \\ T_{\mu\nu}^{\Phi} &= f_\Phi^2\partial_\mu\Phi\partial_\nu\Phi - g_{\mu\nu}\left[\frac{1}{2}f_\Phi^2(\partial\Phi)^2 - V(\Phi)\right]. \end{aligned} \tag{7}$$

Vary a spinor action with respect to the tetrad to include the spin matrices, the volume term, and its spin connection. A composite C gives additional implicit metric or tetrad variations. In a self-consistent solution the gradients of Z exchange energy and momentum between electromagnetic and scalar sectors, and the combined stress with matter is covariantly conserved. For GR plus matter the stress is the gravitational source and the coupling G is already present in the action. Deriving G from a new microscopic model remains a distinct task.

For minimal Einstein–Cartan gravity, start with $(e_\mu{}^a, \omega_\mu{}^{ab})$ independent and vary a metric-compatible spin connection. Torsion is algebraic, proportional to the Dirac axial spin current with coefficient of order G. Eliminating it generates an axial four-fermion contact term of order $M_{\text{P}}^{-2}J_5 \cdot J_5$. An explicit convention, the spin ensemble, and the averaging order are required for its sign and effective pressure. This interaction is short-range in the minimal theory. A propagating torsion extension must state its kinetic action, mode spectrum, and couplings. Laboratory search bounds then depend on range and spin structure. R01 R27

4.4 Effective field theory, quantization, and matching

The operator $S_{\mu\nu}F^{\mu\nu}$ is dimension five below electroweak breaking. In the moment convention $\mathcal{L} \supset (q\,\delta a/4m)\bar{\psi}\sigma^{\mu\nu}\psi F_{\mu\nu}$, an additive Pauli coefficient implies $\delta a = 2m\alpha/q$. Its sign follows the chosen charge convention. The QED contribution $a = (g-2)/2 = \alpha_{\text{em}}/(2\pi) + \cdots$ is already included in Standard Model matching. A new electron residual is tested using the independently inferred fine-structure constant and its error. One can translate a conditional uncertainty ϵ_a into $|\alpha| \lesssim |q|\epsilon_a/(2m)$ in a one-operator fit. The old statement that the same $\chi \sim 10^{-3}$ describes a measured moment, a Lagrangian coefficient, and a torque threshold mixes observables and dimensions. Nucleons carry composite magnetic moments and tensor matrix elements. Their coefficients require hadronic matching instead of the electron formula alone. A2 A6 R02

Above electroweak breaking chirality and gauge charges govern the operator basis. For example $\bar{Q}_L \sigma^{\mu\nu} u_R \tilde{H} B^Y_{\mu\nu}$ and $\bar{Q}_L \sigma^{\mu\nu} T^A u_R \tilde{H} G^A_{\mu\nu}$ are dimension-six electroweak-gauge-invariant dipoles, with Hermitian conjugates and appropriate flavor coefficients. Both chiralities enter a dipole even though $\sigma^{\mu\nu}$ commutes with γ^5, since $\bar{\psi}_L = \bar{\psi} P_R$. Below the Higgs vacuum expectation value, the hypercharge and weak dipoles give photon and Z dipoles and the chromomagnetic dipole gives a separate strong-sector interaction. Electroweak quantum numbers, scale running, hadronic tensor charges, and experimental observables enter the matching. The spin–electromagnetic XF^2 composite is dimension ten. A quark operator $(D_\rho S^q_{\mu\nu})^2$ is dimension eight, with corresponding scale suppression. Keeping the Standard Model gauge symmetries and anomaly-free matter content preserves the usual anomaly cancellations within the effective description. New chiral matter or gauge groups require their own analysis. R03

A concrete matching calculation in the independent branch expands $\Phi = s/f_\Phi$ about zero and $Z = 1 - \xi s/f_\Phi + \cdots$. At energies and momenta well below the scalar mass m_0, the leading tree correction from integrating out s is

$$\Delta\mathcal{L} = \frac{\xi^2}{32 f_\Phi^2 m_0^2} (F^2)^2. \tag{8}$$

This follows by solving $m_0^2 s \simeq \xi F^2/(4 f_\Phi)$ and substituting into the quadratic Lagrangian. With a matched $+\Phi c_X X/M^2$ term the same elimination yields a cross coefficient $\xi c_X/(4 f_\Phi^2 m_0^2 M^2)$ for XF^2, plus X^2 and derivative terms. Equation (8) makes light-by-light or polarization constraints applicable in the specified limit. The Euler–Heisenberg photon operators provide the radiative Standard Model baseline. A finite background changes the canonical photon normalization and the validity of the expansion. For scalar-independent gauge charge, local canonical normalization gives $e_{\text{eff}} \sim e/\sqrt{Z}$ in a neighborhood of nearly constant Φ. Extrapolating to very small Z needs a perturbative-control check. R02 R06

An EFT prediction at a chosen order needs a power counting, a regulator that preserves gauge symmetry, a complete basis for the retained symmetries, and SMEFT or low-energy matching at a specified scale. Loop insertions mix into other allowed operators. A single universal beta function for α cannot be read from the June action without stating species, charge, basis, scheme, and accompanying coefficients. Perturbative unitarity restricts amplitudes as the energy approaches the effective cutoff. In a Wilsonian calculation the finite set of coefficients at each order can be renormalized and fitted. The archived string, asymptotic-safety, and E_8 ideas are potential high-energy contexts. Their relation to this EFT depends on actual matching data. A1 A6 R03

5 A solved ESFD instability

5.1 Equilibrium and the two stability questions

Use the independent branch of (4) with flat metric, uniform background $\mathbf{B} = B\hat{\mathbf{z}}$, zero electric field, no transport current in the local volume, and $V(\Phi) = f_\Phi^2 m_0^2 \Phi^2/2$ with $m_0 > 0$. The external source and mean flux are assumed fixed for the local perturbation problem. A time-independent scalar minimizes $V_B = V + ZB^2/2$ at prescribed B. Define $x = \xi\bar{\Phi}$. The equilibrium equation and fixed-field scalar curvature are

$$xe^x = \frac{\xi^2 B^2}{2 f_\Phi^2 m_0^2}, \qquad m_B^2 = \frac{V''(\bar{\Phi}) + Z''(\bar{\Phi}) B^2/2}{f_\Phi^2} = m_0^2(1+x). \tag{9}$$

For the real branch $x = W_0(\xi^2 B^2/(2 f_\Phi^2 m_0^2)) \geq 0$ this scalar curvature is positive. At fixed magnetic excitation $H = ZB$ the local magnetic Legendre potential is $V - H^2/(2Z)$, whose curvature per f_Φ^2 evaluates to $m_B^2 - g_B^2$, with $g_B = Z' B/(f_\Phi \sqrt{Z})$. Equivalently this is the Schur complement of the magnetic block in the local Hessian. The choice of which magnetic perturbations are permitted changes the question. The appropriate Hamiltonian or energy principle for a real system must account for its sources, flux constraints, plasma, and boundary energy.

5.2 Mixed modes and onset

For $\mathbf{k} = k\hat{\mathbf{x}}$ there is a photon polarization A_y whose magnetic perturbation has a component along the background. Define $p = \sqrt{Z}\,\delta A_y$ and $s = f_\Phi \delta\Phi$. The quadratic Lagrangian contains the mixing $-g_B s\,\partial_x p$. The other transverse polarization has no such term in this geometry. For an angle θ between $\mathbf{k}$ and $\mathbf{B}$ the determinant in the mixed subspace is

$$(\omega^2 - k^2)(\omega^2 - k^2 - m_B^2) - g_B^2 k^2 \sin^2\theta = 0. \tag{10}$$

Let $g_\theta = |g_B \sin\theta|$. The two real eigenvalues in ω^2 are

$$\omega_\pm^2 = k^2 + \frac{m_B^2}{2} \pm \sqrt{\frac{m_B^4}{4} + g_\theta^2 k^2}. \tag{11}$$

For $g_\theta > m_B$ the lower branch is negative for $0 < k < \sqrt{g_\theta^2 - m_B^2}$. Its maximum growth rate is $\gamma_{\max} = (g_\theta^2 - m_B^2)/(2g_\theta)$ at $k_{\max}^2 = (g_\theta^4 - m_B^4)/(4g_\theta^2)$. The positive kinetic Hessian and the relativistic principal part are preserved. This is an energy instability of a coupled background and precedes any nonlinear saturation analysis. Plane waves parallel to the background have $g_\theta = 0$. For a cubic periodic domain aligned with a transverse wave vector, at least one mode fits when $2\pi/L < \sqrt{g_\theta^2 - m_B^2}$. Other boundaries can change both the spectrum and the magnetic constraints.

For the quadratic potential, $g_B^2 = 2m_0^2 x$. The first threshold for transverse propagation is $x = 1$ at

$$B_c = \frac{\sqrt{2e}\, f_\Phi m_0}{|\xi|}, \tag{12}$$

where e in (12) is Euler's number. At $B = 3B_c$, $x = 2.34496$, the unstable transverse band ends at $k = 1.15972\, m_0$, and $\gamma_{\max} = 0.31052\, m_0$ at $k = 0.75898\, m_0$. At this field, unstable wave-vector orientations are possible for $|\sin\theta| > 0.845$, about 57.6° or farther from either orientation along the field. A periodic transverse domain needs $Lm_0 > 5.42$ for a mode to fit. We separately integrated the two coupled second-order mode equations with an initial displacement having both normal-mode components and zero velocity. The projection on the unstable eigenvector agrees with the predicted $\cosh(\gamma_{\max} t)$ to approximately 2.3×10^{-12} relative error on the sampled grid. This is a dimensionless calculation with chosen initial data and convergence tolerances.

A simple test of medium suppression gives the transverse photon an effective gap ω_p in the diagonal of (10). The unstable sign requires $g_\theta^2 > (k^2 + \omega_p^2)(k^2 + m_B^2)/k^2$. The minimum of the right

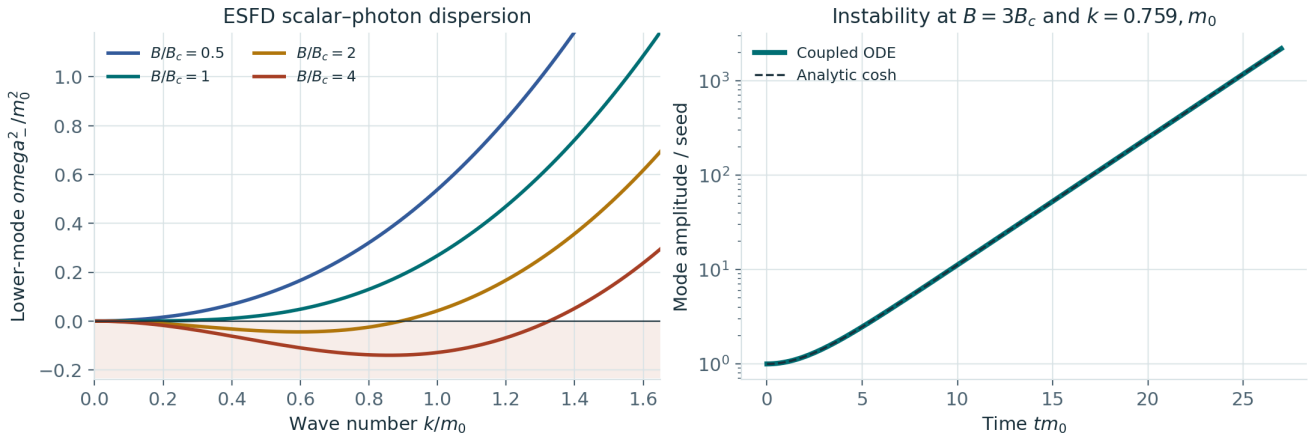

Figure 2. The ESFD independent-scalar threshold. The negative squared-frequency band appears above the transverse threshold. The second panel compares a direct integration of the mixed modes with the analytic growth rate. The calculations use m_0 as the frequency and wave-number scale.

side is $(\omega_p + m_B)^2$ at $k^2 = \omega_p m_B$ when both masses are positive. A positive gap can therefore close the unstable band. Magnetar matter requires an anisotropic response matrix with realistic conductivity, charge density, and plasma and QED polarization. The simple gap is an illustrative modification of the determinant. A stellar prediction additionally requires numerical values of $f_\Phi m_0/|\xi|$, an emission map, and a physically matched source of Φ, including its spin dependence. At zero coupling the modes approach a free photon and a free massive scalar. At high fields a perturbative gauge description and the physical sources of the background must be checked.

The electron QED field provides a unit conversion, $B_Q = m_e^2/|q_e| \simeq 8.62 \times 10^{11}$ eV^2 for 4.414×10^{13} G. For illustration, a transverse $B_c = 10^{15}$ G would need $f_\Phi m_0/|\xi| \simeq 8.4 \times 10^{12}$ eV^2. Choosing $f_\Phi/|\xi| = 10^9$ eV would then imply $m_0 \simeq 8.4$ keV, an inverse mass length $\hbar c/m_0 \simeq 2.4 \times 10^{-11}$ m, and a growth time $\hbar/(0.3105 m_0) \simeq 2.5 \times 10^{-19}$ s at $3B_c$. These are illustrative scales. Assigning the same onset to a stellar flare requires independently matched coupling and plasma physics and a mechanism by which a local mode drives a macroscopic event.

5.3 An independent laboratory check on the onset scale

At weak field, the lower transverse branch of (11) has $\omega^2/k^2 = 1 - g_B^2/m_B^2$ in the long-wavelength limit. Only the polarization with its wave magnetic field aligned to the background mixes at this order. For a transverse external field that wave's electric polarization is perpendicular to the background. With $C_F = \xi^2/(32 f_\Phi^2 m_0^2)$ from (8), its extra index is $n_\perp - 1 \simeq 16 C_F B^2$. The other polarization has no such leading scalar contribution. The tie between the low-energy coefficient and strong-field threshold is $C_F B_c^2 = e/16$, which gives the signed prediction

$$\delta(n_\parallel - n_\perp) = -16 C_F B^2 = -e(B/B_c)^2. \tag{12a}$$

The published PVLAS result at 2.5 T is $(12 \pm 17) \times 10^{-23}$, with QED expectation 2.5×10^{-23}. Treating the published error as approximately Gaussian and using the lower endpoint of a two-sided 95% residual interval gives $\delta(n_\parallel - n_\perp) \gtrsim -2.38 \times 10^{-22}$. Under the stated weak-field, low-energy, adiabatic vacuum assumptions and with this one extra coefficient, it gives $B_c \gtrsim 2.67 \times 10^{15}$ G. A proposed vacuum onset $B_c = 10^{15}$ G would give -1.70×10^{-21} at 2.5 T and lie about 10.6 published

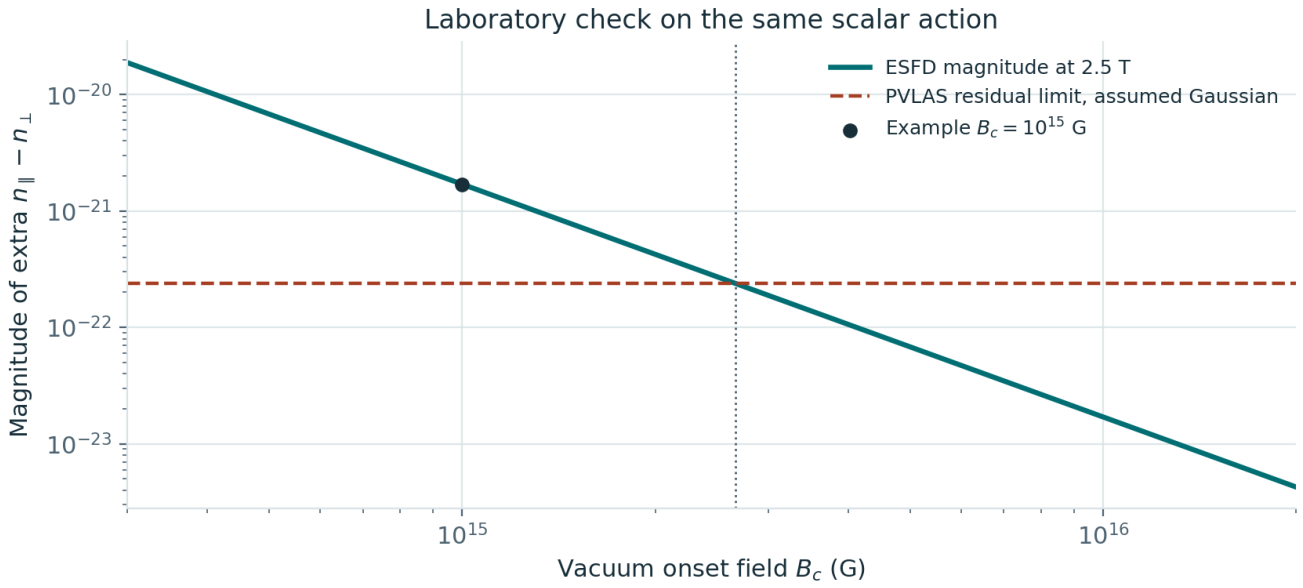

Figure 3. The extra birefringence in the minimal ESFD scalar action and the conditional PVLAS limit. The measurement was made at 2.5 T. The horizontal axis gives a candidate strong-field onset for the same action.

standard errors below the observed central value after adding QED. This is a calculation from the published summary, with the ordinary QED expectation held fixed. Additional optical operators, nonuniform backgrounds where the scalar does not equilibrate, or medium-only couplings require a new propagation analysis. The concrete result is a cross-regime test of the same proposed action without a fitted stellar parameter. R60

5.4 How spin can move the threshold in matter

Let a locally uniform prescribed spin source enter as $+j_s\Phi$. An example is $j_s = c_X\langle X\rangle/M^2$ in the operator convention above. Here j_s has units of energy density and $\langle X\rangle$ is a renormalized, medium-specific correlation. If the source is held fixed in the mode calculation, define $x_s = \xi j_s/(f_\Phi^2 m_0^2)$ and $y = x - x_s$. The background solves $ye^y = \xi^2 B^2 e^{-x_s}/(2f_\Phi^2 m_0^2)$ and the dispersion uses $m_B^2 = m_0^2(1+y)$ and $g_B^2 = 2m_0^2 y$. The no-plasma transverse onset becomes $B_c(j_s) = B_c(0)e^{x_s/2}$. If $B_c(0)$ saturates the conditional PVLAS bound, an onset at 10^{15} G in matter would require $x_s \simeq -1.96$ or more negative, under this particular uniform-source model. The needed backreaction and sign can be calculated once a spin susceptibility and operator matching are supplied. A real compact-star medium has a fluctuating spin source and a plasma response, so a quantitative application must include their variations in the mode matrix.

5.5 Nonlinear endpoint and numerical continuation

Equation (12) determines onset within this toy model. The growing eigenvector consists of correlated scalar and magnetic perturbations. To determine the endpoint, fix a conserved flux $\int B\,dA$, specify the scalar potential away from its minimum and Z over the explored range, and minimize or time-evolve the coupled fields with sources and losses accounted for. In a periodic box the next reproducible checks are the predicted finite-domain threshold, modes on both sides of it,

and convergence of the flux and total energy under refinement. Boundary conditions must allow the magnetic component of the eigenvector and retain comparable background energy. A magnetic domain, an unbounded local response in a fixed-source model, a radiating transient, and collapse of a self-gravitating object have different criteria.

A saturation term of the form $\lambda_\Phi f_\Phi^4 \Phi^4/4$ changes the criterion through V''. A constitutive torque law or $\Phi = C(X)$ has a different linearization. An appropriate route to a rotating-object calculation is a local equilibrium and stability comparison at known field, followed by a rotating multifluid equilibrium and, if the effect survives, a constrained 3+1 evolution. The code in this release solves the reduced Fourier mode system. The older archive describes FDTD, spinning-ring, spin-fluid and magnetosphere tests for which the original numerical models and records are still unavailable. A2 A6

6 Laboratory spin, phase, and inertia

6.1 Spinning tops and preferred environmental alignment

Grenke's earliest examples involve a top, a lighter, and a rotor losing stability when driven away from a local rotational habit. A symmetric top obeys $\dot{\mathbf{L}} = \boldsymbol{\tau}$ and in fast, nearly steady precession $\Omega_{\text{prec}} \simeq Mgd/L$. Euler rigid-body equations predict free wobble and intermediate-axis instability. Contact friction, motion of the contact point, shifting moments of inertia, eddy currents, ferromagnetic hysteresis, the angular distribution of a drive, and support resonances give distinct losses and bifurcations. For ordinary eddy-current braking at low speed one often obtains a dissipative torque that is odd in rotation and even under magnetic field reversal. Purely mechanical instability at matched field-off conditions defines a control. A fixed preferred cosmic direction would introduce a measurable directional dependence and is already subject to precision polarized-spin torsion-pendulum tests. A1 A6 R27

A workable rotational-inertia test models the coupled energy and dissipation. With I fixed, $I\dot{\Omega} = N_{\text{drive}} + N_{\text{environment}} + N_{\text{proposed}}$. If a local preferred direction is represented by a physical axial vector $\mathbf{b}$, the scalar $\Omega_b = \boldsymbol{\Omega} \cdot \hat{\mathbf{b}}$ supplies a directional regressor. Its interpretation requires identifying $\mathbf{b}$ from a local, independently measured field or a specified frame and stating the time and orientation dependence. For a pure reversible interaction $-\lambda\, \boldsymbol{\Omega} \cdot \mathbf{B}$ the observable is a change to canonical angular momentum and forces under gradients. A dissipative torque also requires degrees of freedom that absorb angular momentum and heat. The full apparatus, mount, and surrounding field enter the balance.

In a rotating frame the ordinary spin–rotation Hamiltonian includes $-\boldsymbol{\Omega} \cdot \mathbf{S}$, in addition to the orbital term. A spin with gyromagnetic ratio γ_s behaves in a Barnett field of scale Ω/γ_s in that sense. The reciprocal Einstein–de Haas response transfers changes in magnetization to mechanical angular momentum. These effects supply positive checks that a test is sensitive to spin conversion. A neutral body gives a particularly useful comparison between bulk inertia, a polarized ensemble, and a field acting directly on the supports. Changes in stored energy contribute their own E/c^2 to a closed system's rest mass.

6.2 Clock law, historical units, and a reversal test

The early time-feedback branch proposes expressions such as $d\tau/dt = e^{-\xi\Phi_{\mathrm{EM}}}$ or $e^{-\alpha S:F}$. In (1), $\alpha S : F$ has dimension four, so a separate normalization is required even for a phenomenological exponential clock factor. In the covariant scalar action Z explicitly multiplies the photon kinetic term. Clock frequencies, signals in an optical link, and the metric proper time depend on specified couplings and trajectories. A spin-dependent shift is naturally sought in a transition Hamiltonian or in a defined matter metric. Under a universal conformal scalar factor $\tilde{g}_{\mu\nu} = A(\Phi)^2 g_{\mu\nu}$, massive clocks coupled to $\tilde{g}$ measure $d\tilde{\tau} = A\, d\tau_g$. Local ratios of clocks sharing the same metric require transport and redshift modeling to separate the effect. Nonuniversal coupling generally gives species- and binding-energy-dependent shifts. A1 A6 R23 R24

The June rotor example specifies 4 T and 5.0×10^3 rad/s. The printed $\chi_{\mathrm{tim}} \approx 0.32$ evaluates to 3.18×10^{-7}. A hypothetical clock carried at the 0.10 m rim would move at 500 m/s and have an ordinary leading fractional SR shift $-v^2/(2c^2) \simeq -1.39 \times 10^{-12}$, or -1.20×10^{-7} seconds per day. A stationary reference looking at a rotating mirror measures an optical transfer response whose Doppler, Sagnac, path length, and birefringence terms depend on the geometry. The manuscript's target excess 10^{-10}–10^{-9} seconds per day corresponds to a fractional effect of 1.16×10^{-15}–1.16×10^{-14}. It remains an archived sensitivity target without a matched signal law at the corrected index. A1 R24

Define the response $y = \delta\nu/\nu$ of a specified transition or a calibrated torque channel. Under independent sign flips $\epsilon_B, \epsilon_\Omega, \epsilon_s \in \{-1, +1\}$ of field, bulk rotation, and spin polarization, the coefficient of the term odd in B and Ω and even in spin polarization is $\hat{y}_{B\Omega} = \frac{1}{8}\sum \epsilon_B \epsilon_\Omega y(\epsilon_B, \epsilon_\Omega, \epsilon_s)$. Define analogous contrasts for the other parities before seeing outcomes. Randomize reversal order and blind the contrast used to test the model. A differential measurement can fit $y = y_{\mathrm{known}}(\mathbf{x}) + c\, f(B, \Omega, \mathbf{M}, \theta) + \epsilon$, with $\mathbf{x}$ including temperature, field gradients and vibrations. Use zero rotation/zero field rows, unpolarized material controls, two transition sensitivities, and time-dependent ambient and magnetic controls. Limits constrain the declared function and coefficient. The old proposal $\delta\omega/\omega_L = a_1\chi_{\mathrm{tim}}^2 + a_2\chi_{\mathrm{tim}}^3$ requires independent coefficient predictions and separate parity definitions for each term. A6

6.3 Neutral-particle phase and condensed-matter benchmarks

The Aharonov–Casher phase of a magnetic dipole following a path in an electric field is, in SI for a fixed moment and the appropriate ideal geometry,

$$\Delta\varphi_{\mathrm{AC}} = \frac{1}{\hbar c^2}\oint (\boldsymbol{\mu} \times \mathbf{E}) \cdot d\ell. \tag{13}$$

A line charge λ_e and a transverse circular path with axial moment μ yield $\Delta\varphi_{\mathrm{AC}} = \mu\lambda_e/(\epsilon_0\hbar c^2)$, using the sign of the winding and dipole. Radius independence follows from the $1/r$ electric field and circumference. A reversed winding or spin reverses the phase. The neutron and atom interferometry comparisons in the old discussion therefore have a quantitative quantum baseline. A proposed ESFD phase needs a distinct prediction for geometry, field dependence, polarization, or energy, checked against electric polarizability, dynamical phase, and geometric controls. Phase coherence in a neutral beam does not require a new mechanical drag law. A6 R07

Stern–Gerlach separation, Ramsey precession, nuclear magnetic resonance, the spin Hall effect, spin–orbit torque, and magnetization dynamics are controlled cases for estimating a spin re-

sponse. For spinor Bose condensates a spin-ordering energy, Zeeman terms, density interactions, and trap geometry already permit instabilities and loss of coherence. If a new coupling is proposed, compare $\delta g_s n$, its sign, or a specified mode eigenvalue with the ordinary spin-dependent scattering energy and chemical potential. Without that matching an archived condition $U_{\mathrm{ESFD}} \gtrsim \mu_{\mathrm{BEC}}$ has free normalization. NV-center magnetic readout and spintronics provide useful reversal and noise calibration. They probe specific effective coefficients in their medium. A tokamak or laser experiment similarly needs a plasma equilibrium, ordinary reconnection and radiation-pressure predictors, and a residual observable sensitive to a spin-dependent term. A1 A2 A6

7 Pulsars, magnetars, and flares

7.1 The original line on the timing data

The rebuilt ATNF snapshot contains 4,503 objects. The timing subset is the 2,898 with finite $P > 0$ and $\dot{P} > 0$. There are 1,524 missing period derivatives and 81 supplied nonpositive derivatives. Treat the latter separately because cluster acceleration, kinematic contamination, and measurement noise can enter observed $\dot{P}$. The dipole proxy is the standard equatorial vacuum-convention value $B_{\mathrm{tim}} = 3.2 \times 10^{19}\sqrt{P\dot{P}}$ G for P in seconds. Fix the old normalization before looking at the labels. Writing $\tau_c = P/(2\dot{P})$,

$$\chi_{\mathrm{tim}} = \frac{2\pi(3.2 \times 10^{19})}{\Lambda_{\mathrm{tim}}}\sqrt{\frac{\dot{P}}{P}} = \sqrt{\frac{\tau_*}{\tau_c}}, \qquad \tau_* = \frac{1}{2}\left(\frac{2\pi(3.2 \times 10^{19})}{\Lambda_{\mathrm{tim}}}\right)^2 = 1624.076\,\mathrm{yr}. \tag{14}$$

The numerical identity is satisfied to a maximum reported relative discrepancy of 5.6×10^{-16}. The rank ROC AUC for the ATNF AXP label is 0.9367 for both χ_{tim} and inverse characteristic age. The field proxy has AUC 0.9965 and mean precision over its recall ladder of 0.9143 in this retrospective sample. The high scores reflect the selected labels, population and timing assumptions. They do not supply out-of-population predictive accuracy. At the fixed cut there are 5 tagged passes, 17 tagged misses, and 4 other passes. The descriptive Wilson 95% interval for the tagged pass fraction is 0.101–0.434. Removing the catalogued globular-cluster objects leaves the 5 and 4 counts intact. Among 485 other objects with a matched intrinsic period-derivative estimate, the correction does not change their threshold side. R05 R08

The McGill snapshot lists 24 confirmed magnetars, six candidates, and one outburst pulsar. Twenty-two confirmed sources have uncensored positive timing for this calculation. Five pass the fixed line. Two of the three giant-flare hosts are above it at the selected catalog timing epoch, and SGR 0526−66 is below at $\chi_{\mathrm{tim}} = 0.695$. SGR 1806−20 and SGR 1900+14 give approximately 2.59 and 1.35. Event-time timing and monitoring exposure differ from catalog epochs and are required for a per-event necessary-condition test. The Crab is a rotation-powered pulsar above the line at $\chi_{\mathrm{tim}} \simeq 1.14$. Its nebular gamma-ray flares occur in a different emitting region than a magnetar surface or magnetosphere. The young pulsar J1846−0258 gives a productive intermediate case because a magnetar-like event was observed. SGR 1935+2154 provides a separate magnetar/radio-transient example. The two catalog samples overlap. R08 R09 R10 R11

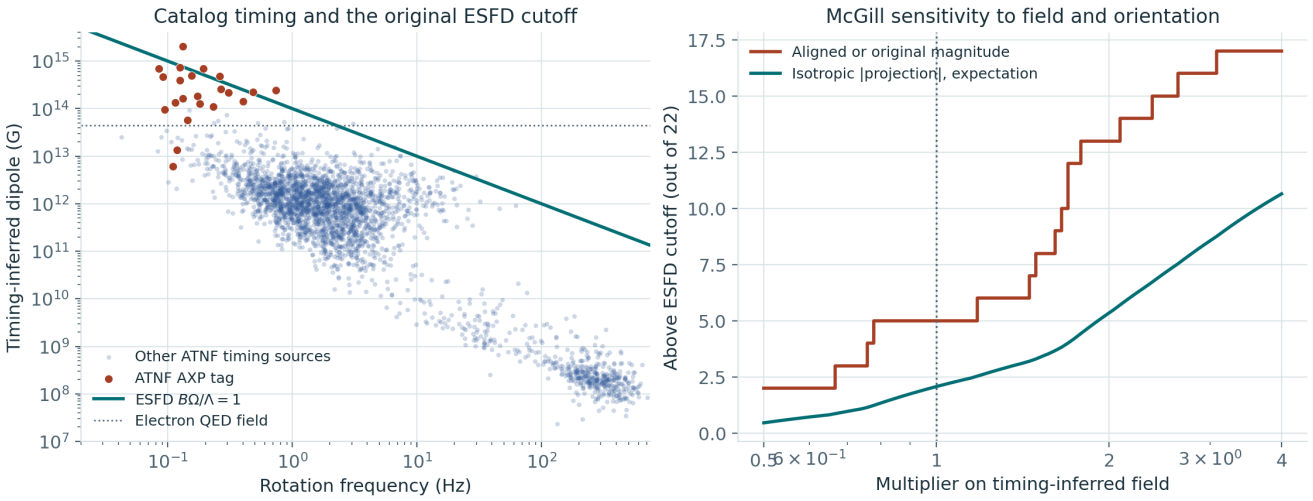

Figure 4. ESFD cutoff explicitly overlaid on ATNF timing data, with the field-scale and orientation-sensitivity calculation for confirmed McGill magnetars. The field coordinates use a timing convention. The right-hand expectations use an illustrative isotropic distribution of angles.

7.2 Orientation and the observed high-field, fast-spin gap

A signed or magnitude-projected threshold can be written $s_B \chi_{\rm tim} \cos\theta$ or $s_B \chi_{\rm tim} |\cos\theta|$, with s_B an assumed field multiplier. For an isotropic independently distributed orientation relative to $\boldsymbol{\Omega}$, $|\cos\theta|$ is uniform on $[0, 1]$. The resulting expected pass probability is $\max(0, 1 - 1/(s_B \chi_{\rm tim}))$ in the magnitude version, and half this for a positive signed cut. Each expectation is the sum over the catalog. At $s_B = 1$ the expected number of McGill passes is 2.07 in the magnitude version, compared with five for the scalar product of magnitudes. At $s_B = 2$ the expected number rises to 5.35, while the aligned or magnitude limit gives 13. For ATNF tags the respective $s_B = 1$ counts are 1.60 expected and five magnitude passes. Orientation or obliquity inference in an actual population needs a different distribution linked to the torque and selection. A projection with multiplier fixed at unity can only reduce the count, point by point. The sensitivity analysis is new and fully reproducible.

Among the eligible ATNF sources the region $P \leq 0.1$ s and $B_{\rm tim} \geq 10^{13}$ G is empty. That is a genuine catalog observation. Birth distributions, short crossing or residence times, field evolution, torque prescriptions, beaming and radio surveys, intermittency and X-ray selection can contribute to the observed occupancy. A force-free spin-down law in the usual dipole notation has $\dot{E}_{\rm sd} \sim \mu^2 \Omega^4 (1 + \sin^2 \alpha_{\rm ob})/c^3$. It gives a nonzero aligned spin-down and changes the mapping from $\dot{P}$ to B relative to the orthogonal vacuum proxy. A hazard or birth-exclusion inference needs a forward population with the relevant selection functions and an age distribution. The empty region by itself supplies no estimate of a universal dynamical boundary. R05 R08 R12

A useful follow-up likelihood conditions on monitored source-time exposure $T_i(t, E)$ and separately models glitch, ordinary burst, giant flare, and radio-transient outcomes. A Poisson intensity, for example $\lambda_i(t) = T_i(t, E) \exp(\alpha_i + \beta^\top \mathbf{x}_i(t) + c_{\rm ESFD} h_i(t))$, permits age, dipole, twist, and activity history to enter separately. Calibrate time-variable spin-down irregularity before evaluating an event. Preselect independent field estimates such as lines with verified identification, phase-resolved emission geometry with model uncertainty, or simulated distinct internal stresses. A timing-based h_i identical to a monotone age transform cannot establish separate age and ESFD

effects without additional structure. Hold out entire sources and later observing time.

7.3 Glitches, energy reservoirs, and timing tests

The rebuilt glitch list has 625 events in 211 objects. The prior-glitch cohort uses 198 with eligible timing and a within-sample recurrence window, yielding 19 repeaters of which 18 sit below $\chi_{\rm tim} = 1$. The age-equivalent AUC is 0.742 and a past-glitch-count baseline gives AUC 0.752 and average precision 0.437, versus 0.220 for $\chi_{\rm tim}$. The recurrence comparison is retrospective and lacks harmonized monitoring exposure. A physically informative model compares pinned-superfluid angular-momentum transfer and crust/magnetospheric reconfiguration, with measured changes in spin frequency and braking. For $\dot{\Omega} = -K(t)\Omega^n$ one obtains $\Omega\ddot{\Omega}/\dot{\Omega}^2 = n + (\Omega/\dot{\Omega})\dot{K}/K$, so timing noise and torque evolution can mimic a new braking index. Quasi-periodic oscillations following giant flares supply a separate magnetoelastic mode diagnostic with uncertain mode identifications. R08 R09 R13

For illustration fix $M = 1.4\,M_\odot$, $R = 12$ km, $I = 0.3MR^2$, and $|W| = 0.6GM^2/R$. The Gaussian estimates $T = I\Omega^2/2$ and $E_B = B_{\rm int}^2 R^3/6$ assume a constant interior field and spherical volume. They give $B_{\rm int} = 9.48 \times 10^{17}$ G or $P = 0.303$ ms when either single term is equated to $|W|$. For $B_{\rm int} = 10^{15}$ G and $P = 5$ s, $(T + E_B)/|W| = 1.12 \times 10^{-6}$. Its illustrative magnetic energy is 2.88×10^{47} erg, above typical burst energies and comparable to the scale contemplated for the largest giant events if even a fraction can be released. The corresponding rotational reservoir is about 9.5×10^{44} erg. Using an illustrative 10^{17} G interior field gives $\chi_E \simeq 0.0111$. At 716 Hz and zero magnetic contribution, $\chi_E \simeq 0.047$. These numbers cohere as energy budgets. Stability depends on magnetic topology, deformation, stratification, cooling, mass shedding, and the equation of state. Flares may draw on local magnetic free energy and cross a reconnection threshold even when $\chi_E \ll 1$. A1 A3 R09 R14

7.4 Strong-field photon propagation and IXPE

The electron field $B_Q = m_e^2 c^3/(e\hbar)$ in Gaussian units is a QED scale independent of rotation. With weak fields and low photon frequency, the Euler–Heisenberg result for propagation at angle θ to the field has $n_\parallel - 1 \simeq 7\alpha_{\rm em}(B\sin\theta/B_Q)^2/(90\pi)$ and $n_\perp - 1 \simeq 4\alpha_{\rm em}(B\sin\theta/B_Q)^2/(90\pi)$. These are low-field expansions. High-field magnetar predictions require the full strong-field dielectric, plasma and vacuum resonances, surface radiative transfer, and line-of-sight geometry. At 1 keV the frequency is 2.42×10^{17} Hz and the angular frequency is 1.52×10^{18} rad/s. Direct substitution corrects the draft's frequency and angular-frequency interchange. The old $\Delta n \propto \alpha S_0/\omega^2$ needs a response tensor with dimensions, dispersion, and Ward identity checked. A competing q^2 form can be predicted from a dynamical scalar or two-form, with polarization specified. A1 R06

For a prescribed, slowly varying $Z(\Phi)$ with Maxwell action, geometric optics yields $k_\mu k^\mu = 0$ and amplitude transport of the form $\nabla_\mu(Z|\mathcal{A}|^2 k^\mu) = 0$ for a source-free ray. Both polarizations share the leading cone. Dynamical mixing as in (10), QED nonlinear terms, or a parity-odd $F\tilde{F}$ coupling yield other signatures. The archived soft X-ray test can thus compare phase, energy, and direction dependent Stokes parameters against a QED, atmosphere, and magnetosphere likelihood. For 4U 0142+61 the timing values give $B_{\rm tim}/B_Q \simeq 3.04$ and $\chi_{\rm tim} \simeq 0.154$. Its measured polarization changes with energy, including substantially different polarization angles across bands. The published polarization is a baseline constraint on emission and propagation. A separate ESFD parameter and an instrument response are required for an ESFD fit. R06 R15

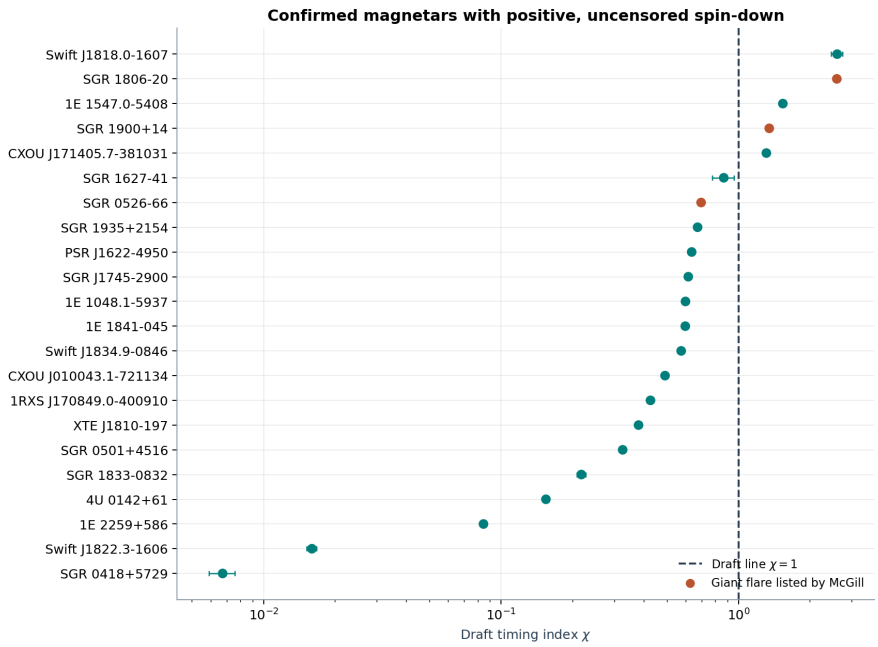

Figure 5. McGill timing relative to the original ESFD line and electron QED field. Spin-down epochs and censoring are discussed in the text.

8 Neutron stars, mergers, and black holes

8.1 TOV, rotation, and matching a spin sector

For spherical perfect-fluid equilibrium in GR with $G = c = 1$,

$$\frac{dm}{dr} = 4\pi r^2 \epsilon, \qquad \frac{dp}{dr} = -\frac{(\epsilon + p)(m + 4\pi r^3 p)}{r(r - 2m)}. \tag{15}$$

Boundary conditions are regular $m(0) = 0$, prescribed central pressure, and $p(R) = 0$. The surface mass is $m(R)$. Six tabulated EOS give 540 equilibria. Their nominal maximum static masses span 2.031–$2.770\, M_\odot$. The AP4 table gives $dp/d\epsilon \simeq 1.34$ at its raw maximum, so that maximum requires a causal EOS treatment. The raw mass-radius curves and sound-speed flags are preserved. A $1.20 M_{\rm TOV}$ proxy illustrates uniform rotational support for a class of EOS. Actual mass shedding, thermal support, differential rotation and magnetic topology depend on the angular-momentum distribution and stability of the remnant. $dM/d\epsilon_c$ along an appropriate sequence is an indicator with hypotheses, and the dynamical boundary can be tested through a radial or nonaxisymmetric mode. Equating a global energy ratio to unity cannot substitute for checking the equilibrium and stability equations. A2 A3 R14 R16

An ESFD stellar model needs an interior $S^{\mu\nu}$, a thermodynamic EOS $p(n, T, Y_e, \ldots)$, composition and transport, a metric, a gauge configuration, and the calibrated relation of the effective spin term to $\delta T^\mu{}_\nu$. If stress is anisotropic, a spherical toy formula gives dp_r/dr an additional $2(p_t - p_r)/r$. In general, rotational/magnetic flattening requires an axisymmetric equilibrium or full evolution. A defensible numerical comparison pairs each ESFD solve with the same baryon mass, angular momentum, initial topology, resolution and EOS in its GRMHD control. Check constraints, surface and asymptotic conditions, gauge dependence and convergence of the proposed observable, such

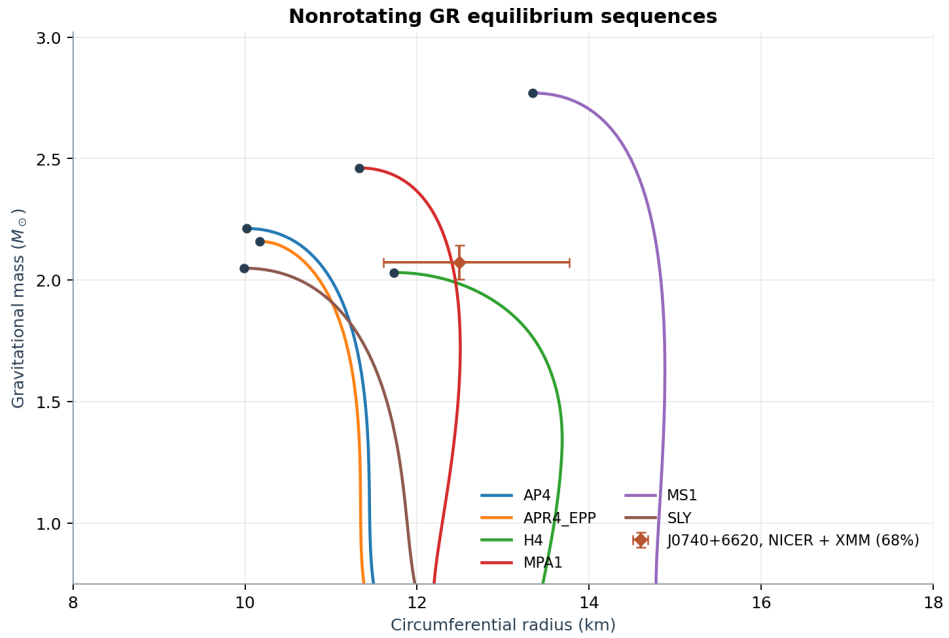

Figure 6. General relativistic stellar benchmark. The integration uses six public tabulated EOS. The AP4 central sound-speed flag applies to its unmodified maximum. A plotted GR sequence supplies the reference for a future matched ESFD stress calculation.

as a shift in mass-radius relation or mode frequency. The GR reference tracks ordinary effects and anchors the $\alpha, \xi \to 0$ limit.

8.2 Kerr spin, observed distribution, and the precursor run

For a Kerr GR black hole $a_* = cJ/(GM^2)$, and its horizon in Boyer–Lindquist radius is $r_+ = (GM/c^2)(1 + \sqrt{1 - a_*^2})$. The horizon angular velocity is $\Omega_H = a_* c^3/[2GM(1 + \sqrt{1 - a_*^2})]$. The Kerr extremal limit $a_* = 1$ follows from the horizon solution. It is used as a control in the historical ESFD extension. An inferred remnant spin is conditional on the waveform and model used to infer it. The cumulative catalog snapshot has 391 distinct confident event summaries through GWTC-5.0, of which 282 have source-frame component medians and intervals. Both listed lower component endpoints exceed $3\,M_\odot$ for 273 of the 282. This count uses the tabulated interval endpoints as an operational mass cut. The uniform-waveform selection from the later PE products yields 189 remnant-spin medians, with median 0.696, 10th and 90th percentiles 0.647 and 0.749. Matched alternate waveform medians differ by 0.0049 in the median absolute difference over 84 pairs. GW190814 and GW230529 illustrate why population, EOS and binary modeling matter near the lower compact-mass boundary. R16 R19

If one inserts Ω_H into the archived timing ratio, the field needed for $\chi_{\rm tim} = 1$ has median about 8.73×10^{11} G in the same remnant subset. This algebraic estimate gives the horizon-threading field at which the timing index would equal unity. In vacuum Kerr the geometry carries angular momentum and a plasma can support currents outside it. The Blandford–Znajek energy-extraction baseline depends on horizon-threading flux and horizon rotation, roughly $P_{\rm BZ} \propto \Phi_B^2 \Omega_H^2 / c$ in one common normalization. An ESFD correction would have to specify horizon flux, disk or jet boundary conditions, charge supply, and an observable such as a residual in the waveform or jet power consistent with those parameters. Horizon flux requires disk and field modeling, independently

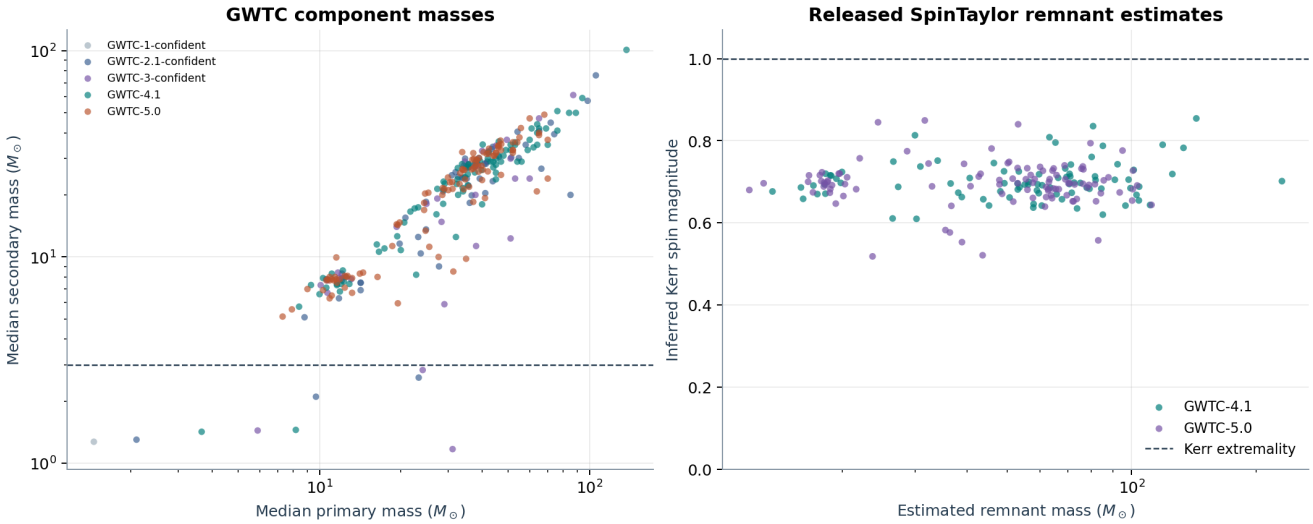

Figure 7. Source mass and waveform-inferred remnant spin distributions from the gravitational-wave data rerun. The displayed spin values are estimated under the selected waveform family.

of pulsar timing. R19 R20

Imaging and long-timescale timing offer complementary controls. EHT ring morphology constrains an exterior metric together with an accretion and emission model. Pulsar timing arrays infer a stochastic background from correlations in timing residuals over the sky. An ESFD signal in either case needs a model for the change in the null rays or the waveform and a covariance that includes the ordinary astrophysical population. Neither observable directly samples an interior spin density. R59

The archived BNS hypothesis predicts a polarized flash between 5 and 0.5 ms before coalescence, with a roughly 90° polarization-angle change. The GW170817 count-space check uses 872,114 raw Fermi/GBM entries across NaI 1, 2, and 5, with 465,709 photons after the pipeline's 10–50 keV channel-center selection. The nominal 4.5 ms window gives counts 2, 1, and 2. The pooled off-source expectation is 8.00 versus five observed. The one-sided excess probability under that Poisson reference is 0.900. An offset scan reaches 13 counts and has an empirical tail probability about 0.947 against 432 off-source control centers. A post-coalescence burst control shows the expected count excess. Clocks, propagation, localization, response matrices, and source timing assumptions delimit this one-event check. Polarimetry, energy fluence limits via response folding, and a population incidence constraint require additional data and calibrated injection recovery. A claimed 22 Hz precursor in another burst, for example the archived GRB 211211A lead, must be tested with that event's data, red-noise nulls, and a prespecified frequency or trials correction. A1 A6 R21 R22

9 Gravity, geometry, and the spin–entropy proposal

9.1 What a derivation of emergent gravity would have to produce

The early proof branch argues that constituent spin and electromagnetic field energy make mass and that long-range spin alignment accounts for inertia and attraction. The later regime-focused

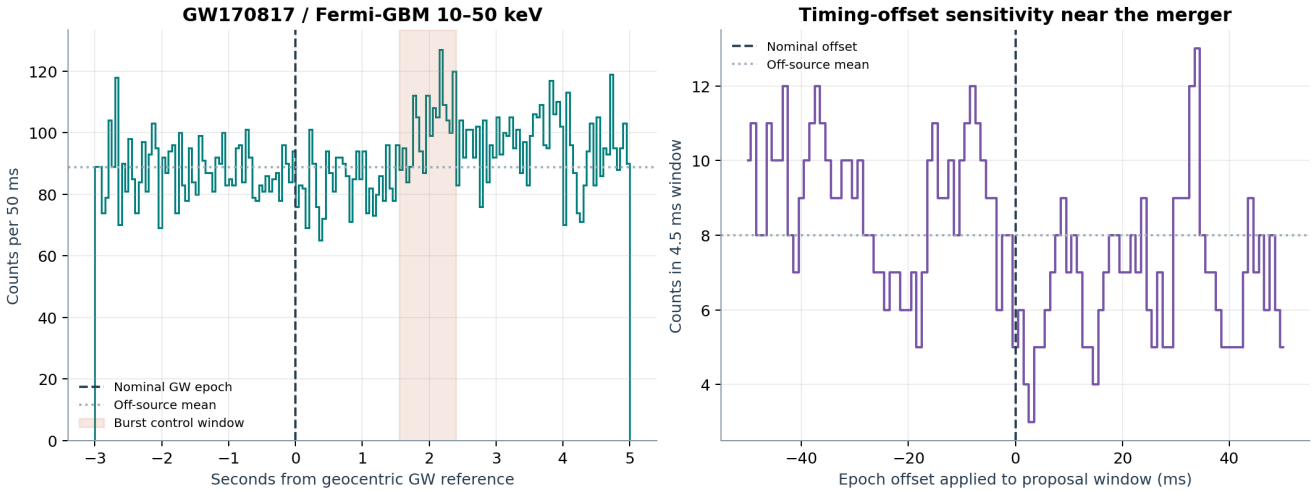

Figure 8. Fermi/GBM count-space test for the old ESFD precursor window in GW170817. The window and offset trials use the same instrument selections. This plot is an intensity test with a single event.

version asks when electromagnetic stresses matter for gravitationally bound systems. In standard GR a localized electromagnetic or spin-dependent interaction contributes through the conserved stress-energy of the complete system. Bulk angular momentum gives gravitomagnetic terms in the exterior metric. Static attraction, light deflection, redshift, inertial response, post-Newtonian corrections, and radiation are additional linked predictions. A derivation of gravity from spin goes beyond computing corrections in an action containing the Einstein–Hilbert term. A4 A6 R23 R25

At distances large compared with neutral source sizes, a static ordinary magnetic dipole pair has energy proportional to $[\boldsymbol{\mu}_1 \cdot \boldsymbol{\mu}_2 - 3(\boldsymbol{\mu}_1 \cdot \hat{\mathbf{r}})(\boldsymbol{\mu}_2 \cdot \hat{\mathbf{r}})]/r^3$ with both signs. Newtonian gravity requires a monopole $-GM_1M_2/r$ whose coupling survives for neutral, unpolarized bodies and for photons in the relativistic description. Polarization variance can be nonzero at zero mean. Its contribution is still set by the range, density scaling and tensor structure of the interaction. A physical source strength and universal charge must be derived. The proof draft's illustrative $G_{\text{naive}} = \alpha_{\text{em}}\hbar c/m_p^2$ is dimensionally possible and numerically 8.25×10^{25} in SI. It exceeds the measured G by about 1.24×10^{36}. It establishes a normalization problem, even before one confronts equivalence. A4

A light scalar with object-dependent charges q_A, q_B gives $U = -q_A q_B e^{-m_s r}/(4\pi r)$ at tree level in natural units. To emulate an extra universal attraction, q_A/M_A must match across compositions and environments or acquire an explicitly modeled screening dependence. Equivalence-principle experiments such as MICROSCOPE compare freely falling materials and bound differential accelerations at the few-10^{-15} scale. Spin-polarized torsion balances constrain orientation-dependent forces for specified ranges and couplings. A putative gravity replacement also has to match photon trajectories and post-Newtonian potentials, plus strong-field binaries. Einstein–Cartan spin contact interactions in the minimal theory and Pauli exchange have their own distance and spin structure. Force-range changes and collective condensates require an additional, specified physical mechanism. R01 R23 R25 R27

The archival connections to Mach and Sciama's inertial induction, Haisch–Rueda–Puthoff vacuum inertia, Sakharov's effective curvature term, Jacobson's thermodynamic Einstein equation, Verlinde's entropic proposal, and Cramer's transactional picture are research analogies. They have different assumptions about microscopic degrees of freedom, state spaces, background geometry,

and coarse graining. For example, integrating out matter can generate a curvature term in an effective action, with coefficient depending on particle content and matching, while a Clausius argument assumes local horizon temperature and an area entropy law. Each of these ideas leaves work for an ESFD mechanism. No recovered derivation gives the observed G, the graviton or other appropriate infrared representation, the equivalence principle, and a complete low-energy matter spectrum from spin–EM data. A2 A4 A6 R31 R32

9.2 Spin–entropy Field Dynamics (SEFD)

The June consolidation records a spin-entropy variable s and current J_s^μ, a gradient term, and the proposed coupling $-\beta_s s \nabla_\mu J_s^\mu$. It gives the combined index $\chi_{\text{tot}} = (B\Omega + \kappa_s s\Omega)/\Lambda_{\text{tim}}$, a separate $\chi_s = s\Omega/\Lambda_s$, and an effective density proportional to $\nabla_i(sJ_s^i)$. These are archived chat-level forms. They can be read as an order-parameter proposal. The thermodynamic entropy density, an entropy current, a microscopic spin tensor, and the von Neumann entropy of a reduced state are different quantities. For entropy density measured in units of k_B per volume, s has natural mass dimension three and κ_s has mass dimension -1 for $s\Omega$ to match $B\Omega$. A dimensionless coarse-grained order parameter would require a different κ_s. An actual entropy current has a constrained divergence under constitutive thermodynamics. A6

The archive form is equivalent to $+\beta_s J_s^\mu \nabla_\mu s$ up to a surface term. A test Lagrangian with $+\gamma_s(\partial s)^2 - U(s)$ and prescribed J_s^μ gives

$$2\gamma_s \Box s + U'(s) = -\beta_s \nabla_\mu J_s^\mu. \tag{16}$$

For a dynamical current, vary and specify its degrees of freedom, mutual response and boundary conditions. If $\gamma_s > 0$ and $U'' > 0$ at the background, the isolated scalar has a healthy kinetic term and positive small-perturbation squared mass. A condition $\chi_s \simeq 1$ becomes predictive once a solution, fluctuation operator, and parameter map are supplied. If using entropy as a hydrodynamic field, dissipation and positivity need a compatible physical closure. A reversible microscopic action and an irreversible coarse-grained entropy functional are connected by the reduction, environment, or stochastic model.

The archived effective gravitational density has a strong integral constraint. With a finite, regular, localized radial flux $s\mathbf{J}_s \to 0$ faster than r^{-2}, its integrated divergence vanishes by Gauss's theorem. For the literal fitted profile with outward amplitude Ce^{-r/r_s}, the enclosed effective mass and density are

$$M_{\text{div}}(< r) = 4\pi C r^2 e^{-r/r_s}, \qquad \rho_{\text{div}}(r) = Ce^{-r/r_s}\left(\frac{2}{r} - \frac{1}{r_s}\right). \tag{17}$$

The solution needs a regular center or a core modification. There is a sign change at $2r_s$ and the total tends to zero. An outer $1/r^2$ flux tail gives a finite boundary charge and requires its own origin. An assumed positive exponential density has a positive asymptotic mass when integrated. Some old drafts use both as halo sources. Treating (17) as a projected effective acceleration is mathematically different from claiming the positive energy of a field. Matching the density to a conserved field stress and to light deflection is essential. An entropy-force ansatz $T\nabla s$ supplies a force once T and s are defined. It does not itself predict a radial law, an observed G, or the same coupling for every test body. A1 A6

9.3 Emergent space from waves and hierarchical spin

In the author's later wave-based description, waves organize into atom-like shells, their relationships build larger structures, and successive additions and reorientations could generate geometry itself. A mathematical version starts with constituent degrees of freedom, an algebra of local observables, and an evolution rule. One example to explore would define a weighted graph through a connected two-point function $C_{ij} = \langle O_i O_j \rangle - \langle O_i \rangle \langle O_j \rangle$ for specified spin or phase observables. An emergent graph distance, a normal-mode or correlation spectral dimension, and a continuum limit could then be studied. The state and the mapping from C to distances have to be declared before assessing whether the result has approximate isotropy, Lorentz symmetry, locality, and an Einstein-like response. Choosing a Hilbert-space tensor factorization or a lattice already uses assumptions about adjacency and independence. An apparent geometric shape formed by a wave visual does not select a unique metric. A6 A7

The required cross-scale checks are concrete. At atomic scales a new interaction must preserve Coulomb hydrogen's spectrum, orbital angular momentum and spin–orbit, Zeeman and hyperfine splittings to observed precision. At molecular scales chemistry depends on exchange, bonding, and electronic states. Macroscopic phase order can arise in spins or a superfluid, with a finite stiffness and correlation length. A field that generates long-range geometry would need independent and covariant predictions as that coarse graining changes. A toy spin network, lattice gauge system, or propagating nonlinear order parameter can test aspects of this proposal. Lattice wave propagation in an already assigned space supplies a dynamical analogy. Emergence of the spatial manifold also requires a reconstruction of geometry from relational observables, along with time evolution and clocks that agree on causal order in the tested limit. R31 R32

10 Galaxies, the Great Attractor, and the dark sector

10.1 What the three archived rotation-curve mechanisms predict

The Electromagnetic Universe and associated galaxy drafts propose (i) a direct field or alignment effect, (ii) a positive spin-supported density with a fitted scale, and (iii) the SEFD divergence source. Some chat versions use $\rho_{\text{spin}} \propto [\langle S \rangle \Omega]^2/(\mu_0 c^2)$ with a coupling, or $V^2_{\text{spin}} \propto \chi\, \alpha(r/R_d) V^2_{\text{bar}}$. These require defined units and an independently measured or predicted $\langle S \rangle$, or a replacement stress law. The older wire estimate with $I = 10^{18}$ A and $r \simeq 3 \times 10^{20}$ m gives $B = 6.67 \times 10^{-10}$ T, 6.67×10^{-6} G, and $\chi_{\text{tim}} \simeq 7.1 \times 10^{-36}$ for a typical orbital rate. The earlier 10^5 G and $\chi \sim 10^{-11}$ values were unit and arithmetic errors. The field of a finite return-current geometry should also replace the ideal infinite-wire approximation when predicting observables. A1 A4 A6

The full SPARC snapshot supplied 3,391 measured radii in 175 galaxies. The rebuilt fit requires quality flag at most 2, inclination at least 30°, finite positive radius and velocity errors, positive measured rotation, and positive baryonic V^2. This leaves 3,166 eligible radii in 153 galaxies and 3,032 radii in 131 galaxies with at least eight points. Baryons use signed contribution $V|V|$ and stellar mass-to-light ratios 0.5 for disks and 0.7 for bulges. The paired profiles were fit with diagonal velocity errors and common fitting choices, and a radial extrapolation comparison trained on the innermost $\lfloor 0.7n \rfloor$ radii and held out 967 outer radii in total. Distances, inclinations, mass-to-light systematic errors, radial covariance and population selection matter for a global astrophysical inference. This is an internally comparable curve-fit test on fixed data choices. R28 R29

For $\rho_{\rm exp} = \rho_0 e^{-r/r_s}$ the enclosed mass is

$$M_{\rm exp}(<r) = 4\pi\rho_0 r_s^3 \left[2 - e^{-x}(x^2+2x+2)\right], \qquad x = r/r_s. \tag{18}$$

As r increases the mass tends to $8\pi\rho_0 r_s^3$ and the outer speed eventually falls as $r^{-1/2}$. At small r the finite central density gives a solid-body rise. Add to the baryonic squared speed using $V_{\rm add}^2 = GM_{\rm exp}(<r)/r$. The fixed historical NGC 2403 example $\rho_0 = 1.7\times10^{-20}$ kg m^{-3}, $r_s = 6$ kpc gives a peak extra speed around 435.7 km/s against a measured peak 136 km/s in this compilation. The earlier fitted examples for NGC 3198 and DDO 154 are addressed with the same fitting code and fixed baryonic choices. A fit with its own ρ_0, r_s per galaxy constrains a shape family. A first-principles ESFD prediction must determine the normalization and spatial structure from spin and field observations or shared parameters.

Profile	Median full-curve RMSE (km/s)	Median outer holdout RMSE (km/s)
Baryons	44.73	55.15
Published RAR control	13.60	11.86
ESFD archived exponential alone	6.34	14.67
Baryons + ESFD archived exponential	5.43	10.13
Baryons + NFW	5.18	7.84
Baryons + pseudo-isothermal	4.25	6.94
Baryons + literal SEFD flux (17)	5.19	8.40

The exponential plus baryons beats NFW on outer RMSE in 52 of 131 galaxies. The paired median per-galaxy excess in RMSE is 4.89 km/s, with a galaxy bootstrap 95% percentile interval of 0.23–7.25 km/s. The fixed published RAR uses overlapping data in its historical calibration, so its comparison supplies a known relation evaluated under the same cuts. The archived Draco scales give $1.68\times10^5\,M_\odot$ within 0.295 kpc, compared with about $1.70\times10^7\,M_\odot$ inferred under standard kinematics. For Abell 1689 the fixed exponential gives $8.59\times10^{14}\,M_\odot$ inside 2.39 Mpc versus a published weak-lensing-derived summary of about $1.87\times10^{15}\,M_\odot$. These fixed comparisons use published summaries and do not reproduce a full kinematic or lensing likelihood. A6 R28 R29 R33

10.2 A stronger energy-budget calculation

To measure the scale mismatch for ordinary electromagnetic energy, use the outermost eligible measured radius of each of the 131 matched galaxies and write $v_x^2 = v_{\rm obs}^2 - v_{\rm bar}^2$. In a deliberately simple spherical, weak-field mass proxy, $M_x = rv_x^2/G$. Set the volume-average Maxwell energy divided by c^2 equal to the corresponding mass density. This gives

$$B_{\rm rms,req} = \sqrt{2\mu_0 c^2 \frac{3v_x^2}{4\pi G r^2}}. \tag{19}$$

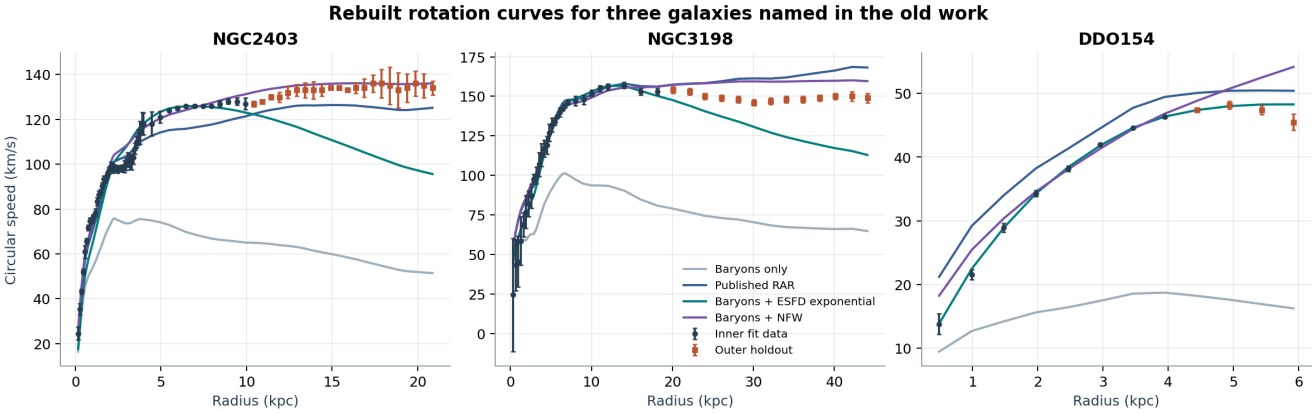

Figure 9. Held-out SPARC radii and inner-fit extrapolations for the three prominently named galaxy examples. The curve labeled exponential in the plot is the archived ESFD profile family in (18).

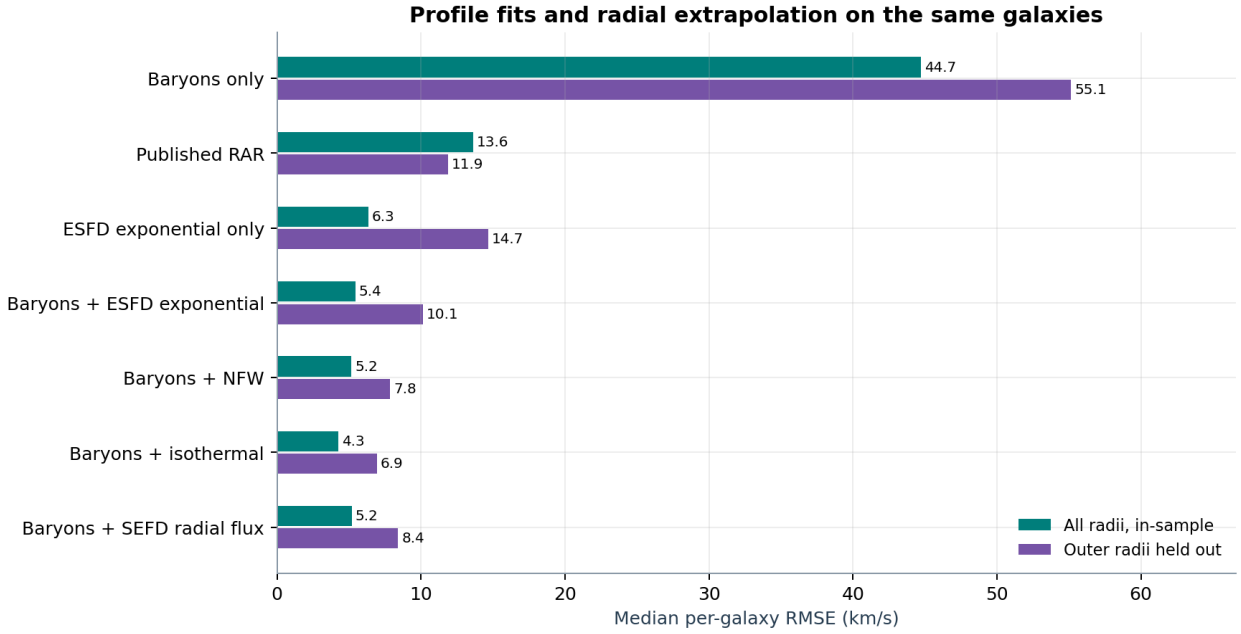

Figure 10. Rebuilt comparison of median galaxy-level residuals. The archival ESFD and SEFD parameterizations appear as the exponential and radial-flux profiles. Both use coefficients fitted to velocity data.

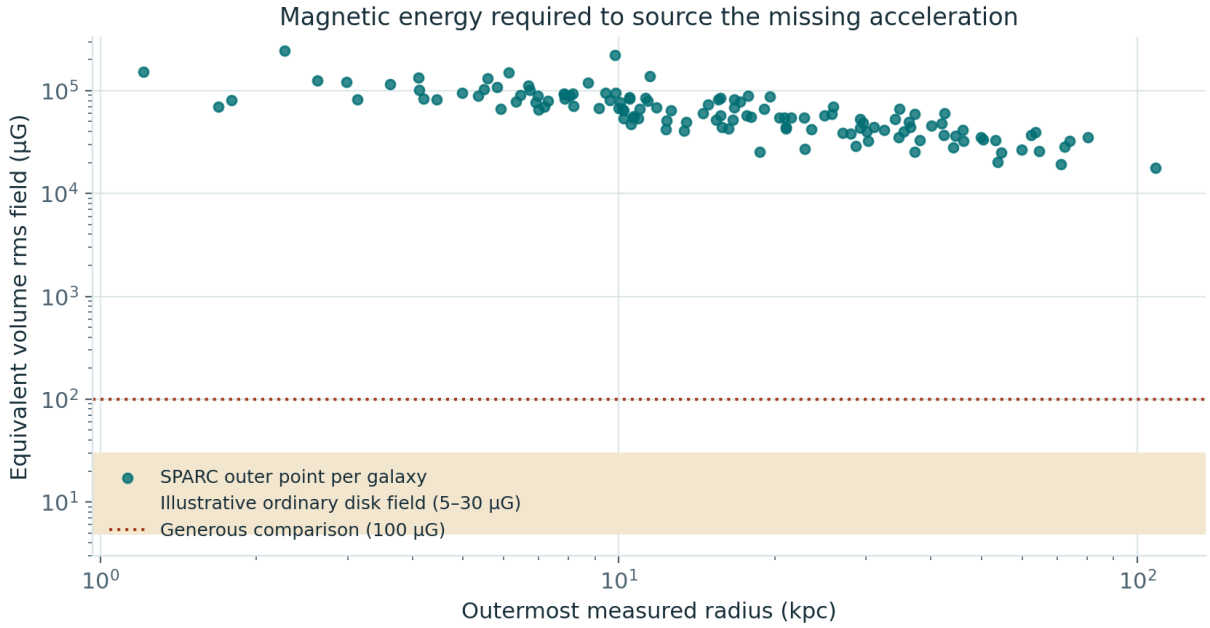

Figure 11. Volume-rms magnetic field that would supply the inferred extra acceleration via ordinary field energy in a spherical mass proxy. One measured outer radius per fitted SPARC galaxy. Comparison bands show assumed field strengths. The plotted points give the required fields.

All 131 selected outer points have positive v_x^2 under the fixed baryonic prescription. The 10th, median and 90th percentiles of the required volume rms field are 3.24×10^4, 5.93×10^4, and 1.04×10^5 μG. For the median point, 10 μG supplies about $1/(3.51\times10^7)$ of this energy budget. Even a uniform 100 μG supplies only about $1/(3.51\times10^5)$. As an example $v_x = 100$ km/s at 10 kpc implies $2.33\times10^{10}\,M_\odot$ and 9.21×10^4 μG. Published spiral-galaxy magnetic studies use synchrotron, polarization and Faraday signals, and ordinary large-scale values are in the μG range. Unknown geometry, anisotropic stresses, volume filling and baryonic uncertainty change (19). The several orders of magnitude in the mismatch cannot be accounted for by an order-unity change to the stress factor. Equation (19) tests gravitation by ordinary measured field energy. A distinct effective field or modified gravity needs its own magnitude from the action. R26 R28

Can the exponential itself close (19)? In the magnetic, quadratic equilibrium of (9), the scalar potential above its vacuum value plus the magnetic energy is $u = V(\bar{\Phi}) + ZB^2/2$. The equilibrium condition gives $V = (x/2)ZB^2/2$, hence $u/u_{\text{Maxwell}} = e^{-x}(1 + x/2)$ at fixed B. For the equilibrium branch $x \geq 0$ this ratio is at most one and decreases, reaching about 0.208 at $3B_c$. This specific exponential response suppresses the local equilibrium energy instead of amplifying it. On a fixed-field energy budget alone, increasing the 10 μG contribution to the median required level would need a factor 3.51×10^7, i.e. a pure multiplicative $Z \simeq e^{17.4}$. That sign and magnitude lie outside the stable homogeneous branch that produced (9). An alternative potential, kinetic energy in inhomogeneous configurations, or explicitly different sourcing of gravity must be developed and checked separately.

For a usable positive ESFD galaxy test, derive a mapping from radio polarization, field reversal, plasma density and vorticity to a prediction for Ψ and Φ_N. A weak-field metric in Newtonian gauge has $g_{00} \simeq 1 + 2\Psi/c^2$ and $g_{ij} \simeq -(1 - 2\Phi_N/c^2)\delta_{ij}$. Slow matter responds to $\nabla\Psi$. Lensing tests transverse gradients of $\Psi + \Phi_N$. A scalar conformal factor can move these potentials in opposite directions and leave null trajectories unchanged for a fixed underlying geometry, even when it

changes dynamics of massive particles. A plasma refraction model also predicts chromaticity. These distinctions are critical in joint gas, stellar-orbit and weak-lensing likelihoods. Begin with galaxies that have matched field and rotation data, fit shared coefficients, and validate on disjoint galaxies with fixed nuisance priors before extrapolating to clusters.

10.3 Cosmic filaments, the Galactic plane, and large-scale flows

The Radcliffe Wave, Galactic disk and supercluster flows connect directly to Grenke's large-scale intuition about organized currents. The Radcliffe Wave is a spatially coherent gas and star-formation structure. Its phase-space motion, vertical velocity and age distribution can distinguish disk gravity and disturbance models. Plasma structures and filamentary magnetic configurations also occur, and morphology alone has weak model specificity. Faraday rotation measures an integral proportional to $\int n_e B_\parallel dl$. Synchrotron intensity and polarization weight electron populations and magnetic fields differently, with foreground and geometry degeneracy. A mechanism claiming that magnetic topology organizes the mass distribution should predict gas, stellar and lensing features with distinct phases or alignment and hold out sky regions. The Great Attractor and Laniakea are first quantified through galaxy peculiar velocities. A field-centered alternative must predict those velocity gradients and a consistent gravitational potential using magnetism data independent of the flows. The localized Galactic magnetic field can affect gas and cosmic rays in a standard approach. A6 R26 R34

A cluster-collision test is essential because the Bullet Cluster shows a separation between much of the X-ray-emitting baryonic plasma and the peaks inferred from weak lensing. A useful prediction specifies the spatial distributions of ordinary gas, collisionless stars and any new spin field before scoring the shear. The old high-redshift rotation, DES or other shear, thermal/kinetic Sunyaev–Zeldovich (SZ), and growth claims need the original samples and predicted covariance, or an independently implemented mechanism with both metric potentials. A scientifically complete alternative should return joint residuals for redshift and scale bins, with covariances, selection, galaxy bias, feedback and projection effects. A circular-speed profile at $z \simeq 0$ has limited reach into these observations. A6 R35

10.4 Early cosmology, magnetogenesis, and dark energy

For statistically isotropic random fields, $\langle B_i B_j \rangle = \langle B^2 \rangle \delta_{ij}/3$. Maxwell stress is traceless and its isotropic coarse-grained equation of state is $p_B = \rho_B/3$ in energy units. Under flux freezing in an expanding background of scale factor a, $B \propto a^{-2}$ and $\rho_B \propto a^{-4}$ for constant Z. A varying Z exchanges energy with the scalar, so the two sectors must be evolved together. The magnetic component has anisotropic stress before the appropriate average, and its contributions to CMB spectra are limited by observations. To behave like cold matter, a proposed spin or scalar component needs sustained clustering with small effective pressure and sound speed on the relevant scales. A coherently oscillating canonical massive scalar with an approximately quadratic potential and $m \gg H$ can have $\langle p \rangle \simeq 0$ in a homogeneous approximation. The perturbations, production and couplings determine whether it is viable. This route adds a dark effective degree of freedom whose properties can be tested. R36 R37

As a background consistency scale, within base ΛCDM the Planck values $\omega_b \simeq 0.0224$ and $\omega_c \simeq 0.120$ with conventional relativistic $\omega_r \simeq 4.18 \times 10^{-5}$ give matter–radiation equality near $z \simeq 3400$. Holding the radiation budget fixed, replacing the matter term by baryons alone gives $z \simeq$

535, after standard recombination. A new theory can change the expansion or add another pre-recombination clustering stress. The required result is a matched calculation of temperature, polarization, peak heights, damping, transfer functions, lensing, BAO and baryon abundance in the alternative model. The archival exponential or SEFD radial flux beside a late galaxy supplies no background stress with these properties. R36

Inflationary magnetogenesis can be explored by evolving $Z(\Phi)$ with the scalar and charged matter. Amplification has backreaction, conductivity, initial state and strong-coupling conditions. A parity-even ZF^2 gauge factor alone does not select one circular polarization at leading fixed-background propagation. Cosmic birefringence can arise with a pseudoscalar coupling $-\frac{1}{4}g_{\varphi\gamma}\varphi F\tilde{F}$ and, in the simple homogeneous slow-background limit, polarization rotation $\Delta\beta = \frac{1}{2}g_{\varphi\gamma}[\varphi_{\rm obs} - \varphi_{\rm em}]$ up to the convention for $\tilde{F}$. Survey calibrations, dust foregrounds and band dependence are required. Any archived order-unity local non-Gaussianity, transfer-function deviation or GW propagation claim needs a defined primordial ensemble and an evolved spectrum, alongside the measured $f_{\rm NL}$, tensor-mode, and CMB constraints. A positive nearly constant scalar potential with small kinetic fraction can mimic vacuum-like $w \simeq -1$. Deriving its magnitude, radiative stability and perturbations is the problem for the dark-energy branch. A6 R36 R37

11 Spin–torsion collapse, white holes, and daughter universes

11.1 A solvable high-density toy model

The early idea treats increasing concentration, spin, and field strength as feedback toward a horizon and then a new phase. In the strongest extension, the high-density core bounces and an expanding region develops on the other side of a global geometry. Start with a toy FLRW patch and a conserved fermion number $n \propto a^{-3}$. Use an effective matter density $\rho_m = mn$ and a negative spin-correlation correction $\rho_s = -\beta_s n^2$, $\beta_s > 0$, motivated by particular averaged spin-fluid treatments, with $p_s = \rho_s$. The sign and magnitude are stipulated here. The quadratic scaling is the essential assumption. For flat geometry and zero vacuum term

$$H^2 = \frac{8\pi G}{3}(\rho_m + \rho_s), \qquad \dot{H} = -4\pi G(\rho_m + 2\rho_s). \tag{20}$$

At the balance $n_b = m/\beta_s$ and $\rho_b = mn_b$, $H = 0$ and $\dot{H} = 4\pi G\rho_b > 0$. Define $t_b = 2/[3\sqrt{(8\pi G/3)\rho_b}]$ and let a_b be the minimum. The result is

$$\frac{a}{a_b} = \left[1 + (t/t_b)^2\right]^{1/3}, \qquad H = \frac{2(t/t_b)}{3t_b[1 + (t/t_b)^2]}. \tag{21}$$

It follows by setting $y = (a/a_b)^3$ and integrating $\dot{y}^2 = 9(8\pi G/3)\rho_b(y-1)$. The expanding branch was independently integrated using the Raychaudhuri equation and $da/dt = aH$, starting at the regular turnaround. The analytic and numerical solutions agree to better than 10^{-9} in the dimensionless scale factor and Hubble parameter over the tested interval. FLRW Ricci and Kretschmann scalars stay finite in this toy solution. Effective negative stiff stress violates the null energy condition near the bounce. Its high-density projection and the validity of the averaged fluid at the balance density require a microphysical model. R01 R38

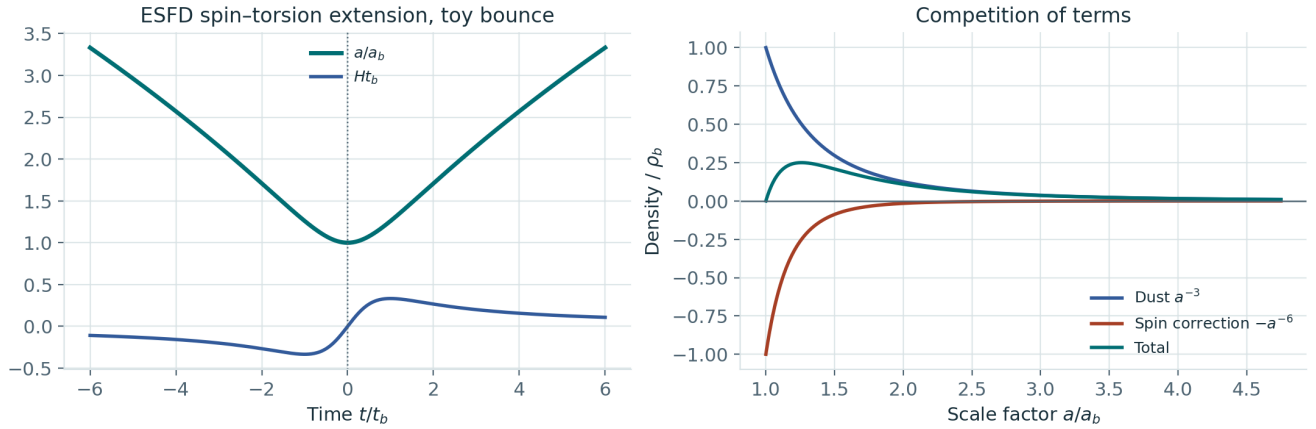

Figure 12. ESFD spin–torsion extension under the chosen homogeneous, isotropic matter and negative-stiff-fluid assumptions. This is the analytic bounce and the two competing density scalings.

A positive shear term in a homogeneous anisotropic model often scales as a^{-6} as well. A bounce driven by the negative spin-fluid term then needs its coefficient to exceed the positive shear contribution in the same Friedmann normalization. For relativistic matter with $\rho \propto n^{4/3}$ the balance density scales as $(\rho/n^{4/3}\beta_s^{-1})^{3/2}$. With an ordinary gravitational-strength contact, the scale is very high. Extrapolation from nuclear densities using a nonrelativistic dust law can badly misestimate the density. Strong-interaction phases, relativistic matter, anisotropic or inhomogeneous collapse, shocks, angular momentum and finite EFT cutoff all matter. This check explains how a bounce can arise and which assumption produces it.

11.2 Global causal structure and observational implications

A trapped surface is defined through the signs of the null expansions. A classical singularity theorem requires causal, energy and global hypotheses. A finite matter density or a regular minimum in $a(t)$ cannot determine the null expansions and event horizon of a rotating exterior. To turn (21) into an astrophysical model, specify initial stellar data and constraints, obtain a regular interior, match across a surface or physical shell to an exterior, track energy and angular momentum including emission, and locate trapped and anti-trapped regions through null geodesics. The interior may describe an expanding patch causally inaccessible to exterior observers. A white-hole-like exterior requires different global matching and a predicted escape channel. Ringdown changes, delayed bursts, and echoes each require a propagation and emission model plus a data likelihood. Existing black-to-white-hole tunneling and Einstein–Cartan daughter-universe proposals supply comparison models with their own assumptions. A6 A7 R38 R39

The reported handedness imbalance in a JWST deep field enters the archive as an observational lead. Projected galaxy winding, the intrinsic rotation vector, and global cosmic vorticity require an inclination and selection model to connect. A credible anisotropy test predefines redshift bins and sky masks, handles image mirroring and algorithmic symmetry, uses sky coverage beyond one field, and includes a kinematic explanation from observer motion and sample selection. An ESFD daughter-universe model would predict an axis, amplitude, sign and redshift dependence before the data split. It must also fit CMB isotropy and directional observables. The observed field imbalance measures its sample. It cannot identify a global formation mechanism without this

model. A7 R36 R40

12 Quark and gluon spin, the Higgs field, and CERN

12.1 Quark spin and the heavy-ion proposal

In the June 2 project discussion Grenke explicitly asked that intrinsic quark spin be part of the master theory. The archived terms are a quark tensor dipole and a gradient correction, $\alpha_q S^q_{\mu\nu} F^{\mu\nu} - \beta_q (\nabla_\rho S^q_{\mu\nu})^2$, with $S^q_{\mu\nu} = \bar{q}\sigma_{\mu\nu}q$ in that version. This normalization differs by two from the June Dirac $S_{\mu\nu}$. The term must be embedded with covariant derivatives and color and electroweak contractions when required. In a proton the total spin decomposition involves quark helicity, orbital angular momentum and gluon contributions, with operator definitions and a scale. In the Ji decomposition $J_q = \frac{1}{2}\Delta\Sigma_q + L_q$ and $J_q + J_g = \frac{1}{2}$, with a sum on flavors. Tensor charges relate transversity to the forward tensor bilinear. They are distinct from axial charges and the moments controlling magnetic couplings. Connecting the proposed operator to nucleon and neutron-star matter needs scale evolution and matched tensor matrix elements in the relevant composition and density. A1 A6 R03 R17

Peripheral high-energy nuclear collisions have orbital angular momentum, electromagnetic fields and short-lived vorticity. A fluid proxy for rotation seen by spin is thermal vorticity $\varpi_{\mu\nu} = -\frac{1}{2}(\partial_\mu \beta_\nu - \partial_\nu \beta_\mu)$ with $\beta_\mu = u_\mu / T$. Hyperon polarization inferred from weak decays and vector-meson spin alignment supply distinct observables. STAR measured global Λ polarization consistent with vortical dynamics, and an isobar blind analysis found no positive chiral magnetic signal under its predefined criterion. Charge-dependent backgrounds and isobar modeling enter the latter study. An ESFD term needs prediction of an additional dependence on flavor, p_T, rapidity, centrality, beam energy and spectator plane, with ordinary strong spin transfer and detector systematics. Compare isobars, matched centralities, and sign reversals only where the physical reaction-plane convention supplies a specified prediction. R04 R18 R30

The old claim of a 10^{-24} s electromagnetic microburst is a proposed formation timescale, an energy scale of $\hbar/\Delta t \simeq 0.66$ GeV. The 10^{-18} s instrumentation mentioned in the same draft is a million times coarser than that timescale. The suggested 10^6–10^7 photons per event in a 1–10 GeV band face a strict collision energy check. A 200 GeV-per-nucleon-pair Au–Au event has at most about 3.94×10^4 GeV of total center-of-mass beam energy before subtracting spectators and ordinary production. A 5.02 TeV Pb–Pb collision has about 1.04×10^6 GeV at the full-incoming-nuclei level. A million photons at 1 GeV already cost 10^6 GeV. The literal yield range therefore cannot describe a routine emitted component of these events. A feasible search uses direct-photon and low-mass dilepton spectra, angular anisotropies, photon correlations or polarization if measured, and comparisons with pp baselines and validated cocktail and thermal contributions. The coefficient should be matched to an emission rate and integrated over the spacetime history of each modeled event, including $\mathbf{B}(t)$ rather than an instantaneous upper estimate. A1 A6 R41

12.2 Higgs and the possibility of a common origin of mass and gravity

The established Higgs field is an electroweak scalar. Its vacuum value gives the weak vector masses and fermion masses through their respective couplings. The physical Higgs has spin zero. Most rest mass of nucleons emerges from the QCD state, including quark and gluon energies and

trace-anomaly physics, with the decomposition depending on scheme and scale. Energy of bound states is a source in GR regardless of how each constituent mass arose. The older ESFD proposal that Higgs, spin, gravity and electromagnetism descend from a common structure needs explicit matching to these distinct established processes. The invariant Φ in (3) is a proposed collective field or composite operator. It would mix with a Higgs-like scalar only through declared gauge-invariant terms and a specified vacuum. A4 A5 A6 R17 R42

Permissible comparison operators include $\Phi H^\dagger H$ with an appropriately dimensioned coefficient for a dimensionless Φ, nonminimal curvature $H^\dagger H R$, or the dimension-six electromagnetic matching contribution $(H^\dagger H)B^Y_{\mu\nu}B_Y^{\mu\nu}/M^2$ and weak-field analogues. After breaking, the last operator affects the gauge normalization and physical Higgs–gauge vertices in correlated ways. The long-range gravitational limit, observed $\gamma\gamma$, ZZ and WW channels, fifth-force limits, and electroweak precision data would jointly constrain such a model. The observed Higgs decay is a control measurement of the available couplings and correlated final states. It does not set the ESFD timing scale. R03 R42 R43

12.3 The off-shell density matrix and an ESFD residual

The September CERN expansion proposed $d\rho(q^2) = \rho_{\text{ESFD}}(q^2) - \rho_{\text{SM}}(q^2)$ in Higgs decays to four leptons, with q^2 the lower dilepton invariant mass squared under a fixed pairing. Timelike lepton currents in $H \to ZZ^{(*)} \to 4\ell$ encode the spin correlations of the vector channel. The second vector is generally off shell because $m_H < 2m_Z$. For a quantitative prediction start with the observable four-lepton amplitude, including identical-particle interference and gauge-complete contact and mixed $Z\gamma$ terms where applicable. Let q_1, q_2 be the dilepton momenta, D_Z the propagator factor, and $J^{(i)}$ the chiral lepton current. A schematic neutral-vector vertex description is

$$\begin{aligned}\mathcal{M}_{ZZ} \propto J^{(1)}_\mu J^{(2)}_\nu D_Z(q_1^2) D_Z(q_2^2)\big[a_1 m_Z^2 g^{\mu\nu} + a_2(q_1\cdot q_2\, g^{\mu\nu} - q_2^\mu q_1^\nu) \\ + a_3 \epsilon^{\mu\nu\rho\sigma} q_{1\rho} q_{2\sigma}\big].\end{aligned} \tag{22}$$

The tensor structures give spin and CP tests in a specified basis, with coefficients and form factors constrained by gauge symmetry and matching. For amplitudes $\mathcal{M}_\lambda$ projected to such a basis, $R_{\lambda\lambda'} = \int \mathcal{M}_\lambda \mathcal{M}^*_{\lambda'} d\Pi$ in a bin and $\rho = R/\operatorname{tr} R$. At first order, $\delta\rho = (\delta R - \rho_{\text{SM}} \operatorname{tr}\delta R)/\operatorname{tr} R_{\text{SM}}$, where δR includes interference. This enforces the trace constraint. Test physical positivity, fit the particular direction in angular coefficient space predicted by the operator, and background-subtract and fold detector acceptance with the same binning. A renormalized electroweak amplitude, joint covariance, and a detector model are necessary for a bound on the new coefficient. A5 R03 R44 R45

ATLAS's two published combined angular coefficients give observed minus Standard Model values $+0.26 \pm 0.45$ and -0.56 ± 0.44 using the quoted experimental marginal errors. The resulting marginal pulls are $+0.58$ and -1.27. They share analysis inputs and have no demonstrated joint ESFD likelihood in the recovered work. The 4.7σ ATLAS result concerns the assumed separable-state comparison in the angular analysis. CMS reports an I_3 95% interval [2.52, 2.75] in a restricted $C_\parallel$ fit and [0.28, 2.87] with both parameters profiled, with the Standard Model central reference 2.60. Event reconstruction and fit assumptions affect these comparisons. The study of top-quark spin entanglement is another Standard Model laboratory for density-matrix validation. It probes a different final state and interactions. A5 R44 R45 R46

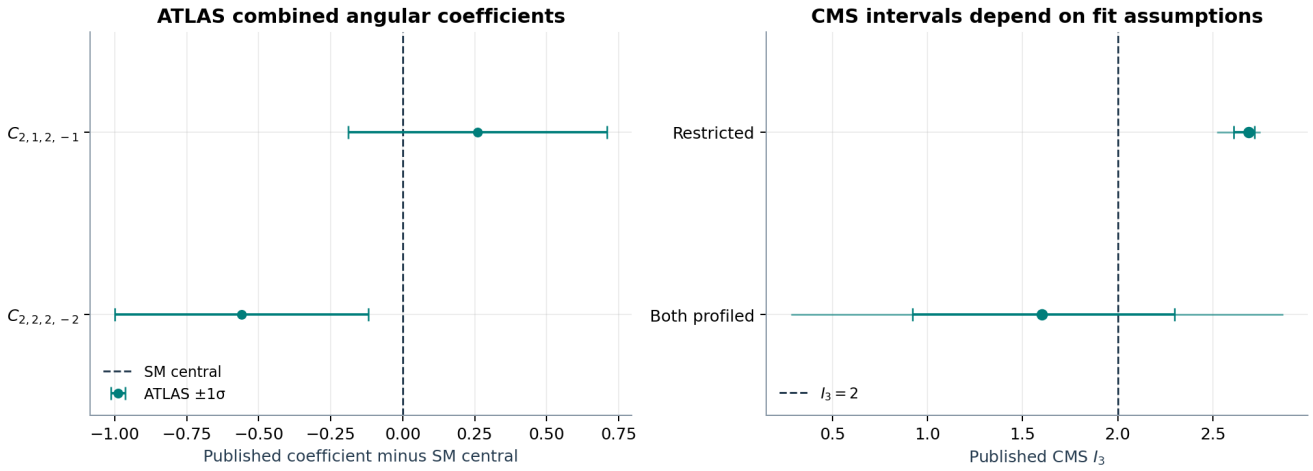

Figure 13. Published measurements used in the ESFD collider residual study. ATLAS points are relative to the reported Standard Model expectations. CMS intervals illustrate how the fit choice affects the witness. The figure contains measured values and Standard Model comparisons. A matched ESFD curve requires the amplitude in (22) to be specified.

13 Exceptional symmetry and ultraviolet completion

The archival July paper sketches $E_8 \supset \mathrm{Spin}(11,3) \to \mathrm{Spin}(3,1) \times H$ and an eventual low-energy Standard Model plus gravity. The frame-Higgs sector would connect a tetrad with a symmetry-breaking field. Heavy off-diagonal modes were proposed as a source of extra fermion, field, and torsion operators, with possible axion-like or heavy electroweak boson signatures. The proposal needs the real form, embedding of hypercharge, representations, chirality and generations, spectrum and vacuum, kinetic signs, symmetry breaking and anomaly checks. A positive identification of a gauge group supplies no Wilson coefficient without this chain. A6 R47

The E_8 root system has 112 vectors $\pm e_i \pm e_j$ for $i < j$ in $\mathbb{R}^8$, and 128 half-integer vectors $\frac{1}{2}(\pm 1, \ldots, \pm 1)$ with an even number of minus signs. Eight Cartan generators give dimension 248. In the compact real algebra or its complexification, the $\mathfrak{so}(16)$ branching reads $\mathbf{248} = \mathbf{120} \oplus \mathbf{128}$. The **120** is the adjoint, and the **128** is one chiral spinor of $\mathfrak{so}(16)$. This elementary representation check does not fix the noncompact embedding or supply four-dimensional chiral matter. Distler and Garibaldi identify representation-theoretic obstructions in the class of direct real/complex E_8 embeddings of gravity and the Standard Model that includes Lisi's proposal. An ESFD construction in the same class faces those assumptions. Higher-dimensional compactification, different algebraic structure, or different representations would have to be specified explicitly for a different proposal. R47

The old estimate $\chi \sim g_{E8}^2/M_X^2$ has mass dimension -2. Integrating out a healthy heavy vector with linear coupling to a fermion current can give a dimension-six current–current term $-g_X^2 J_X^2/(2M_X^2)$ at tree level in the stated vector convention. The low-energy spin–photon dipole of (1) has coefficient dimension -1. Its electroweak-gauge-invariant predecessor is a different dimension-six operator. Depending on the mediating fields, a dipole may first arise at loop level with Yukawa or fermion-mass insertions, or may require additional interactions. The minimal deliverable for this branch is a chiral table, charge and anomaly equations, canonical kinetic terms, an integration-out

calculation, and comparison of a single set of coefficients against multiparticle data. E_8 geometry, exceptional spinors, and analogies with the atomic wave hierarchy are motivations for this calculation. A6 R03 R47

14 Quantum coherence, collapse, and observers

14.1 Entanglement and a constrained spin-decoherence model

The older ESFD "shared envelope" gives spin correlations a common field description. Standard quantum states already permit nonfactorizing spin expectation values at spacelike separation. For a spin singlet $E(\mathbf{a},\mathbf{b}) = -\mathbf{a}\cdot\mathbf{b}$ and the optimal CHSH value is $2\sqrt{2}$. A locally causal model with independent settings and outcomes represented by $A_i(\lambda), B_j(\lambda) \in \{-1,+1\}$ has $|S| \leq 2$. For each hidden variable λ, either B_0+B_1 or B_0-B_1 is zero, so $A_0(B_0+B_1)+A_1(B_0-B_1)$ is ± 2. A shared pre-existing classical spin field and signals restricted to a future light cone still obey this bound under those assumptions. A change imposed at event A reaches only its causal future. Quantum field entanglement, a modified statistical assumption, or explicit nonlocal dynamics with operational no-signalling is needed if the model aims to reproduce the Bell correlations. An entanglement witness extracted from collider distributions has different operational assumptions than a freely chosen, spacelike separated Bell test. A1 A5 R48

A concrete test target for a local spin-sensitive environment is an additional positive dephasing rate $\Gamma(B,\Omega,\mathbf{M})$ above measured noise, with a completely positive Markovian model

$$\frac{d\rho}{dt} = -\frac{i}{\hbar}[H,\rho] + \Gamma(\sigma_z\rho\sigma_z - \rho). \tag{23}$$

The off-diagonal term decays as $e^{-2\Gamma t}$ in the commuting Hamiltonian frame. With independent such channels on the two qubits of $|\Phi^+\rangle$, the coherence multiplier is $\lambda = e^{-2\int(\Gamma_A+\Gamma_B)dt}$, and the maximal CHSH value is $2\sqrt{1+\lambda^2}$. Local completely positive trace-preserving operations preserve the distant marginal for unconditioned outcomes. A proposal coupling this rate to ESFD needs a dimensioned power law and control for magnetic gradients, control pulse noise, bath fluctuations and drift. For an objective-collapse hypothesis, the unconditioned dephasing equation gives an observationally different question from an account of individual outcomes. To go beyond ordinary dephasing, state the stochastic evolution of a run, probability rule, Lorentz/no-signalling limit and any heating or spontaneous radiation. Then use independent interferometry, entanglement visibility or timing constraints to infer a bounded rate. R48 R49

14.2 Time, observer layers, and consciousness

The Trap of Reality proposes that perception and spacetime are stabilized layers, that fields and spin may connect to an underlying observer, and that the nervous system may act as an interface or transducer. The public companion discussion also asks whether individual perspectives, continuity, and the origin of experience admit a broader field account. The analogy to Hoffman's Markovian conscious agents supplies a formal vocabulary for perception, decisions and actions. Tom Bilyeu's identity and continuity discussion supplies a philosophical comparison in the source. The ESFD field action as recovered models A, ψ, Φ and geometry. A consciousness or observer theory needs a defined variable, dynamics and independent observations linking it to these fields.

Connection by analogy, or the existence of spin coherence somewhere in matter, leaves that interface unspecified. A7 R50

For an operational model, assign an observer state o a state space $\mathcal{O}$, a generator $\mathcal{K}_o[\rho, \Phi, u]$, a readout $P(y|o, \rho, \Phi)$ for declared observables, and a reciprocal or explicitly open-system effect on matter. Fix units, a stress or energy account for any physical backreaction, and null limits. This would allow a preregistered laboratory comparison using the same instrument and environment with automated, blinded, and recorded conditions. Standard brain electrophysiology and signal artifacts are controls for a physical field claim. Subjective time and memory need independent definitions from proper time and population coherence. Philosophical claims about identity, free will, death, simulation, or consciousness in AI remain underdetermined by photon, pulsar and collider data. The archived views are retained as questions and can acquire empirical content through a specified discriminator. A7 R49 R50

15 Solar, geophysical, and vacuum extensions

15.1 Solar activity, local shear, and Earth

The rebuilt solar baseline uses the science-quality GOES composite flare measurements and WDC–SILSO daily counts. Removing invalid rows and repeats leaves 82,229 unique valid catalog entries. The monthly intersection has 81,721 flares across 381 complete months from February 1995 through October 2026, including 6,057 M/X flares and 366 X-class flares. A daily-exposure Poisson count baseline uses contemporaneous log-transformed activity, with 299 months before 2020 for the fit and 82 later months for evaluation. Its out-of-time mean Poisson deviance is 12.80 versus 41.71 for a constant-rate model. The all-period Spearman correlation of monthly M/X daily rate with sunspots is 0.863. Dependence within a solar cycle and concurrent activity preclude treating this as an advance warning forecast. The analysis is a calibrated solar-activity control for a later field-threshold model. R51

A generous 10 kG field and the Sun's representative bulk sidereal spin give $\chi_{\text{tim}} \simeq 4.56 \times 10^{-17}$. A model of active-region instability needs local vorticity, field projection and volume, photospheric flux emergence, helicity injection, preflare topology and reconnection physics. Start with a GOES event-to-active-region match, HMI vector magnetograms, and velocity estimates at uniform cadence. Approximately 37,247 solar entries in the full-month joined sample have a region identifier. The rest require an explicit missing-data model or a declared matched-cohort bound. A forecast should fit pre-event time only, and validate by active region and solar cycle, with disk position, sensitivity, false-alarm rate and retries of repeated flares handled consistently. A local plasma model compares magnetohydrodynamic current sheets, shearing and helicity thresholds with the spin closure; Earth's atmospheric response is another system with its own propagation and lags. A6 R51 R52

The older Earth-reset and tectonic proposals can be stated as a time-dependent field or torque claim. At an assumed geomagnetic field of 50 μT the magnetic pressure is about 1.0×10^{-3} Pa. A 100 nT perturbation gives a cross-stress scale $B\delta B/\mu_0 \simeq 4\times10^{-6}$ Pa. Geomagnetic reversals involve the dynamo field and require their own paleomagnetic chronology. They do not imply reversal of the planet's mechanical angular momentum. A missing high-gain triggering mechanism would require an energy pathway, independently observed electric currents or stresses at depth, and a lag, location and magnitude prediction scored on held-out catalogs. USGS reports no established

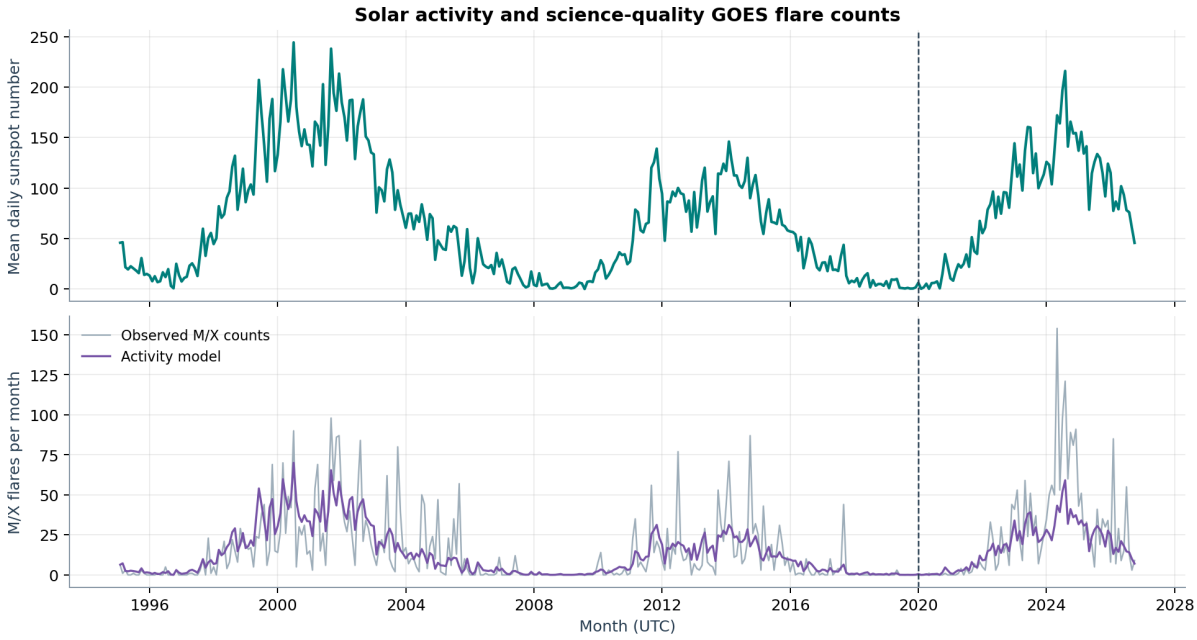

Figure 14. Solar baseline rerun on GOES and SILSO data. The dotted split marks the later monthly evaluation. The activity model uses contemporaneous sunspot measurements. Local spin and magnetic-field geometry remain an active-region-level test.

causal link between solar flares or magnetic storms and earthquakes. Independently demonstrate any such statistical relation against time clustering, catalog completeness, seismic seasonality and multiple searches. Earth-rotation and atmospheric angular-momentum exchange respond to geophysical and fluid forcing. They provide controlled alternative predictions. A6 R52 R53

15.2 Vacuum energy, claimed propulsion, and resonance traditions

The research archive links the early proposed spin torque and “vacuum resistance” to later work on Casimir physics, government research programs, and anomalous observations. The static Casimir energy of ideal parallel plates depends on separation, with $E/A = -\pi^2\hbar c/(720d^3)$ before material and geometry corrections. A closed reversible change of boundary configuration returns that energy difference during reset. The dynamical Casimir experiment generated photons under externally modulated boundaries, with the modulation supplying energy. These results are strong examples of field dynamics under boundary changes. An energy claim requires sustained power delivered under load and a full input, storage and environmental balance across the cycle. Open-circuit voltage alone can persist with very little transferable energy. A8 R54

The related Pattern Nexus work names NASA exploratory efforts, the DARPA vacuum-engineering program, a 2026 proposer slide reporting 100–250 mV at very low current density, a Casimir power-cell patent, and inertial reduction claims in the Pais patent record. These are traceable documents of research proposals, legal claims or reported bench observations. The physically decisive data for a putative vacuum source are long-duration $V(I,t)$ curves, integrated load energy, independent replication, and changes upon control stacks, chemical history, thermal gradients, ambient RF and leakage changes. Likewise for anomalous propulsion one compares the measured force with net momentum flux through the closed system, using calibrated thermal, outgassing, radiated power, cable and magnetic force budgets. A photon beam carrying power P emits mo-

mentum per time P/c in its direction. A closed internal electromagnetic cycle exchanges momentum within its components. A nonzero net thrust needs momentum carried across a boundary or a specified additional coupled field that carries it. The precise EMDrive remeasurement found that conventional thermal and apparatus effects can generate false positives. None of these documents calibrates an ESFD propulsion coefficient. A8 R54 R55 R56

The historical resonance discussion invokes ancient structures, Schumann modes, Tesla, Russell and Schauberger, and rotating or charged structures. The Great Pyramid electromagnetic simulation studied driven scattering and field concentration given specific material and geometry assumptions. For any finite passive resonator, $dU/dt = P_{\text{in}} - P_{\text{out}} - P_{\text{diss}}$ in the chosen convention. At 7.8 Hz, the approximate fundamental Schumann frequency, the free-space wavelength is about 3.84×10^7 m. A 200 m air-filled half-wave path instead has a simple scale of 7.5×10^5 Hz. Real dielectrics, losses and cavities change that scale, and coincidence with a global Earth–ionosphere oscillation requires actual coupling and loaded power measurements. Qualitative precedents of vortices, spirals, cavity modes or luminous discharges supply test geometries. Evidence of a historical energy device needs archaeological or physical records and a working electromagnetic power budget. A6 R57

The archived UAP and metric-engineering discussion maps reported accelerations or missing exhaust signatures to candidate physics. Calibrated range and velocity, platform motion, time-correlated independent sensors, energy and momentum accounting, and a known instrument transfer function are the data that would allow such an inference. An unresolved report supplies no quantitative ESFD coupling. A spacetime engineering claim is more demanding still, requiring a metric, a physical $T_{\mu\nu}$ and boundary data consistent with the source and causality. Public exploratory reports and intellectual overlaps support a history-of-ideas entry. The stronger claims about classified technology or deliberate suppression require independent evidence. A8 R56

16 Local spin-field response

16.1 Direct coupling and the saturation potential

In the printed June action, $V_{\text{sat}}(X) = \lambda_S(X - \Phi_0^2)^2/4$ sets a preferred spin invariant. At fixed magnetic background use a homogeneous magnetic-sector ansatz $S_{12} = s$ and $F_{12} = B$ with the other components zero. Thus $X = 2s^2$ and $S_{\mu\nu}F^{\mu\nu} = 2sB$. In this restricted static calculation, treat s as a material polarization amplitude. Its energy at prescribed B is $B^2/2 + V_{\text{sat}}(2s^2) - 2\alpha Bs$. The electromagnetic term is constant in this variation. With $u = \sqrt{2}s/\Phi_0$ and $\beta = \sqrt{2}\alpha B/(\lambda_S\Phi_0^3)$, the stationary condition is

$$\begin{aligned} \frac{U(u)}{\lambda_S\Phi_0^4} &= \frac{1}{4}(u^2-1)^2 - \beta u + \text{const}, \\ u^3 - u &= \beta, \qquad U_{,uu}/(\lambda_S\Phi_0^4) = 3u^2 - 1. \end{aligned} \tag{25}$$

There are two minima and one maximum when $|\beta| < 2/(3\sqrt{3})$, apart from the endpoint degeneracies. At the folds one minimum meets the maximum. The absolute minimum changes orientation at zero field. The favored large-$|\beta|$ solution grows as $|\beta|^{1/3}$. In particular the potential produces local metastability and a decreasing differential susceptibility without setting a finite hard cap on $|s|$. This calculation gives a concrete instability mechanism within the assumed sector. A real spinor or material must supply the transport law that determines whether a rotor follows that branch, switches at a fold, or nucleates a domain earlier.

The standard spin coupling admits both reactive and dissipative behavior. An equilibrium potential determines the torque $\mathbf{N} = -\partial U/\partial\boldsymbol{\vartheta}$ for an orientation angle $\boldsymbol{\vartheta}$. Damping additionally requires a lagging response. For a stationary medium let $\widehat{S}(\omega) = \chi_S(\omega)\widehat{B}(\omega)$ with the convention $e^{-i\omega t}$. The mean absorbed power for a sinusoidal drive is proportional to $\omega\,\mathrm{Im}\,\chi_S(\omega)|\widehat{B}|^2/2$. A mechanical energy-loss claim can be tested against measured heating and phase lag, while a conservative orientation effect can be tested by measuring precession and reversing a static field. The susceptibility needs units, species dependence and a boundary prescription.

16.2 Spin-built exponential response and two instability scales

The exponential-source excerpts make Φ_{EM} quadratic in a spin tensor. To calculate one regular long-wavelength limit, retain a single real magnetic polarization amplitude s and assign it a canonical collective kinetic term. Here s has mass dimension one, with the tensor normalization absorbed into $g > 0$. This gives $Z(s) = \exp(-gs^2)$ and $V(s) = m^2s^2/2 + \lambda s^4/4$. It is a material closure for the quadratic spin dependence. Its m and λ are new phenomenological coefficients of this calculation. A microscopic prediction would match them to the spin susceptibility and gradient energy of the state. Use a uniform magnetic background and positive m^2, λ. The stationary equation at fixed mean flux is

$$s\left[m^2 + \lambda s^2 - gB^2e^{-gs^2}\right] = 0, \qquad B_0 = \frac{m}{\sqrt{g}}, \quad b = \frac{B}{B_0}, \quad y = gs^2, \quad \ell = \frac{\lambda}{gm^2}. \tag{26}$$

The unpolarized state has no linear photon mixing because $Z'(0) = 0$. Its scalar curvature is $m^2(1-b^2)$. Perturbations with $k^2 < m^2(b^2-1)$ grow when $b > 1$. Exactly at zero polarization the

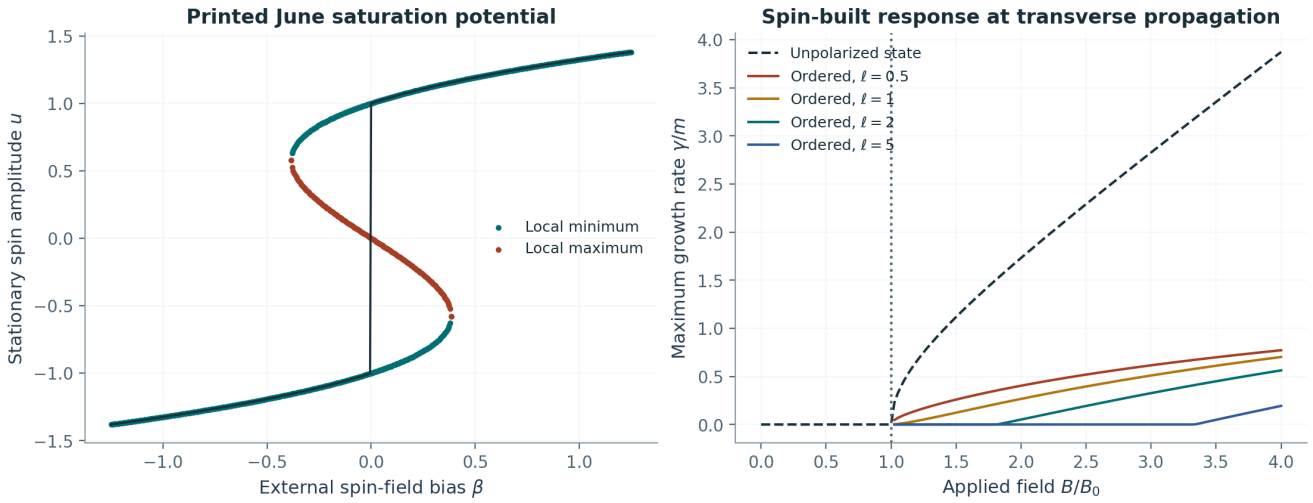

Figure 15. The left panel resolves stationary solutions of the printed June saturation potential. The right panel shows growth rates for the homogeneous unpolarized state and ordered branches in the spin-built exponential model.

photon mode retains its vacuum propagation. The model adds a different prediction once spin order is present. An ordered state satisfies $(1+\ell y)e^{y} = b^{2}$ and has

$$\frac{M^{2}}{m^{2}} = 2y(\ell+1+\ell y), \qquad \frac{\mu_{\mathrm{mix}}^{2}}{m^{2}} = 4y(1+\ell y),$$
$$(\omega^{2}-k^{2})(\omega^{2}-k^{2}-M^{2}) = \mu_{\mathrm{mix}}^{2}k^{2}\sin^{2}\theta. \tag{27}$$

Here $M^{2} = V'' + B^{2}Z''/2$ and $\mu_{\mathrm{mix}}^{2} = B^{2}(Z')^{2}/Z$ on the equilibrium. Holding B fixed when varying s gives the diagonal curvature. Permitting transverse photon fluctuations yields the coupled determinant. The ordinary transverse polarization remains separate. For the mixing polarization a finite unstable band requires $\mu_{\mathrm{mix}}^{2}\sin^{2}\theta > M^{2}$, and its upper edge is $k^{2} = \mu_{\mathrm{mix}}^{2}\sin^{2}\theta - M^{2}$. At $\theta = 90^{\circ}$ and $\ell > 1$ the secondary onset is $y = 1 - 1/\ell$, or $b = \sqrt{\ell}\exp(1-1/\ell)$. For $\ell = 2$ this is $b \approx 1.816$, after the first ordering at $b = 1$. In a periodic direction of length L, the smallest nonzero wave number $2\pi/L$ must fit in the band for this mixed mode.

The direct June coupling can tilt the two spin minima. Pure quadratic dependence on s preserves their two signs. The independent scalar test in the earlier instability chapter has a term linear in its scalar and therefore a different background and mixing law. These are three measurable distinctions of the dynamics, even if their bulk phenomena are all referred to as saturation. The available archival material supplies no unique numerical map from B_{0} or the local bias β to the timing constant Λ_{tim}.

16.3 Long-range gravity and what the Proof action supplies

The vacuum action in the 22-page Proof p. 2 has the factor $+\kappa S^{\mu\nu}F_{\mu\nu}/2$. It gives $\partial_{\mu}(F^{\mu\nu}/\mu_{0} - \kappa S^{\mu\nu}) = 0$ with external current zero. The equivalent polarization current $J^{\nu}_{\mathrm{pol}} = \kappa\partial_{\mu}S^{\mu\nu}$ obeys current conservation by antisymmetry. For a smooth, localized static S, $Q_{\mathrm{pol}} = \kappa\int d^{3}x\,\partial_{i}S^{i0}$ is the surface integral at infinity and vanishes. The tree-level static spin exchange therefore has a momentum factor $k_{i}k_{j}/|\mathbf{k}|^{2}$ from two vertices and the photon Green function. Away from overlap the real-space kernel is proportional to

$$\partial_i \partial_j \frac{1}{4\pi r} = \frac{3\hat{r}_i \hat{r}_j - \delta_{ij}}{4\pi r^3} \quad (r > 0). \tag{28}$$

The simple localized dipole interaction is anisotropic. Obtaining the Proof's proposed universal $-GM_1M_2/r$ requires a different long-distance response, for example an explicitly derived collective pole with a charge proportional to total inertial mass. This requirement remains even if a medium amplifies microscopic alignment. A universal force must also account for light and relativistic stress. In the other recovered branch, an explicit Einstein–Hilbert term with G generates metric dynamics from the outset, so a calculated spin stress there gives a gravity correction.

The Proof §3 gives a magnetic critical scale and discusses a strong-field parameter of a charged particle. The Lorentz scalar

$$\chi_{\text{part}} = \frac{|q|}{m^3}\sqrt{-(F_{\mu\nu}p^\nu)(F^{\mu\rho}p_\rho)} \tag{29}$$

probes the electric field in that particle's rest frame in $c = \hbar = 1$ units. A charged particle instantaneously at rest in a purely magnetic field has $\chi_{\text{part}} = 0$ even when B/B_Q is large. Magnetic quantization and polarized vacuum propagation can still matter. The ratio B/B_Q, the particle invariant, the bulk $B\Omega/\Lambda_{\text{tim}}$ index and an energy-to-binding ratio address different physics.

17 Data-model expansions across scales

17.1 Cold spin contact and static compact stars

The EOS tables give pressure as a function of total energy density. Reconstruct a relative baryon density $z = n/n_\star$ by integrating the cold first law $d\ln n = d\epsilon/(\epsilon + p)$. The reference $n_\star$ is fixed by a rest-mass-equivalent energy density of 5.4×10^{17} kg m^{-3}. For an added energy density $Q(z)$, this same thermodynamics gives the added pressure $zQ'(z) - Q(z)$. Two exploratory contact prescriptions were used:

$$\begin{aligned} Q_{\text{all}}(z) &= \eta\epsilon_\star z^2, \\ Q_{\text{core}}(z) &= \eta\epsilon_\star z^2 \frac{[\max(0, 1 - z_0^2/z^2)]^3}{(1 - z_0^2)^3}, \qquad z_0 = 0.55. \end{aligned} \tag{30}$$

The second choice adds a smooth onset while preserving the quadratic behavior asymptotically. Positive and negative η bracket a stiffness dependence. The sign and magnitude of a microscopic torsion contribution depend on how the spin ensemble is averaged and matched. A density-squared term in this scan is a surrogate for that calculation. It may exceed the minimally normalized torsion term by many orders of magnitude. It may also capture an ordinary change in the nuclear EOS. Measurement of a mass shift alone cannot determine the underlying origin.

The calculation follows the EOS segment connected continuously to the low-pressure crust, enforcing positive pressure and energy, $d\epsilon/dn > 0$, and $0 < dP/d\epsilon \leq 1$ before integration. It reports an interior first mass maximum separately from cases that terminate at an EOS or causality boundary. The six equations of state retain their original pressure and energy arrays in the archive. These sequences are spherical and static. A spinning, magnetized star has anisotropic stress, fluid

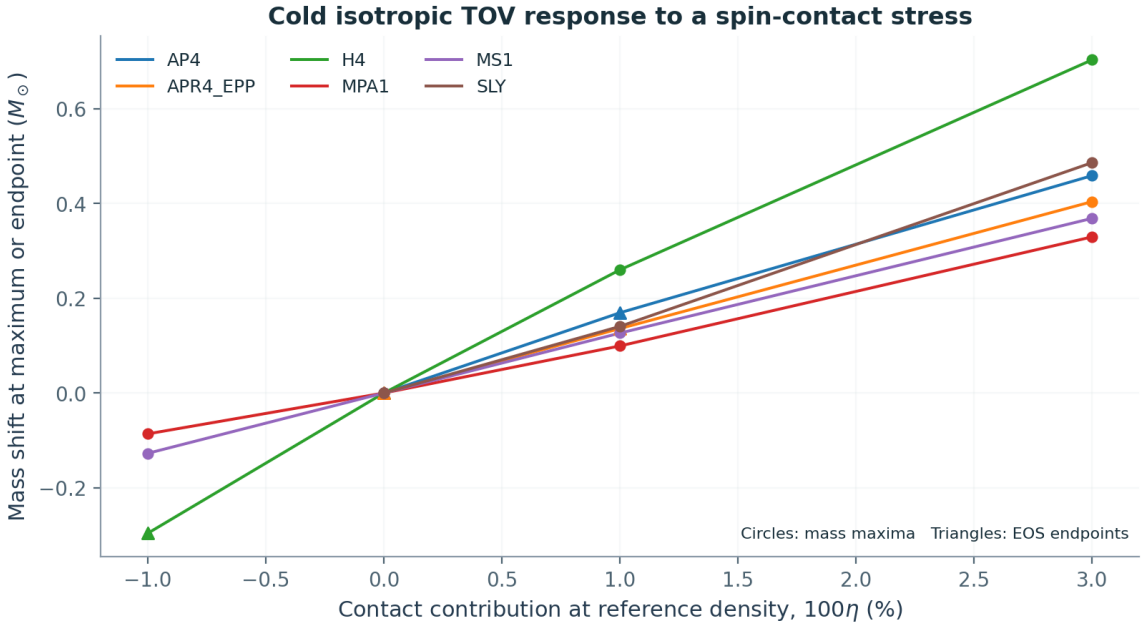

Figure 16. Sensitivity of six tabulated EOS sequences to added contact stress. EOS endpoints and actual mass maxima are marked separately.

rotation and shape changes. The appropriate extension matches conserved baryon mass and angular momentum, then compares magnetized equilibria, turning points and actual modes, with uncertainties from the field geometry.

17.2 Out-of-galaxy transfer of the spin–entropy model

The original galaxy argument contains a local divergence proposal and a separate positive halo-density profile. In spherical symmetry the literal decaying radial flux gives $M_{\rm div}(< r) = 4\pi C r^2 e^{-r/r_s}$. Test this shape using R_d from disk photometry and a baryonic scale $M_b^\star = 0.5L_{3.6} + 1.33M_{\rm HI}$ in solar units. The mass scale is a fixed photometric and atomic-gas proxy for the additional term. The baseline rotation curves still use the radius-dependent gas, disk and bulge contributions. With $x = r/R_d$ and $\ell_r = r_s/R_d$, the two hypotheses are

$$\begin{aligned} v_{\rm flux}^2 - v_{\rm bar}^2 &= \frac{G\eta_g M_b^\star}{r}\, x^2 e^{-x/\ell_r}, \\ v_{\rm exp}^2 - v_{\rm bar}^2 &= \frac{G\eta_g M_b^\star}{r}\, \frac{\gamma(3, x/\ell_r)}{\Gamma(3)}. \end{aligned} \tag{31}$$

Fit only one amplitude η_g and scale ℓ_r to each training subset. Each held-out galaxy is entirely absent from fitting, in contrast with the earlier experiment that withheld exterior radii and retained interior data from the same galaxy. The training residual weights quoted diagonal velocity errors after adding 5 km/s in quadrature and assigns equal influence per point count. The reported test score is each galaxy's unweighted velocity RMSE and the median across galaxies. The comparison RAR uses the published fixed function whose literature calibration used SPARC. It supplies a reference relation on this sample. Both the calibration overlap and the absence of independent magnetic measurements limit the interpretation. The flux-model amplitude is fit from orbits. A

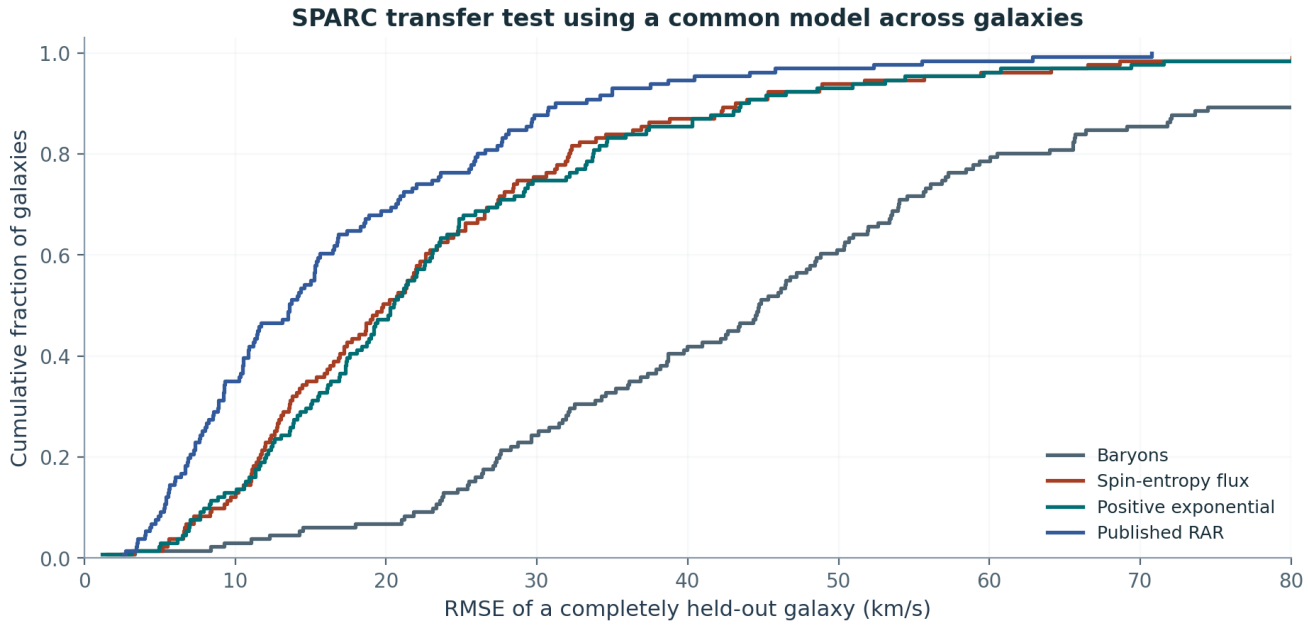

Figure 17. Five-fold prediction with all radii of a test galaxy withheld. Curves farther left have smaller held-out velocity error.

successful physical derivation would predict the amplitude from a matter and field model, and reproduce light deflection with the same parameters.

The divergence imposes $\lim_{r\to\infty} M_{\mathrm{div}}(<r) = 0$ for this profile. Its *density* changes sign at $r = 2r_s$, while its finite enclosed mass is positive if $C > 0$. A positive mass in a finite orbit band can thus be fit even when the asymptotic correction vanishes. The proposed microscopic carrier and the stress that gravitates remain open. Models that use a different current boundary condition or a nonlocal response require their own calculation.

17.3 Time-domain prediction and instrument response

The rebuilt timing pipeline first tests the published $B\Omega$ line with the same normalization and with adopted polar-field and orientation conventions. The extended replay uses three seven-year windows on the frozen ATNF records, selecting pulsars that already had at least one recorded glitch when each window began. The positive cases are later recorded recurrences. Spin data are from the modern catalog and detection exposure varies. These results describe retrospective ranking. Individual pulsars can enter more than one window, so the windows are not independent samples for an error bar. When both timing variables come from $P, \dot{P}$, the $B\Omega$ and inverse-age ranks are identical by algebra and in all three runs. A ground-level prediction of a distinct spin effect needs comparable monitoring and independent field information.

Fermi's event data permit an injection check for the merger precursor proposal. Use the declared 10–50 keV channel-center selection and a 4.5 ms window with a ± 50 ms timing scan. The count statistic is the largest count across the same 101 offsets on the event and each off-source control. Uniform source arrival times within a trial 4.5 ms window constitute a specific signal model. The injection uses detector counts and samples photon numbers from a Poisson distribution. An astrophysical flux or luminosity requires an assumed spectrum, the detector response, geometry and arrival timing. The Fermi control burst after coalescence is included in the base run as an

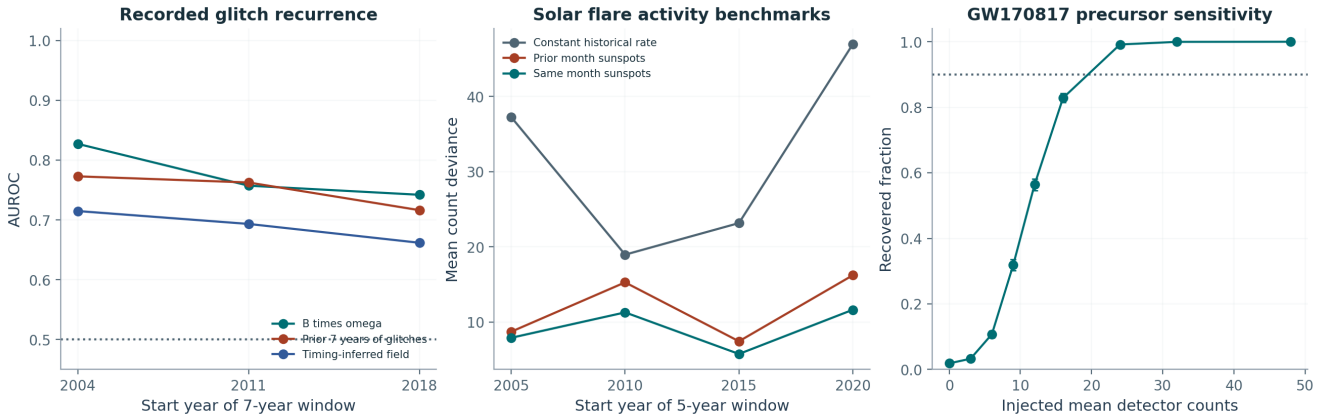

Figure 18. Chronological glitch and solar checks plus the injection-derived detectability of a specified Fermi precursor count signal.

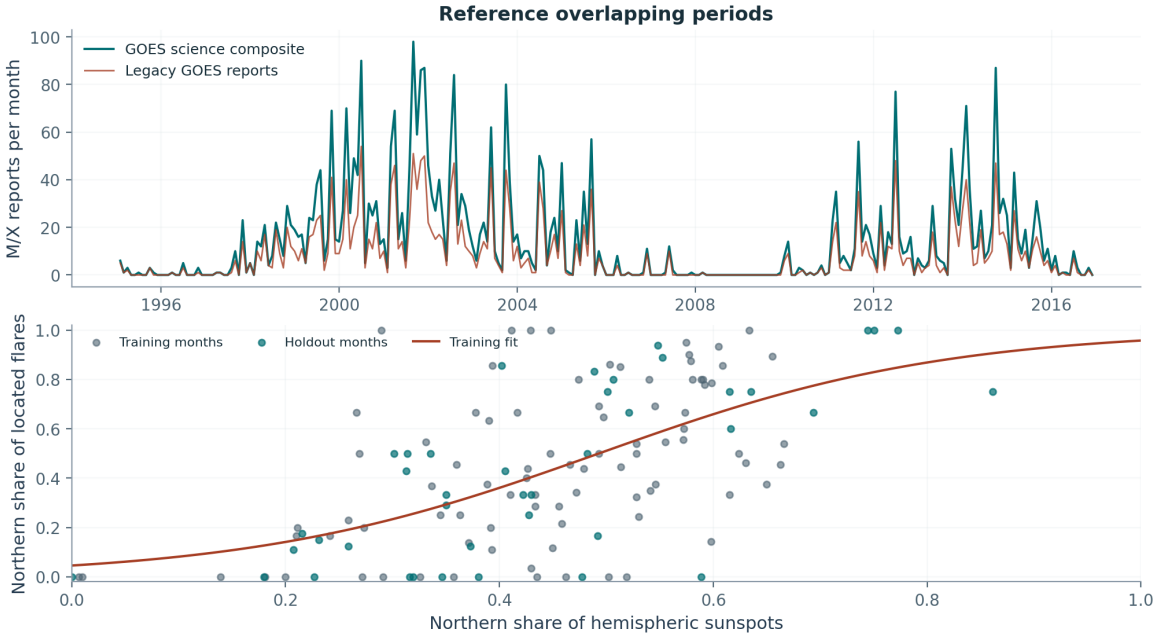

Figure 19. Legacy and science GOES overlap and a held-out check of the northern share of located flare reports.

instrument and time-origin check. R21

The solar time tests compare forward-blocked count predictions based on earlier months and on the same month as the flare count. Current sunspots are a descriptive covariate for the same period. The historical release and hemispheric rerun bring in two additional snapshots. Use overlap counts for catalog comparisons and a binomial northern-share model for events with an explicit non-equatorial heliographic designation. Instrument changes, unlocalized reports and region visibility affect which events enter. Sunspot counts constrain activity correlations. A direct ESFD flare test needs measured local B, vorticity or helicity and sufficient cadence to compare predictions to independent active-region transitions.

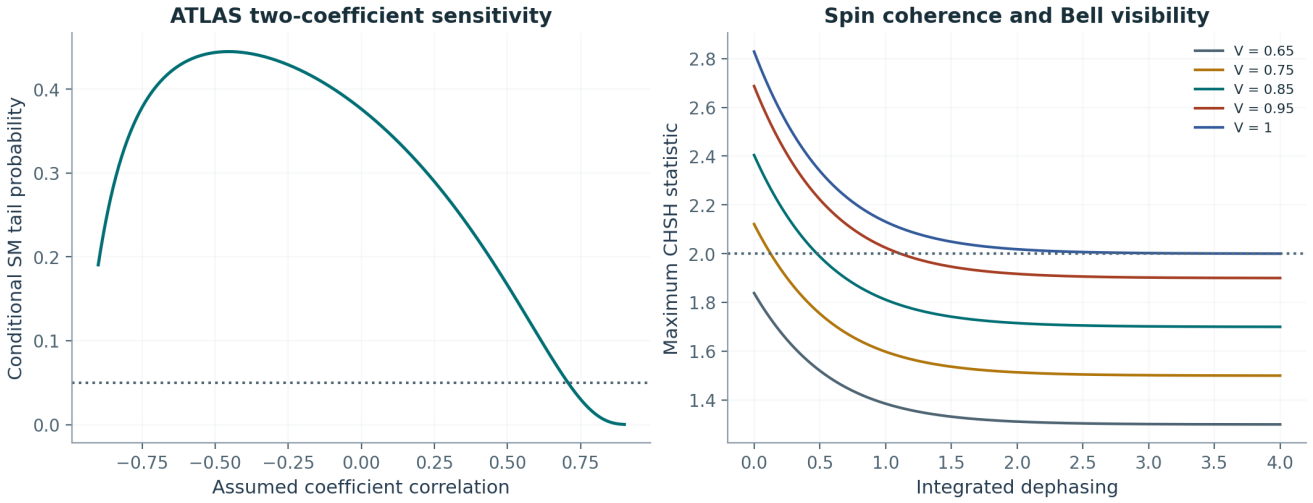

Figure 20. The upper-level collider comparison depends on the coefficient covariance. The companion panel shows the distinct effect of dephasing and visibility on Bell violation for the benchmark state.

17.4 Observable coherence and collider sensitivity

The shared-field picture of quantum measurement can be tested by specifying which degrees of freedom store correlations and how a measurement couples to them. An operational benchmark is a dephased singlet plus a fraction $1 - V$ of white noise. Let D be integrated spin dephasing with $\rho_{01,10} = -Ve^{-D}/2$. In the basis selected by the dephaser the correlation matrix is $\mathrm{diag}(-Ve^{-D}, -Ve^{-D}, -V)$. Positivity follows from the convex state preparation with $0 \le V \le 1$, $D \ge 0$. The two largest eigenvalues of $T^\top T$ give

$$S_{\max} = 2V\sqrt{1 + e^{-2D}}, \qquad \mathcal{C} = \max\{0,\, Ve^{-D} - (1 - V)/2\}. \tag{32}$$

Here $S_{\max}$ is the optimized CHSH statistic and $\mathcal{C}$ is concurrence. The covariance-based calculation in the companion code verifies the first expression at 805 state settings. For $D = 0$, Bell violation requires $V > 1/\sqrt{2}$. Entanglement and a particular Bell violation are experimentally distinguishable. The dephasing map preserves local marginals and supplies a measurable locus for a proposed excess D as field, orientation, dwell time or spin composition changes. A new ESFD noise term would have to predict both this locus and its frequency and species dependence independently of the visibility. R61

For the CERN claim, use a common Standard Model baseline and an ESFD prediction for a differential distribution at fixed fiducial cuts. Fitted spin correlations use the joint quantum decay amplitude including both propagator denominators and interference. The comparison coefficients in the archive are published summaries. The covariance sensitivity scans ρ for the reported pair while holding marginal uncertainties fixed, and reports the conditional statistic $d^\top \Sigma(\rho)^{-1} d$. The correlation scan exposes the effect of omitted covariance on the inference. An actual significance needs the measured covariance and the correlated theoretical and detector errors. In particular the scan cannot serve as evidence for a particular off-shell ESFD vertex. A predictive extension fixes an operator and maps it to several independently measured helicity or angular moments as functions of the reconstructed dilepton masses. A5 R44 R45

18 Limits on proposed macroscopic extensions

18.1 Torsion, anisotropy and a possible bounce

The archive includes a proposal that high-density spin interactions create a cosmological or interior turnaround. A homogeneous negative stiff stress scales like a^{-6}, as does positive Bianchi I shear in the absence of anisotropic sources. To test robustness of the idealized bounce, add shear to the dust model with a nonnegative constant vacuum contribution. With $y = a^3$ and time in units of the inverse reference Hubble scale, the constraint and its positive root are

$$\begin{aligned} \frac{\dot{y}^2}{9} &= \lambda_v y^2 + y - (1-\Sigma), \\ y_b &= \frac{2(1-\Sigma)}{1+\sqrt{1+4\lambda_v(1-\Sigma)}}, \qquad \Sigma < 1, \quad \lambda_v \geq 0. \end{aligned} \tag{33}$$

Σ is the ratio of the positive shear coefficient to the negative spin coefficient at the reference scale. It is constant in this toy system. A positive-volume bounce occurs only when the spin term wins. For $\lambda_v = 0$, $y = y_b + 9t^2/4$. The nonnegative vacuum contribution changes the bounce volume and later expansion without changing the sign criterion. As Σ approaches one from below, the minimum volume shrinks and the curvature scale grows, eventually testing the assumed EFT cutoff. Spin transport, inhomogeneity and anisotropic stress can change the powers and the sign balance. The analytic trajectories and numerical constraint checks in the ZIP cover all three vacuum choices. R38 R62

A credible black-hole or white-hole version needs global matching of interior and exterior geometries, induced metric and extrinsic curvature on the boundary, or a specified physical surface layer. In spherical symmetry one can compare null expansions $2\partial_{\pm} r/r$ using areal radius r and report where they change sign. For a rotating remnant a homogeneous dust metric cannot define those surfaces or preserve the necessary angular-momentum and stress budgets. A daughter-universe hypothesis additionally requires causal connectivity and an observable consequence for an exterior or descendant observer. A proof of a local positive minimum of a settles none of those boundary questions.

18.2 Wave organization, vacuum pressure, and boundary observables

The archive describes recurring waves and shells across atomic, galactic and larger scales. A direct physics test distinguishes a feature in a power spectrum from a dynamical recurrence. One example workflow fixes physical separation bins and a predicted phase relation between independent observables, computes the complex cross spectrum in a common frame and window, and propagates instrument and sampling effects through a null that preserves each field's auto spectrum. A phase relationship or shared dispersion law can reveal coupling where images alone are ambiguous. A cosmological claim further needs a transfer function accounting for redshift, flux freezing and gravitational potential. A galaxy handedness claim can be held out across survey fields and tested with mirror images to check classification symmetry before selecting any preferred axis. A6 R34 R36 R40

An isotropic average of a statistically tangled, source-free magnetic field has $p_B = u_B/3$ and $u_B = B^2/(2\mu_0)$ in SI units. The sign of $u_B + 3p_B$ is positive. A proposed accelerated expansion therefore

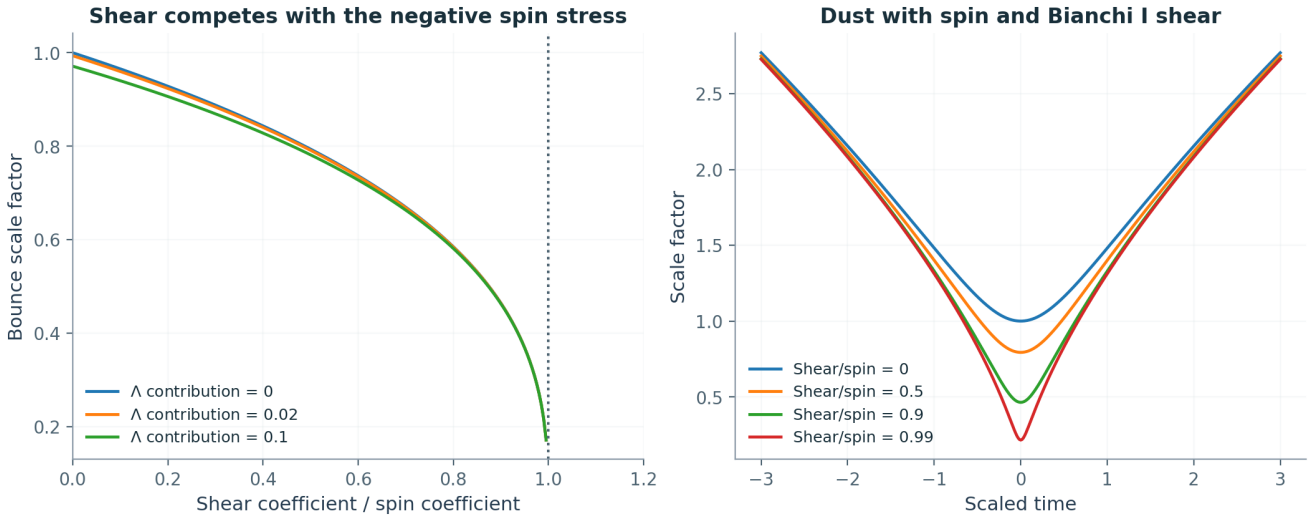

Figure 21. Analytic dust-spin-shear trajectories. Increasing shear lowers the bounce volume and removes the positive root when the shear coefficient equals the spin coefficient.

requires additional spin-dependent stress or a new vacuum response. The archived benchmark compares positive Maxwell energy with $u_\Lambda = \Omega_\Lambda\, 3H_0^2c^2/(8\pi G)$ for a declared reference cosmology. Equal energy magnitude still leaves the pressure and perturbation dynamics to explain. For a dynamical model, simultaneous observables include $H(z)$, matter growth, CMB lensing and the two scalar metric potentials, all computed with shared parameters and consistent initial conditions. R36 R37

18.3 Time, inertia, Earth and resonance claims

An archival clock law writes $d\tau = dt\, \exp(-\alpha S_{\mu\nu}F^{\mu\nu})$. If α is the coefficient in the June action, αSF is an energy density in natural units. The exponent then needs an explicit energy-density normalization. A covariant alternative would give matter a physically defined effective metric or a species-dependent clock Hamiltonian with calibrated sensitivities. Distinguish a common clock rate shift from a shift of one atomic transition. Sampling both clock species at the same location, in two field magnitudes and in reversing orientation, exposes common and differential responses. Coordinate time, proper time and subjective perception describe different variables. An observer-feedback proposal requires an operational state preparation or output and a change to the measured probabilities.

For Earth, a perturbation in an existing magnetic field changes Maxwell pressure by $\Delta(B^2)/(2\mu_0)$. At illustrative $50\ \mu$T background and $1\ \mu$T perturbation the change is around 4.02×10^{-5} Pa. This tests the direct stress route at the assumed field strength. A triggering hypothesis about a metastable fault or a chemical pathway needs its own gain, lag and directional prediction, matched to measured geology and calibration. A prospective study needs time-matched negative controls, treatment of aftershock clustering and solar or geomagnetic covariates known at the forecast time. The presence of nearly coincident events alone supplies no energy, timescale or transport model. For solar flares, the same separation between driver and triggering conditions applies. Global rotation and active-region shear have different gradients and time dependence.

For low-frequency resonance, an isolated loss model gives $\dot{U} = P_{\text{drive}} - \omega_0 U/Q$. Measuring both

the coupling and Q gives a bound on the steady stored energy, $U = QP_{\text{drive}}/\omega_0$. A field-frequency coincidence without a calibrated drive does not determine power. Even a large internal stored field can exchange momentum with supports, radiation and cables. A force or inertial-device claim needs a closed-system momentum measurement, field toggling, heating controls, and real independent readouts before it can be assigned a new mechanism. The historical and speculative topics are mapped to specific observables and conservation relations. Their attribution depends on the original archive, including the missing drafts in the source register. A6 A7

19 Maxwell, Tesla and the ESFD standing wave

The full companion calculation is archived in **provenance/**. A10

Maxwell published twenty component equations in 1865. They included the potentials, electric displacement, conduction and continuity alongside the field equations. Heaviside later reformulated the theory in vector form. In Maxwell's own §100, the field equations propagate transverse disturbances under the assumptions of the derivation. He then explicitly asks about longitudinal oscillations and considers them possible if one adds an electric medium with its own inertia. That passage gives a precise historical question to recover from the original formulation. Maxwell, 1865, §70 · Maxwell, §§95–100 · Heaviside reformulation

Maxwell's groups	Role in a modern formulation
A and C	The total current combines conduction and displacement. Their combination gives $\nabla \times \mathbf{H} = \mathbf{J} + \partial_t \mathbf{D}$ in SI notation.
B and D	Magnetic induction comes from the curl of the vector potential. In the medium at rest the electric field comes from the scalar potential and the time derivative of the vector potential. Taking their curl or divergence gives Faraday's law and the magnetic divergence constraint.
E and F	Dielectric polarization and electrical resistance are material relations. Treating these relations as dynamical can change the modes of the coupled system.
G and H	Electric charge is related to displacement by Gauss's law, and charge and conduction current obey continuity.

This comparison follows the roles of the original groups with present-day units and signs. The potentials can still be used explicitly as $F_{\mu\nu} = \partial_\mu A_\nu - \partial_\nu A_\mu$. A new polarizable or spin-carrying medium needs a constitutive equation of its own. Maxwell, 1865, groups A–H

Tesla's 1900 article describes a stationary electrical wave through the analogy of a signal and an echo. His 1919 explanation discusses transverse and longitudinal excitation around a conductor and uses Earth as the conductor in his transmission proposal. These public accounts provide historical leads for the standing-wave and material-response cases. A universal three-wave law and its alleged removal remain unverified. Tesla, *The Problem of Increasing Human Energy* · Tesla, *The True Wireless*

19.1 Which waves are independent?

The Faraday tensor $F_{\mu\nu}$ has six components, encoding $\mathbf{E}$ and $\mathbf{B}$. In a source-free vacuum plane wave the equations require $\mathbf{k} \cdot \mathbf{E} = 0$ and $\mathbf{B} = (\mathbf{k} \times \mathbf{E})/\Omega$ in natural units. The two remaining independent electric amplitudes are the two photon polarizations. Writing a real field in terms

of complex exponentials introduces a conjugate negative-frequency piece. Reversing the direction of travel at the same positive frequency is a different operation. Quantum fluctuations of the electromagnetic vacuum are correlations of the quantized field, with each free transverse mode quantized as an oscillator. A field component can have zero vacuum mean and a nonzero two-point correlation. The classical equations give the mode structure for that calculation. Tong, *Quantum Field Theory*, §§6.1–6.2 · Cambridge, *Introductory Quantum Optics*

19.2 The wave–anti-wave overlap

For this calculation, an anti-wave is an equal co-polarized wave travelling in the opposite direction. Take $\Omega = k$ and work in $c = \hbar = 1$ units with metric signature $+---$. Define $C_{\pm} = \cos(kz \mp \Omega t)$. The sign flip of the magnetic part follows from the reversed propagation direction.

$$\begin{aligned} \mathbf{E} &= E_0(C_+ + C_-)\,\hat{\mathbf{x}}, \\ \mathbf{B} &= E_0(C_+ - C_-)\,\hat{\mathbf{y}}, \\ F_{\mu\nu}F^{\mu\nu} &= 2(\mathbf{B}^2 - \mathbf{E}^2) = -8E_0^2 C_+ C_- \\ &= -4E_0^2\left[\cos(2kz) + \cos(2\Omega t)\right]. \end{aligned}$$

Either wave by itself gives $F_{\mu\nu}F^{\mu\nu} = 0$. Together they generate a nonzero field invariant, with a fixed spatial pattern and a modulation at twice the wave frequency. This overlap is a precise mathematical place for the idea in the ESFD action. It becomes a new physical response only if another dynamical field couples to it.

19.3 Pumping a dynamical spin mode

Use $Z(s) = e^{-gs^2}$ and $V(s) = m^2 s^2/2 + \lambda s^4/4$ from the spin-built model in the master report. The field s is a canonically normalized collective spin amplitude and $g > 0$ is a specified coupling. The equation in a prescribed electromagnetic background is

$$\Box s + V'(s) + \frac{1}{4}Z'(s)F_{\mu\nu}F^{\mu\nu} = 0.$$

Near $s = 0$, $Z'(s) \simeq -2gs$. The overlap changes the oscillation frequency through the coefficient of s. Project on one spatially uniform spin mode over an integer number of standing-wave periods. The spatial cosine then averages to zero in that mode. With off-resonant spatial sidebands neglected and both electromagnetic waves maintained by an external drive, its amplitude obeys

$$\ddot{s} + \left[m^2 + q\cos(2\Omega t)\right]s = 0, \qquad q = 2gE_0^2.$$

The first resonance is near $\Omega = m$. The weak-pump growth rate at resonance is $|q|/(4m)$. I propagated the two independent solutions for each pump period and computed growth from the larger Floquet multiplier. For an illustrative $q/m^2 = 0.08$, the first growth interval is $0.97990 < \Omega/m < 1.01990$. At its center the calculated rate is $\gamma/m = 0.0199963$. The numerical transfer determinant stayed within 1.9×10^{-14} of unity across 241 frequency settings.

The same quadratic model advances the quantum covariance of a single normalized oscillator from its unpumped ground state. Let U be the real canonical transfer matrix for one pump period. After N periods at the same pump phase, the covariance is $C_N = U^N(U^N)^\top/2$. Switch off

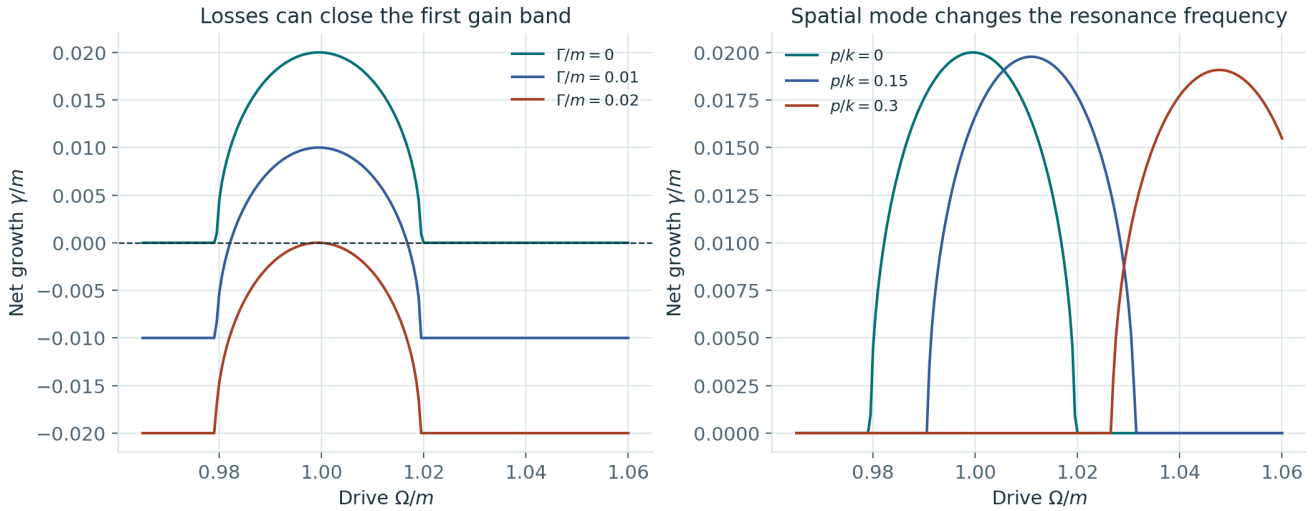

Figure 22. The first growth band with retained spatial sidebands. Left holds Bloch momentum zero and adds damping. Right shows the shift due to spatial momentum with zero damping.

the prescribed drive abruptly and measure occupation in the original oscillator basis. This gives $\langle n_s \rangle = (\operatorname{tr} C_N - 1)/2$. At $\Omega = m$ and $N = 25$ this yields **5.29 spin-mode quanta on average**, conditional on the assumed oscillator and drive. The external electromagnetic waves supply the energy. A classically exact initial state with $s = \dot{s} = 0$ stays at zero under this homogeneous equation. In the quantized model the ground-state variance supplies the initial fluctuations.

19.4 Spatial sidebands and losses

The uniform-mode approximation can be checked with the full linear equation for the prescribed pump. Keep both parts of the invariant and add a phenomenological loss rate Γ that is constant over a cycle.

$$\partial_t^2 s - \partial_z^2 s + 2\Gamma \partial_t s + \left[m^2 + q\cos(2kz) + q\cos(2\Omega t)\right] s = 0. \tag{34}$$

The spatial and temporal drives separate in this idealization. On a periodic spatial cell, allow Bloch momentum p and expand in $e^{i(p+2nk)z}$. The spatial matrix has diagonal $m^2 + (p + 2nk)^2$ and off-diagonal $q/2$ between adjacent Fourier components. For $p = 0$, the two components at $\pm 2k$ shift the lowest stiffness by $-q^2/(8k^2)$ at leading nonzero order. The computed lowest eigenvalue includes all sidebands retained by the Fourier truncation. The limit $p = 0$, $q = 0$ recovers m^2.

For a spatial eigenvalue ϵ_j^2, put the temporal amplitude equal to $e^{-\Gamma t} y_j$. The equation for y_j is a Mathieu oscillator with unmodulated stiffness $\epsilon_j^2 - \Gamma^2$. Its principal growth from one-period transfer is $\Omega \operatorname{acosh}(|\operatorname{tr} U|/2)/\pi$ when $|\operatorname{tr} U| > 2$. Subtract Γ to obtain the physical growth of the amplitude. The new run compares the instability band to independent Mathieu characteristic values and repeats the spatial diagonalization at different Fourier cutoffs. The dissipative model measures classical linear growth. A quantum bath description would add its noise to the finite-loss process.

19.5 When a photon probe sees a third branch

The ordered case is a separate small-signal experiment. Establish a background spin amplitude $s_0 \neq 0$ and magnetic bias $\mathbf{B}_0$, then perturb with a weak electromagnetic probe. One transverse photon polarization mixes with the spin oscillator through $Z'(s_0)\,\mathbf{B}_0\cdot\delta\mathbf{B}$. The other photon polarization propagates with $\omega^2 = k^2$. Define $X = \omega^2 - k^2$, $M^2 = V''(s_0) + B_0^2 Z''(s_0)/2$ and $\mu^2 = B_0^2 Z'(s_0)^2/Z(s_0)$. With θ the angle between propagation and the bias, the complete dispersion determinant is proportional to

$$X\left[X(X-M^2) - \mu^2 k^2 \sin^2\theta\right] = 0.$$

The two mixed solutions and the remaining photon polarization give three normal modes in this reduction. At nonzero mixing they have different frequencies if the roots are stable. The upper branch approaches a pure spin mode as the mixing vanishes. In a photon probe its fractional weight follows from the residue of $(X - M^2)/[X(X - M^2) - \mu^2 k^2 \sin^2\theta]$.

$$W_+^{(\gamma)} = \frac{1}{2}\left(1 - \frac{M^2}{\sqrt{M^4 + 4\mu^2 k^2 \sin^2\theta}}\right).$$

With the master report's illustrative $B/B_0^{\text{crit}} = 1.2$, $B_0^{\text{crit}} = m/\sqrt{g}$, and $\lambda/(gm^2) = 2$, this weight at $k = m$ is **0%** along the bias, **13.75%** at 30°, **24.04%** at 60°, and **26.72%** across the bias. The calculation independently diagonalized the two-field matrix and agreed with the residue to floating-point precision. The weight is a squared photon component of a normalized mode. A measured transmission or power requires an instrument and material model. Standard QED already allows field-dependent nonlinear optical effects, and materials and cavities can add their own resonances. A discriminating test would follow the extra resonance in frequency, spin bias and angle using the same coefficients. Spin-built exponential response, Eq. 27 · PVLAS and its QED baseline

19.6 Why the cosmic claim needs a second calculation

The tensor coupling and the bounce solve different dynamical questions. A minimally coupled Maxwell-plus-canonical-spin action with $Z(s) > 0$ satisfies the null energy condition. For a null vector n^μ, let $v_\alpha = n^\mu F_{\mu\alpha}$. The stress contraction is

$$T_{\mu\nu}n^\mu n^\nu = (n^\mu \partial_\mu s)^2 - Z(s) v_\alpha v^\alpha \geq 0,$$

because v_α is orthogonal to a null vector and hence spacelike or null. In ordinary Einstein gravity with a spatially flat FLRW geometry, $\dot{H} = -4\pi G(\rho + p) \leq 0$. A bounce there requires $\dot{H} > 0$ at $H = 0$. The ESFD bounce example in the master report introduced an additional negative spin–torsion stress that can overcome the shear term. Connecting the local wave calculation to a cosmic solution requires deriving such a stress from the microscopic spin state and checking its regime of validity. A white hole or daughter universe further requires a global spacetime solution with the appropriate horizon and matching conditions. Flat-bounce energy condition · Spin–torsion bounce and shear

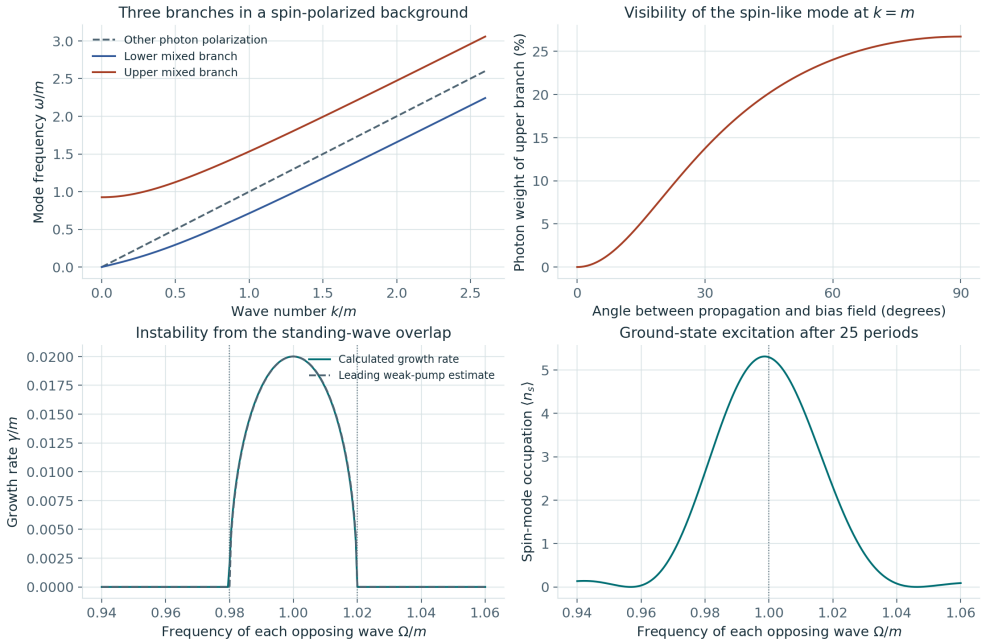

Figure 23. Calculated normal-mode frequencies, photon weight of the spin-like branch, and numerical growth and excitation of the proposed uniform spin mode under two opposing waves. The upper panels use an ordered bias. The lower panels use a zero-mean spin field and a prescribed standing-wave pump.

20 Force balance, curvature, and the ESFD coupling

20.1 What cancels in the electromagnetic calculation

There are three distinct quantities a proposed cancellation can target. An upward force can balance a downward acceleration for a selected body. The metric can change the relative acceleration of freely falling bodies. The source stress can also change the sign of cosmic acceleration in a homogeneous geometry. In weak gravity these are respectively a force law, a Riemann curvature measurement, and a combination of energy density and pressure.

The wave overlap supplies a tunable quantity in the first category whenever matter responds directly to a spin field. Let the two electric polarizations have relative angle φ. Put $I = F_{\mu\nu}F^{\mu\nu}$ and $J = F_{\mu\nu}\widetilde{F}^{\mu\nu}$, with $J = -4\mathbf{E}\cdot\mathbf{B}$. Write $C_\pm = \cos(kz \mp \Omega t)$ for the counterpropagating phase factors. Then

$$\begin{aligned} I &= -8E_0^2 \cos\varphi\, C_+C_-, \\ J &= -8E_0^2 \sin\varphi\, C_+C_-, \\ u &= \tfrac{1}{2}(\mathbf{E}^2+\mathbf{B}^2) = E_0^2(C_+^2+C_-^2), \\ S_z &= E_0^2(C_+^2-C_-^2), \qquad \partial_t u + \partial_z S_z = 0. \end{aligned} \tag{35}$$

The code evaluates the stress and flux on a periodic grid and verifies the energy continuity equation using spectral derivatives. Moving from parallel to orthogonal electric polarizations eliminates I for the ideal pair and maximizes J. The energy, instantaneous energy flux, and cycle-mean energy density are unchanged by this operation. With equal incident amplitudes the latter is E_0^2 at

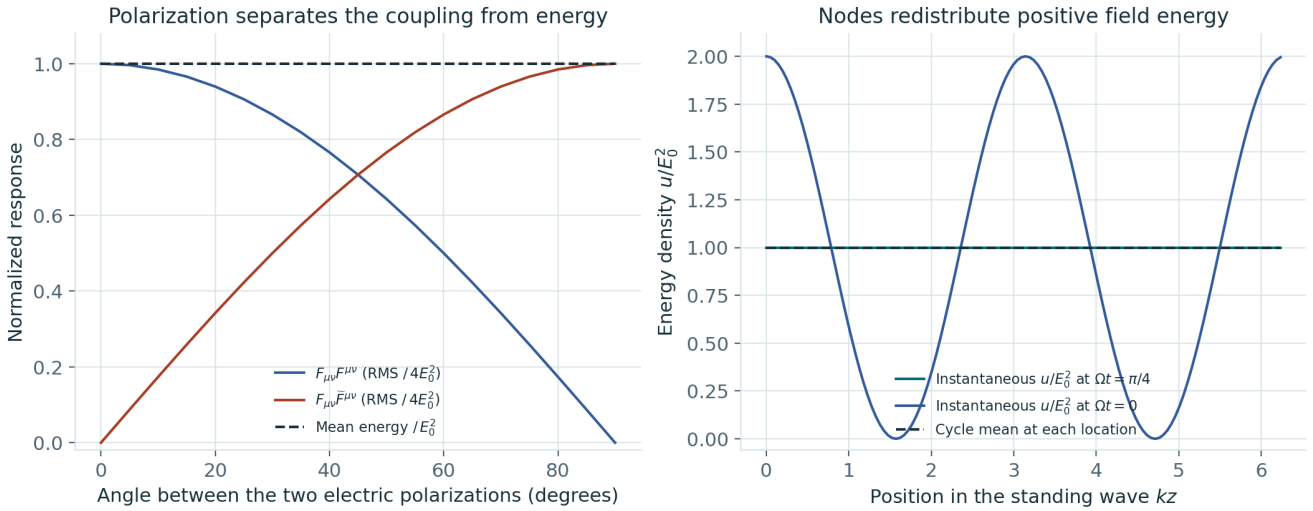

Figure 24. Changing polarization transfers the overlap from one invariant to the other while the energy remains fixed. An instantaneous node and the time-mean energy are shown on the right.

every z. Transverse stresses can vary with position. Averaging over both the spatial and temporal periods gives diagonal stress components $(T_{00}, T_{xx}, T_{yy}, T_{zz}) = (E_0^2, 0, 0, E_0^2)$.

For positive $Z(s)$ and a canonical spin amplitude, the Maxwell and spin kinetic terms satisfy $T_{\mu\nu}n^\mu n^\nu \geq 0$ for any null vector n^μ in the minimal Einstein branch. The vanishing trace of classical Maxwell stress means the Ricci **scalar** can vanish with electromagnetic energy present. The Ricci tensor and full curvature generally remain nonzero. For a localized, stationary weak-gravity system, the active source is the integral of $(T_{00} + \sum_i T_{ii})/c^2$ in an orthonormal rest frame. In a closed apparatus with localized stress, integrating $\partial_j(x^i T^{jk}) = T^{ik}$ gives vanishing integrated total spatial stress. The far-field mass increment then follows the change in the complete apparatus energy divided by c^2. Reflecting walls, supports and steady stress belong in that calculation. R63

This gives a numerical scale for gravity driven directly by stored energy. Balancing g at one point by the pull of an ordinary compact source a metre away requires $E = gc^2r^2/G$ in the monopole estimate, with the source positioned to pull in the opposite direction. Such a balance has its own tidal gradients. Quantum fields can contribute a renormalized interaction energy of either sign. The ideal-plate Casimir value $E_C/\mathcal{A} = -\pi^2\hbar c/(720d^3)$ is a useful benchmark. Its gravitational contribution is part of the total energy of the plates, supports and field. R64

A homogeneous canonical spin scalar adds $\epsilon_s + 3p_s = 2\dot{s}^2 - 2V(s)$ and $\epsilon_s + p_s = \dot{s}^2$ in natural units. A sufficiently positive potential can drive homogeneous cosmic acceleration. The same scalar obeys the null energy condition, so it cannot by itself give $\dot{H} > 0$ in a spatially flat Friedmann bounce within general relativity. The sign of this cosmological source and the sign of the force in Eq. (36) are governed by different terms in the equations.

20.2 How the spin oscillator could acquire a gravitationally relevant charge

An acceleration opposed to ordinary gravity can be calculated if matter has a separately specified scalar charge. In the weak-field illustration, let body i have mass $M_i(s)$ and dimensionless charge $\beta_i = M_{\rm Pl}\partial_s \ln M_i$ at the operating background. Use the reduced Planck mass $M_{\rm Pl}^{-2} = 8\pi G$ in natu-

ral units. In the source-free regime a linear perturbation of the canonical spin amplitude has a positive kinetic term and a mass setting its range L_s. When coupled to nonrelativistic matter, the static linear equation and point-source potential are

$$\begin{aligned}(\nabla^2 - L_s^{-2})\,\delta s &= \frac{\beta_S}{M_{\rm Pl}}\rho_S,\\ U_T(r) &= -\frac{GM_SM_T}{r}\left[1+\alpha_{ST}e^{-r/L_s}\right], \qquad \alpha_{ST}=2\beta_S\beta_T.\end{aligned} \tag{36}$$

Equal-sign charges increase attraction. Opposite-sign charges produce a repulsive contribution. The sign difference is possible as a specified material response. A universal canonical scalar with $\beta_S=\beta_T=\beta$ gives $\alpha_{ST}=2\beta^2\geq 0$. The result assumes a stable linear response and an unscreened scalar. In forming a laboratory or astrophysical prediction the charges must come from the action and the states of the materials.

Here is one way to match a charge to the existing $Z(s)F^2$ coupling. Consider a fixed-geometry isolated configuration with electric displacement and magnetic flux held fixed under a virtual change of s. Use stored energies $U_E=\int \mathbf{D}^2/(2Z)\,d^3x$ and $U_B=\int Z\mathbf{B}^2/2\,d^3x$. If additional binding and mechanical responses are negligible in this idealized calculation, the field part of the charge is

$$\begin{aligned}\left.\frac{\partial(M_ic^2)}{\partial s}\right|_{\mathbf{D},\mathbf{B}} &= \frac{Z'(s)}{Z(s)}(U_B-U_E),\\ \beta_i^{(\rm field)} &= \left[M_{\rm Pl}\,\partial_s \ln Z(s)\right]\frac{U_B-U_E}{M_ic^2}.\end{aligned} \tag{37}$$

This matching is a new result for the stated boundary conditions. A voltage or current source would require including the work and energy of its reservoirs. With $Z=e^{-gs^2}$ and $s_0=0$, $Z'(0)=0$. The original composite wave coupling supplies no linear field charge about that symmetric state. At a biased s_0, the two energy contributions can give opposite signs. An ideal standing wave averaged over full spatial and temporal periods has $U_B=U_E$ and vanishing uniform charge in this approximation. The local, spatially alternating driver in Eq. (35) still exists. Boundary and material responses can change the effective charge, and need separate calculations. The other archived direct tensor coupling has a different spin equation and requires its own matter matching.

20.3 Earth as a finite source

For an exterior point at $r=R_\oplus+h$ and a spherically symmetric, uniformly charged-per-mass Earth, the required radial acceleration is

$$\begin{aligned}g_T(r) &= \frac{GM_\oplus}{r^2}[1+\alpha_{ST}Y(r,L_s)],\\ Y(r,L_s) &= (1+r/L_s)e^{-r/L_s}\,\frac{4\pi}{M_\oplus}\int_0^{R_\oplus}\rho(u)u^2\frac{\sinh(u/L_s)}{u/L_s}\,du.\end{aligned} \tag{38}$$

Here inward is positive. Cancellation at a chosen location fixes $\alpha_{ST}=-1/Y$. The source radius matters because only nearby mass contributes strongly at short range. The benchmark integrates the original PREM density polynomials, including their outer ocean layer, and verifies the kernel

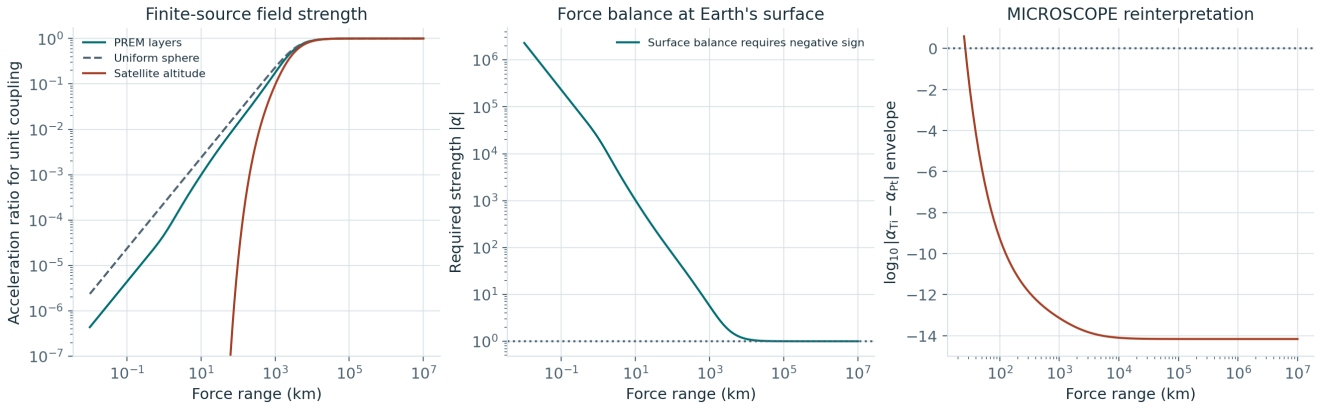

Figure 25. Finite-range acceleration computed from PREM and a homogeneous Earth. A sign-reversed force can produce the given surface balance only for the strengths shown. The third panel reinterprets the published Ti–Pt differential measurement under the unscreened ansatz.

against the exact homogeneous-sphere result $3(x\cosh x-\sinh x)/x^3$ for $x = R_\oplus/L_s$. The numerical evaluation combines the decaying exponent with the hyperbolic function to avoid overflow. The PREM density is a seismic reference model averaged over the Earth. A local short-range experiment needs the site's crust, topography and test geometry. R65 R66

A tuning at one radius still has a residual radial gradient. Holding the coupling fixed at cancellation at $r = r_*$,

$$\left.\frac{dg_T}{dr}\right|_{r_*} = \frac{GM_\oplus}{r_*^2}\frac{r_*}{L_s(L_s+r_*)}. \tag{39}$$

Ordinary metric tides are a separate observable. In a Newtonian Earth exterior the magnitude of the radial tidal gradient is $2GM_\oplus/r^3$. If the scalar modifies test-body acceleration through a conformal matter metric, $\tilde{g}_{\mu\nu} = e^{2\beta_T\delta s/M_{\rm Pl}}g_{\mu\nu}$, the associated shifts in the two weak-field metric potentials have opposite signs. The sum controlling leading light deflection is unchanged by that conformal factor alone. A new stress that changes the Einstein metric can change lensing, and requires including its own stress-energy. Thus an apparent weight change for one body and a change to the gravitational geometry have distinct physical tests.

The MICROSCOPE constraint used here is the published Ti–Pt Eötvös summary with a nominal 710 km altitude. For $a_i = g_N(1+\alpha_i Y)$,

$$\eta = \frac{2(a_{\rm Ti}-a_{\rm Pt})}{a_{\rm Ti}+a_{\rm Pt}} = \frac{(\alpha_{\rm Ti}-\alpha_{\rm Pt})Y}{1+(\alpha_{\rm Ti}+\alpha_{\rm Pt})Y/2}. \tag{40}$$

The quoted illustrative bound uses independent Gaussian statistical and systematic errors in quadrature and a conservative envelope about zero. It constrains the **differential** charge in the small-correction regime at orbital altitude. A hypothetical charge associated with specially prepared spin states absent from that comparison requires a separate free-fall experiment. A short-range or screened field can have a different terrestrial transfer function. R66 R67

21 Dense spin, bounces, and a laboratory discriminator

21.1 The coefficient of the negative stress

The previous ESFD bounce introduced a negative stiff spin component. To test its scale, adopt the published minimal Einstein–Cartan spin-fluid closure

$$\epsilon_s = p_s = -a_{\mathrm{EC}} n_f^2, \qquad a_{\mathrm{EC}} = \frac{\kappa(\hbar c)^2}{32}, \qquad \kappa = \frac{8\pi G}{c^4}. \tag{41}$$

This is a specific averaged spin-fluid model. Its sign and coefficient do not follow from the electromagnetic standing-wave pump. They also need not hold for a differently prepared, correlated many-body state. The numerical benchmark adds Eq. (41) to a cold ideal relativistic neutron gas with $p_F = \hbar(3\pi^2 n_f)^{1/3}$. It separately evaluates the density, null-energy and active-acceleration combinations. R68

Let $r_s = |\epsilon_s|/\epsilon_f$ and $w = p_f/\epsilon_f$ denote the positive matter's equation-of-state ratio with p_f here denoting pressure. Then

$$\begin{gathered}\frac{\epsilon + 3p}{\epsilon_f} = 1 + 3w - 4r_s, \qquad \frac{\epsilon + p}{\epsilon_f} = 1 + w - 2r_s, \\ \frac{\epsilon}{\epsilon_f} = 1 - r_s.\end{gathered} \tag{42}$$

For relativistic matter $w = 1/3$, the three zero crossings are $r_s = 1/2,\ 2/3,\ 1$. They describe onset of accelerated expansion, the null-energy threshold and vanishing density in the flat Friedmann equation respectively. They are different conditions even in a uniform model. The undamped Maxwell-plus-canonical-wave stress does not supply the negative stiff term of Eq. (41).

At high density the ideal gas approaches $\epsilon_f = 3n_f p_F c/4$. With the standard coefficient the formal density zero is $p_F c = 3\sqrt{\pi}\, E_{\mathrm{Pl}}$, where $E_{\mathrm{Pl}} = \sqrt{\hbar c^5/G}$ is the unreduced Planck energy. The numerical solution agrees with this limit. This is beyond the controlled low-energy regime of the assumed action. The original ESFD contact-EOS scan varied an added macroscopic stress. This new comparison tests the actual size of one microscopic normalization against that scan.

The existing dust-and-shear bounce can also be rerun with radiation. Use normalized time and $H^2 = Da^{-3} + Ra^{-4} - (1-\Sigma)a^{-6}$, with $D, R \geq 0$, $D + R = 1$ and Σ the ratio of shear to the positive magnitude of the spin coefficient. A positive root satisfies $Da_b^3 + Ra_b^2 = 1 - \Sigma$. In pure radiation the solution has $a_b = \sqrt{1-\Sigma}$, while dust gives $a_b = (1-\Sigma)^{1/3}$. The numerical test evolves both branches and a mixture, including consistency with the constraint. This remains a homogeneous, conditional bounce. To claim a white hole or daughter universe requires a regime where the microscopic calculation is controlled, plus an interior and exterior solution and a physical causal boundary.

21.2 A null measurement that distinguishes the coupler

The local wave calculation produces a test rather than a conclusion about gravity. In the biased regime, the amplitude of the response to I is odd in the spin bias when read out coherently, because

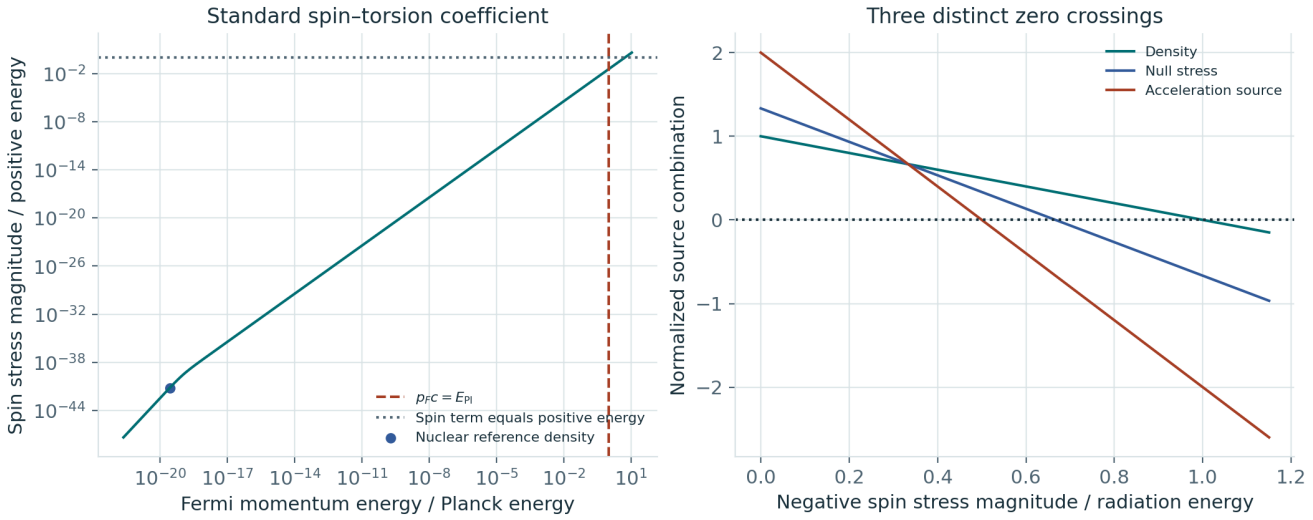

Figure 26. Left compares the exact ideal-gas energy density with the standard spin–torsion normalization. Right separates the three source cancellations under the relativistic-fluid approximation.

$Z'(s_0)$ is odd. Its power is even. Switch between parallel and orthogonal pump polarizations at equal electromagnetic energy, and record the signed response during both spin orientations. A coherent interaction produces an amplitude proportional to $P\cos\varphi$ for spin reversal $P = \pm 1$ in the linear readout model. A suitable four-state contrast is

$$\widehat{A} = \frac{Y_{+,\parallel} - Y_{-,\parallel} - Y_{+,\perp} + Y_{-,\perp}}{2}. \tag{43}$$

This cancels an additive spin-only offset, a polarization-only offset and a common offset. The synthetic run randomizes the state order within a block with within-block correlated noise and drift. Independent magnetic, thermal and polarization monitoring matters because a classical instrumental term with the same joint parity would also survive the contrast. Measure frequency, orientation, pump strength and noise independently of the fit. In particular distinguish the predicted first band from an ordinary material or cavity resonance.

To link a detected spin resonance to a force, first match the static source and probe response coefficients and predict the sign and size of a differential acceleration before testing it. Use an independently monitored reference with a distinct or reversed spin response and measure the position and range dependence. A claim about metric gravity needs a common tidal or lensing prediction rather than just a material force. The wave calculation, galactic acceleration fits, neutron-star equilibria and theoretical bounce then constrain the same coefficients only after an explicit, reproducible mapping across their environments.

21.3 A joint range and frequency prediction

If the resonance and force use the same unscreened relativistic spin field in the same background, the dispersion relation fixes its rest gap from the force range. Let m_{vac} denote its mass in SI. The gap in cycles per second and the corresponding first-band vacuum photon wavelength in the weak-pump, long-spin-wavelength limit are

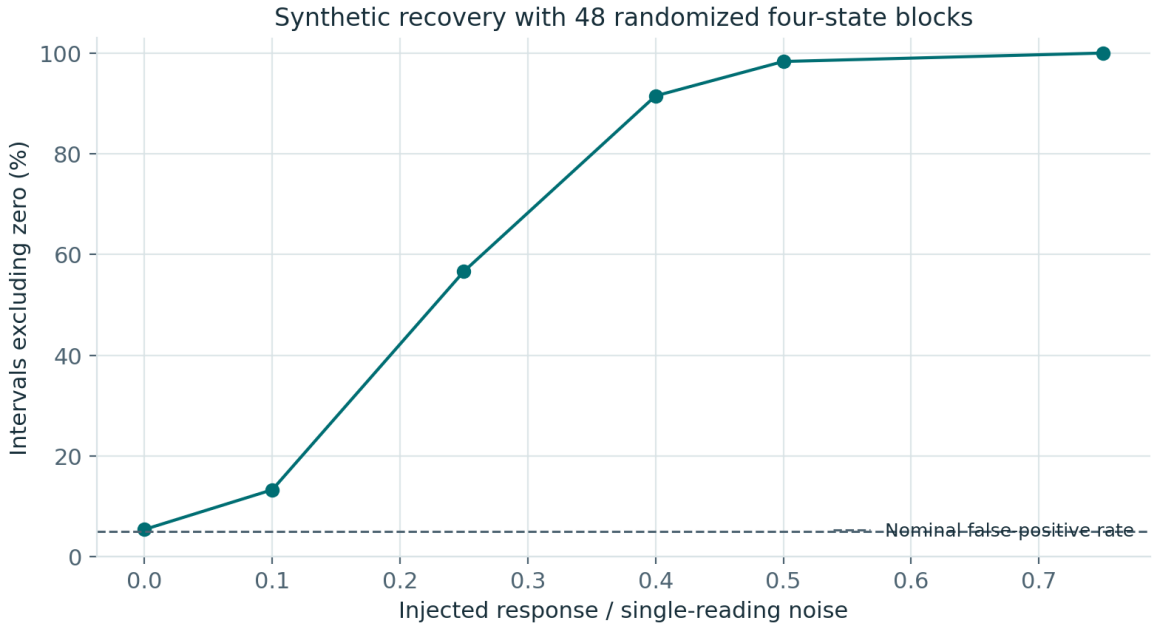

Figure 27. Synthetic null and injection recovery for the four-state test. The horizontal axis is a signal relative to assumed measurement noise, with no inferred ESFD force magnitude.

$$L_s = \frac{\hbar}{m_{\mathrm{vac}} c}, \qquad f_{\mathrm{gap}} = \frac{m_{\mathrm{vac}} c^2}{h} = \frac{c}{2\pi L_s}, \qquad \lambda_{\mathrm{pump}} \simeq 2\pi L_s. \tag{44}$$

This relates two independent measurements with one parameter. A vacuum spin gap of order hertz corresponds to a terrestrial-scale range. A gigahertz rest gap implies a range of only centimetres. An ordinary vacuum standing-wave cavity at the terrestrial gap frequency would require a length of order tens of thousands of kilometres. A compact transducer would need a separately solved geometry, such as a time-dependent near field, with the correct invariant modulation and spin boundary conditions. In a biased or dense medium the effective spin gap and propagation may differ from the vacuum values. A model that uses this effect must compute the medium shift and recover the same underlying mass and coupling when the background changes.

22 Full rerun and extended results

22.1 Input groups reproduced

The November 23 build verified 28 original manifest entries and 2 supplemental archive files. The baseline calculations, expanded spin and data checks, and report figures were regenerated. The legacy zero-byte license entry was retained as provenance and supplies no measurement. Each count below is taken from the rebuilt outputs.

Dataset or calculation	Reproduced coverage and outcome
ATNF timing and HEASARC comparison	ATNF 2.9.0 has 4,503 rows, and 2,898 rows with positive period and period derivative. HEASARC has 4,503 rows. The fixed timing line flags 5 of 22 eligible ATNF AXP tags, with 4 flags outside the tag.
McGill magnetars and epochs	31 catalogued entries. 5 of 22 confirmed, usable timings land above the historical line. 0 sources switch sides at a usable alternate timing epoch.
Pulsar glitches	625 events from 211 sources, plus the three recurrence windows below.
Baseline static neutron stars	540 equilibria across six EOS tables. Computed first static mass maxima range from 2.03 to 2.77 solar masses before imposing the extended EOS screen.
GWOSC and Zenodo PE releases	391 event records. The selected releases provide 189 fiducial remnant spin medians, with a sample median of 0.696.
SPARC	175 galaxies and 3,391 raw radial measurements. Standard eligibility and minimum curve length yield 131 galaxies for the radial holdout and 131 for the full-galaxy transfer exercise.
Fermi photon streams	872,114 photon records across three detectors, with 465,709 in the selected band over the stored streams. The nominal 4.5 ms window has 5 counts versus 8.00 expected background.
Solar	81,721 science-composite flare observations across 381 complete merged months. The extended run incorporates 77,597 legacy GOES records and the SILSO hemispheric series.
Collider and IXPE	6 ATLAS summary rows, 6 CMS scenario rows and 3 IXPE polarization rows. These are published transcriptions. ATLAS shifts in experimental standard-error units are +0.58 and -1.27.

22.2 Spin dynamics and compact-star sensitivity

The printed June static potential folds at $|\beta| = 0.384900$. Its favored branch reaches $u = 2.309$ at $\beta = 10$, consistent with continuing growth after the fold. The spin-built exponential benchmark covers 2,584 field, state and angle settings. At $\ell = 2$ ordering starts at $B/B_0 = 1$. The transverse growing mixed branch starts at $B/B_0 = 1.816$. At $B = 2B_0$ its peak growth rate is 0.0516 in units of

m. The independent-scalar PVLAS check places an onset lower limit of $\simeq 2.67 \times 10^{15}$ G within its own matter-free closure.

The spin-contact run evaluated 42 EOS and closure combinations. It integrated 1,200 configurations and located 18 interior maxima. The other completed sequences end at a table or physical EOS pressure limit. 8 of the twelve negative all-density combinations and 9 of the thirty core-activated combinations fail the continuously admissible EOS test before the sampled NS sequence. The smooth positive $+3\%$ cases have peak or endpoint masses +0.33 to +0.70 solar masses relative to the same EOS at zero added contact. The shifts are sensitivity to a scanned stress term.

22.3 Chronological timing and photon detectability

Window	Eligible sources	Recorded repeaters	Repeaters below fixed line	Timing index AUROC	Prior seven years AUROC	All prior records AUROC
2004–2010	99	53	50	0.827	0.773	0.717
2011–2017	152	46	44	0.757	0.763	0.784
2018–2024	198	19	18	0.742	0.716	0.752

The timing variable gives the same rankings as inverse characteristic age in every window. A useful age proxy can score in rank tests while a fixed cutoff misses most recorded repeaters. A physical recurrence model needs exposure and sensitivity by source and epoch.

The Fermi scan reaches 13 counts at the most favorable tested offset. With 432 matched controls, the first count cutoff with estimated tail area below 5% is 20 counts. The discrete cutoff has a measured control-based tail estimate of 2.1%. The search recovers 56.4% of injections at a mean of 12 added counts and 99.2% at 24. This is a sensitivity calibration for one event and the declared signal and detector band.

22.4 Whole galaxies and exterior radii

The five-fold transfer test covers 131 unseen galaxies and 3,032 radial observations. The pairs are resampled with their fixed out-of-fold predictions. The bootstrap range describes this sample and omits uncertainty from refitting or a different survey selection.

Model	Median curve RMSE (km/s)	Galaxies improving on baryons	Galaxies improving on RAR	Median difference from RAR and 95% paired range (km/s)
Baryons	44.73	0	9	+28.49 [+25.84, +34.37]

Model	Median curve RMSE (km/s)	Galaxies improving on baryons	Galaxies improving on RAR	Median difference from RAR and 95% paired range (km/s)
Spin-entropy flux	19.82	124	36	+6.40 [+3.23, +8.29]
Positive exponential	20.52	125	35	+7.10 [+4.01, +8.56]
Published RAR	13.60	122	0	+0.00 [+0.00, +0.00]

The earlier radial holdout trained on the first 70% of eligible radii within each individual galaxy. Its median outer RMSE is 10.13 km/s for the exponential model added to baryons, 7.84 for NFW and 6.94 for the cored isothermal profile. Both ESFD-motivated shapes improve the baryon-only speeds in most whole-galaxy holdouts. The fixed published acceleration relation scores better overall. The source of the additional stress is still undetermined. Matching the selected outer-point residual using ordinary gravitating Maxwell energy requires a median equivalent rms field of 59,287 microgauss under the spherical approximation.

22.5 Solar archive, collider covariance, and cosmic scales

The GOES releases contain 2,315 legacy M/X reports and 3,855 science-composite events across 263 overlapping months. Monthly ranks correlate at 0.986 and the total counts differ. In the hemisphere check 405 located flares across 41 held-out months contribute. The per-flare log loss is 0.511 for the sunspot-share model and 0.680 for the fixed training share.

GOES M/X count model in 2020–2024	Held-out mean Poisson deviance
Constant historical rate	46.97
Prior month sunspots	16.24
Prior month and prior year sunspots	16.04
Same month sunspots	11.65

At zero assumed covariance the ATLAS pair has a conditional Standard Model tail probability of 0.377. The sensitivity curve depends substantially on the chosen coefficient correlation. A collider test of ESFD requires a supplied matrix element or differential response. A dephasing visibility of 0.85 in the quantum benchmark permits CHSH violation for integrated depth below 0.478.

The spin–shear calculation covers 723 coefficient combinations and 4,812 analytic trajectory points. At zero vacuum term and shear-to-spin ratio 0.9 the scale factor bottoms at 0.464 of the reference. An equal or larger shear term removes the positive-volume turnaround in that model. The Maxwell field at the reference vacuum-energy density is 363.4 microgauss. The illustrative 1 nanogauss field carries only 7.6e-12 of that energy and has the pressure sign of radiation.

The June current calculation with its printed galaxy input gives $B \approx 6.67 \times 10^{-6}$ G and $\chi_{\mathrm{rot}} \approx$

7.08×10^{-36}. The arithmetic correction applies to the specific current, radius and speed. Explaining the orbital residual with a collective mechanism would require field maps, a transfer law and the corresponding metric prediction.

23 Recomputed wave and gravity results

23.1 Electromagnetic and spin response

The companion calculation reproduced the ordered-mode mixing weights. At $k/m = 1$, the illustrative spin-like mode carries a photon fraction of 0% for $\theta = 0^\circ$ and 26.72% for $\theta = 90^\circ$ under the stated bias and parameters. The companion's uniform standing-wave solve reproduced $\langle n\rangle = 5.293$ after 25 pump periods at $q/m^2 = 0.08$ and $\Omega/m = 1$, starting from its specified vacuum state. This is particle production in the effective spin oscillator with an external pump.

The independent stress test used 19 relative polarizations and recovered mean energy density $1E_0^2$ at each angle. The largest dimensionless energy-conservation residual was 1.11×10^{-13}. The spatial and damping sweep evaluated 1,719 combinations of pump, wave number, frequency and damping.

$q/m^2 = 0.08$, central Bloch mode in the undamped periodic domain	Ω/m at lower edge	Ω/m at upper edge
Uniform reference	0.979903	1.019898
Full spatial modulation	0.979477	1.019520

The edges moved down by about $4\times10^{-4}m$ in this example. Increasing the Fourier cutoff changed the lowest spatial eigenvalue by $4.60\times10^{-14}m^2$. At the fixed $\Omega/m = 1$ of the loss scan, the exponent at zero Bloch momentum crosses zero at $\Gamma/m \simeq 0.02000$. A material response therefore needs losses small enough for the proposed gain to survive, or an independently resolvable subthreshold response.

23.2 Conditional force estimates and bounds

The spherical PREM integral gives $M_\oplus = 5.97318 \times 10^{24}$ kg and $g_N(R_\oplus) = 9.82191$ m/s². The solver evaluated 183 ranges. It agrees with the analytic uniform-density kernel to a maximum relative error of 1.89×10^{-11}. Repeating the layered integration at two resolutions changed the result by at most 6.04×10^{-14}. These are numerical checks under a spherical charge-per-mass approximation.

Scalar range	Y at surface	α_{ST} at balance	Residual gradient (s^{-2})	Same-mode vacuum gap (Hz)
1 km	4.69072e-05	-21319	9.82×10^{-3}	47,713.452
10 km	0.000981315	-1019	9.81×10^{-4}	4,771.345
100 km	0.0136468	-73.277	9.67×10^{-5}	477.135

Scalar range	Y at surface	α_{ST} at balance	Residual gradient (s^{-2})	Same-mode vacuum gap (Hz)
1,000 km	0.175994	-5.682	8.49×10^{-6}	47.713
$R_\oplus$	0.798629	-1.2521	7.71×10^{-7}	7.489
63,710 km	0.996145	-1.0039	1.40×10^{-8}	0.749

At a range of one Earth radius the required $\alpha_{ST} = -1.252$ for the selected body comes from an imposed product of opposite charges. The finite-difference check of Eq. (37) includes six ideal fixed-flux or fixed-displacement configurations. Assigning electric or magnetic energy imbalances of opposite signs and fractional magnitude 10^{-6} to source and test bodies would require $|M_{\rm Pl}\partial_s \ln Z| \simeq 7.91 \times 10^5$. These fractions are illustrative inputs, including for the Earth. They do not estimate actual terrestrial or laboratory stored energy. R65 R66

For ordinary Ti and Pt in the unscreened small-correction regime, Eq. (40) converts the published summary at 710 km into a conditional differential envelope $|\Delta\alpha| \lesssim 9.12 \times 10^{-15}$ at the same scalar range. The difference of charges is what enters this envelope. Independently, the ordinary-mass scale at 1 m would be 1.32×10^{28} J for a compact monopole giving one g. One joule changes the energy-equivalent mass by 1.11×10^{-17} kg. For the ideal Casimir interaction at $1\,\mu$m, the signed interaction contribution is -4.82×10^{-27} kg/m². R64 R67

If the same vacuum mode supplies both effects, a range of $R_\oplus$ predicts a rest gap of 7.489 Hz, or 3.10×10^{-14} eV. The corresponding first-band vacuum pump wavelength is 40,030 km. A 1 GHz vacuum rest gap would mediate a force over 4.77 cm. This comparison supplies a falsifiable link between the force-range and wave-response hypotheses under the shared-mode assumption.

23.3 Dense spin and simulated measurements

The minimal spin-fluid contact term is 6.65×10^{-42} times the ideal neutron-gas energy density at $n_f = 0.16$ fm^{-3}. Reaching 3% at that density in this normalization requires a multiplicative enhancement of 4.51×10^{39}. Its formal active-source, null and density zeros occur at $p_F c/E_{\rm Pl} = 3.760,\ 4.342,\ 5.317$, respectively. Extrapolating the model to these scales places the ideal-gas and gravitational approximations outside their controlled regime. The 12 normalized dust, radiation, and mixed trajectories satisfy the Friedmann constraint to a maximum normalized residual of 3.60×10^{-9}. At $\Sigma = 0.9$, the calculated bounce scales are 0.31623 for radiation and 0.46416 for dust. R68

The four-state readout used 24,000 seeded synthetic experiments, 48 randomized blocks per experiment, and six injected amplitude levels. The zero-signal false-positive rate was 5.45%. The interval excluded zero in 98.32% of simulations with an injected effect one-half the single-read noise. This validates the analysis for the assumed noise and additive offsets. The available measurement here is the published free-fall comparison. The laboratory readout is simulated, and the dimensions and noise floor of a physical ESFD detection remain to be measured.

24 What the proposed field equations imply

The original *Proof*, pp. 1–3, starts from a Maxwell term, a local tensor coupling and a potential. It subsequently proposes a separation-dependent spin correlation with potential proportional to $-\kappa^2\langle S_A S_B\rangle/r$. The missing step lies between those statements. Which propagator has a massless pole? Do its sources have a monopole charge in a neutral, unpolarized body? Does that charge track inertial mass? Each question can be answered for a specific action. This chapter tests three explicit readings of the proposal and follows one surviving dynamical possibility into a closed cavity. A1 A4 A10

24.1 A local tensor response can be eliminated exactly

In the normalization of equation (6), let Q be an independent real two-form, $K = dQ$, $F = dA$ and $m_Q > 0$. Contract indices with the $(+---)$ metric. Completing the square gives an identity at arbitrary external momentum,

$$\begin{aligned}\mathcal{L} &= -\tfrac{1}{4}F^2 + \tfrac{1}{12}(dQ)^2 - \tfrac{m_Q^2}{4}Q^2 + \tfrac{g_Q}{2}Q_{\mu\nu}F^{\mu\nu}\\ &= -\tfrac{1}{4}(1-g_Q^2/m_Q^2)F^2 + \tfrac{1}{12}(dQ')^2 - \tfrac{m_Q^2}{4}(Q')^2,\\ Q' &= Q - g_Q F/m_Q^2, \qquad dQ' = dQ.\end{aligned} \tag{45}$$

The last step uses the Bianchi identity $dF = 0$. A minimal external electromagnetic current measures the rescaled Maxwell propagator. A massive two-form can still carry its own initial data, and a separate matter source for Q would couple the sectors again after the change of variables. With the displayed couplings alone, incident light cannot launch an independent third propagating photon polarization. For $|g_Q| < m_Q$ the photon has positive kinetic energy. Equality makes its kinetic operator degenerate and larger mixing reverses its kinetic sign. The massless two-form limit requires a separate gauge analysis. The calculation retains finite frequencies, so the absence of an extra pole extends beyond a static approximation. The supplied test evaluates both sides on 900 independent off-shell field configurations.

The *Proof* prints a potential without a kinetic term for S. In that literal starting expression its spin equation is algebraic. For an auxiliary Q with $V = m_Q^2Q^2/4 + \lambda_Q(Q^2)^2/16$, variation at fixed field gives $(m_Q^2 + \lambda_Q Q^2/2)Q_{\mu\nu} = g_Q F_{\mu\nu}$. Near zero field the regular solution starts at $Q = g_Q F/m_Q^2$. Substitution gives

$$\mathcal{L}_{\text{eff}} = -\tfrac{1}{4}(1-g_Q^2/m_Q^2)F^2 - \frac{\lambda_Q g_Q^4}{16 m_Q^8}(F^2)^2 + O\big((F^2)^3\big)\,. \tag{46}$$

This is a concrete nonlinear-optics mechanism. In a prescribed background it changes the field response, which can be compared with vacuum birefringence. The computation uses a local invertible branch near zero field. A nonanalytic potential, a background condensate or independent derivative couplings require a new expansion. In particular, a composite fermion bilinear in equation (1) has quantum dynamics inherited from its constituents. Treating that bilinear as a free canonical tensor would count different degrees of freedom.

24.2 Neutral spin sources and the range of a force

A microscopic magnetic moment couples to $F_{\mu\nu}$, which contributes one power of exchanged momentum at each vertex. Those two powers remove the scalar $1/\mathbf{q}^2$ monopole singularity in one-photon exchange. In real space two separated permanent moments have the interaction

$$U_{\mathrm{dd}}(\mathbf{r}) = \frac{\mu_0}{4\pi r^3}\left[\boldsymbol{\mu}_1\cdot\boldsymbol{\mu}_2 - 3(\boldsymbol{\mu}_1\cdot\hat{\mathbf{r}})(\boldsymbol{\mu}_2\cdot\hat{\mathbf{r}})\right]. \tag{47}$$

This follows by taking two spatial derivatives of $1/(4\pi r)$ and dropping the contact term at $r = 0$. The interaction can attract or repel as orientation changes. Independent isotropic ensembles have zero first-order average. Induced moments and correlated fluctuations can yield a residual with its own power law and material polarizabilities. An emergent inverse-square force therefore requires a collective long-distance pole **and** a rule for its residue in each material. Writing the observed $1/r$ directly into a spin correlator leaves both to be derived. A4 R79

There is a calculable fluctuation force even when an even gauge coupling $Z(s) = Z(-s)$ has $Z'(0) = 0$. Take a canonical vacuum scalar of mass m, two small stationary bodies far apart compared with their sizes, and a weak coupling $\frac{1}{2}c_i s^2$ at each body. Use $\hbar = c = 1$. After the local self energies are subtracted, the cross term in the Gaussian vacuum determinant is $-c_1c_2/2$ times the integral of a squared Euclidean Green function. At frequency ζ, that Green function is $G_\zeta(r) = \exp[-r\sqrt{\zeta^2+m^2}]/(4\pi r)$. Hence

$$\begin{aligned} U_{12}(r) &= -\frac{c_1c_2}{2}\int_{-\infty}^{\infty}\frac{d\zeta}{2\pi}G_\zeta(r)^2 = -\frac{c_1c_2m}{32\pi^3r^2}K_1(2mr), \\ U_{12}(r)\big|_{m=0} &= -\frac{c_1c_2}{64\pi^3r^3}. \end{aligned} \tag{48}$$

For $m > 0$, putting $\zeta = m\sinh u$ gives the Bessel function. For $m = 0$, the remaining integral is elementary. Equal-sign couplings attract. Their massless force falls as r^{-4}, and a mass supplies two-particle exponential suppression. A numerical integration at 76 values of mr checks the analytic result. This weak, zero-temperature, point-source calculation tests a different physical exchange from the one-photon calculation. Neither derives a universal Newtonian interaction. A linear coupling on a biased background instead permits a single-scalar pole. Its sign and magnitude can be tested with real matter. R69

24.3 An electromagnetic source charge for ordinary matter

Let M_P denote the reduced Planck mass and let $\alpha_{\mathrm{em}} \propto Z^{-1}$. For canonical s, define $d_e = M_P\partial_s \ln\alpha_{\mathrm{em}}$ on the background. Hold quark, electron and gluon-sector couplings fixed. The scalar charge per unit mass of a neutral atom is then $\beta_i = M_P\partial_s \ln m_i = d_e Q_{e,i}$. The published leading electromagnetic charge can be approximated by

$$Q_{e,i} \simeq 10^{-4}\left[-1.4 + 8.2\frac{Z_i}{A_i} + 7.7\frac{Z_i(Z_i-1)}{A_i^{4/3}}\right]. \tag{49}$$

Here Z_i is the proton number, unrelated to the gauge-kinetic function. The nuclear mass prefactor $A_i m_{\mathrm{u}}/m_i$ is set to unity. The primary calculation uses representative mass numbers. A second runs with tabulated mean atomic masses as a composition sensitivity. We form a mass-weighted

charge for each test alloy and Earth layer, with the dominant listed elements renormalized within the core and silicate mantle, a mantle proxy for crust, and water at the outside. PREM supplies the density weighting. These choices approximate composition gradients and crustal heterogeneity. R65 R70 R71

Write the positive orbital Yukawa kernel per unit Newtonian acceleration as $K_q(L,h)$, including source charge and the finite radial profile as in equations (38)–(40). The test-body acceleration enhancement is $2d_e^2 Q_{e,i} K_q$. The predicted free-fall difference is

$$\eta_{\mathrm{Ti,Pt}} = \frac{2d_e^2 K_q (Q_{\mathrm{Ti}} - Q_{\mathrm{Pt}})}{1 + d_e^2 K_q (Q_{\mathrm{Ti}} + Q_{\mathrm{Pt}})}. \tag{50}$$

Every relevant bulk charge has the same sign for the chosen portal. Either sign of d_e gives an **attractive** correction between the Earth and these alloys. The force-balance example in equation (39) permitted freely chosen test charges of opposite signs. Matching them to this specific electromagnetic response removes that freedom. We invert (50) using $|\eta_{\mathrm{obs}}| + 1.96\sqrt{\sigma_{\mathrm{stat}}^2 + \sigma_{\mathrm{syst}}^2}$ as a conservative envelope. It is a reinterpretation of the mission summary, with no access to the mission's acceleration time series. A universal extra coupling, material screening, an external controlled source, or another mediator changes the mapping. A stationary balance of forces on one composition would also leave the surrounding gravitational curvature to be measured. R67 R70

24.4 Finite energy in the proposed standing-wave response

The earlier calculation held the counterpropagating pump fixed. That gives a clean onset condition and allows its energy reservoir to remain indefinitely large. To calculate what happens after onset, project to one real electromagnetic cavity coordinate a and one spatially uniform spin coordinate s. Set the bare spin gap to one, let k be the photon frequency in those units, and choose a positive quartic restoring coefficient λ. A closed-mode Hamiltonian with the same even interaction is

$$H = \frac{p_a^2}{2Z(s)} + \frac{Z(s)k^2a^2}{2} + \frac{p_s^2 + s^2}{2} + \frac{\lambda s^4}{4}, \qquad Z(s) = e^{-gs^2}. \tag{51}$$

With $a(0) = 0$, $p_a(0) = \sqrt{P}$ and a small seed, the photon term produces $\ddot{s} + [1 + gP\cos(2kt)]s = O(s^3)$ before depletion. A resonant growing solution can therefore draw only the initially stored energy. $s = p_s = 0$ is an invariant solution of this classical even system. Thermal, quantum or deliberately seeded excitation would change its initial state. The seven integrations in the results chapter vary the seed, detuning and quartic term and check energy conservation. They describe a material or collective degree of freedom postulated by ESFD, so a laboratory claim requires a separately measured gap, coupling, linewidth and readout response. The calculation supplies a frequency and seed dependence that can be tested.

24.5 Returning to the spinning top

For an axially symmetric rigid body on a fixed pivot, let I_1 and I_3 be its pivot moments, M its mass, ℓ the distance to its centre of mass, and Ω its axial spin. Near the upright equilibrium the horizontal tilt $u = n_x + in_y$ satisfies

$$I_1\ddot{u} - iI_3\Omega\dot{u} - Mg\ell u = 0, \qquad \Omega_c = \frac{2\sqrt{I_1 Mg\ell}}{I_3}. \tag{52}$$

A transition in wobble can occur through rigid-body dynamics alone. The simulations start with a small known tilt and evolve the full vector angular-momentum and axis equations. The tabulated six runs cross (52) without a material spin parameter. A freely slipping tabletop top has contact friction, rolling, dissipation, an evolving spin and sometimes a moving point of contact. Observations of such a top cannot be mapped quantitatively onto the fixed-pivot example without those additional measurements. R72

For a direct spin–field test, consider toggling rotation and applied magnetic field. An ordinary Barnett moment induced by rotation can produce a torque linear in ΩB in a nonparallel geometry. A putative ESFD correction of the same symmetry produces the identical mechanical regression column. The illustrative design $[1, \Omega^2, B, \Omega B, \Omega B]$ has rank four even with multiple signed speeds and field-off controls. A separately calibrated measurement of rotation-induced magnetization adds a fifth independent constraint. Recording field direction, remanent moments, surface geometry, speed, wobble angle and losses would let a replication place a signed bound on the remaining torque. The source archive contains the motivating observation and no synchronized rotor measurements. A1 R72

25 Superconductors as the required experimental phase

Grenke specifies that the laboratory effect requires a superconductor. That condition changes the experiment and the interpretation of a null result. Equation (50) describes a composition coupling that persists in ordinary matter. A term proportional to a superconducting order parameter vanishes in the normal phase and can escape that particular test. It has direct tests of its own. Niobium supplies precision rotation and magnetic-penetration measurements. Yttrium barium copper oxide (YBCO) supplies published gravity tests with a superconducting source. The measurements access different response coefficients.

25.1 Which material is best for which measurement?

Material	Representative transition and operating condition	Measurement it can anchor
Niobium	9.25 K for the cited screening analysis	Best grounded rotation benchmark here. The pair mass-to-charge response was measured in a rotating ring, and depth-resolved magnetic measurements exist on six differently prepared specimens.
Nb_3Sn and NbN	About 18 K and 16 K in the cited materials table	Conventional comparison materials with different stiffness, penetration depth and condensation energy.
MgB_2	39 K at ordinary pressure	A noncuprate, multiband comparison with a higher transition temperature and an independent superconducting transition.
YBCO, a member of the REBCO family	Zero resistance at 91 K in the cited sample. Oxygen content affects the transition.	Best evidenced material here for testing a gravity claim. Static levitated and rotating-disk experiments provide direct benchmarks. The superconducting state is accessible at 77 K in sufficiently oxygenated material.

Material	Representative transition and operating condition	Measurement it can anchor
$HgBa_2Ca_2Cu_3O_{8+\delta}$	About 133 K conventionally. Deng et al. reported a **151 K resistive onset at ambient pressure after pressure quenching**.	High-temperature comparison. The retained metastable specimen and its transition criterion matter. A rotation or weight measurement on this state would require separate evidence.
Lanthanum superhydride	About 250 K at approximately 170 GPa in the cited study	A high-pressure temperature benchmark. Its pressure-cell geometry is a different experiment from rotation of a bulk disk at ordinary pressure.

The transition temperature determines where superconducting order can exist. The proposed force depends additionally on the coupling, the volume that changes state, field penetration and the source and probe geometry. The material with the highest resistive onset need not produce the largest measurable acceleration. R81 R82 R83 R84 R85 R86

25.2 Rotating charge condensate and London moment

Write the macroscopic pair order parameter as $\Psi = \sqrt{n_p}\exp(i\theta)$ with pair charge $q_p = -2e$. A vortex-free contour has phase momentum $m'\mathbf{v}_s + q_p\mathbf{A} = \hbar\nabla\theta$ in the simple isotropic London description. In the co-rotating bulk $\nabla \times \mathbf{v}_s = 2\boldsymbol{\Omega}$. Taking the curl or integrating around a ring gives

$$\mathbf{B}_L = -\frac{2m'}{q_p}\boldsymbol{\Omega}, \qquad \oint (m'\mathbf{v}_s + q_p\mathbf{A})\cdot d\mathbf{l} = nh, \qquad |\Phi_0| = \frac{h}{2e}. \tag{53}$$

Niobium ring measurements gave $m'/(2m_e) = 1.000084(21)$. The difference from the historical electrochemical calculation 0.999992 is 92 ± 21 ppm using experimental uncertainty alone. The 1989 letter and 1990 full study concern the same result. A field at 100 rad s^{-1} inferred from the measured slope is 1.1372 nT. That last number is a calculated scale at a chosen angular velocity. The observable is flux or magnetic field and its slope with rotation. An independent acceleration readout would be needed to assign a gravitational coupling to it. London moments have also been measured in high-temperature superconductors. A spin-singlet pair has zero total intrinsic spin, while the condensate phase, charge current and magnetic flux can be sharply defined. ESFD must specify which of these quantities carries its effect. R81 R87

25.3 Measured magnetic screening in niobium

We refit the six niobium specimens reported in the staged local analysis of McFadden et al., supplement Table S4. At measured temperatures near 3 K the authors give extrapolated penetration

depths and impurity-derived electronic mean free paths. The test uses the quoted errors on both coordinates,

$$\lambda_0(\ell) = \lambda_L\sqrt{1+\frac{\pi\xi_0}{2\ell}}, \qquad \chi^2 = \sum_i \left[\frac{(\ell_i-\ell_{i,\mathrm{obs}})^2}{\sigma_{\ell,i}^2} + \frac{(\lambda_0(\ell_i)-\lambda_{i,\mathrm{obs}})^2}{\sigma_{\lambda,i}^2}\right]. \tag{54}$$

The fitted local quantities are $\lambda_L = 33.15$ nm and $\xi_0 = 32.24$ nm, with $\chi^2 = 3.78$ for four degrees of freedom. Leaving out each specimen in turn gives 2.54 nm RMS error for its measured penetration depth using the held-out mean free path. The authors' staged local extraction gives 33.1 and 32.6 nm. Their preferred nonlocal analysis gives 29.1 ± 1.0 and 39.9 ± 2.5 nm. Preparation and electrodynamic model alter the inferred length on the same element. This comparison starts from six published specimen summaries. Their signal extraction from the muon arrival histograms precedes our fit. R82

25.4 Coupling a superconducting phase to the ESFD variable

For a minimal, separately identified extension, take a neutral scalar s with $s \mapsto -s$ symmetry and a charged superconducting order parameter Ψ. Add the usual gauge-covariant gradient energy $|(-i\hbar\nabla - q_p\mathbf{A})\Psi|^2/(2m_p)$ and electromagnetic energy to the homogeneous free energy

$$f = a(T)n + \frac{b}{2}n^2 + \frac{m_s^2}{2}s^2 + \frac{\lambda_s}{4}s^4 + \frac{u}{2}ns^2, \qquad n = |\Psi|^2, \qquad b, \lambda_s > 0. \tag{55}$$

At $s = 0$ the superconducting order is $n_0 = \max[0, -a(T)/b]$. The curvature in the spin direction is $m_s^2 + un_0$. A positive u raises the gap and a sufficiently negative u allows a second transition. Eliminating n on the positive-occupation branch gives $\lambda_{\mathrm{eff}} = \lambda_s - u^2/(2b)$. We use $\lambda_{\mathrm{eff}} > 0$ for the continuous transition. The analytic minimum and an independent bounded numerical minimization agree over 453 temperature and coupling combinations. With normalized $a = T/T_c - 1$, $b = \lambda_s = 1$, $m_s^2 = 0.02$ and $u = -0.5$, the second onset is $T/T_c = 0.96$. This value is selected by the illustrative coefficients. Neither the 151 K report nor the niobium fit measures u. A low-drive spectroscopic test would measure a change of **squared mode frequency** with independently inferred condensate density, followed by a predicted onset or upper bound with the same u. A mean-field expansion near T_c gives no controlled prediction of the entire low-temperature spectrum.

In this even model an unperturbed state gives a shift in the spin gap as soon as superconductivity sets in. A linear source for a long-range scalar requires a distinct term, for example $g_1 ns$ if the symmetry permits it, or a quantified bias. Even then, motion of a separate neutral body requires a coupling to that probe. For a signed weight signal, magnetic forces, trapped vortices, changing buoyancy, thermal gradients and vibration each have independently observable controls. Recording a co-located superconducting transition, pickup flux and differential acceleration at several heights tests the three links separately. A superconducting ring can respond strongly through (53) in the absence of any change of the external gravitational field.

25.5 Direct gravitational tests and geometric reach

Li et al. compared the acceleration over a static, magnetically levitated YBCO sample and reported changes below $2 \times 10^{-8} g$. The earlier reported stationary weight change of 5×10^{-4} is 25,000 times

that sensitivity. Hathaway et al. also reported a null in their rotating YBCO apparatus. Its approximately 50 g test body and 0.5 mg repeatable balance sensitivity correspond to roughly 10^{-5} in fractional weight. They reached at most about 550 rpm, measured at a different height, and described differences in levitation and disk preparation. These values constrain the experiments that were actually run. Their sensitivities are quoted as reported and do not define universal confidence limits over every spin speed, material or interaction range. R83

To express what the static result can test, suppose the superconducting material changes a uniformly distributed, weak, attractive or repulsive Yukawa source with range L. Approximate its active volume by a cylinder of radius R and thickness d. Let z be the on-axis probe height above the top face and A_0 the acceleration of an infinite slab of the same integrated effective source density in the unsuppressed Newtonian limit. Integrating the Yukawa Green function over the actual finite disk gives

$$\frac{|\Delta a(z)|}{|A_0|} = \frac{L}{d}\left[F(z) - F(z+d)\right], \qquad F(h) = e^{-h/L} - e^{-\sqrt{R^2+h^2}/L}. \tag{56}$$

We use the reported 10 cm diameter, 1.25 cm thickness and the nominal 18 cm height. At a 10 cm range the transfer is 0.01491. For this point-probe geometry, the reported sensitivity corresponds to $|A_0|/g$ of about 1.34×10^{-6}. The table explores 104 ranges and verifies the analytic result by direct integration. Source screening, a surface-only source, a response confined to vortices, or a finite sensor with a different location would alter the kernel. A uniform reduction of Earth's gravity has a different spatial dependence. R83

There is also a conventional energy scale. At low temperature the condensation free-energy density approaches $B_c^2/(2\mu_0)$. Using a representative thermodynamic $B_c = 0.21$ T for Nb, the corresponding energy of one cubic centimetre is about 0.0175 J, equivalent to about 1.9×10^{-18} N of weight in Earth's field. At finite temperature internal-energy and free-energy differences differ by $T\Delta S$. A cycle that includes the apparatus, cooling bath and heat exchange must account for the full energy balance. This scale applies to the sample's equilibrium condensation energy. The accelerometer above a disk measures a different quantity again. R84

25.6 The superconducting condition in a neutron star

A proton-paired stellar core supplies a physically motivated way to revisit the magnetar hypothesis. In a type-II core sustaining magnetic flux tubes, the areal proton flux-tube density is $n_\Phi = B_{\rm core}/\Phi_0$. The neutron superfluid instead carries circulation, with vortex density $n_v = 2\Omega/\kappa_n$ and $\kappa_n = h/(2m_n)$. The two densities scale with different observables. In a dilute array the characteristic magnetic tension can scale as $B_{\rm core}B_{c1}/\mu_0$ compared with the normal Maxwell tension $B_{\rm core}^2/\mu_0$. Formation history and trapped flux matter below the nominal lower critical field. The core field, proton pairing gap, topology and entrainment cannot be inferred uniquely from the timing dipole. R90

We evaluated three explicitly assumed core-to-timing-field ratios (0.1, 1 and 10) for all 22 confirmed magnetars with usable uncensored timing. For the equal-field illustration the median triangular flux-tube spacing is 3.08×10^{-13} m and the median ratio of flux tubes to neutron vortices per unit area is 8.86×10^{17}. Only three of the 22 fall below our conservative dilute-domain cut of one-tenth of a representative $B_{c1} = 10^{15}$ G. The code reports tension ratios solely inside that domain. These are conditional scales, not observations of stellar interiors. A physical extension

would couple the relative orientation, pinning and motion of the two arrays to an independently timed glitch, precession or thermal observable. Percent-level static contact stresses tested against NICER are a different model and are not derived from these flux counts.

If the superconducting condition is required at galactic scales as well, the rotation, radio and lensing catalogs used here do not measure such a phase in the galactic disk. Extending the mechanism from a stellar core to a galaxy requires identifying the paired species, its critical temperature and field, the occupied volume, and the stress it communicates to neutral stars and to light. The galaxy fits cannot identify that material for the theory.

26 Independent observations and a revised galaxy equation

The June synthesis names the *spin–entropy* extension SEFD. ESFD is the wider project. Neither "SFFT" nor the speech variant "SCFD" identifies another validated galaxy theory in the recovered source record. The literal divergence profile in equation (17) can improve a baryons-only curve. Its enclosed effective mass approaches zero at very large radius. The central question is whether a physically motivated replacement can transfer from one galaxy to another, predict weak lensing, and retain evidence for an electromagnetic origin. The three tests here probe those questions with different observations. A6 R28 R29

26.1 A regular core with a flat outer rotation speed

For an isolated spherical effective field, write the extra speed as a fraction of a limiting speed V_∞. One simple closure with a linear central acceleration and an asymptotically flat rotation curve is

$$\begin{aligned} V^2_{\mathrm{pred}}(r) &= V_b^2(r) + V_\infty^2 \frac{r^2}{r^2+r_c^2}, \qquad V_\infty^4 = GM_b a_\star, \qquad r_c = \eta R_d, \\ \Phi_f(r) &= \frac{V_\infty^2}{2}\ln\frac{r^2+r_c^2}{r_0^2}, \qquad \rho_f(r) = \frac{V_\infty^2(r^2+3r_c^2)}{4\pi G(r^2+r_c^2)^2}. \end{aligned} \tag{57}$$

Here R_d is the stellar disk scale length and r_0 is an arbitrary reference length. M_b is set by the photometry and gas catalog. $a_\star$ and η are shared by an entire training population. This radial potential is the established spherical logarithmic halo form, with the baryonic Tully–Fisher scaling imposed. Its empirical success can select a radial shape while leaving the source ambiguous. One explicit mapping to the archival equation $\rho_f = \nabla\cdot(s\mathbf{J}_s)$ is

$$(sJ_s)_r = \frac{M_f(<r)}{4\pi r^2} = \frac{V_\infty^2}{4\pi G}\frac{r}{r^2+r_c^2}. \tag{58}$$

The required weighted flux is regular at the center, falls as $1/r$ in the outer galaxy and has nonzero divergence there. If sJ_s were instead strictly conserved and source-free in a stationary exterior, spherical symmetry would force $r^2 sJ_s$ to be constant. Both conditions cannot hold over the same extended region. The required mass grows linearly at large radius. A cosmological embedding, an outer cutoff and a budget for the sustained weighted flux remain necessary. No microscopic ESFD coefficient has been used to calculate $a_\star$. R77

The flat tail can also follow from an ordinary modified-Poisson construction. For a scalar potential with $\nabla\cdot[\mu(|\nabla\Phi|/a_\star)\nabla\Phi] = 4\pi G\rho_b$, spherical symmetry integrates to $\mu(g/a_\star)g = GM_b/r^2$ outside the matter. Taking $\mu(x)\simeq x$ gives $g = \sqrt{GM_b a_\star}/r$ exactly in that limit. A Newtonian field from the effective density in (57), a nonlinear gravitational response, and a hypothetical organized spin source can therefore share a velocity asymptote. The same measured $a_\star$ must predict an observable involving field or spin for the interpretation to become mechanism-specific. R29 R78

26.2 Whole galaxies and comparisons with dark-matter profiles

We use the archived five mass-balanced folds, holding out entire galaxies and all their radii. The training objective weights each velocity residual by $1/[\sqrt{N_g}\sqrt{\sigma_v^2 + (5\ \mathrm{km\,s^{-1}})^2}]$. The empirical radial acceleration relation (RAR) is refit on each training set with one free acceleration scale. The alternative NFW and Burkert halos have a common dimensionless mass normalization proportional to M_b, and a scale radius proportional to R_d, with two trainable population constants per profile. For $x = r/(\eta_h R_d)$ their dimensionless enclosed-mass shapes are $\ln(1+x) - x/(1+x)$ and $\frac{1}{2}\ln(1+x) + \frac{1}{4}\ln(1+x^2) - \frac{1}{2}\arctan x$. Per-galaxy halo fits and the fixed published RAR remain in the earlier chapters. The population comparison does not marginalize cosmological halo scatter, varying stellar mass-to-light ratios or adiabatic response. NFW and Burkert are dark-matter comparators. RAR is an observed baryonic–dynamical acceleration relation that can have several physical interpretations.

We first calculate the RMS velocity error within each galaxy, then report its median across galaxies. For paired inference we calculate the difference of the two errors *within each galaxy*, then bootstrap that median difference with 5,000 galaxy-level resamples. A difference between separate sample medians and a median paired difference generally disagree. The new profile was developed with knowledge of the earlier project's results. The five folds test parameter transfer within SPARC. They cannot turn today's choice of profile into a prediction registered before the survey. R28 R29

26.3 LITTLE THINGS provides a distinct reduction of dwarf-galaxy kinematics

Oh et al. published normalized rotation curves for 26 systems, the normalization radii and speeds, and independent stellar and gas estimates. We recover the dimensional observed velocity and radius using the supplied scale factors. Only the rows marked as data enter the test. Inclination of at least 30°, available positive stellar and gas masses, an optical scale height, and positive finite radii, speeds and errors define eligibility. All 175 SPARC positions were matched against the 26 published centers with a conservative ten-arcminute sky radius, including alias names. Every training galaxy within that radius of any LITTLE THINGS source was removed before fitting the global constants. Results are also supplied for only the targets without a SPARC positional match. R73 R28

The public figure inputs do not give an independent resolved baryonic velocity curve for every point in this standardized comparison. Approximate each stellar and gas contribution with a thin exponential disk of total mass M_d and scale length h. With $y = r/(2h)$ its speed contribution is

$$V_d^2(r) = \frac{2GM_d}{h}\, y^2[I_0(y)K_0(y) - I_1(y)K_1(y)]. \tag{59}$$

The stellar scale is five times the catalogued height, in the authors' convention. The gas scale is assumed to be twice the stellar scale, varied to 1.5 and 3 in sensitivity tests. The stellar and helium-corrected gas masses are from the LITTLE THINGS tables. Gas irregularity, inclination uncertainty, radial pressure support, distance selection and baryonic profile approximations can all move the scores. Ratios or scale lengths are never tuned on the test velocities.

26.4 Transfer to gravitational lensing

We take the authors' deprojected circular-speed equivalents and published statistical and systematic errors from the revised KiDS machine-readable table. For each mass and morphology bin the baryonic source is approximated as a point mass with the published bin mean. The primary comparison uses late-type objects and 50–300 kpc. The longer range to 1 Mpc and early-type and combined samples are tabulated. The code uses within-bin SPARC disk-size percentiles 16, 50 and 84 as a sensitivity. No lens bin is used to fit the speed law. We use a spherical metric interpretation under which the inferred lensing potential responds to the same additional potential as nonrelativistic dynamics. A field that only pushes magnetized material would instead contribute no new lens potential. R74

In weak-field metric language light responds to $(\Phi + \Psi_g)/2$, while slow neutral tracers measure Φ. With $V_b^2 = GM_b/r$, the bin diagnostic $[V_{\rm lens}^2 - V_b^2]/[V_{\rm pred}^2 - V_b^2]$ equals one for the assumed common response at fixed mass. Binning, redshift distribution, deprojection, environment, baryon inventory and disk-to-lens population differences all enter this diagnostic. The public table supplies bin errors but no complete inter-bin covariance for our experiment. We therefore report unweighted speed RMS and no likelihood or gravitational-slip detection. R74

26.5 Can actual magnetic data add predictive information?

Tabatabaei et al. reported integrated total and polarized 4.8 GHz flux densities scaled to 10 Mpc, an optical radius, star-formation rate (SFR) and a rotation speed for each of 26 nearby galaxies. We transcribed all 26 central values and used galaxy-level leave-one-out predictions of $\log_{10} V$. We successively included $\log_{10}$ SFR, $\log_{10} R_{25}$, total radio flux and polarized radio flux. The influence of polarization is assessed against the model already containing the first three controls. A residual-permutation calculation uses 9,999 draws with those controls retained. It is exploratory and assumes approximately exchangeable residuals. R80

The measured radio signal does not use the velocity being predicted, but disk size, gas density, inclination, magnetic ordering, cosmic-ray electrons, star formation and distance calibration can jointly affect these quantities. Only three galaxies match the 131-object SPARC fold set by normalized names and aliases in the packaged crossmatch. That overlap cannot establish an incremental magnetic effect on the *unexplained radial acceleration*. Predicting a galaxy's characteristic speed and predicting a radius-by-radius residual after baryons are different observational questions. A decisive sample needs resolved radio polarization, Faraday information or another field proxy and independent gas and stellar kinematics over the same radii. R80

27 Compact stars, quantum measurements and cosmic horizons

27.1 Two observed stars against each common stellar equation of state

Choudhury et al. and Salmi et al. released equally weighted joint samples of gravitational mass and equatorial radius for PSR J0437–4715 and PSR J0740+6620 respectively. We retain each original mass–radius pair. For every admissible static stellar sequence in the preceding chapters we retain the first stable branch up to its refined mass maximum or causal endpoint. We interpolate

linearly in mass between computed radii and never extrapolate beyond that branch. For each of the authors' posterior draws j, the compatibility statistic is the posterior fraction

$$C_i(\epsilon,\delta) = \frac{1}{N_i}\sum_j \mathbf{1}_{M_{ij}\in\mathcal{M}}\,\mathbf{1}_{|R_{ij}-R_{\mathrm{TOV}}(M_{ij})-\delta|\le\epsilon}. \tag{60}$$

The primary half-width is 0.5 km and the nominal static offset is zero. Alternative half-widths of 0.25 and 1 km and illustrative equatorial offsets of 0.3 and 0.6 km appear in the tables. C_1C_2 quantifies joint overlap for statistically independent posterior draws on the same EOS and contact coefficient. A Bayesian comparison of EOS models would require reconstructing the likelihood relative to each original prior, a central-density or mass population prior, a rotational stellar solver, and nuisance and EOS uncertainties. The band width itself sets the normalization of this descriptive measure. R75 R76

27.2 Bell outcomes, characteristic age and causal boundaries

The Delft event-ready experiment allows an end-to-end test of the quantum branch using original herald timing, settings and spin readouts. We apply the released herald windows, opposite detector channels, excitation and invalid-marker exclusions, and published readout gates before forming trial outcomes. For settings (a,b) and signs (x,y) the game is won when $xy=(-1)^{ab}$. Conditional correlators give $S = E_{00}+E_{01}+E_{10}-E_{11}$. The single-game binomial upper tail under the local bound also includes the authors' small allowed input bias. An independent, identical Werner-noise model with ideal CHSH axes has $p_{\mathrm{win}} = \frac{1}{2}+v/\sqrt{8}$ and can be inverted for an illustrative visibility v. That assumption applies only to the visibility interval. The data directly challenge a local classical account satisfying the Bell assumptions. A spin-field theory with the usual entangled quantum probabilities is compatible with this test and owes a separate predicted deviation to become distinguishable. R88

For the timing branch, $B_{\mathrm{timing}} \propto \sqrt{P\dot{P}}$ and $\Omega = 2\pi/P$ imply $\chi_{\mathrm{timing}} \propto \sqrt{\dot{P}/P} \propto \tau_c^{-1/2}$. The catalog test now calculates an exact binomial reference interval and counts the objects missed by the historical cutoff. The catalog is a selected population, so this interval describes sampling variability for an idealized population with the same eligibility. A false-positive rate for all neutron stars requires a separate comparison population and selection model. R08

Finally, a reversal of collapse does not itself specify the formation of a white hole or a daughter universe. For a spatially flat **isotropic** FLRW metric choose $c=1$, areal radius $R=a(t)r$ and future radial light rays $dr/dt = \pm 1/a$. Their fractional area expansions for a positive time normalization and the Misner–Sharp compactness are

$$\theta_\pm = \frac{2}{R}(HR\pm 1), \qquad \frac{2GM_{\mathrm{MS}}}{R} = H^2R^2 = 1+\frac{R^2}{4}\theta_+\theta_-. \tag{61}$$

At $H=0$ a finite sphere has opposite expansion signs. Larger spheres can be future trapped in the contracting phase or anti-trapped during expansion. The test reflects the smooth homogeneous trajectories in time and uses only the zero-shear subset. Nonzero shear in the archived model would spoil the assumed spherical geometry. Extending an interior to a black-hole exterior requires matching the induced metric and extrinsic curvature, or specifying a material shell, and tracing null geodesics through the matched solution. A causal connection to a separate asymptotic region is a global statement that no homogeneous turnaround alone settles. R68 R89

28 Numerical outcomes from this revision

28.1 Galaxy-by-galaxy predictions and independent light deflection

Each speed entry is in km/s. The first three numeric columns are medians of within-galaxy RMS errors. The lens column is RMS across 24 late-type radial and mass-bin cells at 50–300 kpc. All model coefficients used for the external samples were fixed using SPARC alone. R28 R73 R74

Model	SPARC, 131	Dwarfs, 17	Unmatched dwarfs, 10	KiDS lensing
Baryons	44.73	20.40	16.82	139.32
Spin-entropy flux	19.82	14.77	13.72	112.48
Shared NFW halo	19.43	14.49	13.50	54.36
Shared Burkert halo	19.32	14.26	13.50	69.87
RAR fitted on training galaxies	13.11	8.94	9.35	23.89
Cored flat-speed law	12.45	8.63	9.38	26.69

The revised equation wins 67 of 131 whole-galaxy comparisons against the refitted RAR. Its median paired change is -0.003 km/s, with a galaxy-resampled 95% interval of -0.67 to +0.68 km/s. Against the shared NFW and Burkert assumptions it wins 100 and 99 times. These restrictions matter. Allowing individual halos their own inferred scales changes the question and the outcome in the earlier radial holdouts.

The dwarf calibration excludes 4 potential training matches and uses 127 training galaxies. Of 26 published dwarf curves, 17 supply the required inputs, giving 706 selected radii. The revised law wins 8 of 17 comparisons against RAR. The median paired change is +0.005 km/s, with a 95% interval of -0.54 to +0.79. The order of the sample medians reverses in the ten objects without any SPARC positional match.

On all 131 training galaxies the revision gives an acceleration scale of 8.81e-11 m/s^2 and a core radius of 1.393 stellar disk scale lengths. The lens release has 158 populated cells across overlapping morphology subsets and mass bins. The median observed-to-predicted excess in squared speed is 1.26 in the primary subset under the stated potential and mass assumptions. Uncertainty in the bin covariance, source mass model and environmental contribution prevents interpreting this ratio as a measured coupling.

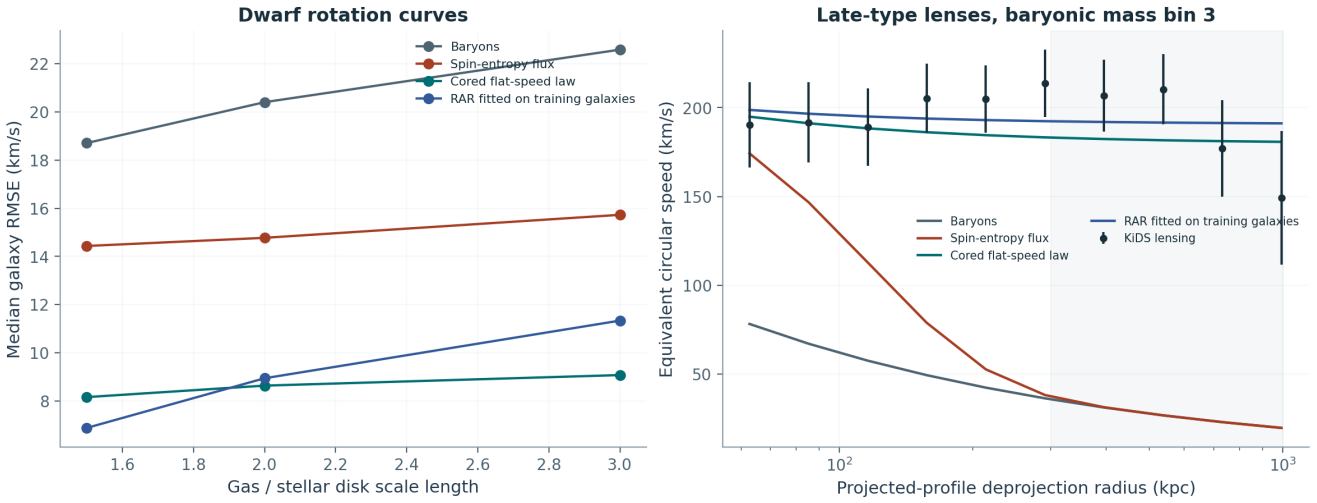

Figure 28. Independent dwarf-galaxy velocities and a late-type weak-lensing stack. The shaded region extends beyond the primary scoring range. Error bars in this figure combine the published statistical and systematic magnitudes in quadrature for display.

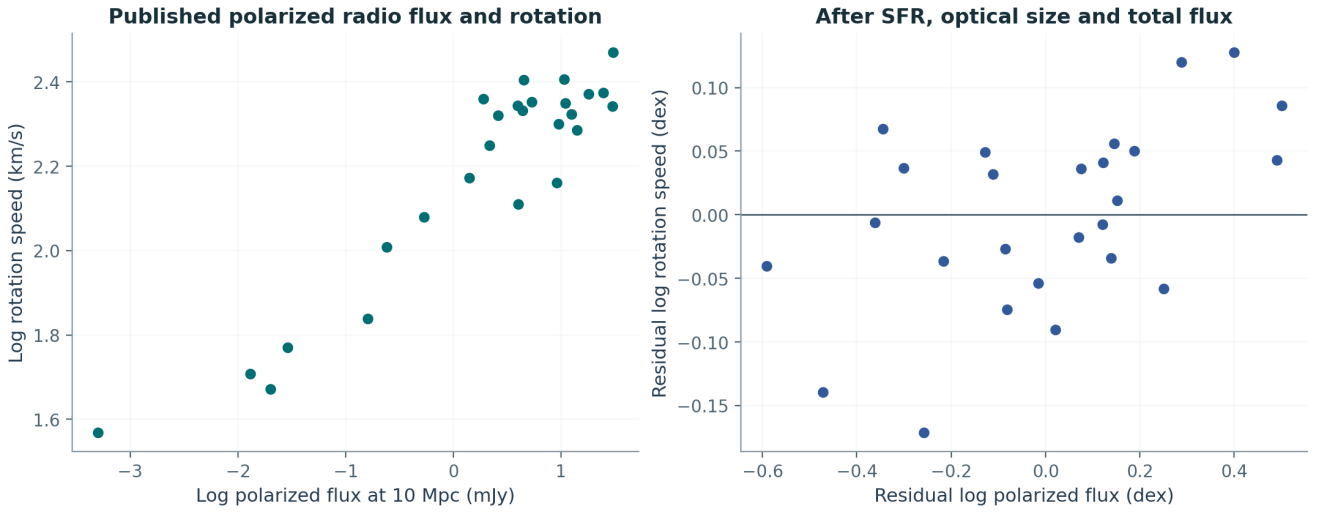

Figure 29. Measured radio polarization versus rotation before and after controlling for star formation, optical size and total radio emission. Both axes on the right are residuals from the same three-predictor fit.

28.2 Polarization measured independently of the rotation curve

The raw rank correlation between polarized radio flux and rotation speed is 0.778 across 26 systems. After linear control in log space for SFR, optical size and total radio emission, the partial Pearson coefficient is 0.510. The residual-permutation value is 0.0113. Adding polarization changes leave-one-galaxy-out RMS from 0.0835 to 0.0758 dex. The integrated polarization observable carries information about rotation in this selected catalog. A dynamo ordered by galactic motion, cosmic-ray transport or a common driver can produce an association. The three named matches to the held-out SPARC sample are too few to establish a magnetic explanation of the velocity residuals. R80

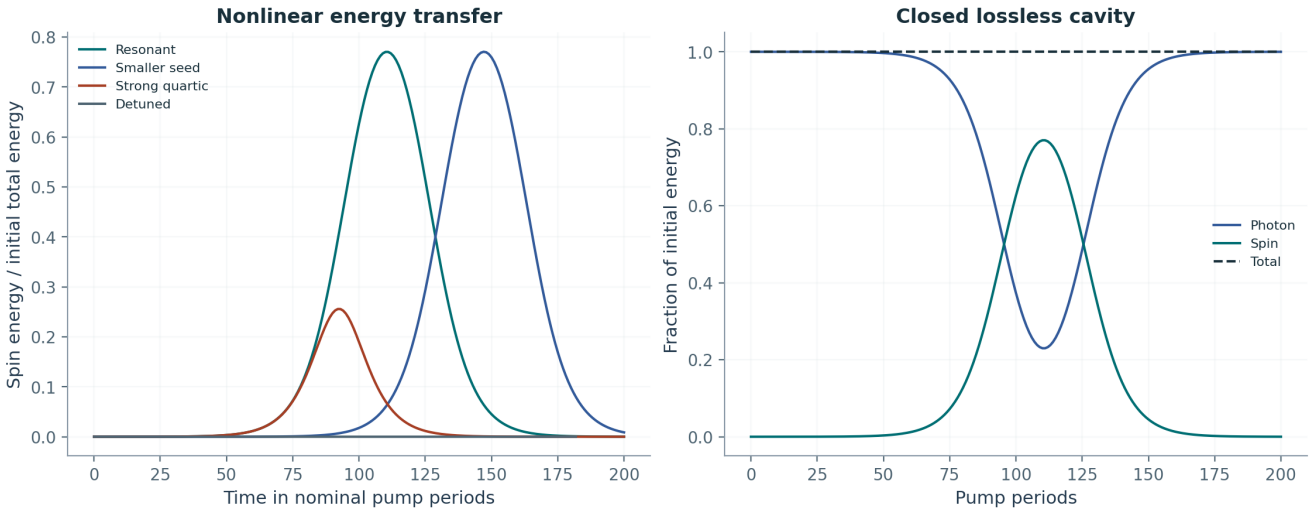

Figure 30. Numerical energy transfer into the assumed collective mode and energy conservation in a lossless two-mode cavity.

28.3 Field, rotor and superconducting tests

The two-form action equality holds to 3.1e-15 in the strongest normalized discrepancy over 900 configurations. The two-scalar vacuum-force quadrature differs from its closed form by at most 6.7e-16. These are cross-checks of the analytic identities under their stated hypotheses.

The resonant cavity grows at 0.01983 per unit gap time in the early fit, compared with 0.02000 from the fixed-pump calculation. Its spin coordinate reaches 77.28% of initial total energy. Increasing the quartic coefficient from 0.4 to 4 reduces the peak to 25.61%. Detuning the frequency ratio to 1.10 gives a peak fraction of 1.27e-05. The zero-seed trajectory stays at zero. Across all seven closed integrations the largest relative energy error is 3.7e-10.

The structural threshold of the example 45 g rotor is 65.09 rad/s, or 621.5 rpm. Six full rigid-body integrations reproduce small-tilt behavior to a maximum relative disagreement of 3.4e-07 within the selected small-angle window. This benchmark gives a calibration target for the original tabletop question. The specimen, friction and time trace from the motivating observation are unknown.

For the pure linear electromagnetic portal at a range of one Earth radius, the conservative free-fall envelope gives a coupling magnitude below 3.48e-05 in the reduced-Planck normalization. The corresponding added titanium-alloy surface acceleration is below 8.41e-15 times ordinary gravity. The composition-dependent force points inward. Equation (55) considers the separate possibility of an interaction activated specifically by superconducting order. R67 R70 R71

The niobium refit predicts held-out specimens to 2.54 nm. Its rotating-ring slope implies 1.1372 nT at 100 rad/s. The static YBCO test reported a sensitivity of 2e-08 of gravity and the rotating-disk balance had repeatability corresponding to approximately 1e-05. The right panel illustrates how an additional collective mode could have a separate temperature onset in a superconducting phase. None of these laboratory publications reports such a mode as a gravitational signal. R81 R82 R83

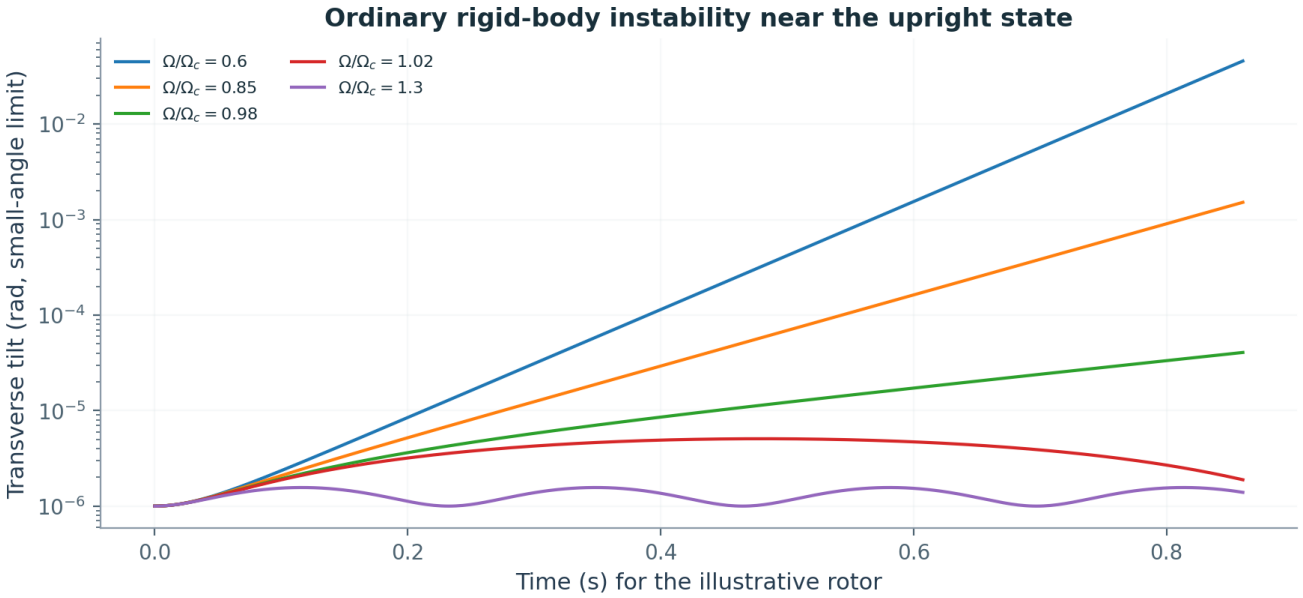

Figure 31. Tilt in the fixed-pivot rotor simulation. Small initial departures grow below the classical threshold.

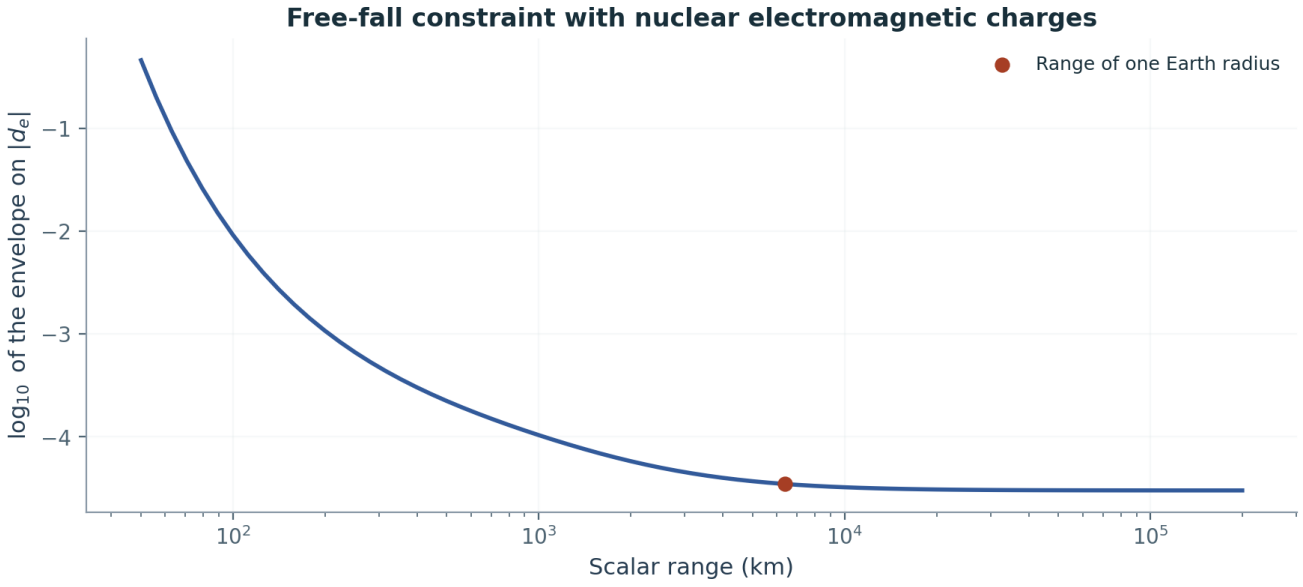

Figure 32. Finite-range scalar coupling envelope calculated from the published differential free-fall summary and material-matched terrestrial charge.

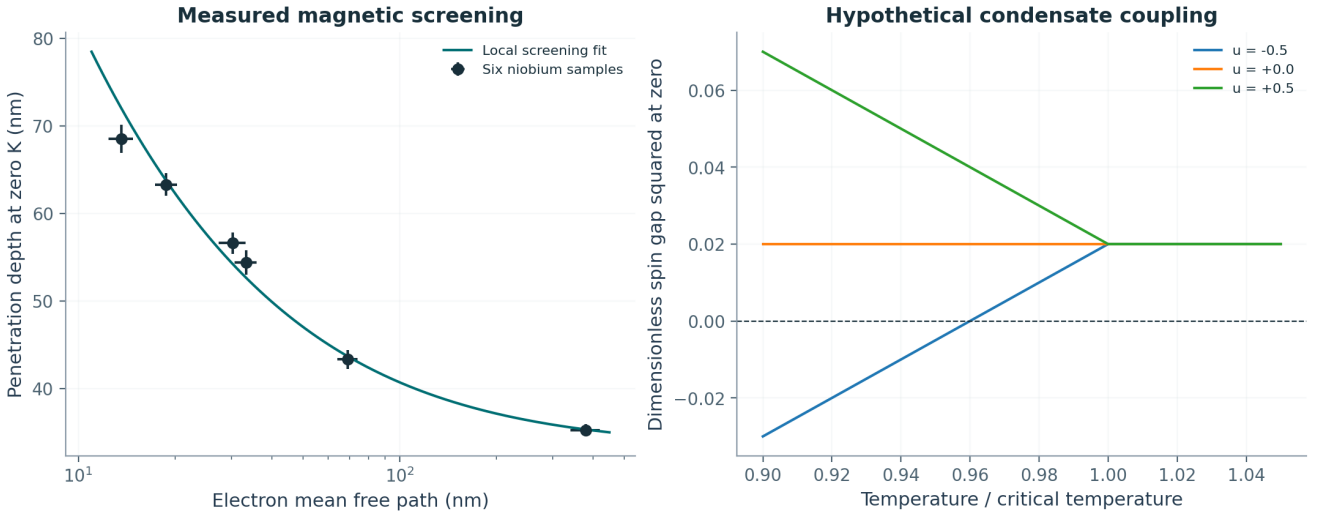

Figure 33. Left, six measured niobium screening depths with errors on both coordinates. Right, a simulated squared spin gap near the superconducting transition for three assumed couplings.

28.4 Two neutron stars tested with the same stress parameter

PSR J0437 contributes 218,553 joint posterior samples. The median and central 68% span are 1.418 (1.381–1.454) solar masses and 11.36 (10.73–12.30) km. The sampled mass–radius correlation is 0.261. The median dimensionless rotation scale, computed as angular frequency squared times radius cubed divided by GM, is 0.009. R75 R76

PSR J0740 contributes 379,669 joint posterior samples. The median and central 68% span are 2.073 (2.004–2.142) solar masses and 12.49 (11.61–13.76) km. The sampled mass–radius correlation is 0.272. The median dimensionless rotation scale, computed as angular frequency squared times radius cubed divided by GM, is 0.033. R75 R76

Of 42 EOS/contact cases, 25 have admissible first branches over part of the tested mass range. The best shared primary overlap is the MPA1 core model with a −1% energy contribution at the reference density. Its fractions are 0.474 and 0.281, with product 0.133. The strongest zero-contact comparator is MPA1 with fractions 0.199 and 0.371, with product 0.074. The negative contact improves agreement with J0437 and worsens it with J0740 individually. It leads among these fixed curves over all nine width/offset choices. Prior-weighted relativistic inference and additional stars would be required to infer such a term in nature.

28.5 Counterexamples in the remaining branches

The historical cutoff exceeds one in 5 of 22 confirmed McGill sources with eligible timing. The exact binomial reference interval on that 22.7% fraction is 7.8%–45.4%. Seventeen catalogued magnetars lie at or below the proposed necessary condition. Changing the cutoff after inspecting these stars cannot restore its original interpretation. R08

The Delft raw archive yields 245 accepted Bell trials from 4,746 candidate records. We recover 196 wins and S = 2.4225 ± 0.2038. The one-sided local-null tail is 0.03917 with the published random-input allowance. Under the additional identical Werner-visibility model, the fitted visibility is 0.849 with exact-binomial transformed 95% interval 0.691–0.985. A model of observer-

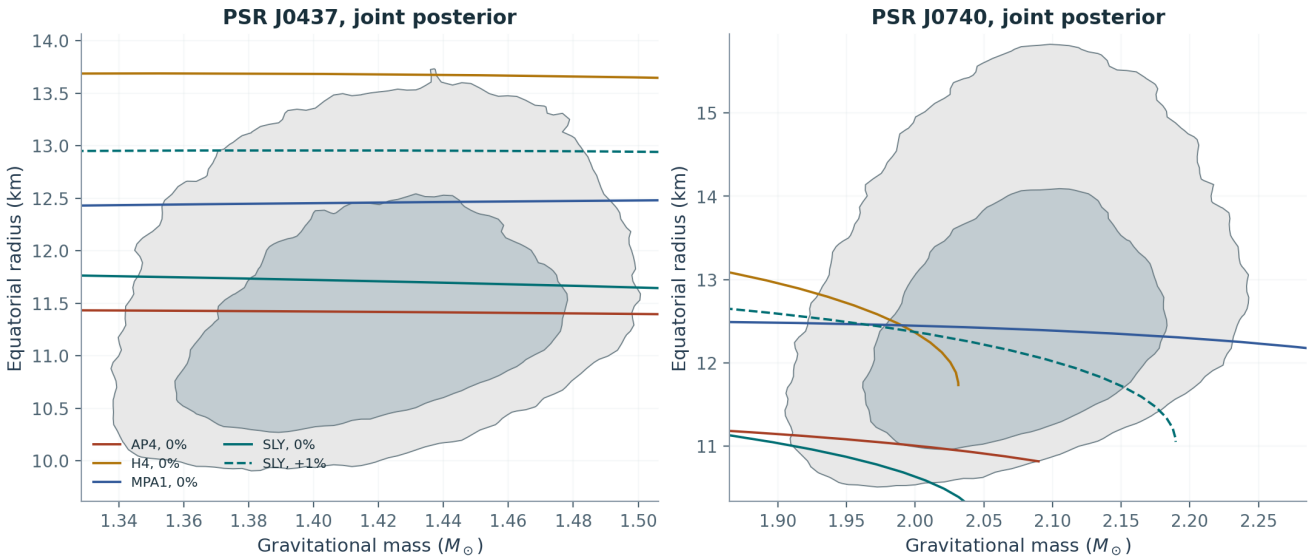

Figure 34. Highest-density 68% and 95% joint mass–radius regions estimated from the two released posteriors. Curves illustrate the spread across static EOS choices.

induced collapse needs to predict an outcome distribution conditional on a measurable intervention. These data verify a known quantum result. R88

Across 18 worldtubes in three isotropic backgrounds, none of the finite spheres is trapped at the instant of the bounce. 8 become future trapped in the contracting part of the simulated time window. The null-expansion identity agrees to 3.6e-16 in scaled units. A bouncing scale factor alone cannot certify a white-hole exterior or a daughter universe.

29 Validation plan and decision criteria

The research question to carry forward is whether measured spin or spin correlations cause a residual that survives known electromagnetic, nuclear, gravitational and instrumental effects. The most constrained formulation starts with one operator or response law, one physical system, and one predeclared observable. A cross-scale model must produce several observables from shared coefficients and observable scale-matching functions. The tests below use that requirement to assign actual risk to competing branches.

29.1 Experiment and analysis specifications

Claim or observable	Matched control and data	Decision criterion
Extra local magnetic dipole	Species, charge and state matched against QED and hadronic moments, with independent fine-structure or lattice inputs.	Fit a signed new coefficient in a declared scheme. A replicated residual with correct operator dependence is needed. Limits are conditional on the operator basis.
Scalar mode onset (9)–(12)	Canonical scalar/photon, fixed magnetic topology, calibrated dimensions, independent f_Φ, m_0 or ξ if accessible.	Lower eigenvalue crosses zero in the predicted mode, angular or gap scaling, and finite-domain threshold. Require the same coefficient in propagation and onset.
Standing-wave spin response (34), (43)	Equal-energy polarization and spin reversal, randomized order, signed readout, independently measured losses and spurious material resonances.	Signed overlap obeys the predicted spin parity and polarization dependence. Fit the gain band only after bounding joint spin and polarization backgrounds.
Induced force and curvature (35)–(40)	Independently matched charge for source and probe, conventional electromagnetic controls, recorded height, material and orientation, and a reference body.	Static acceleration follows the prespecified sign, magnitude and range from shared coefficients. A curvature claim also needs a tidal or light-deflection observable.
Shared spin mode (44)	Vacuum or independently characterized medium, frequency and range measured in the same regime.	The inferred mediator range and gap satisfy $2\pi L_s f_{\mathrm{gap}} = c$ for the canonical vacuum action. A medium shift requires its own calculated dispersion.
Rotation, chirality, clock or inertia	Reversal factorial, matched inertial mass and spin composition, clock sensitivities or torque null channels.	A reproducible prespecified parity contrast and its amplitude bound, after measured environmental regressors.
Spin coherence or state reduction	Bell/Ramsey sequence with field/exposure windows and process noise calibrated.	Rate and basis dependence agree with the specified dynamical map. Compare to noise and use raw outcomes to check marginals.

Claim or observable	Matched control and data	Decision criterion
Pulsar–magnetar threshold	Timing, independent field proxy, exposure and event-era data, source-disjoint validation.	Calibrated out-of-sample incremental likelihood above age, dipole and activity. Hard legacy class split already fails fixed counts.
Flares and glitches	Superfluid, torque and magnetoelastic timing, calibrated event exposures and contemporaneous field geometry.	Separate likelihoods per event family and a measurable dependence on the declared instability variable.
Magnetar polarimetry	QED, atmosphere, plasma and instrument transfer at the same phase and energy.	Joint Stokes likelihood for a single predicted residual over multiple sources or epochs.
New compact remnant stress	Shared GR and ESFD EOS, mass, angular momentum and topology, plus convergence-tested 3+1 data.	Stable, resolvable shift in equilibrium, oscillation, collapse or waveform mapped to a separately estimated field and spin.
Compact-merger precursor	Arrival correction, independent detectors, live time, response matrices and matched off-source windows.	Population fluence/incidence or polarization bound with trials included and injection recovery. Positive candidate requires timed, replicated signal.
Galactic excess gravity	SPARC and new disjoint magnetic maps with baryons, stars, and lensing samples.	Same normalization predicts $V(r)$ and gravitational slip/lensing on disjoint galaxies. Fixed per-galaxy scale fitting supplies a shape comparison.
Cluster, CMB or cosmic structure	Joint lensing and baryon templates, BAO, CMB TT/TE/EE and growth, common selection support.	A consistent perturbation cosmology fits background, structure and lensing over redshift with shared parameters.
QGP or CERN residual	Standard Model amplitude/transport, background, detector full response and correlated fitting.	Operator-specific spectrum or angular direction, tested at fixed pairing and cuts in independent or withheld data.

Claim or observable	Matched control and data	Decision criterion
Spin–torsion bounce	Covariant connection variation, microphysical equation of state, realistic shear and global geometry.	A stable bounce below computed validity scales and a predeclared external or cosmological observable.
Earth, vacuum devices, or field-observer	Matched environmental, energy and momentum channels, independent measurement and replicable protocol.	A predictive, dimensioned effect above the relevant baseline. Without a physical map the archive supplies a conjecture or proposal.

29.2 Statistical and numerical standards

Define the scientific unit before fitting. Repeated radii within a galaxy and repeated flares within an active region are correlated. Resample at the galaxy, source, or interval-block level as appropriate. A positive comparison against a flat null tests explanatory variation. To test an incremental spin mechanism, use a state-of-the-art baseline plus the measured spin predictor with equivalent access to inputs. For detection-like data, retain upper limits, exposure and selection efficiency. A measured effective field with geometry uncertainty is a latent-variable likelihood. For model comparison report pointwise residuals, a held-out score with uncertainty, and sensitivity to likelihood and priors. Any empirical choice of optimum threshold is trained in a development-only split, and legacy signed predictions remain frozen as archival controls.

An observational forward model is $\mathbf{y} = \mathcal{R}[\mathbf{h}_{\text{baseline}}(\boldsymbol{\eta}) + c_{\text{ESFD}}\,\mathbf{h}_{\text{spin}}(\boldsymbol{\theta})] + \boldsymbol{\epsilon}$ where $\mathcal{R}$ is the telescope, detector, or lab response and $\boldsymbol{\eta}$ holds nuisance parameters. Document the physical meaning, units, sign, and domain of validity of c_{ESFD} and $\boldsymbol{\theta}$. When available, quantify identifiability with the covariance-weighted derivative of the expected data after nuisance projection. If the predicted residual lies in the same direction as an age or calibration change, collect independent information that changes that degeneracy before interpreting a fitted coefficient. For a search across masses, bands, time windows or coefficients, estimate the global false-alarm probability using the same selection and entire search on the control set. Report a tested range for a null result, with sensitivity to injection and population assumptions.

For field computations validate conserved quantities and constraints, eigenvalue benchmarks, background recovery, units and numerical convergence. Vary mesh, time step, domain and dissipation settings. Record equations and their regularization, commits, compiler or Python versions, initial and boundary conditions, numerical cutoffs, and the parameter grid. Prespecify stability and nonlinear diagnostics. Qualitative agreement of an image or plot can be tested through its corresponding quantitative observable. A higher-order EFT term can sometimes be used perturbatively despite unphysical solutions of a fully resummed truncated equation. State explicitly which equations are solved and where their cutoffs lie.

29.3 Results that carry forward

The full rebuilt catalog pipeline and its summaries reproduce from the archived input snapshots. The longest-lived number in the original argument, Λ_{tim}, is useful as a historical comparison line,

and with timing-inferred dipoles it carries exactly the information of a characteristic-age threshold. The class and recurrence tests do not support the hard cut. The new exponential-action analysis provides a separate result in a fully specified local problem. An exponential gauge coupling with a quadratic independent scalar can destabilize a transverse electromagnetic mode even when its prescribed-B scalar curvature is positive. The unstable band and rate are mathematical predictions under the stated action and boundaries. The matched vacuum birefringence gives a conditional lower bound of $2.67 times 10^{15}$ G on its onset. A prescribed spin source and a photon gap alter the threshold in distinct ways, giving quantitative targets for a real spin-polarized plasma model.

The expanded calculations derive a fold for the printed June potential and find a separate ordering and mixed-mode onset in a spin-composite closure. The galaxy exercises now include exterior-radii and whole-galaxy prediction, absolute energy checks and a metric target for a joint fit with lensing. The stellar sequences show how a cold contact correction changes static equilibrium and where stability or causality terminate a tested EOS. The spin–shear calculation gives exact conditions for a turnaround within its homogeneous assumptions. Verifying a universal extra force, inertia of nonmagnetic matter, quantum measurement dynamics, and black-hole geometry still depends on measurements or derivations with explicit shared couplings.

30 Appendix A. Reconstruction ledger

The file **branch_register.csv** contains the more granular evidence and inference ledger. The table here identifies the version families and places their claims within this paper.

Version family and date evidence	Reconstructed content and disposition
June 2–3, 2025 project discussions and June Word version	Intrinsic spin, quark tensor, rigid rotors, the $B\Omega$ rule, saturation potential, clocks, QGP, solar or stellar flares, and merger precursor. Equations (1)–(2) and (13)–(15).
June 3 covariant synthesis in chat, later 2026 recap	Equation (3), historical ambiguity of independent versus composite Φ, time-feedback law, and torsion proposal. This edition restores the action from an excerpt and gives separate consistent variations, (4)–(7).
June consolidated SEFD, Electromagnetic Universe and quantum rewrite	Spin entropy, effective divergences, space and dark-matter alternatives, Pauli coupling, entanglement. Equations (8), (16)–(19), (23), and EFT matching.
June–July E_8, non-Abelian and UV extensions	Frame-Higgs and threshold narrative, masses and dipoles, Spin$(11,3)$, anomalous symmetry breaking, contact versus dipole matching. Section Exceptional symmetry.

Version family and date evidence	Reconstructed content and disposition
Three project PDF manuscripts and December proof copy	Population separation, global energies, compact limits, spin-generated gravity and inertia, relativity and simulations. Rebuilt data and several numerical corrections. Original analyses omitted by old exports are catalogued as unavailable inputs.
2026 Aharonov–Casher and spin reorientation discussion	Neutral-particle phase, response mapping, conventional quantum controls, proposed rotation/field reversal. Section Laboratory spin.
September 17, 2026 CERN versions	Higgs entanglement, off-shell vector density matrix, later distinction between ESFD residual and standard baseline. Equation (22), ATLAS and CMS comparisons.
Later observer and wave discussion, September 2026 cosmology	Observer interface, nested wave geometry, spin–torsion bounce and white-hole/daughter-universe scenarios. Equations (20)–(21), global matching and Bell/observer analysis.
Later related vacuum and astrophysical essays	Resonance, propulsion, anomalous observations, cosmic structure, Earth and vacuum questions. Environmental energy balance, field strength and evidence requirements.
Maxwell and Tesla project companion and gravity extension	Wave stress and invariants, spatial Floquet resonance, material response, finite Earth Yukawa integration, MICROSCOPE comparison and synthetic laboratory readout. Equations (34)–(44).

Additional historical numerical claims discussed in the project records include oscillation and glitch correlations in tiny hand-selected samples, predicted suppression scales near 100 MeV or 10–100 GeV depending on the draft, $\chi \lesssim 10^{-3}$ as an unspecified low-energy coefficient, and cosmic f_{NL} of order unity. A proposed value without operator definitions and a computed response remains an archival claim. In the re-evaluation PDF an external magnetosphere difference under 1%, a spin-fluid Poisson correction of order 10^{-8}, and a null spinning-ring or inertia test are described. The required equations, source parameters and run records are absent from the recovered inputs. They enter this edition as attributed statements. The new local stability solve, verified radius profiles, and TOV benchmarks provide independent calculations with defined assumptions. A1 A2 A6

31 Appendix B. Reproducible calculations and data dictionary

31.1 Included reruns

The companion ZIP places the archived inputs and baseline pipeline in **baseline/**. The 28 baseline manifest entries include ATNF and McGill timing snapshots and a HEASARC mirror, SPARC profiles, GOES and SILSO series, six LALSuite EOS tables, GWOSC and later Zenodo PE summaries, Fermi TTE files, and transcriptions of selected ATLAS, CMS and IXPE results. The inputs folder lists SHA-256 hashes for the two solar inputs, PREM density polynomials and published MICROSCOPE summary. The original 19-file recovery archive, its 40-lead inventory and the Maxwell companion travel with the data. The scripts check all three input manifests and reconstruct the summaries, data tables and figures. Definitions such as “confirmed,” “tagged,” “included event,” or “published interval” use the relevant source criteria.

Computation	Machine-readable outputs in the master package
Catalogs and historical cutoff	**baseline/results/atnf_catalog_with_metrics.csv**, **mcgill_catalog_with_metrics.csv**, **mcgill_alternate_timing_values.csv**, **glitch_recurrence_cohort.csv**.
TOV and mass/spin	**baseline/results/tov_sequences.csv**, **tov_maxima.csv**, **canonical_compact_energy_checks.csv**, **gwtc_cumulative_events.csv**, **gwtc_remnant_spin_summary.csv**.
Rotation and mass-scale checks	**baseline/results/sparc_all_radii.csv**, **sparc_model_fits.csv**, **sparc_model_predictions.csv**, **legacy_dwarf_and_cluster_scale_checks.csv**.
Transients, solar and collider	**baseline/results/gw170817_gbm_detectors.csv**, **gw170817_gbm_offset_scan.csv**, **gw170817_gbm_offsource_controls.csv**, **goes_silso_joined_months.csv**, **atlas_angular_residuals.csv**, **cms_polarization_witness_checks.csv**, **ixpe_polarization_benchmark.csv**.
Scalar growth and finite-size threshold	**results/esfd_scalar_stability.csv**, **esfd_scalar_dispersion.csv**, **esfd_scalar_evolution.csv**, **esfd_scalar_pvlas.csv**.
Spin alignment, flags and polarization	**results/esfd_timing_orientation.csv**, **esfd_spin_polarization.csv**, **esfd_spin_coarse_graining.csv**.
Gravitating magnetic field and torsion	**results/esfd_galaxy_magnetic_energy_budget.csv**, **esfd_torsion_bounce.csv**.

Computation	Machine-readable outputs in the master package
Original spin-potential and composite stability	**results/june_direct_saturation_branches.csv**, **spin_composite_mixed_modes.csv**.
Cold contact sensitivity	**results/stellar_spin_contact_sequences.csv**, **stellar_spin_contact_maxima.csv**.
Entire-galaxy transfer	**results/sparc_galaxy_holdout_predictions.csv**, **sparc_galaxy_holdout_metrics.csv**, **sparc_galaxy_holdout_coefficients.csv**.
Extended archive and timing checks	**results/glitch_chronological_cohorts.csv**, **glitch_chronological_scores.csv**, **solar_blocked_predictions.csv**, **solar_blocked_scores.csv**, **solar_archive_overlap_and_hemispheres.csv**, **gw170817_gbm_precursor_injections.csv**.
Quantum, shear and field-scale tests	**results/atlas_spin_coefficient_covariance_sensitivity.csv**, **esfd_quantum_dephasing_visibility.csv**, **spin_torsion_shear_thresholds.csv**, **spin_torsion_shear_trajectories.csv**, **esfd_cross_scale_field_rotation_scenarios.csv**.
Wave stress and resonance	**results/maxwell_polarization_stress_exchange.csv**, **standing_wave_spatial_band_convergence.csv**, **standing_wave_bloch_floquet_response.csv**. Normalized polarization, wave invariant, energy, stress, frequency, damping and Floquet observables.
Finite range, Earth and stored energy	**results/earth_scalar_force_cancellation.csv**, **electromagnetic_energy_scalar_charge.csv**. SI range and radial gradient, dimensionless transfer and signed coupling, same-mode gap and fixed-boundary charge checks.
Microscopic spin fluid and laboratory readout	**results/einstein_cartan_contact_scale.csv**, **spin_torsion_radiation_dust_bounces.csv**, **phase_sensitive_four_state_recovery.csv**. Density in SI, normalized bounce trajectories and synthetic response in single-read noise units.

The scalar sweep uses $B/B_c = 0$ to 4 and angles 0° to 90°. Azimuth enters only through the stated background symmetry. The illustrative time integration includes an otherwise stable normal-mode admixture. Galaxy residual estimates use the largest eligible measured radius per matched

fit and the square root of a volume-equivalent mass budget. The orientation calculation uses $0.5 \leq s_B \leq 4$ including exact rows at unity and two, and analytic probabilities under an assumed isotropic axis distribution. The degenerate gas model uses the neutron magnetic moment from the software constants and a density 0.16 fm^{-3}. The torsion toy sets $a/a_b = 1$ and $Ht_b = 0$ at the bounce. **baseline/results/summary.json** and **results/spin_benchmarks_summary.json** provide exact summary values. Reproduction commands, dependency versions and reference information accompany this document.

results/wave_gravity_summary.json records the exact new benchmark parameters and outputs. The wave calculation uses periodic spatial boundaries, a frozen pump and linearized spin perturbations. The force calculation is static and assumes a spherical, unscreened source with constant scalar charge per unit mass. The laboratory readout uses seeded synthetic noise and known injected amplitudes. The separately reported published free-fall input is a differential measurement of ordinary test masses.

31.2 Cross-scale correspondence and invalidation

The data cover mostly one-variable or reduced-model consequences. To claim a common ESFD mechanism across scales, a parameter matched to a dipole measurement must give the same low-energy scattering result, and a spin susceptibility calibrated in a stated medium must predict the sign and magnitude of the response in the qualified domain. A claimed relation between susceptibility and spin-down damping needs competing torques and independent B, and a claim about curvature needs independent dynamics and lensing. Predefined uncertainty envelopes convert failures to operator bounds. When multiple independently normalized operators are allowed, tests constrain each measured response and the rank of the joint inference. These requirements prevent a new expression for χ from absorbing a failed prediction by changing its definition after the measurement.

32 What would establish the unified claim?

The project began with a change in the behavior of a spinning object. The clearest experimental statement that can now be made about that idea is conditional on a material phase and a readout. For a superconducting specimen, simultaneous measurements of rotation, superconducting stiffness or penetration depth, magnetic moment and the acceleration of a separate body are needed to connect the proposed chain. A single trace of motion cannot establish which step supplied the signal. The archived spinning-top observation by itself supplies no estimate of the coupling in equation (55).

32.1 A superconducting test with a definite outcome

For a claim that is odd in both signed angular speed and applied axial field, write $y = a_z^{\text{above}} - a_z^{\text{reference}}$, where the reference is offset from the proposed source response and its geometric transfer is measured. At fixed magnitudes of rotation and field define

$$D(T) = \frac{y_{++} - y_{+-} - y_{-+} + y_{--}}{4}, \qquad D_{\text{phase}} = D(T < T_c) - D(T > T_c). \tag{62}$$

This contrast has acceleration units. It removes contributions depending on a single reversal alone. London fields, ordinary rotation-induced magnetization coupled to field gradients, trapped flux, temperature-dependent susceptibility and correlated mechanical vibration can share the same parity. Each therefore requires a simultaneously measured magnetic or mechanical transfer function. A normal metal and a stationary specimen supply additional null channels. Changing sensor height tests the fixed geometric response in (56). An even-in-rotation shielding claim instead belongs in the temperature-switched average over the four states. Using only (62) would cancel such a signal.

Measure T_c and the superconducting response in the actual specimen, record its field-cooling and vortex history, and retain every acquisition interval with its selection flag. Independently determine the gap and the slope of its squared frequency against pair density. Lock the sign, geometry, exposure and predicted gravity signal using that calibration before evaluating a reserved set of temperatures, speeds or a second material. A second measurement of ordinary London flux alone would leave the proposed acceleration coupling unidentified. A repeatable excess in a calibrated free-body or tidal channel, with the correct height and phase dependence across material and field controls, would materially change the case. A null with a known sensitivity narrows the dimensioned coupling for those settings.

32.2 How the source branches stand after the rerun

Branch in the research program	Result or remaining discriminating evidence
Mechanical rotation, inertia and clocks	A measured angular velocity is distinct from microscopic polarization. Classical fixed-pivot stability has an exact threshold. A clock or inertial deviation needs a calibrated geometry, environment and species response. The historical rotor/clock series is unavailable.
Maxwell, Tesla and vacuum fluctuations	The standing-wave invariant changes with polarization at matched mean energy. Historical sources describe stationary waves. A propagating extra material coordinate, its coupling and a measurable pole are separate hypotheses.
Pauli, quark, Higgs and exceptional-symmetry branches	The dimensioned Pauli operator, quark-tensor matrix elements and electroweak embedding are stated earlier. The available records supply no evaluated flow from an E_8 embedding to common low-energy coefficients or measured Higgs, gravitational and galactic parameters.

Branch in the research program	Result or remaining discriminating evidence
Condensate, spin tensor and nonlinear response	The quadratic tensor shift, two-scalar exchange, coupled free energy and finite-energy cavity yield exact or numerical consequences within declared actions. Fitted magnetic length and rotation response are available for Nb. An independently measured second spin mode would bridge the theories.
Laboratory gravity and dense spin matter	Couplings present in normal matter meet terrestrial free-fall limits. Couplings confined to superconductivity meet YBCO limits under specified conditions. A negative spin–torsion stress can influence the idealized dense-fluid model, although minimal normalization is negligible at ordinary nuclear density.
Pulsars, magnetars, black holes and neutron stars	Timing alone reduces the legacy index to characteristic age. Glitches, X-ray polarization, EOS and merger information measure separate quantities. The primary shared NICER overlap favors one negative surrogate term in one EOS, with opposing effects on the two observed stars.
Solar cycling, flaring and merger precursors	The available GOES/SILSO archives, hemisphere tests and Fermi event/off-source/injection analyses reproduce in the full run. Exposure, event selection and independently predicted timing remain necessary for a distinctive ESFD signal.
Galaxies, filaments, clusters and the Great Attractor	The revised profile survives dwarf kinematics and faces a quantitative lensing test. Radio polarization contributes information about global rotation. Anisotropy, a relativistic stress tensor, lensing slip and predicted cluster-scale mass maps remain open. A disk fit cannot account for those scales by extrapolation.
Collapse, horizons, white holes and daughter universes	The computed homogeneous bounce has ordinary finite-sphere null expansions at its turning point. No matched exterior, global causal diagram and distinctive observed signature have been derived from the recovered action.

Branch in the research program	Result or remaining discriminating evidence
Quantum coherence, the observer and emergent spacetime	The Delft trial record reproduces quantum correlations incompatible with the tested local classical assumptions. The field-observer extension needs an operational intervention and outcome probabilities. A hierarchy of patterns still needs an inferred metric and causal propagation law.

The packaged **branch_register.csv** retains 75 individually identified claims, sources, tests and evidence gaps. The original *Proof*, *Re-Evaluation* and *Testing* project PDFs, the recovered Word manuscript and the Maxwell companion remain identified in the source records. The old long master called v150 was located as a historical document reference. Its underlying manuscript and the raw runs for some early FDTD, GRMHD and rotor claims could not be recovered. This master reconstructs the equations from accessible originals, preserves historical alternatives, and supplies new explicit completions. An unavailable derivation has not been treated as a successful reproduction.

33 Sources and references

33.1 ESFD project sources

A1 Grenke, Christopher. *Spin–Field Saturation Dynamics (ESFD): A Unified Framework for Emergent Gravity, Collapse, and Quantum Coherence*. June 3, 2025 Word metadata, archived as **6-3-spin ESFD current .docx**. Sections 3, 5, 8–11 and 14–17 supply the principal original equations, phenomenological cutoff, laboratory proposals and extensions.

A2 *Re-Evaluation of Electromagnetic Spin–Field Dynamics (ESFD) Theory*. Recovered 18-page project PDF. The text reports weak-coupling tests and a set of simulations. Section 3 is the historical record of those simulations.

A3 *Testing Electromagnetic Spin–Field Dynamics (ESFD) Theory with Astrophysical Data*. Recovered five-page project PDF. Sections 1–3 introduce the canonical energy comparison and pulsar, magnetar and compact-object reference values.

A4 *Proof of the Electromagnetic Spin–Field Dynamics (ESFD) Theory*. Recovered 22-page project PDF and editable counterpart, with the latter dated December 10, 2025 in its metadata. The proof title identifies the historical document. Sections 2–6 include the action sketch, emergent-gravity case and normalized saturation variables.

A5 Grenke, Christopher. 2026 September 17 CERN-era drafts, including **PN_ESFD_CERN_FULL_FRAMEWORK_CMS_BODY.html**, the original and corrected Higgs entanglement articles, and their entry/source records. ESFD project topic at Pattern Nexus.

A6 ESFD project conversation excerpts from June–September 2025, December 2025, and June–September 2026. The package's **provenance/historical_notes.md** identifies dates and speaker roles where recovered. The 2025 June 3 covariant-action excerpt and the later corrected-model recap are distinct from the available June Word file. The **recovery_leads.csv** record inside the

original archive identifies unavailable original bytes and runs.

A7 Grenke, Christopher. *The Trap of Reality: Consciousness, the Observer, and the Field Layer Beneath Spacetime*. Three archived 2026 text versions and a later related Pattern Nexus consciousness preview. The wave-emergence discussion is dated December 2025. Published observer essay.

A8 Grenke, Christopher. *The Vacuum Program: Zero-Point Energy, UAP Disclosure, and the Physics Hiding in Plain Sight*. Related project working HTML and sources in **provenance/related/**, alongside the prior recovery register and research histories.

A9 ESFD source and equation reconciliation, November 23, 2026. Direct source checks, June Word metadata, three project PDF versions, archival lead identifiers, and the contrasting composite-field and independent-field interpretations. Included in **provenance/**.

A10 *Maxwell, Tesla, and an ESFD standing-wave calculation*, November 23, 2026. Project companion on counterpropagating waves, the composite gauge coefficient, mixed modes and a uniform Floquet calculation. The original **ESFD_Maxwell_Standing_Wave_Response.html** is included in **provenance/**. The extended derivation and numerical checks are incorporated into this master paper.

33.2 Physics literature and data

R01 Hehl, F. W., von der Heyde, P., Kerlick, G. D., and Nester, J. M. (1976). *General relativity with spin and torsion: Foundations and prospects*. Reviews of Modern Physics 48, 393. Shapiro, I. L. (2002). *Physical aspects of the space-time torsion*. Physics Reports 357, 113–213. Hehl et al. · Shapiro.

R02 Fan, X., Myers, T. G., Sukra, B. A. D., and Gabrielse, G. (2023). *Measurement of the electron magnetic moment*. Physical Review Letters 130, 071801. Schwinger, J. (1948). Leading radiative magnetic moment result. Fan et al. · Schwinger.

R03 Grzadkowski, B., Iskrzyński, M., Misiak, M., and Rosiek, J. (2010). *Dimension-six terms in the Standard Model Lagrangian*. JHEP 10, 085. Operator basis and conventions.

R04 Becattini, F., and Lisa, M. A. (2020). *Polarization and vorticity in the quark–gluon plasma*. Annual Review of Nuclear and Particle Science 70, 395–423. Review.

R05 Spitkovsky, A. (2006). *Time-dependent force-free pulsar magnetospheres: axisymmetric and oblique rotators*. Astrophysical Journal Letters 648, L51–L54. Paper.

R06 Adler, S. L. (1971). *Photon splitting and photon dispersion in a strong magnetic field*. Annals of Physics 67, 599–647. Dunne, G. V. (2004). *Heisenberg–Euler effective Lagrangians: basics and extensions*. Adler · Dunne.

R07 Aharonov, Y., and Casher, A. (1984). *Topological quantum effects for neutral particles*. Physical Review Letters 53, 319. Cimmino, A., et al. (1989). Neutron interferometry measurement. Sangster, K., et al. (1993). Atom interferometry measurement. Theory · Neutrons · Atoms.

R08 Manchester, R. N., Hobbs, G. B., Teoh, A., and Hobbs, M. (2005). *The Australia Telescope National Facility pulsar catalogue*. Astronomical Journal 129, 1993. Public 2.9.0 timing and glitch snapshots and HEASARC compilation. Olausen, S. A., and Kaspi, V. M. (2014). McGill magnetar catalog. ATNF paper · CSIRO catalog · HEASARC mirror · McGill paper · McGill tables.

R09 Kaspi, V. M., and Beloborodov, A. M. (2017). *Magnetars*. Annual Review of Astronomy and Astrophysics 55, 261–301. Review.

R10 Gavriil, F. P., et al. (2008). *Magnetar-like emission from the young pulsar in Kes 75*. Science 319, 1802–1805. NASA Fermi Crab Nebula flare summary. Kes 75 study · Crab Nebula observations.

R11 CHIME/FRB Collaboration (2020). *A bright millisecond-duration radio burst from a Galactic magnetar*. Nature 587, 54–58. Observation.

R12 Viganò, D., et al. (2013). *Unifying the observational diversity of isolated neutron stars via magneto-thermal evolution models*. Monthly Notices of the Royal Astronomical Society 434, 123–141. Magneto-thermal comparison.

R13 Israel, G. L., et al. (2005). *The discovery of rapid X-ray oscillations in the tail of the SGR 1806–20 hyperflare*. Astrophysical Journal Letters 628, L53. QPO study.

R14 Hessels, J. W. T., et al. (2006). *A radio pulsar spinning at 716 Hz*. Science 311, 1901–1904. Breu, C., and Rezzolla, L. (2016). *Maximum mass, moment of inertia and compactness of relativistic stars*. MNRAS 459, 646–656. 716 Hz observation · Uniform rotation estimates.

R15 Taverna, R., et al. (2022). *Polarized X-rays from a magnetar*. Science 378, 646–650. IXPE result.

R16 Tolman, R. C. (1939). Static relativistic fluid solutions. Oppenheimer, J. R., and Volkoff, G. M. (1939). Massive neutron core equilibrium. LALSuite public EOS tables, software release 8.0.2 in the snapshot. Tolman · Oppenheimer–Volkoff · LALSuite.

R17 Ji, X. (1997). *Gauge-invariant decomposition of nucleon spin*. Physical Review Letters 78, 610. Yang, Y.-B., et al. (2018). *Proton mass decomposition from the QCD energy momentum tensor*. Physical Review Letters 121, 212001. Ji · Yang et al..

R18 STAR Collaboration (2017). *Global Λ hyperon polarization in nuclear collisions*. Nature 548, 62–65. STAR Collaboration (2022). Blind analysis of the chiral magnetic effect in isobar collisions. Physical Review C 105, 014901. Polarization · Isobar analysis.

R19 Kerr, R. P. (1963). *Gravitational field of a spinning mass as an example of algebraically special metrics*. Physical Review Letters 11, 237. GWOSC cumulative event snapshot and GWTC-4.1/5.0 PE tables. LVK GW230529 event. Kerr · GWOSC · GWTC-4.1 PE · GWTC-5.0 PE · GW230529.

R20 Blandford, R. D., and Znajek, R. L. (1977). *Electromagnetic extraction of energy from Kerr black holes*. MNRAS 179, 433–456. Paper.

R21 LIGO, Virgo, Fermi GBM and INTEGRAL (2017). *Gravitational waves and gamma-rays from a binary neutron star merger: GW170817 and GRB 170817A*. ApJL 848, L13. Public Fermi GRB170817A time-tagged events. Joint analysis · GBM data.

R22 Xiao, S., et al. (2022). *The peculiar precursor of a gamma-ray burst from a binary merger involving a magnetar*. Precursor study and QPO candidate.

R23 Touboul, P., et al. (2022). *MICROSCOPE mission: final results of the test of the equivalence principle*. Physical Review Letters 129, 121102. Final result.

R24 Bothwell, T., et al. (2022). *Resolving the gravitational redshift across a millimetre-scale atomic sample*. Nature 602, 420–424. Clock measurement.

R25 Everitt, C. W. F., et al. (2011). *Gravity Probe B: final results of a space experiment to test general relativity*. Physical Review Letters 106, 221101. Frame-dragging measurement.

R26 Beck, R. (2016). *Magnetic fields in spiral galaxies*. Astronomy and Astrophysics Review 24, 4. Observational review.

R27 Heckel, B. R., et al. (2008). *Preferred-frame and CP-violation tests with polarized electrons*. Physical Review D 78, 092006. Polarized torsion pendulum.

R28 Lelli, F., McGaugh, S. S., and Schombert, J. M. (2016). *SPARC: mass models for 175 disk galaxies with Spitzer photometry and accurate rotation curves*. Astronomical Journal 152, 157. Paper · Data.

R29 McGaugh, S. S., Lelli, F., and Schombert, J. M. (2016). *Radial acceleration relation in rotationally supported galaxies*. Physical Review Letters 117, 201101. Reference relation.

R30 Fukushima, K., Kharzeev, D. E., and Warringa, H. J. (2008). *The chiral magnetic effect*. Physical Review D 78, 074033. Constitutive effect.

R31 Visser, M. (2002), review of Sakharov induced gravity. Jacobson, T. (1995), thermodynamic field-equation argument. Verlinde, E. (2011), entropic-gravity proposal. Visser · Jacobson · Verlinde.

R32 Haisch, B., Rueda, A., and Puthoff, H. E. (1994). *Inertia as a zero-point-field Lorentz force*. Physical Review A 49, 678. Cramer, J. G. (1986). *The transactional interpretation of quantum mechanics*. Reviews of Modern Physics 58, 647. Vacuum-inertia proposal · Transactional interpretation.

R33 Wolf, J., et al. (2010). Masses of dispersion-supported galaxies. Umetsu, K., et al. (2015). Weak-lensing analysis of Abell 1689. Draco half-light estimate · Abell 1689 comparison.

R34 Alves, J., et al. (2020). *A Galactic-scale gas wave in the solar neighbourhood*. Nature 578, 237–239. Konietzka, R., et al. (2024). *The Radcliffe Wave is oscillating*. Nature 628, 62–65. Tully, R. B., et al. (2014). *The Laniakea supercluster of galaxies*. Nature 513, 71–73. Radcliffe discovery · Wave kinematics · Peculiar velocity structure.

R35 Clowe, D., et al. (2006). Bullet Cluster weak-lensing and baryon offset. Astrophysical Journal Letters 648, L109–L113. Weak-lensing study.

R36 Planck Collaboration (2020). Planck 2018 cosmological parameters and primordial non-Gaussianity analyses. Parameter results · Non-Gaussianity constraints.

R37 Planck Collaboration (2016), primordial magnetic fields. Minami, Y., and Komatsu, E. (2020), cosmic polarization analysis. Magnetic field constraints · Birefringence methods.

R38 Popławski, N. J. (2010, 2016, 2020). Einstein–Cartan cosmology and spin-fluid collapse examples. Cosmology with torsion · Universe in a black hole · Collapse with torsion.

R39 Penrose, R. (1965), gravitational collapse and spacetime singularities. Haggard, H. M., and Rovelli, C. (2015), black-to-white hole tunneling proposal. LVK (2021), GR tests with GWTC-3. Singularity theorem · Tunneling proposal · Waveform tests.

R40 Shamir, L. (2025). *The distribution of galaxy rotation in JWST Advanced Deep Extragalactic Survey*. MNRAS 538, 76–91. Deep-field result.

R41 ALICE Collaboration (2016). *Direct photon production in Pb–Pb collisions at 2.76 TeV*. Physics Letters B 754, 235–248. Photon spectra.

R42 CERN. Higgs field and boson, physical context and discovery summary. Higgs overview.

R43 Bezrukov, F. L., and Shaposhnikov, M. (2008). *The Standard Model Higgs boson as the inflaton*. Physics Letters B 659, 703–706. Nonminimal-curvature model.

R44 ATLAS Collaboration (2026). *Measurements of Z-boson pair entanglement in decays of Higgs bosons at the ATLAS experiment*. Relevant angular coefficients are in Table 1. Paper with table · Result record.

R45 CMS Collaboration. *Study of spin correlations in Higgs boson decays to four leptons*. CMS-PAS-HIG-25-011. Results, figures and covariance context.

R46 ATLAS Collaboration (2024). *Observation of quantum entanglement with top quarks at the ATLAS detector*. Nature 633, 542–547. Top-quark result.

R47 Lisi, A. G. (2007). *An exceptionally simple theory of everything*. Distler, J., and Garibaldi, S. (2010). *There is no "theory of everything" inside E_8*. Communications in Mathematical Physics 298,

419–436. Lisi proposal · Distler–Garibaldi obstruction.

R48 Clauser, J. F., Horne, M. A., Shimony, A., and Holt, R. A. (1969), correlation inequality. Horodecki, R., Horodecki, P., and Horodecki, M. (1995), criterion for two-qubit CHSH violation. Hensen, B., et al. (2015), loophole-free spin test. CHSH · Two-qubit criterion · Spin experiment.

R49 Lindblad, G. (1976). *On the generators of quantum dynamical semigroups*. Communications in Mathematical Physics 48, 119–130. Bassi, A., et al. (2013). Collapse models and experimental tests. Reviews of Modern Physics 85, 471. Generator · Collapse models.

R50 Hoffman, D. D., and Prakash, C. (2014). *Objects of consciousness*. Frontiers in Psychology 5, 577. Conscious-agent proposal.

R51 NOAA National Centers for Environmental Information, GOES science-quality flare report. WDC–SILSO, Royal Observatory of Belgium, Brussels, daily sunspot numbers. The package contains project-provided snapshots of the two sources. GOES documentation · SILSO data.

R52 Bobra, M. G., et al. (2014). HMI vector magnetic field pipeline and Space-Weather HMI Active Region Patches. Solar Physics 289, 3549–3578. NOAA Space Weather Prediction Center. SHARP field data methods · Space weather reference.

R53 U.S. Geological Survey. Geomagnetic disturbances and earthquake science. USGS earthquake causation FAQ.

R54 Jaffe, R. L. (2005). *Casimir effect and the quantum vacuum*. Physical Review D 72, 021301. Wilson, C. M., et al. (2011). *Observation of the dynamical Casimir effect in a superconducting circuit*. Nature 479, 376–379. Static interpretation · Driven experiment.

R55 Tajmar, M., Neunzig, O., and Weikert, M. (2021). *High-accuracy thrust measurements of the EMDrive and elimination of false-positive effects*. Pais, S. C., U.S. Patent 10,144,532. Precision thrust study · Patent record.

R56 DARPA ARRIVE research description and 2026 ExPEDitions proposer lightning talks, including the reported power-cell voltages. NASA independent UAP report and public scientific FAQ. Related vacuum documentation in A8. ARRIVE · Proposer slides · NASA UAP scientific summary.

R57 Balezin, M., et al. (2018). *Electromagnetic properties of the Great Pyramid: first multipole resonances and energy concentration*. Journal of Applied Physics 124, 034903. Driven-scattering study.

R58 Wigner, E. P. (1939). *On unitary representations of the inhomogeneous Lorentz group*. Annals of Mathematics 40, 149–204. Particle spin representations.

R61 Horodecki, R., Horodecki, P., and Horodecki, M. (1995). *Violating Bell inequality by mixed spin-1/2 states, necessary and sufficient condition*. Physics Letters A 200, 340–344. Two-qubit CHSH criterion.

R62 Popławski, N. J. (2012). *Nonsingular, big-bounce cosmology from spinor-torsion coupling*. Physical Review D 85, 107502. See also the author's 2021 IBERICOS proceedings on shear competition. Spinor-torsion paper · Shear discussion.

R59 Event Horizon Telescope Collaboration (2019), first M87 shadow results. NANOGrav Collaboration (2023), 15-year stochastic-background evidence. EHT baseline · NANOGrav baseline.

R60 Ejlli, A., Della Valle, F., Gastaldi, U., Messineo, G., Pengo, R., Ruoso, G., and Zavattini, G. (2020). *The PVLAS experiment: a 25 year effort to measure vacuum magnetic birefringence*. Physics Reports 871, 1–74. Final measurement and convention.

R63 Giulini, D. (2018). *Laue's theorem revisited: Energy-momentum tensors, symmetries, and the habitat of globally conserved quantities*. International Journal of Geometric Methods in Modern

Physics 15, 1850182. Stationary integrated stress.

R64 Fulling, S. A., et al. (2007). *How does Casimir energy fall?* Physical Review D 76, 025004. Including the interaction energy in the complete system.

R65 Dziewonski, A. M., and Anderson, D. L. (1981). *Preliminary reference Earth model*. Physics of the Earth and Planetary Interiors 25, 297–356. Original PREM, density polynomials in Table I.

R66 Fayet, P. (2026). *Hyperbolic form factors for Yukawa interactions, and applications to the Earth*. European Physical Journal C 86, 1125. Finite-source kernel and nominal satellite altitude.

R67 Touboul, P., et al. (MICROSCOPE Collaboration, 2022). *MICROSCOPE mission: Final results of the test of the equivalence principle*. Physical Review Letters 129, 121102. Final Ti–Pt free-fall measurement.

R68 Popławski, N. (2016). *Universe in a black hole in Einstein–Cartan gravity*. Astrophysical Journal 832, 96. Journal article · Author's preprint with spin-fluid coefficient.

33.3 Sources for the independent data and proofs

R69 Ferrer, F., and Grifols, J. A. (2001). Vacuum and thermal two-scalar exchange. The vacuum expression gives the $K_1(2mr)/r^2$ dependence used here. Physical Review D 63, 025020.

R70 Damour, T., and Donoghue, J. F. (2010). Nuclear electromagnetic dilaton charges and equivalence-principle tests. Operator normalization and composition dependence.

R71 McDonough, W. F. (2003), *Compositional Model for the Earth's Core*, Table 5. Fayet, P. (2018), *MICROSCOPE limits for new long-range forces and implications for unified theories*, test alloy compositions. Commission on Isotopic Abundances and Atomic Weights, standard atomic weights. Earth chemistry · Alloy composition · Atomic weights.

R72 Tong, D., *Classical Dynamics*, rigid bodies and the sleeping top. Barnett, S. J. (1915), *Magnetization by Rotation*. Stability derivation · Rotation-induced magnetization.

R73 Oh, S.-H., et al. (2015). *High-resolution Mass Models of Dwarf Galaxies from LITTLE THINGS*. Astronomical Journal 149, 180. Tables 1–2 and data behind Figures 2–4. SPARC comparison positions from VizieR J/AJ/152/157. Article and figure data · Position catalog.

R74 Mistele, T., McGaugh, S., Lelli, F., Schombert, J., and Li, P. (2024). *Indefinitely Flat Circular Velocities and the Baryonic Tully–Fisher Relation from Weak Lensing*. Astrophysical Journal Letters 969, L3. Revised Table 1 and tabulated mass-bin means in Table 2. Article · Machine-readable table.

R75 Choudhury, D., et al. (2024). *A NICER View of the Nearest and Brightest Millisecond Pulsar, PSR J0437–4715*. The headline equally weighted joint mass–radius posterior and authors' documentation are included in the computational package. Data and original report.

R76 Salmi, T., et al. (2024). *The Radius of the High-mass Pulsar PSR J0740+6620 with 3.6 yr of NICER Data*. The selected joint posterior and authors' documentation are included. Data and original report.

R77 Bovy, J., *galpy*, logarithmic halo potential and its spherical limit. Potential and normalization.

R78 Bekenstein, J., and Milgrom, M. (1984). *Does the missing mass problem signal the breakdown of Newtonian gravity?* Astrophysical Journal 286, 7–14. Modified Poisson action and limits.

R79 Power, E. A., and Thirunamachandran, T. (1993). *Casimir–Polder potential as an interaction between induced dipoles*. Vacuum fluctuation and dipole calculation.

R80 Tabatabaei, F. S., et al. (2016). *An Empirical Relation Between the Large-scale Magnetic Field and the Dynamical Mass in Galaxies*. Astrophysical Journal Letters 818, L10. All integrated 4.8 GHz flux and global-property measurements used here are central values from Table 1. Paper and table.

R81 Tate, J., et al. (1989, 1990). Precision niobium rotating-ring measurements of the London moment and the observable Cooper-pair mass. Cabrera, B., and Peskin, M. E. (1989), *Cooper-pair mass*. Letter · Full measurement · Historical theoretical reference.

R82 McFadden, R. M. L., et al. (2026). Niobium penetration depth and coherence length from muon spin spectroscopy and secondary-ion mass spectrometry, supplement Table S4 and main Table II. Journal · Report with supplement.

R83 Podkletnov, E., and Nieminen, R. (1992), original YBCO claim. Li, N., et al. (1997), static gravimeter test. Hathaway, G., Cleveland, B., and Bao, Y. (2003), rotating-disk weight test. Original · Static measurement · Rotating test.

R84 Liarte, D. B., et al. (2017), Fermilab report PUB-16-699-TD, Table I, representative thermodynamic critical fields of Nb, Nb_3Sn, NbN and MgB_2. Nagamatsu, J., et al. (2001), superconductivity at 39 K in MgB_2. Cava, R. J., et al. (1987), bulk superconductivity at 91 K in a single-phase yttrium barium cuprate. Materials table · MgB_2 · YBCO.

R85 Hg-1223 ambient-pressure benchmarks. The earlier report attributed a transition as high as 133 K to Hg-1223. Deng, L., et al. (2026) reported a resistive onset as high as 151 K in a pressure-quenched metastable sample. Earlier measurement · 2026 paper.

R86 Drozdov, A. P., et al. (2019). *Superconductivity at 250 K in lanthanum hydride under high pressures*. Nature 569, 528–531.

R87 Verheijen, A. A., et al. (1990). *Measurement of the London moment in two high-temperature superconductors*. Nature 345, 418–419.

R88 Hensen, B., et al. (2015). *Loophole-free Bell inequality violation using electron spins separated by 1.3 kilometres*. Nature 526, 682–686. The original archive includes recorded events, readout and input definitions and the authors' gate example. Experiment · 4TU data.

R89 Faraoni, V. (2011). *Cosmological apparent and trapping horizons*. Physical Review D 84, 024003. Expansions and apparent horizon in FLRW geometry.

R90 Lander, S. K. (2013), *Magnetic Fields in Superconducting Neutron Stars*. Neutron-vortex and proton-flux-tube dynamics are treated separately in work on interlinked arrays. Type-II core equilibrium · Vortex and flux densities.

Does the galaxy equation travel?

The revised ESFD-project equation predicted the shapes of 245 further galaxy rotation curves using two coefficients carried over from SPARC. Most galaxies improved substantially over stars and gas alone. An established one-parameter acceleration law reached essentially the same accuracy.

Prediction	Median galaxy error (km/s)	Lower error with revised core
Stars and gas alone	64.82	236 / 245
Original spin–entropy flux	36.12	193 / 245
Shared NFW halo	34.74	186 / 245
Shared Burkert halo	35.66	202 / 245
Radial acceleration relation	30.06	112 / 245
Revised cored law	29.92	—

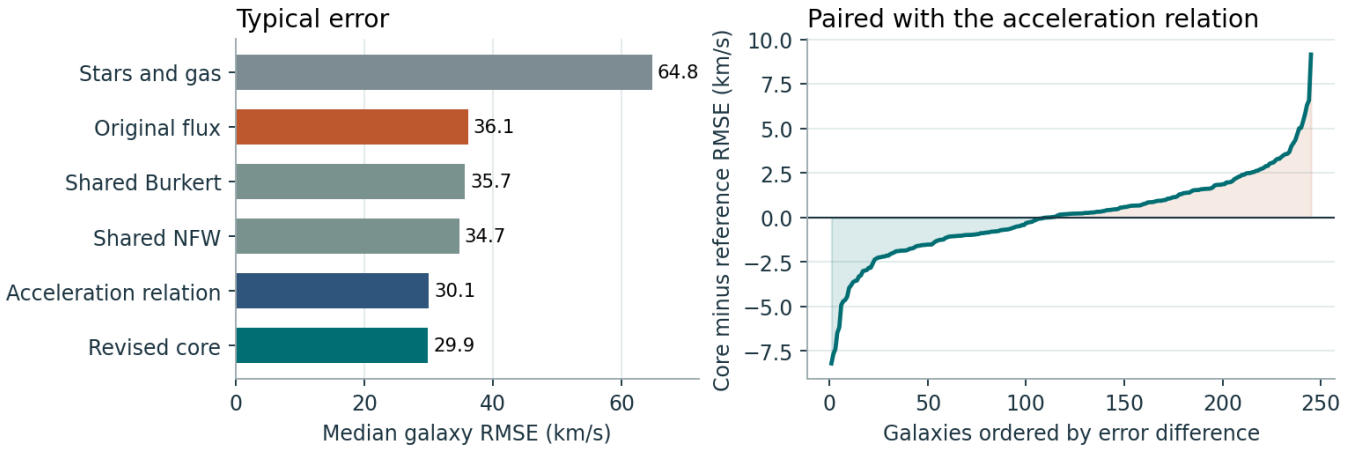

The left panel gives each galaxy equal weight. On the right each galaxy is compared with itself. Values below zero favor the revised core. The median paired difference is +0.21 km/s, with a galaxy-bootstrap 95% interval of −0.06 to +0.33 km/s.

At each measured position, the test asked how fast the material should orbit based on the galaxy's visible contents and size. The empirical correction captured a pattern across many galaxies. Its inputs are mass and size. Identifying an electromagnetic cause requires an independent magnetic observable that predicts the remaining speed differences.

Research update for Christopher Grenke's ESFD project · November 23, 2026. The revised core and original flux prescription belong to the galaxy branch developed alongside Spin–Entropy Field Dynamics (SEFD). The full spin–field framework contains additional equations and predictions.

PROBES I data and documentation · ALFALFA and optical counterpart tables · McGaugh, Lelli & Schombert (2016)

How the external test was built

PROBES I contains 3,163 rotation curves. Its radial velocity data were already centered by the survey. The selection required a suitable optical counterpart and a high-confidence ALFALFA neutral-hydrogen detection within 30 arcseconds and 300 km/s. We excluded SPARC provenance, matches within three arcminutes of all 175 SPARC locations or the earlier LITTLE THINGS comparison sample, very nearby recession speeds, uncertain inclinations, and inadequate radial sampling. This left 245 galaxies and 16,120 measured positions on the approaching and receding sides.

We used the absolute velocities, corrected for inclination and redshift, using the r-band inclination at the 23.5 mag/arcsec² isophote. We used CMB-frame recession distances with H_0 = 73 km/s/Mpc, scaled stellar masses from photometry to those distances, and inferred atomic gas mass from H I flux with a factor of 1.33 for helium. We represented stars and gas as two thin exponential disks. The stellar length R_d was estimated from the half-light radius divided by 1.678. Molecular gas, bulge structure, individual gas maps, peculiar velocities and noncircular motions remain sources of error.

$$V^2(r) = V^2_{bar}(r) + \sqrt{(G\, M_{bar}\, a_*)}\, r^2 / [r^2 + (\eta R_d)^2]$$

Here r is distance from the center, V_{bar} is the Newtonian speed from the two disks, and M_{bar} is the sum of stellar and gas masses. The preceding SPARC fit supplied $a_* = 8.8127 \times 10^{-11}$ m/s² and $\eta = 1.3929$. The comparison law used $g_{obs} = g_{bar} / [1 - \exp(-\sqrt{(g_{bar}/a_0)})]$, with $a_0 = 1.1171 \times 10^{-10}$ m/s² calibrated on those same SPARC data. Each halo comparison used one shared pair of parameters. A ΛCDM population analysis would also include a distribution of halo properties.

Change in assumed mass distribution	Core (km/s)	Acceleration law (km/s)
Gas scale = 2 stellar scales	29.92	30.06
Gas scale = 1.5 stellar scales	29.27	27.86
Gas scale = 3 stellar scales	30.79	32.42
Stellar masses × 0.71	36.93	37.36
Stellar masses × 1.41	27.43	26.63

We computed the root-mean-square speed error within each galaxy, then took the median across galaxies. The core won 112 individual comparisons against the acceleration law and lost 133. Changing the assumed gas scale reversed their ranking. Each of 10,000 paired bootstrap draws resampled whole galaxies. The interval quantifies sampling variability for this selected set only.

PROBES I data and documentation · SPARC data and mass models · McGaugh, Lelli & Schombert (2016)

A larger test of overall speed

For 11,758 additional galaxies, the archive supplies a single hydrogen-line width and an optical stellar mass. These measurements can test the predicted speed scale even when they give no information about the shape of a rotation curve.

At very large radius, the revised formula gives $V_{\infty} = (G\, M_{bar}\, a_{*})^{1/4}$. This familiar mass-to-the-one-quarter scaling is shared with the baryonic Tully–Fisher relation and the low-acceleration limit of the comparison law. We used the same fixed a_{*} as in the resolved test. The 245 galaxies in the preceding test and previous comparison positions were excluded.

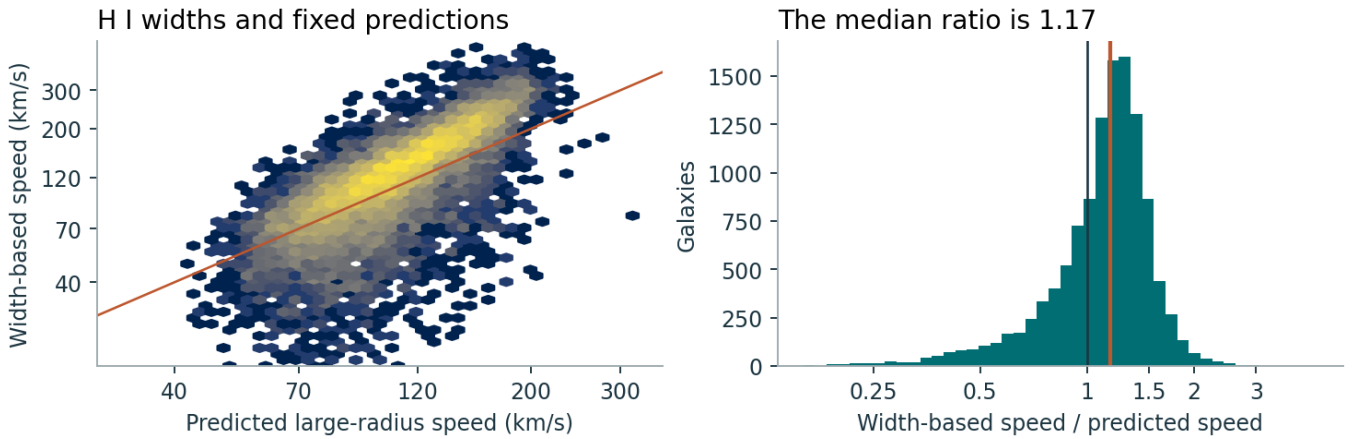

Each galaxy contributes once. Brighter regions contain more objects. The orange diagonal marks agreement. The histogram shows how far each galaxy's measured width-based speed lies above or below the prediction.

Stellar-mass estimate	Galaxies	Median speed ratio[1]	Median |error| (km/s)	Within 20%
Taylor	11,758	1.167	26.0	40%
McGaugh	11,647	1.092	22.1	51%

[1] Width-based speed divided by the predicted asymptotic speed. Taylor optical masses define the primary test. The McGaugh photometric prescription is a sensitivity check on the subset where both inputs exist.

We corrected W_{50} for inclination and redshift and divided it by two. Published widths already include the instrumental correction. Turbulence, profile shape and where the gas is emitting can change the result. At fixed Taylor masses the acceleration-law asymptote had a median ratio of 1.100 and median absolute error of 22.9 km/s. The core's 16.7% median excess in measured relative to predicted speed identifies a calibration or tracer mismatch worth resolving with direct outer velocities.

ALFALFA and optical counterpart tables · ALFALFA width conventions

Do magnetic fields predict the errors?

The LOFAR survey estimated field strength from radio emission under an energy-equipartition assumption. Of 39 published galaxies, 14 matched SPARC galaxies with held-out speed predictions. Stronger average fields had a weak negative association with the outer speed discrepancy (Spearman ρ = −0.30, two-sided permutation p = 0.30). The discrepancy is the median measured minus predicted speed in the outer third of each observed curve.

Leaving one whole galaxy out at a time, the mean absolute error was 16.3 km/s with the original speed, 16.5 with a constant correction and 18.9 with a correction based on log field strength. Adding field strength to a correction based on predicted outer speed moved error from 16.9 to 17.7 km/s. The published field errors are large and several systems are nearly edge-on.

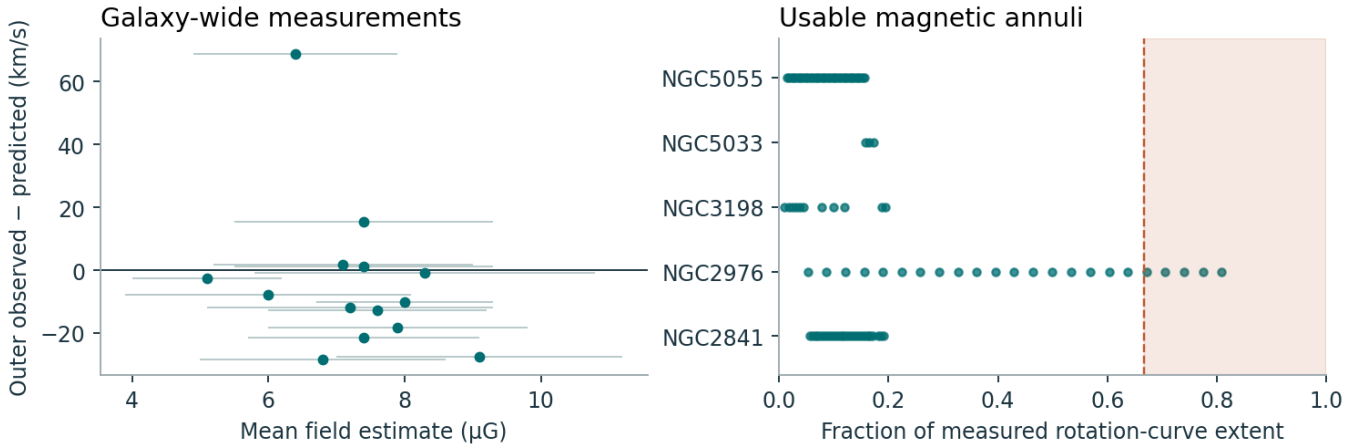

The 14 field estimates appear on the left with their published uncertainties. Each mark on the right represents a usable magnetic annulus. The shaded region is the outer third of the measured rotation curve.

Galaxy	Matched / digitized rings	Last match / last speed (kpc)	Outer rings
NGC2841	28 / 40	12.1 / 63.6	0
NGC2976	23 / 24	1.8 / 2.3	5
NGC3198	11 / 12	8.6 / 44.1	0
NGC5033	3 / 56	7.7 / 44.6	0
NGC5055	37 / 69	8.5 / 54.6	0

We digitized 201 measured annuli from the original authors' five applicable radial profiles, converted their radii to the SPARC distance, and matched 102 inside kinematic brackets at most 1.5 kpc wide. A radius-plus-field correction improved three of five individual results relative to radius alone, while median galaxy RMSE rose from 25.7 to 35.8 km/s. The mean of galaxy RMSEs fell slightly, from 32.1 to 31.4. The original uncorrected predictions had a median RMSE of 12.9. Neighbouring annuli share a radio beam and each withheld galaxy was excluded in its entirety. Only NGC 2976 supplied outer-third matches, even when the bracket limit was relaxed.

Heesen et al. (2023) · Heesen electronic tables

What would explain NGC 2403?

At 20.87 kpc the gas was measured at 134.0 ± 3.12 km/s. The frozen prediction was 114.90 km/s. Closing that 19.10 km/s gap requires an additional inward acceleration of about 7.4×10^{-12} m/s² at that radius.

Westerbork detected polarized radio emission from NGC 2403. Its integrated polarized flux was 28 ± 5 mJy and total intensity 360 mJy, giving roughly 7.8% polarization. The diffuse signal was faint even after 45-arcsecond smoothing. Heald and colleagues listed three unresolved background rotation measures and estimated a foreground of +11 ± 30 rad/m² from the field. A background source samples magnetized plasma along the entire line of sight.

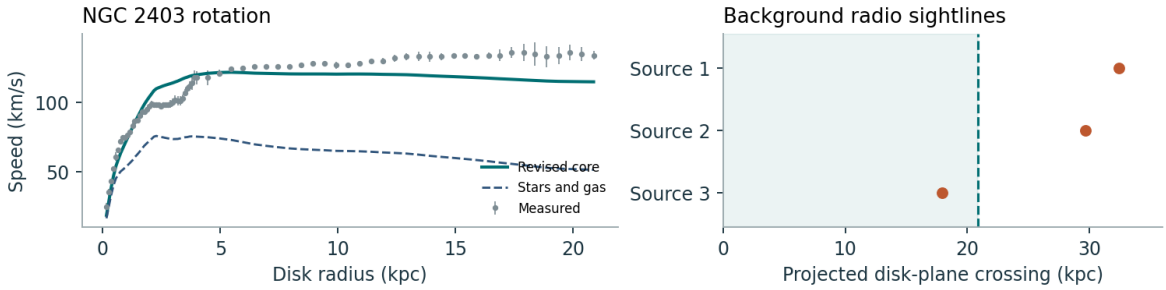

The shaded area spans the measured rotation curve. Only source 3 crosses that portion of the disk plane. The radio positions locate pencil-beam paths and supply no local disk force measurement.

Background source	Rotation measure (rad/m²)	Sky radius (kpc)	Disk-plane radius[1] (kpc)
sightline 1	+13 ± 3	16.4	32.4
sightline 2	-22 ± 3	13.5	29.7
sightline 3	+42 ± 2	10.9	17.9

[1] Geometric crossing of the assumed disk midplane at distance 3.16 Mpc, inclination 63° and major-axis position angle 124°. The foreground estimate shares these sightlines. Subtracting it as an independent, precise estimate of NGC 2403's field would overstate the information.

A measurable target for the gas

For a steady, axisymmetric, purely azimuthal ordered field in a conducting fluid, the inward magnetic contribution to the squared speed is

$$\Delta V^2_{mag} = [B_\varphi{}^2 / (\mu_0\, \rho)]\, [1 + d \ln |B_\varphi| / d \ln r].$$

At this radius $V^2_{obs} - V^2_{core} = 4{,}754$ (km/s)². If the hydrogen number density were 0.10 cm⁻³, with helium included in the gas mass, a locally constant azimuthal field would require **11.8 μG**. A field falling as $r^{-½}$ would require **16.7 μG**. If it falls as r^{-1}, tension and magnetic pressure gradient cancel in this geometry. A steeper decline gives an outward contribution. The assumed density and slope are scenarios. The available radio values do not determine them at 20.87 kpc.

This predicts a sign as well as a size. To test it, combine the direction and radial slope of the ordered field, gas volume density and gas rotation in the same outer annuli. Stellar motions in the same region give an independent control because ordinary magnetic stresses act directly on conducting gas. A universal spin–gravity coupling would require its own stellar and lensing predictions.

Heald, Braun & Edmonds (2009) · Elstner et al. (2014) · SPARC data and mass models

Spin and field strength in magnetars

Two magnetars reveal how much the choice of magnetic measurement changes the proposed ESFD threshold. A period and its rate of change estimate a large-scale dipole. A spectral line can sample a much stronger field in a small region near the star.

$$\chi = (2\pi/P)\, B / \Lambda, \quad \Lambda = 6.28 \times 10^{14}\ \mathrm{G\ rad/s}.$$

Here P is the rotation period, B is the specified magnetic field and the proposed boundary is $\chi = 1$. We evaluated the scalar field-magnitude version at maximum coupling. An orientation-dependent projection or a core-volume average would define a different test. With the usual rotation-derived dipole B proportional to $\sqrt{(P\,\dot{P})}$, this index depends on $\sqrt{(\dot{P}/P)}$ and therefore largely repeats a spin-down age measure. Spectral measurements supply independent information.

SGR 0418+5729 showed a phase-dependent feature spanning about 1–5 keV with P = 9.0784 s. The main feature of Swift J1822.3−1606 spanned about 5–12 keV with P = 8.4377 s. Under a proton fundamental identification, $B \approx 10^{14}\ \mathrm{G} \times E(\mathrm{keV}) \times (1 + z)/0.63$. Taking z = 0.25 yields the following dimensionless ratios.

Magnetar	χ from timing	χ from local line	Photon energy at χ = 1
SGR 0418+5729	0.0066	0.22–1.09	4.57 keV
Swift J1822.3−1606	0.0356	1.18–2.82	4.25 keV

The SGR range crosses one and the Swift range lies above it. Both remain below using timing dipoles. The range is sampled over rotational phase and can result from seeing different parts of a magnetic structure. It does not time a physical transition of the star. Changing z between 0.15 and 0.35 shifts inferred fields proportionally. An electron fundamental would reduce the inferred field by roughly a factor of 1,840 at the same redshift.

What the stellar branch can predict next

These two sources were selected because they exhibit a measurable feature. They cannot estimate event rates or the fraction of magnetars crossing the boundary. A predictive threshold needs to name the field in advance, specify an observable event such as a flare during a defined interval, and predict its rate or onset. A sample covering both event and quiet epochs, with observing exposure recorded, could then be compared with the ordinary timing, field and activity measures. A claim about global collapse additionally requires a mechanism connecting the local volume to the star as a whole.

Tiengo et al. (2013) · Rodríguez Castillo et al. (2016)

What the superconducting experiment measured

Carter, Pate and Goedecke drove an electromagnet beneath a cooled YBCO disk and measured the field needed to lift it. We recovered all 27 plotted measurements and their two-axis reading uncertainties from the original vector figure, then refit the experiment.

The disk measured 14 mm across and 6 mm thick at 77 K. Under Faraday's law, a sinusoidal field produces pickup-coil peak voltage $V = 2\pi f\, N\, A\, B_{peak}$. At a fixed levitation threshold, constant field therefore gives a straight voltage-versus-frequency line. We fit an intercept to absorb instrument offset and used errors along both axes.

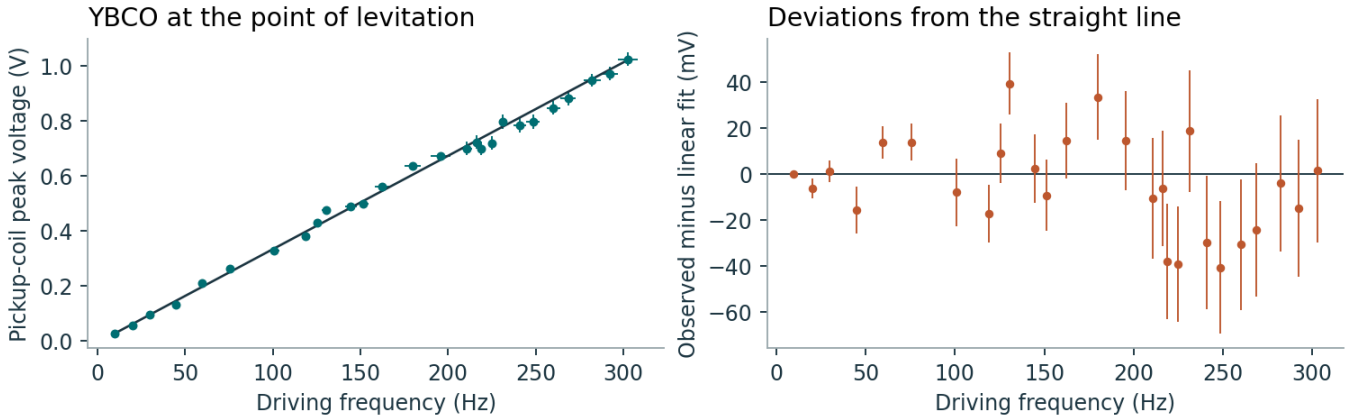

The pickup-coil voltage rises with frequency at the levitation threshold. The right panel shows the residuals against the fitted straight line, with the voltage and frequency reading errors propagated to the voltage axis.

Voltage fit	Offset (V)	Linear term (mV/Hz)	χ² / d.o.f.	Held-out RMSE (mV)
Linear	-0.0068	3.400	1.52	22.1
Quadratic	-0.0095	3.576	1.35	20.6

The recovered slope of 3.400 mV/Hz closely reproduces the published 3.4 ± 0.03 mV/Hz, equivalent in their apparatus to 37.2 ± 0.3 mT RMS. The gently curved fit improves held-out error by about 1.5 mV. Smooth curvature supplies no measured resonant frequency. A narrow mode between sampled frequencies, a different geometry and a different material remain separate hypotheses. This is a reanalysis of one specimen and a magnetic-levitation readout.

A separate NASA experiment reported an acceleration change below 2×10^{-8} g in its YBCO configuration with a 0.6 T DC field, 60 Hz lateral AC excitation and rotation. The project's driven-superconductor proposal needs a specified mode, frequency, line width, coupling and an independent gravity readout. A frequency peak in coil voltage or specimen motion alone cannot identify gravity cancellation.

Carter, Pate & Goedecke (2012 preprint) · Noever et al. (1999), NASA NTRS

What connects the rest of ESFD?

The galaxy result earns the revised formula a place as an empirical predictor. The unified claim requires a common spin–field interaction whose measured strength in one setting makes a successful prediction in another.

Research branch	Evidence and a discriminating test
Spin, rotors and superconductors	The original spinning-top observation motivates reversal tests. At fixed mechanics and temperature, a theory must predict the change when rotation or magnetization reverses, after ordinary friction, induction and magnetic forces are accounted for.
Maxwell and standing waves	The master calculates interference and field invariants. An extra degree of freedom needs a predicted frequency, polarization, energy scale or phase signature beyond the ordinary electromagnetic and material response.
Pulsars, magnetars and compact stars	The observations in this chapter show that a surface field and a timing dipole can put a single source on opposite sides of the same threshold. Specify field, geometry, event and exposure before extending to another star.
Gravitation, lensing and cosmic structure	The previous master includes an independent weak-lensing comparison under an assumed conversion from the disk law. A universal theory must calculate both matter acceleration and light deflection from its stress-energy or metric, including clusters and filaments.
Quantum spin, Higgs and the E_8 proposal	An explicit, dimensioned interaction is needed to derive low-energy coefficients and an observable residual after known magnetic moments and quantum effects. The empirical galaxy acceleration supplies no such matching relation.
Collapse, white holes and daughter universes	The existing homogeneous bounce is a mathematical example. Extending it to a physical prediction requires an exterior spacetime, consistent horizon evolution and an observational signature that distinguishes the outcome.

The accompanying research package contains the previous 106-page master, its 75-entry research register, the recovered archive and equation guide, the three supplied source papers, the pulsed-superconductor work and this chapter’s data and executable Python. Upstream input transformations, selection reasons, every scored prediction and per-galaxy results are included. A fresh replay of the earlier master and pulsed-superconductor packages reproduced all 104 archived numerical result files byte for byte. Some historical simulations and the complete v150 manuscript remain unavailable. The derivation connecting magnetic-field measurements, laboratory response and the galaxy coefficients remains open.

Christopher Grenke's ESFD research program · November 23, 2026

NGC 2403 and the missing outer speed

At 4.97 kpc the shared core equation predicts 121.6 km/s and the gas moves at 121. At 20.87 kpc it predicts 114.9 and the gas moves at 134 ± 3.1. The equation levels off too early to compensate for the falling contribution of the observed stars and gas.

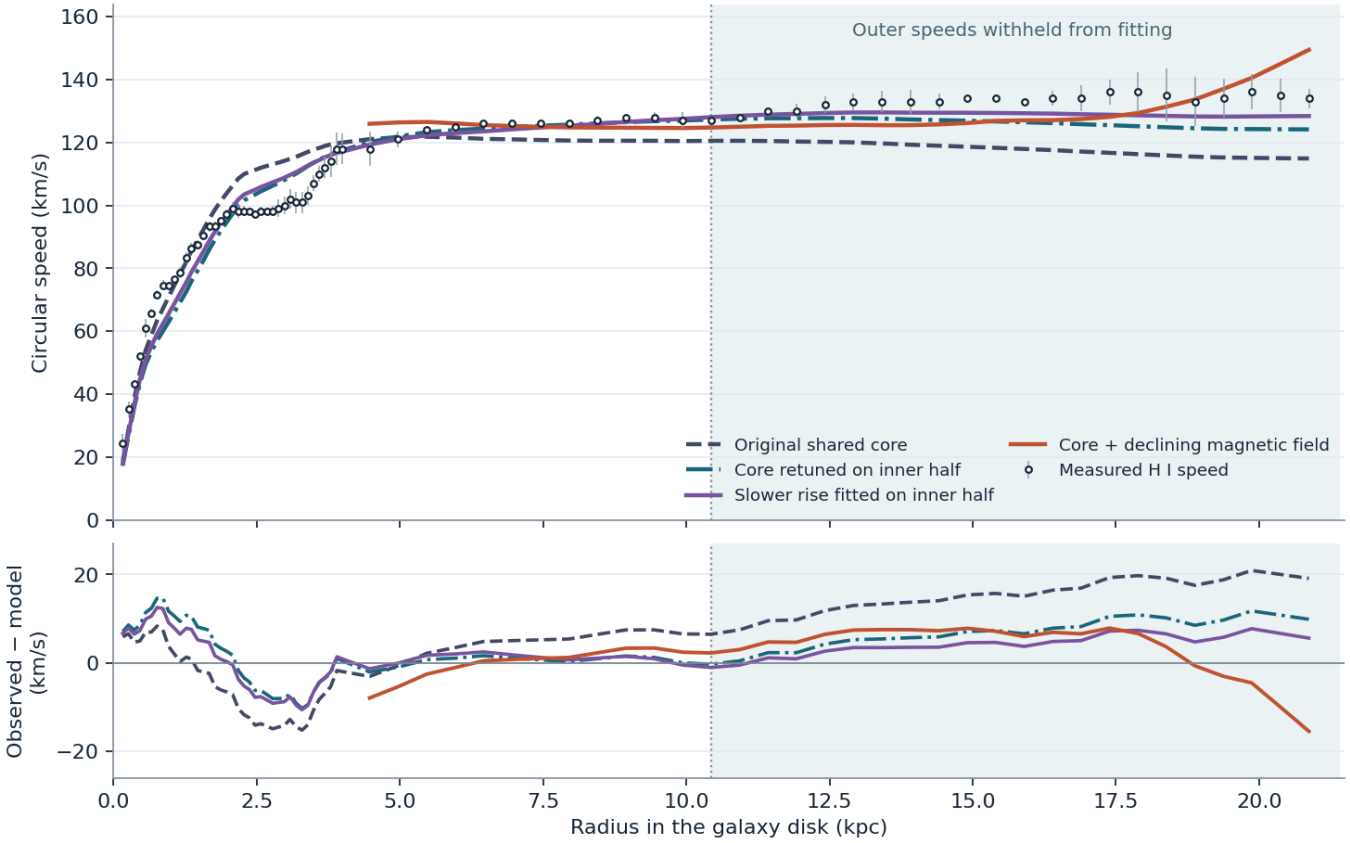

Figure 1. The shaded region contains the 21 radii held out of the local fits. In the lower panel, positive values mean the galaxy rotates faster than the equation predicts. The magnetic curve uses measured H I columns, an assumed 1 kpc gas scale height, and an inner-disk estimate of the field amplitude.

The original shared core missed the outer points by 16.0 km/s root-mean-square. Retuning its two coefficients cut that to 7.8. A slower-rising core gave 4.9. A magnetic correction gave 7.0 under the primary assumptions, yet overshot the last measurement by 15.5 km/s.

A radio reanalysis shows a spiral field pattern. A separate compilation estimates a galaxy-wide total field of 5.7 μG. The crucial quantity is the strength *and radial change* of the field circling the galaxy in the 20–22 kpc gas ring. The available observations do not determine either quantity there. [1–5]

What goes wrong in the two equations

The gray “stars and gas” curve in the original figure gives the speed expected from the measured baryonic mass distribution. The project’s orange spin–entropy flux curve and teal revised core add a contribution to *squared* speed. The galaxy’s falling baryonic contribution makes the radial shape of that addition decisive. [1]

$$v_{core}^2 = v_{bar}^2 + \sqrt{(G\, M_{bar}\, a_*)}\; r^2 / [r^2 + (\eta R_d)^2]$$

Here r is radius, G the gravitational constant, M_{bar} the adopted stars-plus-gas mass, R_d the stellar disk scale length, a_* an acceleration scale and ηR_d the core radius. For this galaxy the inputs are 9.275 × 10^9 solar masses and 1.39 kpc. The shared coefficients are $a_* = 0.920 \times 10^{-10}$ m/s² and η = 1.352. Inner tuning gives 1.383×10^{-10} and 2.233, expanding the core from 1.88 to 3.10 kpc.

$$v_{flux}^2 = v_{bar}^2 + (G\, M_{bar}/r)\; A\; (r/R_d)^2\; \exp[-r/(\lambda\, R_d)]$$

This is the archived computable SEFD spin–entropy flux prescription. Its extra term scales as $r \exp[-r/(\lambda R_d)]$, so it peaks at λR_d and then falls. The frozen and retuned peak radii are 9.19 and 13.86 kpc. The revised core flattens instead. Both eventually supply too little inward acceleration here. The slower-rise comparison uses the profile $1 - \arctan(x)/x$, with $x = r/(\eta R_d)$. It also occurs in a pseudo-isothermal halo. Rotation fits alone cannot identify which physics produced that shape.

Radius	Observed	Stars + gas	Shared core	Extra v² required	Extra v² supplied
4.97 kpc	121.0	74.1	121.6	9,157	9,311
20.87 kpc	134.0	51.4	114.9	15,310	10,556

Speeds are in km/s. Squared speeds are in (km/s)². At the endpoint the missing 4,754 (km/s)² corresponds to 7.38×10^{-12} m/s² of inward acceleration. The speed gap itself is 19.1 km/s.

Holding the published line-of-sight speed and the model fixed, correcting the last point by inclination alone would require $\sin(i) = 1.039$. That simple adjustment is impossible. A varying disk position angle, distorted gas, incomplete azimuthal sampling or a changed mass model can still shift a fitted outer speed. The original H I analysis identified a separate, slower gas component. [1, 2, 6]

How much of the outer curve can we predict?

I froze distances, inclinations, baryonic decompositions and galaxy-fold assignments from the preceding master. For NGC 2403 the adopted distance is 3.16 Mpc and the inclination is 63°. Measured speeds at 52 radii through 10.435 kpc determined local coefficients. I scored all 21 farther radii with no additional velocity fitting. The previous diagram had already revealed the endpoint miss, so this is a retrospective extrapolation test. [1]

Model and parameter source	Outer RMSE	Speed at 20.87 kpc
Stars + gas + original flux, shared parameters	19.89	102.19
Stars + gas + original flux, inner fit	8.63	119.83
Revised core, shared parameters	15.98	114.90
Core, amplitude retuned	14.15	116.85
Core, amplitude and size retuned	7.80	124.15
Slower-rise profile, two inner-fit parameters	4.90	128.40
Constant from last three inner speeds	6.64	127.00
Radial acceleration relation, training-galaxy calibration	9.34	124.00
Shared NFW halo calibration from the archive	14.00	114.90
Shared Burkert halo calibration from the archive	21.11	105.23
Core + inner-fit declining field, whole-ring gas	7.04	149.46
Measured endpoint	—	134.00 ± 3.12

All speeds and errors are in km/s. RMSE is the square root of the average squared speed error. The shared curves were calibrated with other galaxies. Each occupied 1 kpc bin has equal total weight in the local training loss. The magnetic fit uses the 13 training radii at or above 4 kpc. Frozen halo rows describe these specific calibrations.

The fit depends on how much of the disk we already know. Training through only 5 kpc gives outer errors of 23.68 for the retuned core and 19.30 for the slower rise. Training through 40% gives 8.14 and 4.62. At 60% the errors are 7.06 and 4.47, and a simple constant scores 4.26. Fitting all 73 speeds yields a final 133.10 for the slow profile. That last value uses the measurements it describes.

Where the radio observations actually reach

Heald and colleagues detected diffuse polarized synchrotron emission in NGC 2403, typically 30–50 μJy per beam after smoothing, with brighter patches near 100 μJy per beam. Their integrated polarized flux was 28 ± 5 mJy. Drzazga's 2014 reprocessing of the same observations recovered an asymmetric spiral pattern and a Faraday-depth map, with most polarization on the western side. The latter used 765 frequency channels and a 49.5″ × 45″ beam. [3, 4]

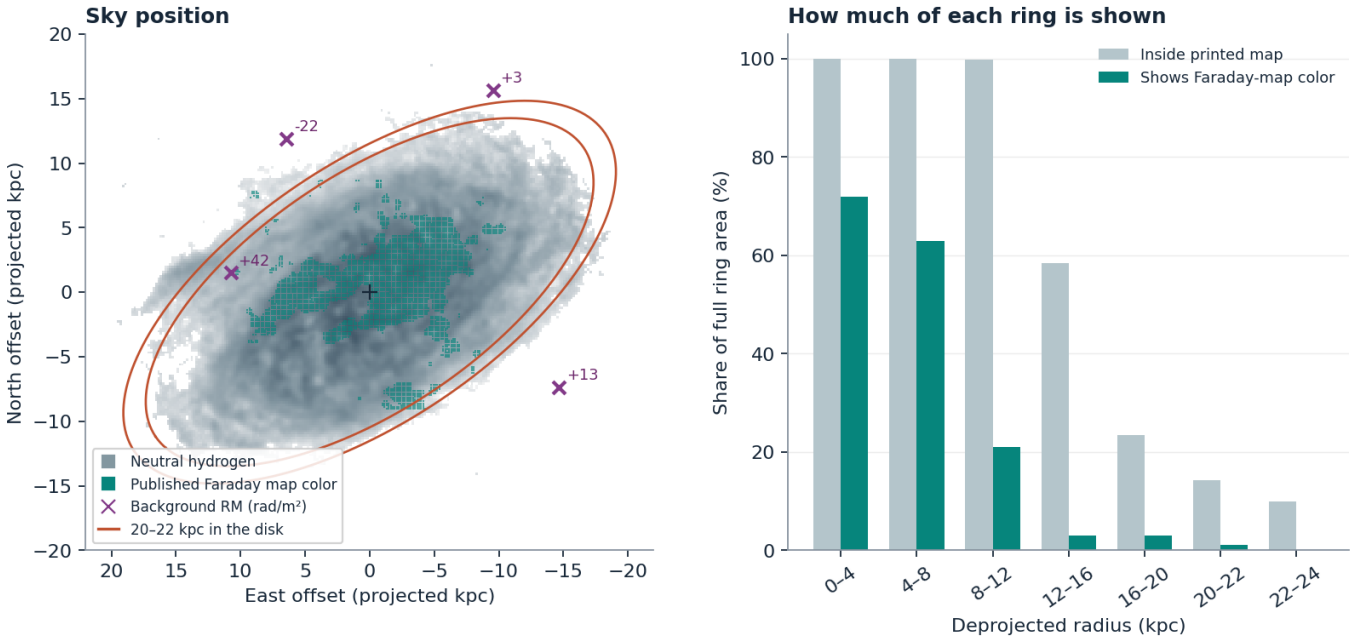

Figure 2. East is on the left. The pale gray disk is measured H I. Teal marks colored pixels in Drzazga's Fig. A.3 as registered from its printed coordinate ticks. They indicate where peak Faraday depth is displayed. The purple crosses are distinct background sources. Blank areas can result from sensitivity, depolarization or the figure boundary.

In the adopted geometry, the printed map includes approximately 14% of the area of the 20–22 kpc ring. About 1.1% of the full ring shows plotted Faraday-depth color. These pixels lie near the projected minor axis, where circular rotation produces little line-of-sight velocity. Changing inclination by ±3° and position angle by ±5° gives 0–2.7% displayed color for the full ring. This estimate measures published figure coverage. The original survey field of view can extend farther.

The consolidated RM catalog has a +42 ± 2 rad/m² background-source measurement at a projected disk radius of 17.95 kpc. An independent NVSS value is +3.3 ± 15.4 at 23.70 kpc. The searched RM catalog has zero entries in the 20–22 kpc ring. Its one NVSS catalog *continuum* component has polarized flux 0.49 ± 0.51 mJy, below even a 3σ selection. The three Heald sightlines also underlie the quoted Milky Way foreground of +11 ± 30 rad/m². Subtracting it as an independent measurement would double-count information. [3, 7, 8]

What a magnetic force would have to do

Relativistic electrons spiraling in a magnetic field emit polarized radio waves. Their polarization tells us about field orientation and about material crossed on the way here. An ordered field can also bend and exert tension on magnetically coupled gas. Inward tension competes with the radial magnetic-pressure gradient. Detecting radio waves, even polarized ones, does not establish wave interference or the size and direction of this force. [3, 4, 9]

> $\Delta v_B^2 = [B_\varphi^2/(\mu_0\rho)]\,[1 + d \ln |B_\varphi|/d \ln r]$

This steady, axisymmetric illustration keeps a toroidal field, B_φ, and gas mass density ρ. A slowly declining field can add inward force. If $B_\varphi \propto 1/r$ the tension and pressure cancel. A steeper local decline reverses the sign. Vertical and radial fields, random-field pressure, cosmic rays, gas pressure, spiral shocks and departures from steady motion can all change the calculation. Earlier MHD work found that outer-disk fields can impede rotation. [9]

From the HALOGAS 20–22 kpc ring, the coarser map gives a face-on neutral hydrogen column of 2.33 × 10^{19} atoms/cm², or 0.187 solar masses/pc² of H I. The higher-resolution map gives 1.48 × 10^{19}. The fractions of positive pixels in the source-masked maps are 44% and 21%. Detected pixels alone give 5.27 and 6.89 × 10^{19}. These are two different ways of averaging patchy gas. Unseen gas below the mask and other phases can raise the relevant mass density. [2]

For a Gaussian layer with a 1 kpc vertical standard deviation, $n_H = N_{HI,face}/(\sqrt{(2\pi)}\, h)$ gives 0.0030 hydrogen atoms/cm³ for the coarse whole-ring mean. Taking $\rho = 1.4\, m_p n_H$, the table gives the local field needed to close the old core's entire endpoint gap.

Gas sampled in coarse map	Locally constant Bφ	Bφ declines as $r^{-1/2}$
Whole ring	2.05 μG	2.91 μG
Detected pixels	3.09 μG	4.37 μG

Chyży and colleagues estimate 5.7 μG for this galaxy's *average total* field under synchrotron energy equipartition. Its presence makes an outer-field test meaningful. The local circling component and its slope at 20.87 kpc remain unknown. At fixed column the required field varies as $1/\sqrt{h}$. Changing h from 0.5 to 1.5 kpc moves the coarse whole-ring target for the declining field from 4.11 to 2.37 μG. [5]

Putting the field into the velocity prediction

I fixed the old core, tested $B_\varphi(r) = B_{10}(r/10\ \mathrm{kpc})^s$ with $s = 0$ or $-½$, and inferred only the nonnegative amplitude from speeds between 4 and 10.435 kpc. The measured hydrogen columns at each outer radius enter the prediction. All outer velocities stay out of the fit. The primary case uses the coarse whole-ring column and a 1 kpc height.

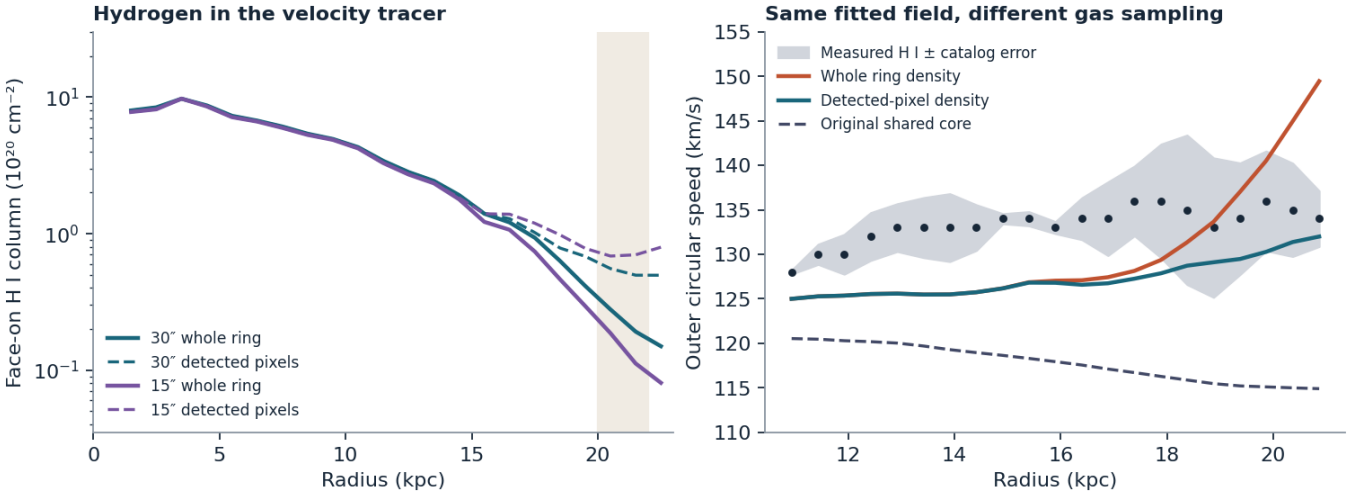

Figure 3. Both solid velocity curves use the same magnetic amplitude fitted in the inner disk. They diverge in the outskirts because the two gas-density averages diverge there. The shaded observed range uses the quoted point errors only.

A constant 5.12 μG field predicts 203.1 km/s at the tip and an outer RMSE of 24.53. A field falling as $r^{-½}$ fits B_{10} = 5.97 μG, scores 7.04 and reaches 149.46. The same declining field using only pixels with detected gas gives 132.00 at the endpoint and an outer RMSE of 6.33. The higher-resolution whole-ring calculation reaches 164.61. Choosing the gas sample because it matches 134 would use the answer to define the model.

An exploratory test ties B_{10} to the published 5.7 μG disk mean with no velocity fitting. At an assumed fraction of one half and slope $-½$ the last prediction is 123.63. At fraction one it is 146.73. The unknown fraction prevents a unique prediction from the radio measurement.

As a thickness sensitivity, the included calculation uses the flaring profile digitized from the 2024 Bacchini et al. figure. It is a hydrostatic modeling result, reaching 18.6 kpc after distance rescaling. Holding its last height, roughly 0.81 kpc, beyond that radius gives 183.6 on the coarse whole-ring declining-field test. The journal lists a 2026 corrigendum whose implications for that profile were unverified here. The primary fixed-height results are independent of this source. [10]

Can the result travel to other galaxies?

I applied NGC 2403's inner-fit coefficients without adjustment to 245 separate PROBES galaxies and repeated the comparison on 130 other SPARC galaxies. The external sample contributes 16,120 velocity entries. Each galaxy counts once in the median. Both cohorts come from the previous release's eligibility and cross-match rules. PROBES uses different baryonic inputs and samples a different distribution of radii. [1, 11]

Model applied to other galaxies	PROBES median RMSE	Improved / 245	Other SPARC median
Original shared core	29.92	—	12.55
NGC 2403 amplitude alone	29.02	176	12.38
NGC 2403 amplitude and core size	34.01	36	13.88
NGC 2403 slower-rise coefficients	32.66	40	14.11

Units are km/s. The paired median change for the two-coefficient core is +5.55 km/s, with a galaxy-bootstrap 95% interval of +4.97 to +5.98. A positive change means greater error. The amplitude-only change was promising on PROBES, though it improved only 58 of the 130 other SPARC galaxies.

A different question is whether each galaxy's own inner speeds help predict its outer speeds. On the 242 PROBES objects with adequate sampling, this cut median outer error from 26.76 to 23.31 km/s and improved 141 of them. A flat extrapolation gave 24.77. In 60 galaxies the two-parameter fit reached a parameter bound. For 94 eligible other SPARC disks, the corresponding errors were 12.54, 9.24 and 10.01.

I also applied NGC 2403's fitted magnetic amplitude and slope to two other HALOGAS disks, using each galaxy's own hydrogen map and the same assumed 1 kpc height. These were a small direct check on the field prescription. Their old curves already overpredicted the endpoint, so adding an inward force pushed both farther from the measurements.

Disk and sampled range	Radii	Old core RMSE	Declining field RMSE
NGC 3198, 11.04–20.05 kpc	6	7.30	9.45
NGC 5055, 11.49–20.07 kpc	4	34.33	36.62

With no velocity fitting, substituting each control's own published total-field estimate, 4.9 and 8.5 μG, as the circling component at 10 kpc also worsens both errors. A common correction needs an independently observable way to predict its sign and amplitude. [2, 5]

An observation that could decide the case

Target both ends of the projected major axis from 15 to 23 kpc. At 20.87 kpc the two centers are (RA, Dec) = (114.96745°, +65.38907°) southeast and (113.44848°, +65.81224°) northwest in J2000 coordinates, 22.70′ from the center. Add comparison pointings near the minor axis and beyond the disk. Obtain sensitive broadband Stokes Q and U, multi-frequency synchrotron intensity, and a grid of background rotation measures. Sensitivity to diffuse angular scales, thermal-emission removal and a model for cosmic-ray electrons matter for converting brightness to field strength. Foreground rotation, turbulent fields and the density of free electrons matter for interpreting Faraday depth. Measure gas thickness or constrain it from independent observations and fit the projected H I velocity field with a varying disk geometry. [3, 4, 6, 9]

The specific prediction is a positive inward contribution of roughly 7.4×10^{-12} m/s² at 20.87 kpc relative to the shared core. Freeze the reconstructed field and gas-density model before computing gas speeds in the reserved sectors. If the independently constrained circling field falls locally as $1/r$ or faster, this axisymmetric term cannot supply that positive gap. Compare both disk sides and compare young or old stellar tracers where feasible. A gas-specific force and an additional gravitational potential can have different observational signatures.

The new release includes the gas maps at two resolutions, magnetic catalog positions, the registered published map support, all model predictions and source code. It also includes an explicit inverse calculation. For an assumed density it integrates $\mathrm{d}(r^2 B_\varphi{}^2)/\mathrm{d}r = 2r\,\mu_0 \rho \Delta v^2$ in consistent units. A boundary field must be supplied. This reconstruction uses the velocity data and yields possible profiles for a later measurement to challenge.

Fixed-geometry checks on the 20–22 kpc H I velocity maps give about 127.4 and 130.1 km/s at the two beam sizes. Changing the position angle by 5° moves the coarse estimate to 135.8 or 139.5. This annular first-moment calculation and the catalog’s last point sample gas differently and share the same underlying VLA observations. A full cube fit and independent stellar velocities would improve the dynamical comparison. [2, 6]

The galaxy test evaluates an empirical galactic rotation law and an ordinary magnetic gas force. A favorable result could guide the galaxy branch of ESFD. A connection to the unified spin–field equations requires a derivation of the field law from those equations and independent predictions in the other branches.

Sources and reproducibility

1. SPARC data and mass models. Lelli, McGaugh & Schombert (2016). Rotation speeds, baryonic decomposition, distance and inclination.
2. HALOGAS Data Release 1. Heald and collaborators. Native column-density and velocity FITS. NGC 2403 uses archival VLA AS649 observations from Fraternali et al. (2002).
3. Westerbork SINGS II. Heald, Braun & Edmonds (2009), §4 and Table 1. Diffuse polarization, integrated flux and background lines of sight.
4. Galactic magnetized plasma exposed to winds and tidal interactions. Drzazga (2014), dissertation Appendix A, Figs. A.2–A.3. Re-imaging of the same visibility data.
5. What drives galactic magnetism?. Chyży et al. (2017), A&A 603, A121. Galaxy-average equipartition fields from Table A.1.
6. THINGS high-resolution rotation curves. de Blok et al. (2008). Comparison of NGC 2403 curves and outer-ring geometry.
7. RMTable version 1.2.0. Van Eck et al. Consolidated rotation-measure catalog, including the Taylor et al. NVSS measurements. The LoTSS DR2 radio-polarization TAP catalog also returned zero entries within 2°.
8. 1.4 GHz NRAO VLA Sky Survey. Condon et al. (1998). Cataloged continuum sources and integrated polarized flux within 45 arcmin.
9. Do magnetic fields influence gas rotation in galaxies?. Elstner, Beck & Gressel (2014). Radial force from tension and pressure in galactic gas disks.
10. 3D local instability of cold gas disks. Bacchini et al. (2024), Fig. B.6. The optional sensitivity uses that edition. 2026 corrigendum DOI 10.1051/0004-6361/202662855e.
11. PROBES I rotation curves and photometry. Stone et al. (2022), survey release. The selected compact sample follows the preceding ESFD observational release.

This research made use of data from WSRT HALOGAS-DR1. The Westerbork Synthesis Radio Telescope is operated by ASTRON (Netherlands Institute for Radio Astronomy) with support from the Netherlands Foundation for Scientific Research NWO.

The research package contains the analysis choices recorded before fitting, input data, eight original HALOGAS FITS products, published-map digitization coordinates, 24-sector gas summaries, per-radius speed predictions, per-galaxy transfer scores and an offline Python runner. Assumptions and figure-derived quantities are identified in the tables and in the methods above.